THE HONG KONG POLYTECHNIC UNIVERSITY
香港理工大學
Pao Yue-kong Library
包玉剛圖書館

Copyright Undertaking

This thesis is protected by copyright, with all rights reserved.

By reading and using the thesis, the reader understands and agrees to the following terms:

1. The reader will abide by the rules and legal ordinances governing copyright regarding the use of the thesis.
2. The reader will use the thesis for the purpose of research or private study only and not for distribution or further reproduction or any other purpose.
3. The reader agrees to indemnify and hold the University harmless from and against any loss, damage, cost, liability or expenses arising from copyright infringement or unauthorized usage.

IMPORTANT

If you have reasons to believe that any materials in this thesis are deemed not suitable to be distributed in this form, or a copyright owner having difficulty with the material being included in our database, please contact lbsys@polyu.edu.hk providing details. The Library will look into your claim and consider taking remedial action upon receipt of the written requests.

Pao Yue-kong Library, The Hong Kong Polytechnic University, Hung Hom, Kowloon, Hong Kong

http://www.lib.polyu.edu.hk

LOW-CARBON ASPHALT MIXTURE WITH SOLID WASTE FILLERS: COMPOSITION-PERFORMANCE RELATIONSHIP INVESTIGATION AND OPTIMIZATION

JIAQIU XU

PhD

The Hong Kong Polytechnic University

This programme is jointly offered by The Hong Kong Polytechnic University and Harbin Institute of Technology

2026

The Hong Kong Polytechnic University
Department of Civil and Environmental Engineering

Low-Carbon Asphalt Mixture with Solid Waste Fillers: Composition-Performance Relationship Investigation and Optimization

Jiaqiu Xu

A thesis submitted in partial fulfilment of the requirements for the degree of Doctor of Philosophy

August 2025

CERTIFICATE OF ORIGINALITY

I hereby declare that this thesis is my own work and that, to the best of my knowledge and belief, it reproduces no material previously published or written, nor material that has been accepted for the award of any other degree or diploma, except where due acknowledgement has been made in the text.

________(Signed)

___Jiaqiu Xu______(Name of student)

To my family

ABSTRACT

Asphalt mastic, composed of bitumen and filler, plays an important role in the overall performance of asphalt mixture, as the bitumen-filler and mastic-aggregate interfaces are often weak locations where the deterioration of asphalt mixture initiates. Meanwhile, facing the challenges of global warming and climate change, recycling solid wastes into pavement, including using solid waste fillers, has become an effective approach for the transportation industry to achieve the carbon neutrality goal. However, solid waste differs significantly from traditional mineral fillers in terms of its physical and chemical composition, which can significantly affect the physico-chemical interactions at the bitumen-filler interface, and consequently the cohesive and adhesive properties of asphalt mastic.

Currently, a comprehensive understanding of the interfacial interactions between bitumen and solid waste fillers, as well as the composition–performance relationships governing the performance evolution of asphalt mastic under complex service conditions, has not been achieved yet. Furthermore, a holistic framework for the value-added application of solid wastes as fillers in asphalt pavement construction, including the evaluation of the mechanical properties of asphalt mastic and mixtures, environmental impact assessment, and life cycle assessment, is still missing.

To fill the above research gaps, three conventional mineral fillers (granite, basalt, and limestone) and five solid waste fillers (steel slag, desulfurization gypsum, blast furnace slag, expired cement, and iron tailings) were selected and investigated in this study. A multiscale approach was adopted to understand the behavior of the bitumen–filler interface, and elucidate the composition–performance relationship of asphalt mastic from two perspectives: qualitative analysis based on raw material characteristics and quantitative assessment based on micromechanics calculation. The investigation unfolds in a sequential manner. First, molecular dynamic (MD) simulation was conducted to reveal the interaction and failure mechanisms at

the bitumen-filler interface. Then, the composition-performance relationship between the composition of asphalt mastic and its mechanical performance was investigated through microscopic and macroscopic tests combined with multifactorial statistical analysis. Further, the micromechanical theory was applied to develop the composition-performance relationship between the microstructural parameters and the macroscopic modulus attributes of asphalt mastics. Finally, the optimum strategy for utilizing solid wastes as bitumen fillers in asphalt pavement systems was developed through comprehensive asphalt mixture tests, life cycle assessment (LCA), and leaching behaviour analysis.

Based on the analysis at the molecular level, it was found that mineral composition of the filler plays a crucial role in the interaction between bitumen and fillers. Compared with conventional mineral fillers, the rock-forming minerals of solid waste fillers exhibit significantly stronger interactions and adhesion properties with bitumen molecules. The failure mode of the bitumen-filler interface transits from pure adhesive failure to a combination of adhesive and cohesive failure, and eventually to complete cohesive failure as the tensile rate decreases. The results of microscopic and macroscopic tests validated the findings from the MD simulations. The synergistic evaluation framework developed in this study offers an accurate and comprehensive characterization of the interfacial interactions between bitumen and filler by integrating surface free energy theory, pull-off tests, rheological characterization, and the essential work of fracture theory. Unlike mineral fillers, solid waste fillers exhibit chemical reactions with weakly acidic bitumen, presenting more complex micro-morphologies that effectively increase the interaction area between bitumen and fillers. The high-temperature rutting resistance of asphalt mastic is jointly governed by the penetration of the bitumen and the particle size of the filler. The fatigue resistance shows a significant positive correlation with the resin content of the bitumen, as well as the specific surface area and fine particle content of the filler. The low-temperature property depends on both the penetration of the bitumen and the particle size parameters of the filler. Compared with classical micromechanical models, the modified Ju-Chen model (MJCM), which incorporates enhancements by solving the radial distribution function, achieves the highest accuracy in modulus prediction among all models, with an average fitting coefficient of 0.984 for all asphalt mastics. The combination of the two-step homogenization method and the MJCM overcomes the limitations of traditional micromechanical models, which enables precise prediction of the dynamic modulus of asphalt mixtures across the entire frequency range and successfully establishes the composition-performance relationship between the microstructural parameters of the mixture and its modulus. Asphalt mixtures with solid waste fillers, especially steel slag, expired cement, and iron tailings, exhibit superior resistance to rutting, moisture damage, and fatigue compared with those with conventional mineral fillers. Furthermore, LCA reveals that the use of solid waste substitution technology systematically optimizes key environmental indicators, such as ecosystem quality and resource availability, throughout the service life of pavement materials, providing a reliable technical pathway for green pavement construction. The outcomes of this study can serve as a reference for improving the theoretical system of bitumen-filler interface behaviour, improving the moisture stability of asphalt pavements, and enhancing the sustainability and durability of road infrastructure.

LIST OF PUBLICATIONS

Journal papers (Published)

Xu, J., Chen, Z., Zou, F., Leng, Z., Fan, Z., Lu, G., & Wang, D. (2025). Recycling solid wastes into asphalt mastics for low-carbon pavements: Performance investigation and environmental impact assessment. Journal of Cleaner Production, 530, 146851.

Xu, J., Pan, F., Fan, Z., Liu, J., Lu, G., & Wang, D. (2025). Multi-scale insights of recycling solid waste-based fillers into asphalt mastics: Surface adsorption configuration, microstructural morphology, and mechanical performances. Colloids and Surfaces A: Physicochemical and Engineering Aspects, 138920.

Xu, J., Fan, Z., Accornero, F., Wang, D., Carpinteri, A., & Cai, J. (2025). Atomic scale mechanism of bitumen-aggregate interfacial cracking: Insights from molecular dynamics simulation. Journal of Materials in Civil Engineering.

Xu, J., Fan, Z., Lu, G., Wang, D., & Liu, P. (2024). Effects of bitumen origins and filler types on the micromechanics prediction of complex modulus of asphalt mastics considering interparticle interactions. Journal of Materials in Civil Engineering, 36(1), 04023521.

Xu, J., Fan, Z., Wang, D., Leng, Z., Lu, G., & Liu, P. (2023). Experimental characterization of the compatibility between bitumen and fillers from a perspective of bitumen components and filler characteristics. Materials and Structures, 56(7), 116.

Journal papers (under review)

Xu, J., Zhang S., Fan, Z., Chen Z., Leng, Z., & Wang, D. Interfacial interaction behavior between asphalt and solid waste fillers: Atomic-scale debonding mechanism and experimental investigation[J]. Construction and Building Materials.

ACKNOWLEDGEMENTS

First and foremost, I would like to express my deepest gratitude to my chief supervisor, Professor Zhen Leng, the cornerstone of this remarkable academic journey. Professor Leng's erudition, optimism, and wit have been constant sources of inspiration. His ever-present smile and insightful guidance on both academic pursuits and career development have been invaluable. I particularly admire his rigorous self-discipline and unwavering composure. His invaluable advice, continuous support, and immense patience throughout my doctoral studies have nurtured my optimism, confidence, and intellectual curiosity.

My sincere appreciation goes to Professor Dawei Wang from Harbin Institute of Technology, my co-supervisor. His constructive feedback on my research, regular discussions about my academic progress, and timely solutions to research challenges have been instrumental in maintaining my focus and productivity.

I am deeply grateful to my colleagues at ZL Group. Despite arriving in Hong Kong during the challenging final phase of the pandemic, your companionship, assistance, and support transformed my three-year stay into an unforgettable chapter of my life. My heartfelt thanks also extend to my colleagues at Harbin Institute of Technology and Southwest Jiaotong University for their academic and personal support.

Last but certainly not least, I owe immeasurable gratitude to my parents. Your understanding, encouragement, and unconditional love have been the driving force behind my perseverance. To my fiancée, Ms. Ningpan Pan, our paths first crossed in the picturesque campus during our master's studies. Since then, through the laid-back charm of Chengdu, the icy winters of Harbin, to the vibrant cityscape of Hong Kong, you have been my steadfast companion on this journey of life. May we continue to embrace life's journey together, savouring its myriad flavours. To my parents-in-law, your unwavering support and encouragement behind every achievement of mine are truly cherished. Finally, to my beloved cat, Tuotuo - your joyful presence has been a constant source of happiness. May you continue to thrive and frolic in good health.

TABLE OF CONTENTS

LIST OF TABLES

LIST OF FIGURES

LIST OF ABBREVIATIONS

AASHTO	American Association of State Highway and Transportation Officials
AFM	Atomic force microscopy
ANOVA	Analysis of variance
ASTM	American Society for Testing and Materials
ATR	Attenuated total reflection
BBR	Bending beam rheometer
BBS	Binder bonding strength
BF	Blast furnace slag
CAM	Christensen-Anderson-Marasteanu
CED	Cohesive energy density
CLAYFF	Clay Force Field
CSM	Composite sphere model
CTOD	Crack tip opening displacement
CZM	Cohesive zone model
DALY	Disability-adjusted life years
DEM	Discrete element model
DENT	Double edge notched tension
DFM	Differential model
DG	Desulfurization gypsum
DM	Dilute model
DSR	Dynamic shear rheometer
EQ	Ecosystem quality
FEM	Finite element model
FI	Flexibility index
FTIR	Fourier transform infrared spectroscopy
GRA	Grey relational analysis
GSCM	Generalized self-consistent model
HH	Human health

H-MRP	Homogeneous morphologically representative model
HWT	Hamburg wheel-track
IT	Iron tailings
ITF	Indirect tensile fatigue
JCM	Ju-Chen model
LAMMPS	Large-scale Atomic/Molecular Massively Parallel Simulator
LAS	Linear amplitude sweep
LCA	Life cycle assessment
LCI	Life cycle inventory
MD	Molecular dynamics
MSCR	Multiple stress creep recovery
MSD	Mean squared displacement
MTM	Mori–Tanaka model
NPT	Constant number of particles, constant-pressure, and constant temperature
NVE	Constant number of particles, constant volume, and constant energy
NVT	Constant number of particles, constant volume, and constant temperature
PAV	Pressurized aging vessel
PCFF	Polymer Consistent Force Field
PG	Performance grade
PSM	Periodic structure model
P-Y	Percus-Yevick
RA	Resource availability
RDF	Radial distribution function
RTFO	Rolling thin-film oven
SARA	Saturates, Aromatics, Resins, and Asphaltenes
SCB	Semi-circular bending
SCM	Self-consistent model
SEM	Scanning electron microscopy
SFE	Surface free energy
SGC	Superpave gyratory compacted

SIP	Stripping inflection point
species.yr	Species lost in overtime
SS	Steel slag
SSA	Specific surface area
USD2013	U.S. dollar reference year in 2013
WLF	Williams-Landel-Ferry
XRD	X-ray diffractometer
XRF	X-ray Fluorescence
VECD	Viscoelastic continuum damage

CHAPTER 1 INTRODUCTION

1.1 Background

With the acceleration of global urbanization, the demand for asphalt mixtures in road transportation infrastructure construction continues to rise [1, 2]. Due to their excellent mechanical performance and durability, asphalt mixtures have become indispensable paving materials in modern road engineering [3-5]. According to modern mortar theory, the asphalt mixture is a three-phase dispersion system [6]. In this three-level dispersion system, the asphalt mastic composed of bitumen and filler plays an actual bonding role [7]. The bitumen-filler interface is the transition points between the rigid and flexible interfaces of the material structure, and the weak points of the structural strength of asphalt mixtures. The fatigue cracking damage of asphalt mixtures under repeated traffic loads and cyclic temperature loads, as well as the pavement moisture damage induced by environmental moisture intrusion into the bitumen-filler interface, are directly related to the adhesion performance of the interface. How to thoroughly reveal the physical and chemical nature of the interaction between bitumen and fillers, and elucidate the underlying mechanism and composition-performance relationship behind the mechanical performance of asphalt mastic, is not only a long-standing research hotspot and difficulty in the road engineering field, but also a key factor in enhancing the resilience and service durability of road infrastructure.

The complex physical and chemical interactions between bitumen and fillers are referred to as the bitumen-filler interaction, which includes the adsorption, diffusion, and infiltration of bitumen on the surface of fillers [8-11]. The macroscopic performance of asphalt mastics is highly influenced by the interaction between bitumen and filler. Therefore, precise characterization and evaluation of the interaction between bitumen and fillers can provide a deeper understanding of the performance and characteristics of asphalt mastics. Due to the significant changes in the macroscopic properties of asphalt mastics after adding fillers, early researchers used indicators such as penetration, ductility, softening point, and Brookfield viscosity to evaluate the interaction of between bitumen and fillers [12-14]. These methods can intuitively reflect the overall impact of fillers on asphalt performance, but the results are not accurate. Furthermore, researchers have proposed rheological-based methods to characterize the interaction between bitumen and fillers, including indicators such as complex modulus[15], phase angle [16], complex viscosity[17], and micromechanical models [9]. In addition, contact angle tests based on surface free energy theory [18, 19] and pull-out tests [20, 21] originally applied in the field of coatings have been introduced to characterize the interaction between bitumen and fillers. With the development of testing technology, the interaction between bitumen and fillers can be further studied from a microscopic or nanoscopic perspective. For example, scanning electron microscopy (SEM) and atomic force microscopy (AFM) can be adopted to investigate the changes in the microstructure and nanomechanical properties of bitumen due to the interaction between bitumen and fillers [22-24]. These methods can not only qualitatively analyse the interaction between bitumen and filler through morphological images, but also quantitatively study the mechanical properties of the bitumen-filler interface. Besides, the development of numerical simulation technology provides technical support for studying the interaction between bitumen and fillers at the molecular level. Molecular dynamics (MD) simulation technology can be used to study the interactions between different mineral components of fillers and different components of bitumen [8, 25-28]. These methods can help road researchers to select fillers based on mineral composition and explain the interaction mechanism of bitumen-filler at the molecular scale. It can be found that the characterization and evaluation of bitumen-filler interaction have become a hot topic and focus on the research field of asphalt pavements. However, the mechanism and characteristics of the physical and chemical interactions between bitumen and fillers are not fully understood so far.

According to the classical tetrahedron theory in materials science, the so-called " composition-performance relationship" refers to the relationship between the four vertices of the materials science tetrahedron [29]. In recent years, the concept of composition-performance relationship has gradually been introduced into the field of asphalt materials science [30, 31], aiming to characterize the relationship between the performance of asphalt materials and their compositional structure. In current domestic and international specification systems, the pavement performance of asphalt mixtures is primarily controlled by regulating various properties of bitumen. Nevertheless, in the three-dimensional dispersion system of asphalt mixtures, it is the asphalt mastic composed of bitumen and fillers, rather than bitumen alone, that performs the binding function in the dispersion system. Some researchers have even proposed that asphalt mixture design should be based on the mastic system. Undoubtedly, the performance of asphalt mastic is crucial in determining the durability and service performance of asphalt pavements. Therefore, to achieve better performance of asphalt mastic and consequently enhance the service durability of asphalt pavements, it is essential to conduct research on the composition-performance relationship of asphalt mastic's service performance.

Asphalt mastic and asphalt mixtures, being typical multiphase particulate composites, exhibit elastic characteristics under low-temperature or high-speed loading conditions, while demonstrating viscoelastic properties under high-temperature or high-stress loading conditions. Traditionally, the performance analysis of such materials has primarily relied on a combination of macroscopic testing and empirical formulas. However, this conventional approach fails to reflect the influence of the internal meso-structure of composites on their overall macroscopic properties and is both time-consuming and labour-intensive. Furthermore, particle interactions exist in composite materials across various dimensions, including asphalt mastic, asphalt mortar, and asphalt mixtures. Understanding these particle interactions under different temperature and loading conditions, as well as establishing the relationship between the meso-structure and macroscopic performance of composites—known as the cross-scale composition-performance relationship—has been a focal point for researchers. Micromechanics theory provides a framework for correlating the meso-structure, compositional characteristics, and interfacial constitutive behaviour of composites, enabling the characterization of the overall mechanical response of materials under external loads [32-35]. Therefore, developing micromechanical models for asphalt mastic and asphalt mixtures based on the mesoscale can establish quantitative relationships between the macroscopic mechanical performance and meso-structural parameters of the materials. This approach is significant for clarifying the cross-scale transfer mechanisms of the composition-performance relationship in asphalt mastic and mixtures, as well as for the refined design of asphalt pavement materials.

As a multiphase particle composite material, the asphalt mixture is mainly composed of various irregularly sized and randomly oriented aggregates embedded in the asphalt matrix. Filler refers to the finest aggregate in asphalt mixture (less than 0.075mm in the USA and China, and less than 0.063mm in Europe) [36, 37], which plays a role in filling small voids and serving as a skeleton structure in asphalt mixture and can significantly improve the density and strength of mixtures. In the entire composite system of asphalt mixtures, the asphalt mastic composed of bitumen and filler is the adhesive that adheres to the surface of the aggregate and provides adhesion. Therefore, the properties of fillers play a crucial role in the performance of asphalt mixtures. To ensure that the fillers have excellent performance, the most used fillers are mineral fillers made by grinding natural ores such as limestone, basalt, and granite. However, all these minerals are non-renewable resources. Every year, a large amount of natural mineral materials are consumed globally as fillers for asphalt mixtures, which imposes a huge burden on the natural environment. Furthermore, during the mining process of mineral fillers, a variety of environmental problems will be caused, such as serious damage to land resources and leading to disasters such as mudslides, collapses, and falling rocks, which in turn deteriorate the living environment and reduce crop yields. In addition to environmental issues, the inflation of virgin material costs and the gradual reduction in the number of natural resources have forced decision-makers to use waste/secondary materials as substitutes for traditional building materials. Therefore, seeking suitable alternative materials to alleviate the shortage of natural ores and conducting multi-scale research and analysis on the performance of mixtures has become a hot research direction in recent years.

In recent decades, the concept of sustainable development has received widespread attention and recognition in the field of civil engineering. In road engineering, the sustainable development goal of materials is to minimize and improve the impact of the project on the environment and enhance road resilience by reducing natural resource and energy consumption, reducing emissions, or improving solid waste recycling and utilization rates while meeting the performance requirements of pavement service. In recent years, world cities generate approximately 1.3 billion tons of solid waste annually, and it is expected to increase to 2.2 billion tons by 2025 [38]. The subsequent disposal and reuse of these solid wastes have always been a difficult problem for people, posing a great threat to global sustainability. Existing research indicates that mixtures with various solid wastes have similar performance in terms of construction performance and high- and low-temperature performance compared to traditional mineral aggregates, and some characteristics are even superior to traditional minerals [39-41]. Thus, it can be concluded that solid wastes replacing mineral fillers in asphalt mixtures are highly competitive and feasible, and research on this topic has also been common in recent years. However, current research lacks systematic and in-depth analysis regarding the application of various types of solid waste as fillers in asphalt mixtures. Furthermore, several critical issues remain to be addressed, including potential environmental safety concerns associated with the utilization of solid waste in asphalt pavements, as well as the life cycle assessment of replacing conventional mineral fillers with solid waste alternatives.

This project is based on this background and aims to open the multiscale field of cognition of bitumen-filler interface behaviour and promote the utilization of solid waste on asphalt pavements. Firstly, typical rock-forming minerals from solid waste and conventional mineral fillers were selected to construct filler molecular models and bitumen-filler interface models. The thermodynamic characteristics and surface adsorption configurations of the bitumen-filler interface were investigated using molecular dynamics simulations. A tensile simulation of the bitumen-filler interface was developed to elucidate the failure mechanisms, and a cross-scale analysis of bitumen-filler interactions was conducted in conjunction with macroscopic tests. Secondly, through the integration of macro- and micro-scale testing methods, the mechanical properties of asphalt mastic were meticulously examined. Grey relational analysis (GRA) was employed to explore the composition-performance relationship between the compositional structure of the mastic and its service performance. Thirdly, based on micromechanics theory, a composition-performance relationship between the meso-structural parameters and macroscopic modulus of asphalt mastic was established, and the complex shear modulus of the mastic was estimated. The Ju-Chen model was improved by solving the radial distribution function between particles, and a cross-scale composition-performance relationship construction scheme for asphalt mixture modulus was proposed by combining a two-step homogenization approach. Finally, the pavement performance of asphalt mixtures incorporating solid waste as fillers was comprehensively characterized through laboratory tests. The leaching behaviour of heavy metals and potential environmental risks during the service life of solid waste fillers were studied. The environmental advantages of recycling solid waste as fillers in asphalt pavements were quantified through LCA. The research findings are expected to provide valuable references for improving the theoretical system of bitumen-filler interface interactions, enhancing the resilience of road infrastructure, and increasing service durability.

1.2 Research Objectives and Scope

Based on the knowledge gaps discussed above, this project aims to advance the multiscale understanding of bitumen-filler interface behaviour and enhance solid waste utilization in asphalt pavements by investigating micro-nano scale interaction mechanisms and cross-scale composition-performance relationships. To this end, several research tasks should be completed and five subgoals are determined as follows:

(1) To reveal the effect of filler mineralogy on the interaction behaviour of the bitumen-filler interface and the adsorption configuration of bitumen on the filler surface.

(2) To explore the failure mechanism of the bitumen-filler interface at different loading rates and conduct a cross-scale analysis of bitumen-filler interactions in conjunction with macroscopic tests.

(3) To construct the composition-performance relationship between raw material characteristics, microstructure morphology, and macroscopic performance of asphalt mastics through macroscopic, microscopic, and nanoscopic investigations.

(4) To establish a comprehensive micromechanical model grounded in composite materials theory, which effectively accounts for particle interaction mechanisms, thereby achieving accurate characterization and prediction of the mechanical performance of asphalt mastic.

(5) To develop a composition-performance relationship framework that correlate asphalt mixture modulus with meso-structural characteristics based on micromechanics theory, facilitating precise modulus prediction of asphalt mixtures.

(6) To conduct performance comparison of asphalt mixtures with solid waste versus mineral fillers and quantify environmental benefits of recycling solid wastes as sustainable filler alternatives.

1.3 Significance of this Research

Upon the completion of this research, the following original contributions will be achieved:

(1) The adsorption configuration of bitumen on the filler surface and the failure mode of the bitumen-filler interface were revealed, which provided atomic-scale insights into the interaction mechanism of the bitumen-filler interface behaviour.

(2) The composition-performance relationship between the raw material properties of bitumen and filler and the service performance of asphalt mastics was established, which provides a basis for the performance optimization design of asphalt mastic system.

(3) Through solving the radial distribution function between particles, the micromechanical model was refined, successfully establishing a quantitative relationship between meso-structural parameters and macroscopic modulus characteristics of asphalt mastic, which significantly advances the understanding of its composition-performance relationships.

(4) Based on the improved micromechanical model combined with a two-step homogenization approach, a quantitative composition-performance relationship between meso-structural parameters and modulus characteristics of asphalt mixtures was successfully established, providing valuable guidance for the refined design of asphalt mixtures.

(5) The mechanical performance advantages and environmental benefits of recycling solid waste fillers to replace traditional mineral fillers in asphalt mixture production were quantified, which provides a win-win solution to alleviate the shortage of mineral sources and improper disposal of municipal solid wastes.

1.4 Research Framework

This dissertation is organized into eight chapters to fulfil the research objectives, as summarized below:

- Chapter 1 introduces the general background, research objectives, and scope of this research.
- Chapter 2 provides a comprehensive literature review on the experimental characterization of asphalt mastics from the macroscopic and microscopic scales, the micromechanical model prediction of performances of asphalt mastics, bitumen-filler interaction behaviour from an experimental perspective, MD simulation of bitumen-filler interaction behaviour, and recycling of solid wastes as bitumen fillers towards sustainable pavements, which helps to identify the research gaps.
- Chapter 3 presents a multiscale investigation of the interaction behaviour of bitumen-filler including the adsorption configuration, interfacial failure mechanism, and experimental characterization.
- Chapter 4 focuses on the composition-performance relationship qualitative analysis of the mechanical performance of asphalt mastics. Both macroscopic and microscopic tests were carried out on the asphalt mastics, and the grey relational analysis was conducted to investigate the qualitative relationship between raw material characteristics and performances of asphalt mastics.
- Chapter 5 investigates the micromechanical prediction of asphalt mastic modulus and the quantitative modelling of its composition-performance relationships. The Ju-Chen model was refined through solving particle radial distribution function, enabling accurate prediction of asphalt mastic's shear modulus. By integrating the modified Ju-Chen model (MJCM) with a two-step homogenization approach, a quantitative composition-performance relationship is established between meso-structural parameters and modulus characteristics of asphalt mixtures.

- Chapter 6 provides a comprehensive assessment of the recycling of solid wastes as asphalt mixture fillers towards sustainable pavements based on performance evaluation and LCA.
- Chapter 7 summarizes the major findings and conclusions of this research and provides recommendations for future studies.

The overall research framework of this dissertation is illustrated in Figure 1.1.

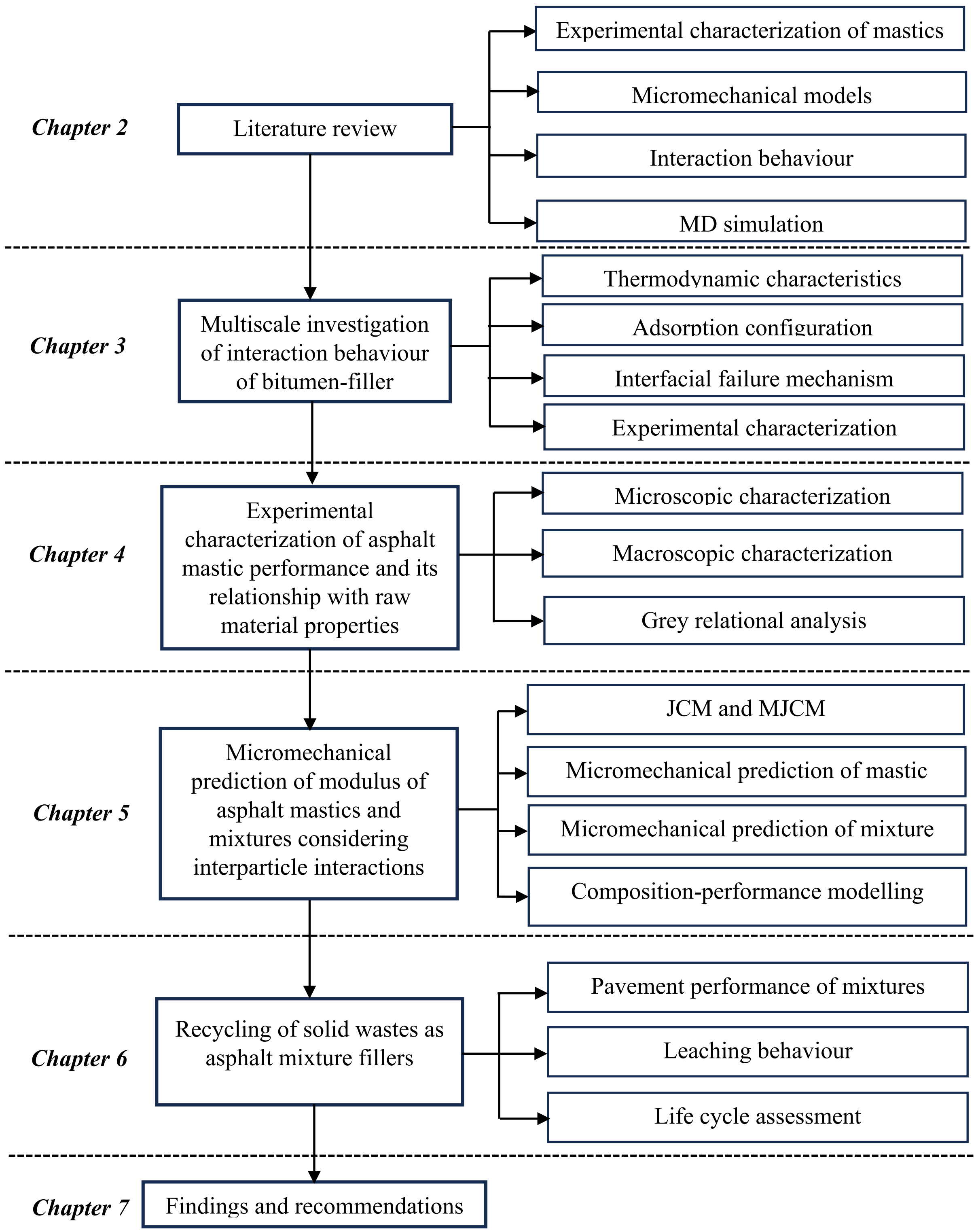

Figure 1.1 Thesis framework

CHAPTER 2 LITERATURE REVIEW

In this chapter, a literature review is presented, which builds a theorical foundation for the investigation of the interaction behaviour and compatibility mechanism between bitumen and fillers. Section 2.1 introduces the experimental characterization of asphalt mastics from macroscopic and microscopic scales. Section 2.2 introduces the micromechanical model prediction of performances of asphalt mastics. Section 2.3 introduces the bitumen-filler interaction behaviour from an experimental perspective. Section 2.4 introduces the MD Simulation of bitumen-filler interaction behaviour. Section 2.5 introduces the recycling of solid wastes as bitumen fillers towards sustainable pavements. Section 2.6 summarizes the literatures to identify the research gaps and formulate the research problems.

2.1 Experimental Characterization of Asphalt Mastics from Macroscopic and Microscopic Scales

So far, researchers have carried out lots of experimental studies on asphalt mastics from the macroscopic and microscopic scales. Nazary et al. [12] prepared asphalt mastics with three penetration grades of bitumen and three fillers and found that zeolite has better high-temperature properties and limestone has better low-temperature properties through analysis of variance (ANOVA). Shukry et al. [42] showed that diatomite has the most significant improvement in the high-temperature performance of modified bitumen and attributed it to the high silica content in diatomite using multiple stress creep recovery (MSCR) test. Li et al. [43] proposed a modified MSCR test for asphalt mastics and investigated the effect of filler on the rutting performance of bitumen. Jiang et al. [44] designed an improved LAS test, combined with the morphology analysis of SEM, to study the impact of the concentration and particle size of fillers on the fatigue performance of asphalt mastics. Zhang et al. [45] conducted a comprehensive evaluation of the mechanical properties of epoxy asphalt mastics including rutting, fatigue, low-temperature, tensile, and viscosity performances. Rys and Szydlowski [46] investigated the fatigue and healing properties of asphalt mastics based on pseudo strain energy density. Yan et al. [47] evaluated the high-temperature performance of hydraulic asphalt mastics using the MSCR, Brookfield viscosity, and zero shear viscosity tests at different asphalt types and filler contents. It can be seen from the above that the filler characteristics have a potential impact on many properties of asphalt mastics, such as rutting, fatigue, low-temperature cracking, and anti-aging. In addition, there were part of researchers putting forward the test methods of asphalt mastics based on the bitumen test methods by increasing the load levels [43, 44]. Nevertheless, these studies did not lead to broad consensus or standardized tests. The more common option is that the researchers still tested the asphalt mastics entirely according to the bitumen test method.

The macroscopic viscoelastic properties and complex rheological behaviour of the asphalt mastic depend primarily on its microstructure and morphology, and researchers have also conducted much research on this. In terms of microstructure, Tan et al. [48] studied the interaction between bitumen and fillers using the Fourier transform infrared spectroscopy (FTIR), finding that the interaction between bitumen and fillers was mainly physical action and the disappearance of individual peaks corresponded to weak chemical action. Zhang et al. [49] investigated the microscopic characteristics of asphalt mastics and found no chemical reaction between bitumen and fillers. Xu et al. [50] found that the peak area of sulfoxide of limestone asphalt mastic was larger than diabase and granite asphalt mastics because limestone had the most substantial interaction with bitumen. Li et al. [51] investigated the aging resistance of bitumen through the FTIR test, finding that fillers can enhance the anti-aging performance of bitumen, and fly ash showed the most substantial enhancing effect because of its porous surface. Motevalizadeh et al. conducted an in-depth investigation into the aging characteristics of asphalt mortar through Fourier transform infrared spectroscopy and multivariate statistical analysis [52, 53], and further revealed the chemical and rheological changes occurring during the aging process by combining DSR tests with machine learning methods [54]. To conclude, the existing research shows that the interaction between mineral fillers and bitumen is mainly a physical process.

Table 2-1 Summary of macroscopic and microscopic experimental studies on the compatibility of bitumen-filler

Studies	Experimental scales	Fill types	Test methods	Key raw material characteristics	Mechanical performances
Nazary et al. [12]	Macroscopic	Limestone, pumice, and natural zeolite	Penetration and softening point tests	Bitumen penetrations	High-temperature property
Cheng et al. [55]	Macroscopic	Limestone, hydrated lime, fly-ash and diatomite	Softening point, viscosity, force-ductility and DSR tests	SSA of fillers	High- and medium-temperature properties
Shukry et al. [42]	Macroscopic	Hydrated lime, cement and diatomite	Frequency sweep and MSCR tests	SiO_2 content of fillers	High-temperature property
Jiang et al. [44]	Macroscopic and microscopic	Limestone	DSR and SEM tests	Content and size distribution of fillers	Fatigue property
Tan et al. [48]	Microscopic	Andesite and granite	AFM and FTIR	Microscopic surface morphology of fillers	Adhesion property
Li et al. [51]	Microscopic	Fly ash and limestone	AFM and FTIR	Porous micro surface of fillers	Anti-aging property
Moraes et al. [56]	Macroscopic and microscopic	Limestone, granite, and dolomite	GPC and DSR tests	Filler types and filler contents	Anti-aging property
Xing et al. [57, 58]	Macroscopic and microscopic	Limestone	DSR and SEM tests	Particle size of fillers	Rutting and fatigue property

In terms of morphology, Tan et al. [59] adopted the AFM to characterize the morphological characteristics and mechanical properties of asphalt binder at different distances from the filler surface. Xing et al. [57, 58] studied the effects of filler particle size on the fatigue of asphalt mastics based on SEM, finding that the fatigue performance of asphalt mastics prepared by coarse particle filler was worse. Xu et al. [50] captured the SEM results of three asphalt mastics, finding that the existence of rich folds and protrusions of limestone can effectively increase the contact area with bitumen and thus increase the adhesion ability. Cheng et al. [60] investigated the creep evolution behavior of asphalt mastics under salt erosion by combining SEM with mechanical experiments. Wang et al. [23] investigated the fatigue performance and micro-morphology of asphalt mortar before and after aging under different filler types and filler–binder ratios by combining AFM analysis with fatigue testing. Li et al. [61] elucidated the evolution of the microstructure of asphalt mastic in acidic and alkaline environments through the integrated application of FTIR, SEM, and AFM.

2.2 Micromechanical Model Prediction of Performances of Asphalt Mastics

Experimental tests, empirical models, and numerical simulations are the primary traditional analysis methods of dynamic modulus of asphalt mastics. Firstly, laboratory tests provide a way to test the asphalt mastics' dynamic modulus at various loads and temperatures, while preparing and testing specimens requires a lot of time and money. The empirical model method is generally based on vast amounts of test data to fit the performance of asphalt mastics, such as the Little Dallas complex modulus model [62], Al-Khateeb complex modulus model [63], etc. These models often include indicators reflecting the performance of filler and bitumen and filler concentration. Theoretically, the empirical model method is more instructive, but it relies heavily on modelling parameters and data volume, leading to significant differences in models built by different researchers, significantly reducing its usability [64]. In addition, many researchers adopted numerical micromechanical models to predict the properties of mixtures, including discrete element model (DEM) [65, 66] and finite element model (FEM) [67, 68]. However, these studies usually require FEM/DEM grids with detailed information to generate the microstructure of the mixture, requiring large-scale computing facilities and X-ray computed tomography scans, which greatly limit the practical application of such models.

As an alternative, micromechanical models developed based on continuum mechanics are anticipated to offer accurate forecasts of the mechanical properties of composites without the need for significant calculations and laboratory testing [69]. Several micromechanical models have been developed and effectively employed to predict the modulus of composite materials like asphalt mastic and asphalt mixture based on Eshelby's inclusion theory [70, 71]. Underwood et al. [71] proposed a new physico-chemical interaction model to predict the modulus of asphalt mastics at different particle concentrations, and exiting micromechanical models including the composite sphere model (CSM), Mori–Tanaka model (MTM), self-consistent model (SCM), generalized self-consistent model (GSCM), differential model (DFM), and periodic structure model (PSM) were adopted for comparison, finding that all models lose accuracy at the high filler volume concentrations. Cao et al. [72] found that the GSCM underestimated the dynamic modulus of asphalt mixtures at low loading frequencies and overestimated it at high frequencies, and achieved improved prediction accuracy by modifying the two-phase micromechanical model. Ma et al. [73] compared the prediction accuracy of GSCM, Ju-Chen model (JCM), and the four-phase model for the complex shear modulus of asphalt mastics, finding that GSCM is applicable for lower filler volume fractions, JCM is inapplicable when the filler volume fraction exceeds 0.53, and the deviations of all three models increase sharply with increasing filler volume fraction. Al-Khateeb et al. [63] proposed a simplified model based on GSCM, which, however, tends to exhibit more accurate predictions at higher temperatures and/or lower loading frequencies. Jia et al. [74] combined the micromechanical models and fractal statistic principles and predicted the dynamic modulus of asphalt mastics. Hajikarimi et al. [75] proposed a heterogeneous micromechanical model for bituminous composites containing taconite or crumb rubber with different volume concentrations. Wang et al. [76] calculated the absorbed bitumen film thickness and compared the interaction between bitumen and solid waste fillers and mineral fillers based on micromechanical models. Nguyen et al. [32] compared the modulus prediction performance of SCM and GSCM for asphalt mastic and mixtures, finding that both methods achieved good accuracy for asphalt mastic with filler volume fractions below 35%, whereas only GSCM exhibited relatively good prediction accuracy for mixtures with particle volume fractions as high as 87% in high frequency region. It can be observed that the prediction accuracy of these classical models decreases significantly under certain conditions. This is maybe because these models often assume weak or negligible interactions between inclusions, which may not be valid for systems with high filler concentrations or strong particle interactions, such as those incorporating solid waste fillers [77]. As a result, the prediction accuracy of classical models may be significantly compromised under these conditions.

Table 2-2 Summary of micromechanical models of asphalt mastics

Studies	Models	Findings
Yin et al. [78]	Dilute model (DM), MTM, SCM, and GSCM	SCM performs best, DM overestimates, MTM and GSCM underestimate
Underwood et al. [71]	CSM, MTM, SCM, GSCM, DFM, PSM, and four phase model	All models lose accuracy at the high filler volume concentrations
Rahim et al. [79]	Maron–Pierce, Lewis Nielsen, Mooney, Krieger–Dougherty, Chong, Robinson, and Hashin models	The model predictions are accurate only at low filler volume fractions.
Wang et al. [80]	Homogeneous morphologically representative model (H-MRP)	It exhibits underestimated modulus at low frequencies when filler volume fractions are 30% and 40%
Jin et al. [81]	H-MRP	H-MRP model can achieve good accuracy after choosing a structural asphalt layer of appropriate thickness.
Tanakizadeh et al. [82]	Inverse rule of mixtures, Hashin-Shtrikman, GSCM, and four-phase models	The 4-phase model had the best modulus predictability followed by the inverse rule of mixtures, Hashin-Shtrikman, and GSCS models at the bitumen-filler mass ratio of 1
Pei et al. [83]	MTM, DFM and JCM	The combination of parameter ς and JCM can achieve good accuracy when filler volume fraction is lower than 0.5.
Ma et al. [73]	GSCM, JCM, and four-phase model	GSCM is suitable for low filler volume fraction, JCM loses accuracy when the fraction is higher than 0.53, and four-phase model performs well at moderate and high fractions
Jia et al. [74]	DM, MTM, and SCM	The fractal statistic principle by the equivalent force was adopted to improve the models.

2.3 Bitumen-Filler Interaction Behaviour from an Experimental Perspective

2.3.1 Critical volume fraction theory

Faheem and Bahia [84, 85] studied the interaction model between bitumen and fillers in asphalt mastics and defined the critical volume fraction of fillers, as shown in Figure 2.1. The x-axis in the figure represents the volume fraction of fillers (the ratio of filler volume to total volume of asphalt mastics), and the y-axis represents the complex modulus ratio of asphalt mastics (the ratio of complex modulus of asphalt mastics to complex modulus of matrix bitumen). This model divides the hardening process of asphalt mastics into three stages: (1) low concentration stage, in which the filler is dispersed in the bitumen and interacts with the bitumen to form a structural bitumen. There is more free bitumen in the entire asphalt mastics, and the distance between the filler particles is relatively large. Therefore, at this stage, the complex modulus of the mastics slowly increases; (2) At the critical concentration stage, all free bitumen in the mastics is converted into structural bitumen, and the volume fraction of the filler in this stage is defined as the critical volume fraction; (3) During the particle contact stage, the concentration of fillers is relatively high, and bitumen cannot completely disperse the fillers. Therefore, particles come into direct contact, and since the fillers can be considered rigid particles, the complex modulus of the mastics increases sharply. The slopes of Line 1 and Line 2 are defined as the initial hardening rate and the final hardening rate, respectively. The critical volume fraction of the filler is the transition point between the low concentration stage and the particle contact stage, which is the intersection point of the initial hardening rate and the final hardening rate. The smaller the critical volume fraction of the filler, the stronger its ability to convert asphalt into structural asphalt. Therefore, the critical volume fraction of the filler reflects the strength of bitumen-filler interaction from a macroscopic perspective, that is, under the same conditions, the smaller the critical volume fraction, the stronger the interaction. Based on this theory, Ma Xiaoyan et al. [86], Wang et al. [76], as well as Dong et al. [87] calculated the critical volume fraction of the filler to evaluate the bitumen-filler interaction ability.

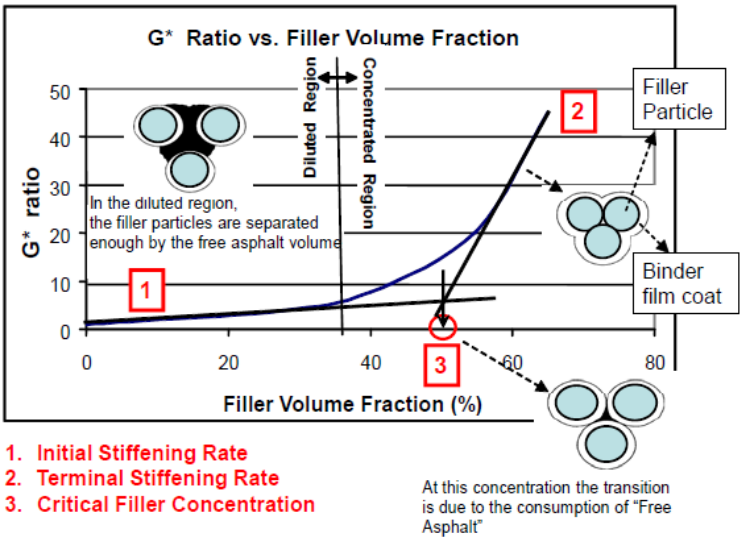

Figure 2.1 Critical volume fraction model of fillers [84]

2.3.2 Rheology theory

Obviously, the addition of filler will increase the modulus of bitumen, and evaluation methods based on rheology have also been widely studied to evaluate the interaction ability of bitumen and filler, mainly including complex modulus, phase angle and complex viscosity. In terms of complex modulus indicators, Tan et al. [88] proposed the complex modulus coefficient ΔG* (the ratio of the difference between the complex modulus of asphalt mastic and bitumen to the complex modulus of bitumen) to evaluate the interaction between asphalt and fillers, but this indicator failed to reflect the influence of filler type on the interaction ability. Zhang et al. [7] deduced another evaluation index K-B-G* based on the palierene lotion model. This indicator not only eliminates the influence of volume filling effect on the calculation results, but also introduces the volume fraction of the filler to analyze the interaction between bitumen and filler at different concentrations. Liu et al. [89] adopted Einstein coefficient K_E to evaluate the interaction between bitumen and fillers. The larger the Einstein coefficient K_E, the stronger the interaction between bitumen and fillers.

In terms of phase angle indicators, it mainly includes Luis Ibrarra-A-δ (abbreviated as L-A-δ) model and K.D. Ziegel-B-δ (abbreviated as K-B-δ) model. Among them, the L-A-δ model considers asphalt mastic as a three-phase model composed of matrix phase (bitumen), reinforcement phase (filler), and interface phase (bitumen-filler interaction area), and evaluates the interaction ability of bitumen-filler through interface energy loss [90]. The K-B-δ model was first proposed by Ziegel and Romanov for the interaction between polymers and fillers, and has been widely used in the field of asphalt mastics [7, 91]. Zhang et al. [7] selected three types of fillers and two kinds of bitumen, and the K-B-δ model was used to study the influence of material properties on the interaction ability between bitumen and fillers, finding that the order of influence from high to low was filler particle size, asphaltene and resin contents, filler volume fraction, and SiO_2 content.

In terms of complex viscosity indicators, Tan et al. [92] proposed the concept of complex viscosity coefficient $\Delta\eta^*$ (the ratio of the difference in complex viscosity between asphalt mastic and bitumen to the complex viscosity of bitumen), but this indicator failed to reflect the impact of filler type on the interaction ability.

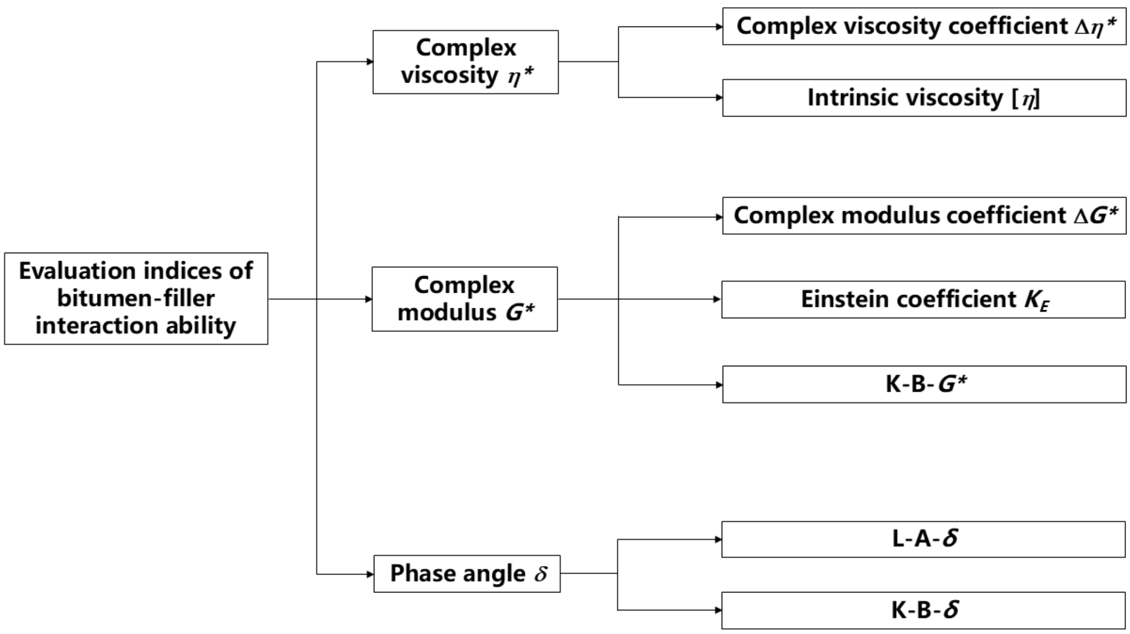

Figure 2.2 Evaluation index of bitumen-filler interaction based on rheology theory [7]

2.3.3 Adsorbed bitumen film thickness theory

In the process of bitumen-filler interaction, the bitumen components will rearrange on the surface of the filler particles, forming a certain thickness of bitumen film, as shown in Figure 2.3 [93]. When different fillers interact with different bitumen, the thickness of the affected bitumen varies. The stronger the interaction, the thicker the thickness of the bitumen film, and vice versa. Therefore, the interaction ability between bitumen and fillers can be characterized by the thickness of the affected bitumen on the surface of the filler, which is the thickness of the adsorbed bitumen film.

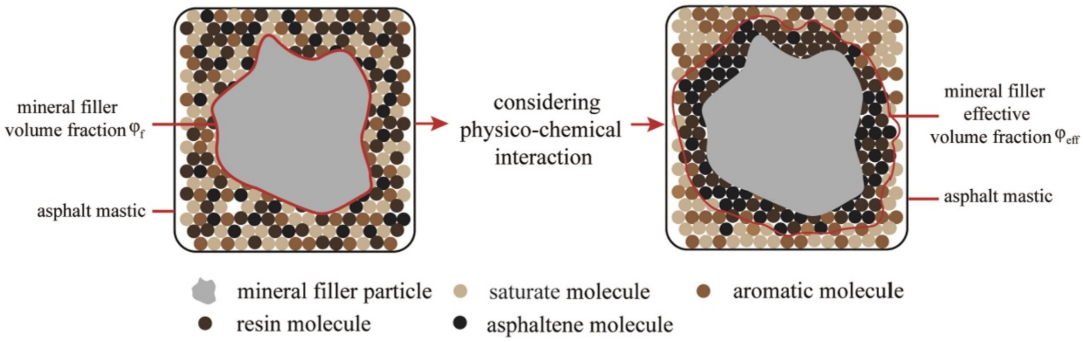

Figure 2.3 Schematic diagram of bitumen-filler interaction process [93]

Li et al. [93] used two methods to calculate the thickness of adsorbed bitumen films to evaluate the interaction ability of bitumen-filler, namely the Hashin model method [94] and the K-B-G* model method. The study found that the calculated adsorption film thickness was within 0.14 μm, and the Hashin model's calculation value was greater than the K-B-G* model. Tan and Guo [95] calculated the thickness of adsorbed bitumen film through DSC testing to evaluate the interaction between bitumen and filler. The study found that the thickness of bitumen film adsorbed by limestone and Andesite is similar, about half of that of granite.

2.3.4 Surface free energy (SFE) theory

According to the SFE theory, the interaction between bitumen and filler is caused by the energy exchange between the surface of bitumen and filler, which is related to the physical and chemical properties of the filler. Researchers often evaluate this interaction by calculating the adhesion energy at the interface between the filler and bitumen. The main method for testing the surface free energy of bitumen is the contact angle method, while the most used method for measuring the surface free energy of fillers is the capillary rise test, as shown in Figure 2.4.

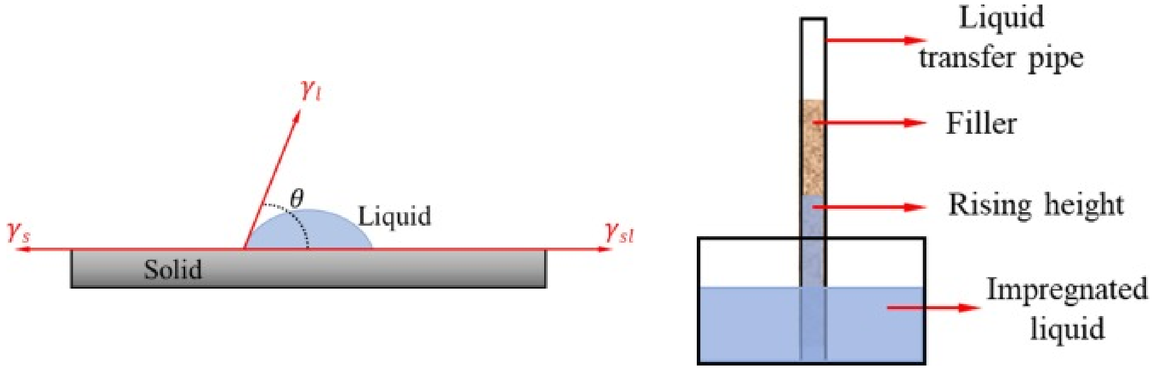

(a) (b)

Figure 2.4 Test methods for the surface free energy of bitumen and filler: (a) contact angle method; (b) capillary rise test [96]

Tan and Guo [97] studied the interaction ability between three fillers and two bitumen through the above SFE theory, contact angle method and capillary rise test. The results show that the matrix bitumen has higher free energy than the modified bitumen. The interaction ability between three fillers and bitumen is in the order of granite>andesite>limestone. Liu and Wang [98] compared the interaction ability of two fillers of activated carbon powder and mineral powder with matrix bitumen under dry and humid conditions.

2.4 MD Simulation of Bitumen-Filler Interaction Behaviour

MD simulation is a novel research method based on classical mechanics theory and modern computer technology to study molecular motion. It has been widely used in computational chemistry, materials science, pavement engineering materials and other fields. Zhu et al. [8] used silica nanoparticles and the twelve-component bitumen model to form the bitumen/silica nanoparticles composite system to represent asphalt mastics, and studied the reinforcement mechanism of filler in bitumen-filler system by using structural characteristic parameters such as free volume and radial distribution function (RDF), and thermodynamic parameters such as density, glass transition temperature T_g and cohesive energy density (CED). Xu et al. [99] studied the adhesion behaviour and mechanism between bitumen and filler using a combination of silica and twelve-component bitumen model, finding that the addition of silica particles significantly improved the self-aggregation of polar components in the matrix bitumen. Li and Yang [100] studied the effect of temperature on the thickness of bitumen film adsorbed by asphalt mastic system through MD simulation. The results indicated that increasing temperature caused non-polar bitumen components to detach from filler surfaces, while polar components were increasingly adsorbed, leading to a thicker adsorption film and stronger interactions between mineral fillers and bitumen. Du et al. [26] studied the diffusion and structural characteristics of water (water molecules) in asphalt binder and asphalt mastic, and found that in the asphalt mastic system, silica particles not only introduce more free volume, accelerate the diffusion of water, but also enhance the affinity between water and asphalt mastic system. Li et al. [101] tracked the initiation of fatigue cracks in the bitumen-filler composite system under fatigue shear load through fatigue rheological testing, surface energy testing, and MD simulation. Luo et al. [102] constructed models of four bitumen components and Al_2O_3 fillers, and then added the bitumen layer and mineral layer to construct an Al_2O_3-bitumen interface model. Li et al. [27] evaluated the coal gangue as asphalt fillers using rheological tests and constructed the molecular models of waste fillers by selecting the main oxide components of coal gangue. Sun et al. [28] investigated the interaction mechanism between fly ash filler and asphalt within a multi-scale framework, calculating the adhesion work and relative concentration at the asphalt-filler interface using MD simulations.

2.5 Recycling of Solid Wastes as Bitumen Fillers towards Sustainable Pavements

Recent years have seen a growing body of research focused on the incorporation of solid waste as bitumen fillers in asphalt mixtures [103-106]. Yang et al. [104, 107] investigated the applicability of three solid waste fillers (fly ash, diatomite, and red mud) to asphalt pavements and explored the environmental impact of waste fillers on porous asphalt mixtures. Antunes et al. [108] evaluated the interaction between three waste fillers and bitumen and found that mastics mixed with waste fillers showed strong moisture resistance. Choudhary et al. [105, 109] investigated the performances of asphalt mixtures containing five solid waste fillers and analyzed their material cost and CO_2 emission. Russo et al. [110, 111] utilized four solid wastes of construction and demolition waste, fly ash, bottom ash, and jet grouting into bitumen and investigated their rheological properties and environmental compatibility. Lin et al. [112] and Ou et al. [113] explored the prospects of using glass fiber-reinforced polymer and waste phosphogypsum as alternatives to traditional mineral fillers in bitumen by designing systematic experimental plans. Yang et al. [36] selected three kinds of graphite tailings to prepare the asphalt mastics and investigated their microscopic properties, mechanical performances, and interaction ability. Sun et al. [28] investigated the interaction mechanisms between municipal solid waste incineration fly ash and asphalt using a multiscale approach that combines molecular dynamics (MD) simulations, microscopic testing, and macroscopic rheological modeling. Yin et al. [114, 115] demonstrated that incorporating coal-based synthetic natural gas slag filler into asphalt mixtures slightly weakened the low-temperature performance of the mixture, but significantly improved other performances such as rutting, fatigue, and moisture damage resistance. Li et al. [27, 116] treated coal gangue using a thermal activation method and found that the treated coal gangue, when used as a filler, exhibited stronger interaction and bonding energy with asphalt. Lei et al. [117] investigated the application prospects of copper tailings as an asphalt filler and found that copper tailings exhibited stronger interactions with asphalt, and heavy metal leaching tests confirmed that their large-scale use in pavements poses no environmental risk. Research has shown that some solid waste fillers can not only replace natural mineral fillers, but also improve the rutting property, moisture stability, and aging resistance of asphalt mixtures [36, 118, 119]. In addition, the incorporation of solid waste fillers contributes to lowering the production costs of asphalt mixtures while facilitating resource utilization and waste reduction, which aligns with the concepts of circular economy and green production.

2.6 Summary

This chapter provides a thorough review of research literature on the interaction behaviour and compatibility between bitumen and fillers. Based on this literature review, the following key research gaps can be identified:

1) Researchers have conducted extensive research on the macroscopic and microscopic properties of asphalt mastics and have achieved many research results. However, the conclusions of such research are mainly based on the experimental data established by the research itself, lacking consideration of the underlying mechanisms and making it difficult to form universal and convincing findings.

2) The current micromechanical models have not fully and effectively considered the interactions between particles, which may result in inaccurate predictions of the performance of asphalt mastics when the volume concentration of fillers is high. For composite materials with high inclusion concentration such as asphalt mixtures, the current models are even less useful.

3) Most of the current MD simulation studies mainly use single oxide molecules to simulate fillers, which is quite different from the actual filler composition and is not accurate. Besides, research at the molecular scale has mostly focused on the thermodynamic

parameters of the bitumen-filler interface, while lacking research on the failure mechanism of the bitumen-filler interface.

4) There are few studies comparing the various theories of bitumen-filler interaction evaluation. How to consider the applicable scope of different interaction indicators and how to select the optimal indicator remain to be solved.

5) Current research mainly focuses on the mechanical performances and economic benefits of utilizing solid waste in asphalt mixtures, while neglecting the detailed and comprehensive LCA of solid waste fillers used in asphalt pavements.

CHAPTER 3 MULTISCALE INVESTIGATION OF INTERACTION BEHAVIOUR OF BITUMEN-FILLER: ADSORPTION CONFIGURATION, INTERFACIAL FAILURE MECHANISM, AND EXPERIMENTAL CHARACTERIZATION

The interaction between bitumen and filler is a multifaceted process influenced not only by the intrinsic properties of their raw material composition and surface texture characteristics but also indirectly modulated by external factors such as the microstructure of the mixture, environmental conditions (moisture and temperature), and traffic load characteristics. This interaction is inherently a multi-factor coupled process, where the characteristic scales of influence span an impressive nine orders of magnitude, ranging from the molecular level to the macroscopic scale. The complexity of the bitumen-filler interfacial behaviour is fundamentally rooted in its multi-factorial and multi-scale nature. At its core, the interaction between bitumen and filler is governed by the chemistry of the bitumen and the mineralogy of the filler. Bitumen chemistry pertains to the colloidal chemical composition of the bitumen, while filler mineralogy refers to the types of rock-forming minerals that constitute the filler and the surface structure of these minerals. The wetting and adhesion behaviour of bitumen on the filler surface arises from the aggregation of bitumen molecules on the filler surface. Active sites on the filler surface attract and redistribute bitumen molecules through interactions such as electrostatic forces, hydrogen bonding, or van der Waals forces. The direct outcome of this interaction is the formation of an interface zone, whose configuration and thermodynamic properties are intricately linked to the chemical and mineralogical characteristics of both the bitumen and the filler. Consequently, a comprehensive understanding of the interfacial interaction mechanism between the bitumen and the filler necessitates an investigation that begins at the molecular scale.

Based on the above background, this study collected five kinds of solid wastes belonging to three categories, studied their interactions with bitumen, and selected three commonly used mineral fillers for comparison. Based on materials dynamic (MD) simulation, representative mineral molecular models and bitumen-mineral interface models were constructed by selecting the main rock-forming minerals of waste and mineral fillers on the Materials Studio platform. The adsorption configuration of bitumen on mineral surfaces was revealed at the atomic level, and the effect of filler mineralogy was studied. Based on the Large-scale Atomic/Molecular Massively Parallel Simulator (LAMMPS) platform, the interfacial failure mechanism of the bitumen-filler interface under various loading rates was revealed. Finally, the molecular-scale findings were validated through macroscopic interaction experiments.

3.1 Materials and Methodology

3.1.1 Materials and sample preparation

The base bitumen with a penetration of 60/70 and a PG of 64-22 was selected in this chapter. Table 3.1 presents the detailed physical properties of bitumen.

Table 3-1 Physical properties of the base bitumen

Items	Penetration at 25 °C (0.1 mm)	Ductility at 15 °C (cm)	Softening point (°C)	Brookfield viscosity at 135 °C (Pa/s)
Test results	62.2	>100	50.85	0.493
Requirements	60-80	>100	≥43	-
Specification	AASHTO T49	AASHTO T51	AASHTO T53	AASHTO T 316

With the widespread application of asphalt mixtures, the over-exploitation of non-renewable stone materials is not in line with the strategy of sustainable development. The continuous growth of solid waste is becoming an increasing environmental concern worldwide. Considering that solid waste and mineral fillers have similar elements and components [120], recycling solid waste into asphalt mixtures proposes a promising solution to cope with the shortage of mineral sources and improper disposal of municipal solid wastes.

According to the sources of solid waste, they can be mainly divided into industrial waste, construction waste, mining waste, agricultural waste, etc. The representatives of industrial waste include steel slag (SS) powder, desulfurization gypsum (DG), and blast furnace slag (BF). SS is a byproduct of the steelmaking process, which is composed of various oxides formed by the oxidation of impurities in pig iron such as silicon, manganese, phosphorus, and sulfur during the smelting process. China's annual slag production exceeds 100 million tons, but its utilization rate is only 29.5% [121]. DG, also known as flue gas desulfurized gypsum, mainly comes from thermal power plants, smelters, and large enterprise boilers. As the largest producer in the world, China's annual generation of DG exceeded 100 million tons by 2020 [122]. However, due to the high decomposition temperature and complex composition of DG, only a small portion of DG is currently recycled in China, and most of it is directly discarded as waste. BF is a by-product of the ironmaking process of blast furnaces. During the ironmaking process, impurities such as silica and alumina in the iron ore react with lime to form a molten substance with silicates and aluminosilicates as the main components, which is BF. The annual production of BF in China's steel and metallurgical industry is approximately 150 million tons [123]. Cement, as one of the most widely used building materials in the world, is expected to achieve a global production of 5.8 billion tons by 2050 [124]. If stored improperly or beyond the recommended shelf life, the value of this energy-intensive resource will be greatly reduced, so recycling this material is an important environmental effort. Iron tailings (IT) are the representative mining waste. As of 2015, China has produced a total of 5 billion tons of IT, with an annual discharge amount of over 600 million tons [125]. However, according to the reports, the comprehensive utilization rate of tailings in China was only 27.69% in 2018 [126]. Therefore, the comprehensive recycling and utilization of IT has received widespread attention.

Through the above analysis, considering the current reserves and utilization rates of different types of solid waste, five wastes from three categories were selected in this chapter, including three industrial wastes: SS, DG, and BF, one construction waste: waste cement (CE), and one mining waste: IT. In addition, consistent with the previous chapters, this chapter selects three traditional mineral fillers: granite (G), basalt (B), and limestone (L) for comparison. The specific sources of these waste materials are as follows: SS is a by-product of steelmaking from Laiwu Ironworks in Laiwu City, China. Both DG and BF are products of flue gas desulfurization, obtained from a power plant in Ningbo City, China. The CE was provided by a building materials company in Shijiazhuang City, China, and consisted of cement that had exceeded its shelf life by more than three years. The IT was sourced from an iron ore mining company in Zibo City, China, as a by-product of the ore beneficiation process. Regarding preprocessing, the SS and IT required drying, crushing, and grinding to achieve the desired particle size for use as fillers. In contrast, the DG, BF, and CE only underwent drying and sieving before being employed as fillers in this study. Table 3-2 lists the basic physical properties of the fillers. In this table, SSA refers to the specific surface area of the fillers. D10, D50, and D90 refer to the corresponding particle diameter when the pass rate of the filler is 10, 50 and 90%. P20, P10, and P5 refer to the content of fillers with a diameter of less than 0.02, 0.01, and 0.005 mm, respectively.

Table 3-2 Basic physical properties of the fillers

Properties	Mineral fillers			Solid waste fillers				
	G	B	L	SS	DG	BF	CE	IT
Density (g/cm3)	2.674	2.947	2.719	3.723	2.914	2.877	3.135	4.877
SSA (m2/kg)	206.1	251	286.9	343.2	312.9	313.5	318.3	324
D10 (μm)	5.342	3.992	3.584	2.629	3.472	3.494	3.272	3.364
D50 (μm)	15.77	10.77	9.865	5.366	8.751	8.84	8.519	8.346
D90 (μm)	36.34	22.5	17.39	11.15	14.16	14.23	14.14	13.77
P20 (%)	61.25	86.38	95.12	99.98	99.81	99.81	99.81	99.85
P10 (%)	28.14	44.82	51.04	84.63	61.47	60.69	62.71	65.23
P5 (%)	9.01	14.82	18.61	45.92	20.98	20.43	24.10	23.11
Mineral components	SiO_2, Al_2O_3	SiO_2, Al_2O_3	CaO	CaO, Fe_2O_3	CaO, SiO_2	CaO, SiO_2	CaO, SiO_2	Fe_2O_3

The X'PERT X-ray diffractometer (XRD) produced by Panalystic and D8 advanced X-ray

Fluorescence (XRF) Spectrometer produced by Bruker was adopted to investigate the lithological composition and oxide composition of fillers. The test results of XRD and XRF are presented in Figure 3.1 and Table 3.3, respectively. From Figure 3.1, the IT filler is mainly composed of Magnetite (Fe_3O_4), Hematite (Fe_2O_3), and Quartz (SiO_2). The main component of CE is Calcium Silicate (Ca_3SiO_5, C3S). For the three industrial waste fillers, the main components of SS are Wuestite (FeO), Calcite ($CaCO_3$), and Larnite (Ca_2SiO_4), DG consists mostly of Gehlenite ($Ca_2Al_2SiO_7$), and BF is mainly composed of Calcite and Gehlenite. For the three mineral fillers, G consists mostly of Quartz, Albite ($NaAlSi_3O_8$), and Dolomite ($Ca_3Mg_3C_6O_{18}$). B is mainly composed of Anorthite ($CaAl_2Si_2O_8$), Quartz, and Calcite. The main component of L is Calcite. It can be found from Table 5.1 the oxide concentration results of the fillers verified above XRD test results. The IT filler consists mainly of Fe_2O_3, with a content of up to 92%. The main components of SS are CaO, Fe_2O_3, and SiO_2. For three fillers of DG, BF, and CE, are all composed of CaO and SiO_2. As for the three mineral fillers, G is the only acid filler among all fillers and contains 67.39% SiO_2 and 17.89% Al_2O_3. B consists mainly of SiO_2, Al_2O_3, and Fe_2O_3. The main component of L is CaO, with a concentration of 74.61%.

Table 3-3 XRF test results of waste and mineral fillers

Filler types		Oxide concentrations (%)								
		SiO_2	Al_2O_3	Na_2O	CaO	K_2O	MgO	Fe_2O_3	SO_3	MnO
Mineral fillers	G	**67.39**	**17.89**	7.34	3.08	2.84	1.13	0.21	0.03	0.02
	B	**40.57**	**13.37**	4.35	8.99	2.33	8.27	**12.76**	0.14	0.20
	L	2.68	1.00	0.13	**74.61**	0.22	0.70	0.58	0.04	0.02
Solid waste fillers	SS	**22.00**	8.47	0.36	**29.54**	0.15	6.00	**24.16**	0.63	3.86
	DG	**23.70**	13.9	0.79	**41.90**	0.395	14.7	0.722	2.14	0.736
	BF	**23.40**	13.7	0.746	**42.00**	0.411	14.8	0.718	2.10	0.732
	CE	**15.98**	4.93	0.16	**50.00**	0.95	3.23	2.61	4.21	0.07
	IT	3.99	1.00	-	0.285	0.156	0.770	**92.0**	0.056	0.174

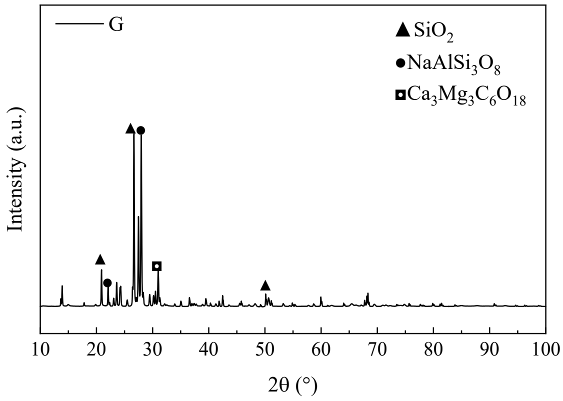
G
SiO2
NaAlSi3O8
Ca3Mg3C6O18
Intensity (a.u.)
2θ (°)
10 20 30 40 50 60 70 80 90 100

(a)

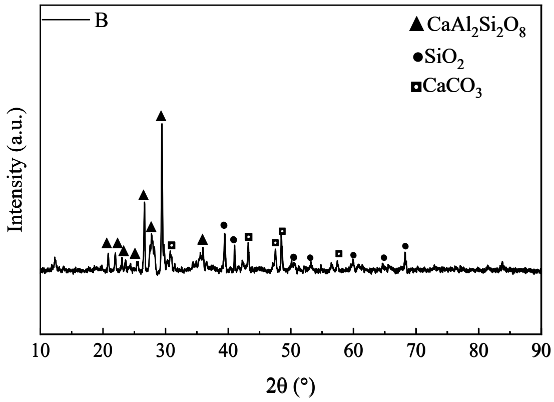
B
CaAl2Si2O8
SiO2
CaCO3
Intensity (a.u.)
2θ (°)
10 20 30 40 50 60 70 80 90

(b)

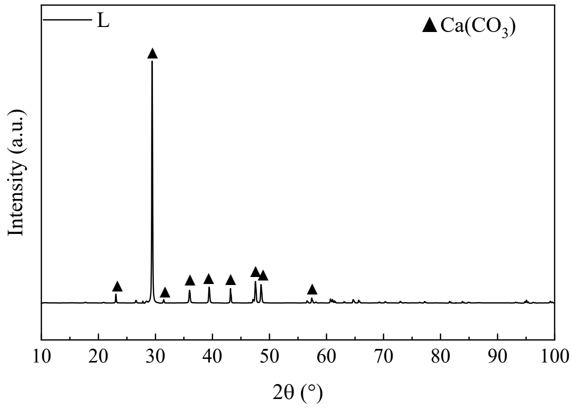
L
Ca(CO3)
Intensity (a.u.)
2θ (°)
10 20 30 40 50 60 70 80 90 100

(c)

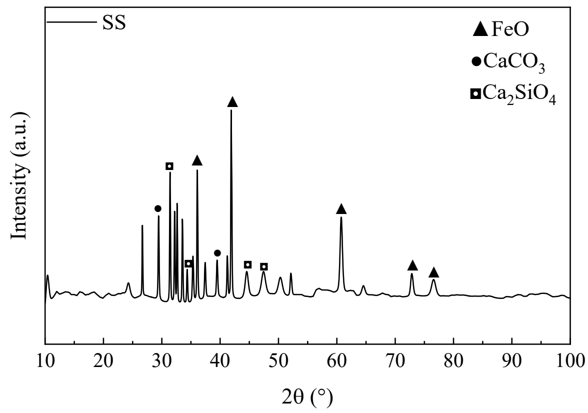
SS
FeO
CaCO3
Ca2SiO4
Intensity (a.u.)
2θ (°)
10 20 30 40 50 60 70 80 90 100

(d)

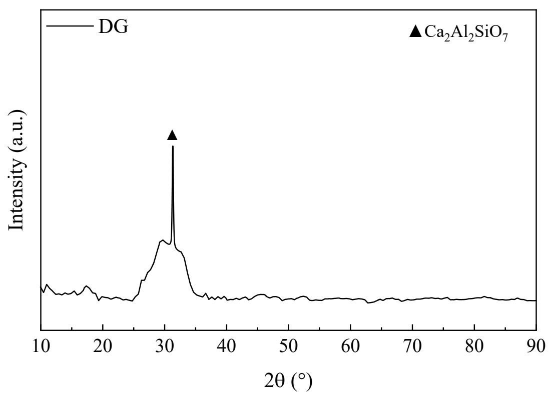
DG
Ca2Al2SiO7
Intensity (a.u.)
2θ (°)
10 20 30 40 50 60 70 80 90

(e)

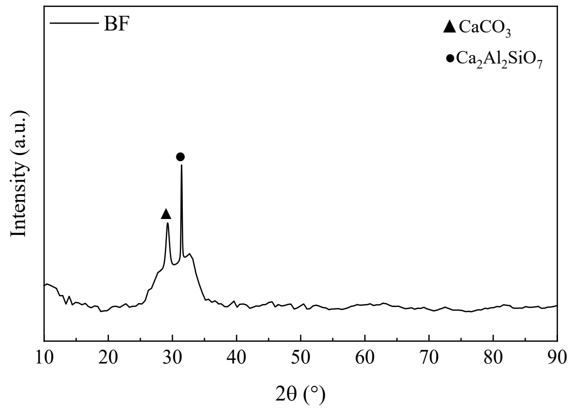
BF
CaCO3
Ca2Al2SiO7
Intensity (a.u.)
2θ (°)
10 20 30 40 50 60 70 80 90

(f)

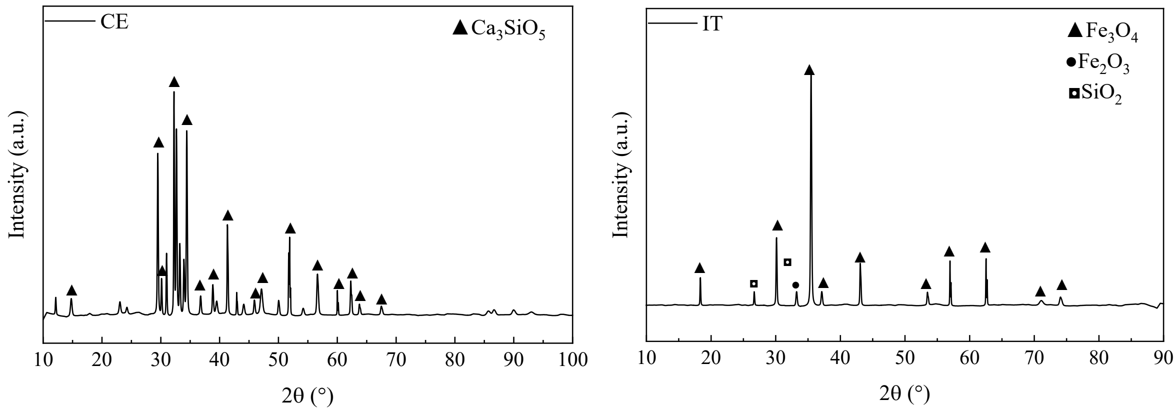

(g) (h)

Figure 3.1 XRD test results of fillers: (a) G; (b) B; (c) L; (d) SS; (e) DG; (f) BF; (g) CE and (h) IT

3.1.2 MD simulation of thermodynamic characteristics and adsorption configuration of bitumen-mineral interface

3.1.2.1 Molecular models of bitumen and fillers

Bitumen is a complex chemical mixture that is difficult to accurately characterize its molecular compositions. The widely used practice divides the bitumen composition into four components of SARA, as adopted in ASTM D 4124. Based on this four-component theory, Li and Greenfield [127] developed a 12-component molecular model to characterize the SARA components of bitumen, which has been widely used. The 12-component molecular model was adopted in this study, and the corresponding molecular structures are shown in Figure 3.2.

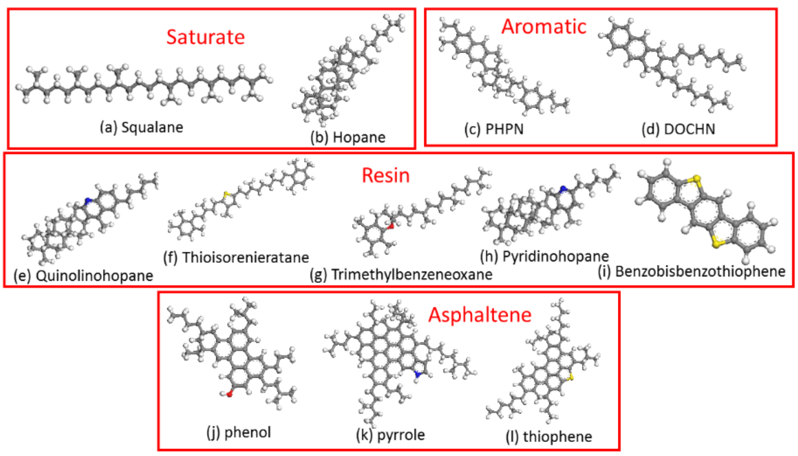

Figure 3.2 Molecular structure of 12-component bitumen model

Oxides are usually selected as the representative elements of mineral models in molecular simulation. However, from a mineralogical perspective, rock-forming minerals are the basis for the constitution of minerals, and each rock-forming mineral usually contains more than one oxide. It is inevitably inaccurate to construct a mineral model using only a single type of oxide, and rock-forming minerals should be a better choice in MD simulation [128]. Therefore, this study selected the main essential rock-forming mineral of each filler to construct the corresponding mineral model based on the XRD and XRF test results of the fillers above. Specifically, Quartz is adopted to characterize Granite, Anorthite for Basalt, Calcite for Limestone, Magnetite for IT, C3S for CE, Wuestite for SS, and Gehlenite for DG. Since the main rock-forming minerals of BF are Calcite and Gehlenite, no additional mineral model is constructed for BF. The molecular structures of the minerals in this study are shown in Figure 3.3, and the chemical formulas and lattice parameters of representative minerals are listed in Table 3.4. Nevertheless, it is worth noting that the real-world composition of these fillers is highly complex and variable. The approach adopted in this study, which uses the most dominant rock-forming minerals to construct molecular models of the fillers, inevitably involves certain simplifications and limitations. The purpose of this simplification in our MD simulations is to focus on the dominant components that are most likely to affect the performance of asphalt mastic, while recognizing that minor constituents and trace elements may also play a role. This approach allows us to compare different filler types in a controlled and scientifically meaningful manner, despite the inherent complexity of their actual compositions.

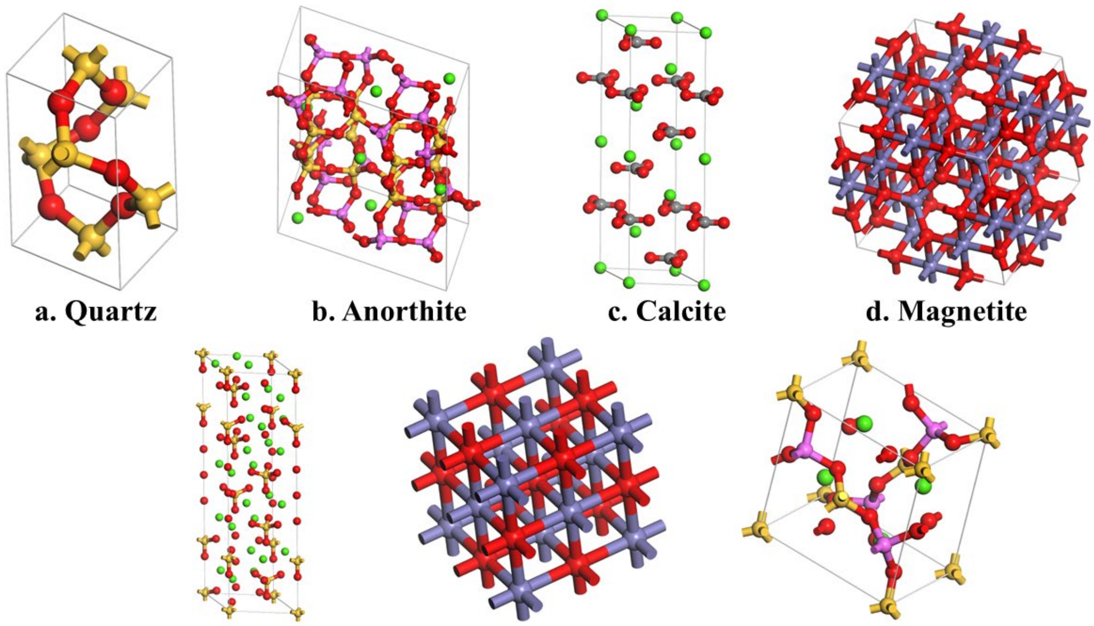

Figure 3.3 Molecular structure of representative mineral models

Table 3-4 Chemical formulas and lattice parameters of representative minerals

Mineral	Chemical formula	Lattice constants						
		Space group	Crossing angle (°)			Edge length (Å)		
			α	β	γ	a	b	c
Quartz	SiO_2	$P3_221$	90	90	120	4.91	4.91	5.4
Anorthite	$CaAl_2Si_2O_8$	$P\overline{1}$	93.3	115.79	91.12	8.19	12.88	14.18
Calcite	$CaCO_3$	R-3c	90	90	120	4.99	4.99	17.061
Magnetite	Fe_3O_4	Fd-3m	90	90	90	8.394	8.394	8.394
C3S	Ca_3SiO_5	r3m	90	90	120	7.0	7.0	25.0
Wuestite	FeO	Fm-3m	90	90	90	4.332	4.332	4.332
Gehlenite	$Ca_2Al_2SiO_7$	P-421m	90	90	90	7.69	7.69	5.10

3.1.2.2 Bitumen-mineral interface model and dynamic simulation

The molecular model construction and dynamic simulation in this study were performed in the materials studio platform. The bitumen model was first created by assembling the 12-component models of SARA. After that, the geometry optimization was carried out to minimize the energy and optimize the structure of the bitumen model. A dynamic process composed of a 1000 picosecond (ps) constant number of particles, constant-pressure, and constant temperature

(NPT) ensemble plus a 500 ps constant number of particles, constant volume, and constant temperature (NVT) ensemble was then performed on the bitumen model. For the construction of the mineral models, the crystal cells of seven selected mineral models were cleaved along the (0 0 1) plane to generate the surface layers with a thickness of 20 Å [129]. After that, the supercell of the selected mineral models was created by extending the individual surface layers in the *x* and *y* directions to ensure that the dimensions of the finalized supercells were close to that of the bitumen model. The finalized mineral and bitumen models were then used to create the bitumen-mineral interface models by placing the bitumen layer on the mineral surfaces. An additional 30 Å thick vacuum slab was placed on the top of the bitumen layer to eliminate the direct interaction between the bitumen layer and the periodic image of the mineral layer. Before the geometry optimization and dynamic simulation process of the interface model were performed, the mineral layers of the seven interface models were frozen. Finally, a dynamic process of 500 ps under NVT ensemble was performed on all seven bitumen-mineral interface models. A snapshot of the constructed bitumen-quartz interface model is shown in Figure 3.4, and the configurations of the other six bitumen-mineral interface models are similar. Throughout the MD simulation processes of seven constructed bitumen-mineral interface models, the force field was always selected as the COMPASS II.

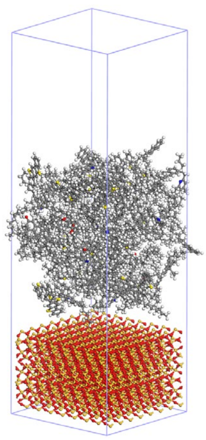

Figure 3.4 Snapshot of the bitumen-quartz interface model

3.1.3 Molecular dynamic simulation of bitumen-mineral interfacial failure

In this section, the establishment of the bitumen molecular, mineral molecular, and bitumen-mineral interface models was carried out in Materials Studio software. Similarly, the 12-component molecular model proposed by Li and Greenfield [127] was adopted in this study to construct the bitumen molecular model. The initial number of molecules in the 12-component model was proportionally enlarged five times to construct the bitumen molecular model. The size of the constructed bitumen model was 50Å×50Å×120Å.

Similarly, the main rock-forming minerals of solid wastes and mineral fillers were selected in this study as basics to construct the filler models. First, the unit cell of the selected rock-forming mineral was cut along the (0 0 1) direction [130] to form the corresponding crystal surface layer with a thickness of 20 Å. Next, the supercell of the selected mineral model was created by extending each surface layer in the x and y directions, and the cross-sectional size of the supercell should be as consistent as possible with the cross-sectional size of the bitumen model.

The bitumen-mineral interface models were established based on the bitumen and mineral models constructed above. The interface model mainly includes three layers: the first layer is the mineral structure, and the second layer is the bitumen structure. To avoid the influence of periodic boundary conditions, a thick vacuum layer of 30 Å was placed on the top of the bitumen layer to form the third layer. Subsequently, after freezing the mineral layer of the model, the interface model was subjected to a 200 ps dynamic process under the NVT ensemble, and the temperature was selected as 298K. The force field was selected as the Polymer Consistent Force Field (PCFF) and the cut-off distance was set as 15 Å at all simulation steps. Snapshots of the seven interface models constructed in this study are shown in Figure 3.5. At this point, all the steps in the MS software were completed, and the balanced bitumen-mineral interface model was imported into the LAMMPS platform for the following interfacial failure simulation.

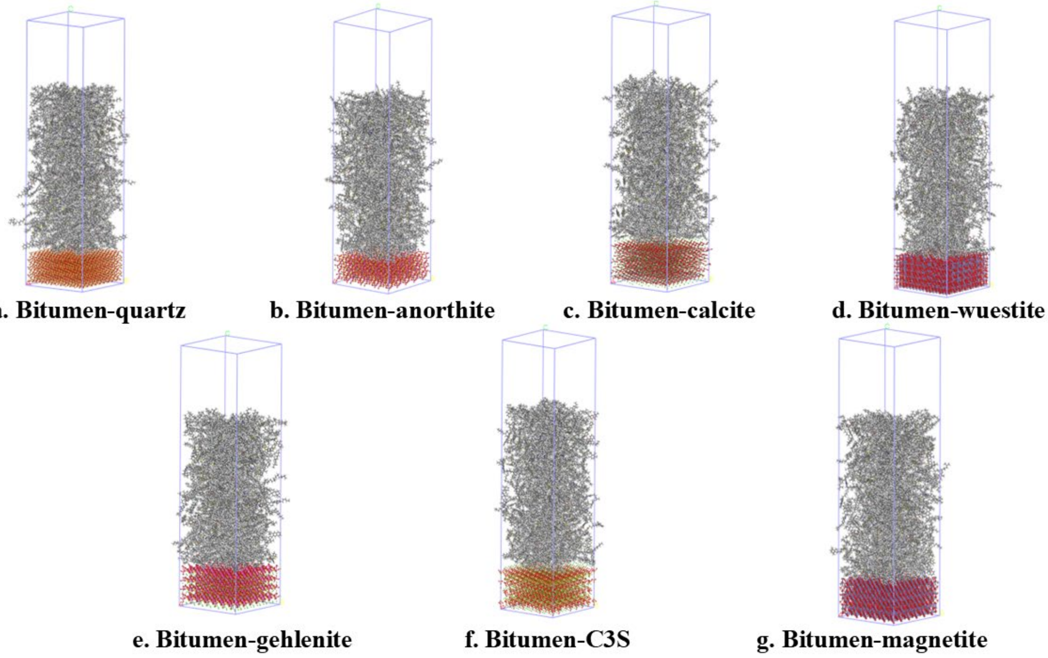

Figure 3.5 Snapshots of the seven interface models constructed in this study

After the model was imported into the LAMMPS platform, the interface model was first subjected to a 200 ps dynamic relaxation process under the constant number of particles, constant volume, and constant energy (NVE) ensemble. Next, the bitumen layer was divided into two regions: bulk bitumen (within a thickness range of 100 Å from the mineral surface) and fixed bitumen. Finally, the top of the bitumen layer was fixed, the mineral layer was set as a rigid body, and the mineral layer was pulled out of the bitumen using a fixed loading rate. The tensile distance was set to 80Å at three loading rates of 0.01, 0.001, and 0.0001 Å/fs [131]. During all LAMMPS simulations, the force field was set to a combination of PCFF and Clay Force Field (CLAYFF). The cut-off distance was 15 Å.

3.1.4 Experimental characterization of interaction behaviour of bitumen-filler

3.1.4.1 Surface free energy theory and contact angle test

Based on the Good-van Oss-Chaudhury theory [132], the surface energy of every material can be divided into three quantities according to the type of molecular force: nonpolar component (γ^{LW}), also known as van der Waals force, Lewis acid force component (γ^{+}), and Lewis basic component (γ^{-}). The detailed calculation formula is as follows:

$$\gamma = \gamma^{LW} + \gamma^{+-} = \gamma^{LW} + 2\sqrt{\gamma^{+}\gamma^{-}} \tag{3-1}$$

where γ is the surface energy. According to the Young-Dupre equation [21], the adhesion work between solid and liquid can be calculated as follows:

$$W_{SL} = \gamma_L\left(1+\cos\theta\right) = 2\left(\sqrt{\gamma_S^{LW}\gamma_L^{LW}} + \sqrt{\gamma_S^{-}\gamma_L^{+}} + \sqrt{\gamma_S^{+}\gamma_L^{-}}\right) \tag{3-2}$$

where W_{SL} is the interfacial adhesion work; S and L refer to solid and liquid, respectively; θ refers to the interfacial contact angle between solid and liquid. Based on Equation (3-2), the contact angle between the standard liquid and the solid can be measured by selecting a variety of reagents with known surface energy parameters, and the surface energy parameters of the solid can be calculated then by solving the equation group. In this study, a total of four standard solutions (distilled water, ethylene glycol, propylene glycol, and formamide) were selected, and the surface energy parameters of these four standard liquids at 20°C are listed in Table 3-5 below.

Table 3-5 Surface energy parameters of four standard solutions at 20°C

Standard solutions	Surface energy parameters (erg/cm^2)				
	γ_L^{LW}	γ_L^{+}	γ_L^{-}	γ_L^{+-}	γ_L
Distilled water	21.8	25.5	25.5	51.0	72.8
Ethylene glycol	29.0	1.92	47.0	19.0	48.0
Propylene glycol	34.0	3.92	57.4	30.0	64.0
Formamide	39.0	2.28	39.6	19.0	58.0

In this study, the contact angle of asphalt mastics and aggregate substrate was tested using the sessile drop method [133]. Figure 3.6 (a) presents the optical contact angle instrument used in this study. A pipette (Eppendorf, Germany) with a range of 0.5 ~10 μL was adopted to drip standard solutions into the sample, and the drop volume was 2 μL, as shown in Figure 3.6 (b). At least six parallel tests were conducted for each sample, and the coefficient of variation of the contact angle test results was guaranteed to be no more than 3%. In addition, to achieve better consistency between the contact angle test and the subsequent BBS test, the aggregate substrate used in these two tests is the same. The material of the aggregate substrate is granite, which is the most used aggregate category for asphalt pavements in Hong Kong. First, the granite stone was cut into cylindrical sheets, and then it was fully polished with 800-mesh gauze. The treated granite substrate is shown in Figure 3.6 (c).

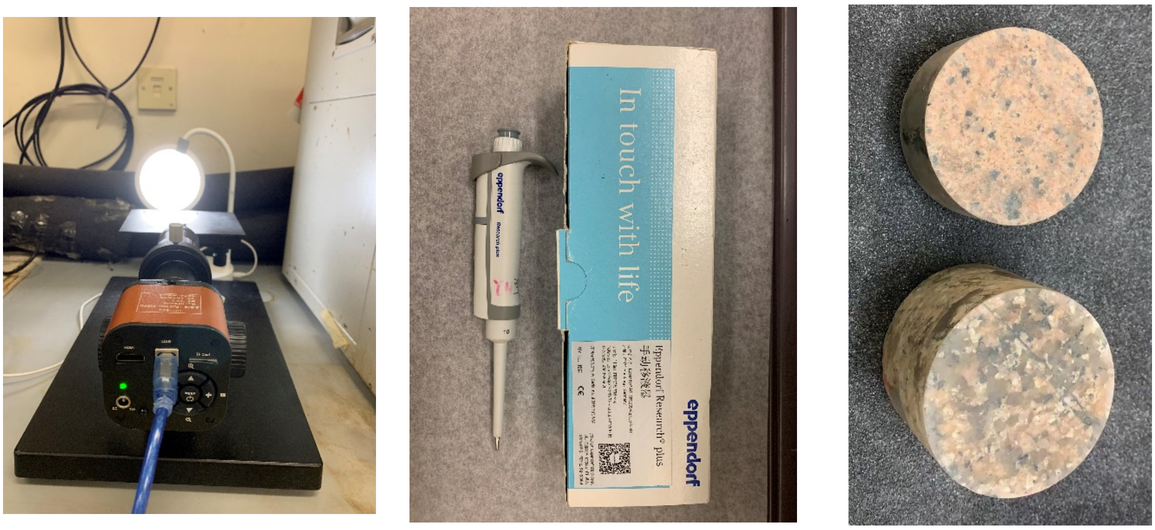

(a) (b) (c)

Figure 3.6 Equipment and materials used in the contact angle test: (a) optical contact angle meter; (b) pipette and (c) granite substrate

Based on the above surface energy and contact angle test, the surface energy parameters of asphalt mastics and aggregate substrate can be calculated. In the following, the solution method for the adhesion work between asphalt mastics and aggregates will be introduced. Adhesion work refers to the work that needs to be done by the external environment per unit area for the separation of two substances. Depending on whether there is water intrusion on the interface, the adhesion work between asphalt mastics and aggregates can be divided into two categories:

adhesion work under dry conditions and peeling work under wet conditions. The adhesion work between asphalt mastics and aggregates under dry conditions can be calculated using the following equation:

$$W_{MA} = \gamma_M + \gamma_A - \gamma_{MA} = 2\left(\sqrt{\gamma_M^{LW}\gamma_A^{LW}} + \sqrt{\gamma_M^{+}\gamma_A^{-}} + \sqrt{\gamma_M^{-}\gamma_A^{+}}\right) \tag{3-3}$$

where W_{MA} is the adhesion work; subscript M is the asphalt mastic, and subscript A is the aggregate. Refer to the computation of the interface bonding energy of the three-phase medium, the peeling work between asphalt mastics and aggregates under wet conditions can be calculated as follows:

$$W_{MAW} = 2\left[\begin{array}{l} \sqrt{\gamma_M^{LW}\gamma_W^{LW}} + \sqrt{\gamma_A^{LW}\gamma_W^{LW}} - \sqrt{\gamma_M^{LW}\gamma_A^{LW}} - \\ \gamma_W^{LW} + \sqrt{\gamma_W^{+}}\left(\sqrt{\gamma_M^{-}} + \sqrt{\gamma_A^{-}} - \sqrt{\gamma_W^{-}}\right) + \\ \sqrt{\gamma_W^{-}}\left(\sqrt{\gamma_M^{+}} + \sqrt{\gamma_A^{+}} - \sqrt{\gamma_W^{+}}\right) - \sqrt{\gamma_M^{+}\gamma_A^{-}} - \sqrt{\gamma_M^{-}\gamma_A^{+}} \end{array}\right] \tag{3-4}$$

where W_{MAM} is the peeling work, and subscript W is water. W_{MA} represents the work required to separate asphalt mastics from the aggregate substrate, which is generally a positive number and is positively correlated with the adhesion between mastics and aggregate. W_{MAM} represents the energy released at the medium interface when water penetrates the mastic-aggregate system, which is generally a negative number and has a positive correlation with the adhesion property. Furthermore, based on the above two indicators of W_{MA} and W_{MAM}, the researchers also constructed energy ratio parameters ER_1 and ER_2 to characterize the moisture resistance of asphalt mixtures [19]:

$$ER_1 = \left|\frac{W_{MA}}{W_{MAW}}\right| \tag{3-5}$$

$$ER_2 = \left| \frac{W_{MA} - W_{MM}}{W_{MAW}} \right| \tag{3-6}$$

where $W_{MM} = 2\gamma_M$ is the cohesive energy of asphalt mastics. The larger the values of ER_1 and ER_2, the better the moisture resistance of asphalt mixtures.

3.1.4.2 Binder bonding strength (BBS) test

Referring to AASHTO T361, the BBS test was carried out to determine the bonding strength between asphalt mastics and the aggregate. The pull-off instrument used in this study is the PosiTest AT-A fully automatic digital display pull-off adhesion tester produced by DeFelsko, USA, as shown in Figure 3.7 (a). To control the thickness of the bitumen film in the BBS test, the bottom of the pull-off stub is processed into an annular groove with an inner diameter of 18 mm, an outer diameter of 20 mm, and a depth of 0.2 mm, as shown in Figure 3.7 (b). To reduce the source of experimental errors and maintain consistency between different tests, the aggregate substrate in the BBS test is the same as the substrate in the above contact angle test. The detailed test steps of the BBS test are as follows. First, the fully cleaned pull-off stub and aggregate substrate are placed in an oven with a temperature of 160°C for one hour. Second, the asphalt mastic sample heated to a fully fluid state is poured into the center of the aggregate base. Third, a stone plate with a fixed mass and volume is placed on the pull-off stub to provide a certain pressure to make the excess mastic flow out and the bitumen film thickness remains at 0.2 mm [134]. Fourth, the stone plate is removed after four hours, and the excess mastic around each pull-off stub is cleaned. The surface of the cleaned pull-off stub is shown in Figure 3.7 (c). Fifth, this step can divide the samples into two categories: dry group and immersion group. For the dry group samples, they were placed in a 25°C environmental box for curing for 25 hours. For the immersion group, the whole mastic-aggregate substrate system was placed in a 40°C constant temperature water tank for 24 hours, and then taken out and placed in a 25°C constant temperature environment box for one hour to return to the test temperature. Finally, the dry and immersion group samples were subjected to a BBS test. The pull-out rate was set to 0.7MPa/s [134]. For each group of samples, at least six repeated tests were required.

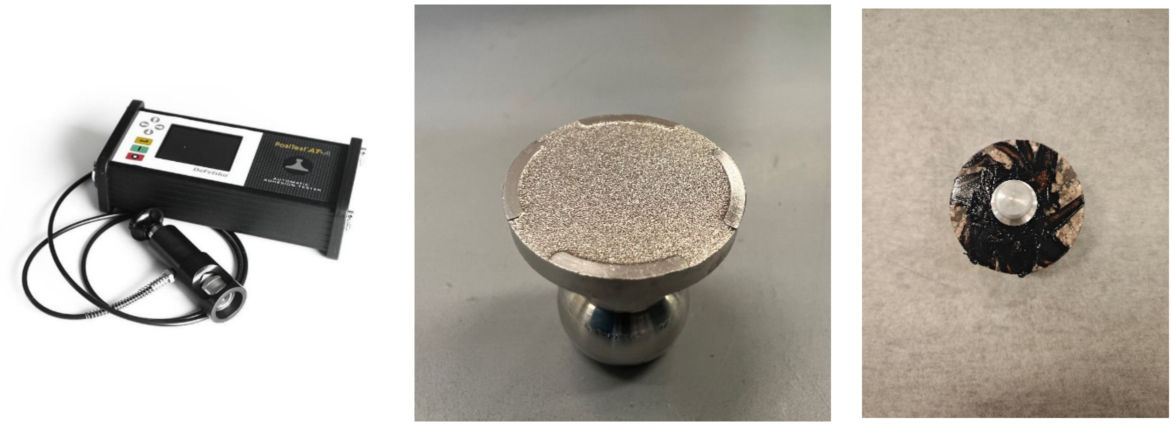

(a) (b) (c)

Figure 3.7 Equipment and materials used in the BBS test: (a) pull-off instrument; (b) pull-off stub and (c) aggregate substrate

3.1.4.3 Interaction characterization based on rheology

As one of the most common methods for evaluating bitumen materials, rheology is also widely used to characterize the ability of bitumen to interact with fillers. There is no doubt that the rheological indicators of bitumen after the addition of fillers will change significantly, such as increased modulus, increased viscosity, decreased phase angle, etc. Researchers have also proposed a series of bitumen-filler interaction ability characterization indicators based on the above rheological parameters. Three commonly used indexes of rheology interaction ability, including K.D. Ziegel-B-G* (B_{G*}), Luis Ibrarra-A-δ (A_{δ}), and K.D. Ziegel-B-δ (B_{δ}) was adopted in this study, and corresponding computational formulas are listed as follows:

$$B_{G^*} = \frac{\frac{G_c^*}{G_m^*} - 1}{(1.5 + \frac{G_c^*}{G_m^*})\phi_f} \quad (3\text{-}7)$$

$$A_\delta = \frac{\tan \delta_c}{\tan \delta_m (1-\phi_f)} - 1 \tag{3-8}$$

$$B_\delta = \frac{\frac{\tan \delta_m}{\tan \delta_c} - 1}{1.5\phi_f} \tag{3-9}$$

where G_c^* and G_m^* are the complex modulus of asphalt mastics and bitumen, respectively; ϕ_f is the volume fraction of the filler; δ_c and δ_m are the phase angle of asphalt mastics and bitumen, respectively. The MCR 702e dynamic shear rheometer (DSR) (Anton Paar GmbH, Austria) was adopted to carry out the DSR tests of asphalt mastics, as shown in Figure 3.8. Three test temperatures of 48, 60, and 72 °C were selected in this study [15, 36]. The complex modulus and phase angle data of the samples were collected to calculate the rheology indicators of interaction between bitumen and fillers.

Figure 3.8 MCR 702e dynamic shear rheometer (DSR)

3.1.4.4 Double edge notched tension (DENT) test based on essential work of fracture theory

Referring to AASHTO TP 113-15, the DENT test was carried out on the asphalt mastics with waste and mineral fillers to characterize the cohesive failure resistance. For each mastic, three samples with different ligament lengths of 5mm, 10mm and 15mm need to be formed, as shown in Figure 3.9 (a). After two hours of water bath curing at the temperature of 25 °C, the samples were subjected to loading at the constant tensile rate of 50 mm/min and the test temperature of 25 °C, as shown in Figure 3.9 (b). The DENT test divides the total fracture work consumed during the tensile fracture process into two parts as shown in this equation:

$$W_t = W_e + W_p \tag{3-10}$$

where W_t is the total fracture work (J); and $W_e = w_e \cdot B \cdot L$ is the basic fracture work (J), which represents the energy required for crack extension during the fracture process; $W_p = \beta \cdot w_p \cdot L^2$ is the plastic deformation work outside the fracture zone (J), which represents the energy required for plastic deformation or non-essential fracture. Dividing both sides of Equation (3-10) by $B \cdot L$, the equation can be rewritten as:

$$w_t = w_e + \beta \cdot w_p \cdot L \tag{3-11}$$

where $w_t = W_t / B \cdot L$ is the specific total fracture work (J/m^2); w_e is the specific essential work of fracture (J/m^2), which is the energy consumed per unit area of crack propagation; w_p is the specific plastic work of fracture (J/m^2), which is the energy consumed by plastic deformation per unit volume; β is the geometrical factor describing the shape of the plastic zone; and B and L are the thickness (m) and ligament length (m) of the sample, respectively. Finally, the crack tip opening displacement (CTOD) was proposed to characterize the resistance of the crack tip material to fracture [135].

$$\delta_t = w_e / \sigma_n \tag{3-12}$$

where σ_n is the maximum net section pressure under all the ligament width specimens (MPa), i.e., the net section pressure of the specimen at a ligament length of 5 mm. The larger the CTOD value, the better the fracture toughness of the bitumen.

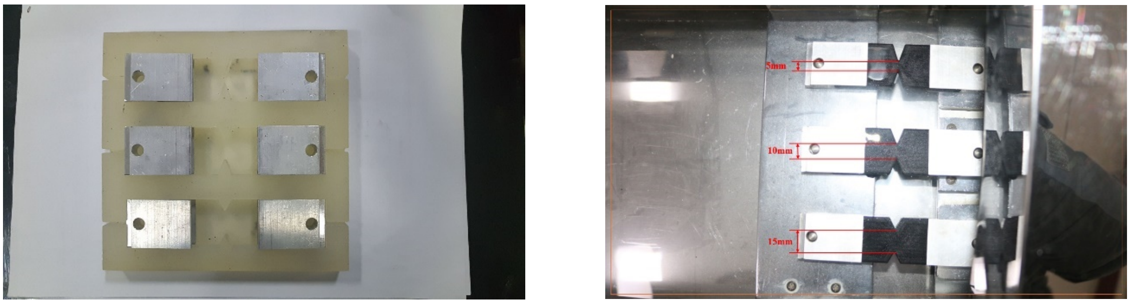

(a) (b)

Figure 3.9 Schematic diagram of the DENT test

3.2 Results and Discussion

3.2.1 MD simulation results of thermodynamic characteristics and adsorption configuration of bitumen-mineral interface

3.2.1.1 Work of adhesion between bitumen and rock-forming mineral

The work of adhesion (W_{ad}) between bitumen and different rock-forming minerals was calculated to characterize the adhesion performance of the bitumen-mineral interface. The W_{ad} can be computed as follows:

$$E_{\mathrm{int}} = E_{\mathrm{int}erface} - (E_{bitumen} + E_{\mathrm{min}eral}) \tag{3-13}$$

$$W_{ad} = \frac{E_{\mathrm{int}}}{A} \tag{3-14}$$

where E_{int} is the interaction energy between bitumen and mineral; $E_{interface}$, $E_{bitunmen}$, and $E_{mineral}$ are the potential energies of the bitumen-mineral interface, bitumen layer, and mineral layer, respectively; A is the contact area of the bitumen-mineral interface. These above parameters can be directly derived from the trajectory structure files of the bitumen-mineral interface models. Therefore, the W_{ad} results between bitumen and different rock-forming minerals are presented in Figure 3.10. It can be found from the figure that the quartz mineral shows the lowest W_{ad} results, followed by anorthite, calcite, gehlenite, Wuestite, magnetite, and C3S. It can be concluded that fillers with higher quartz mineral contents will exhibit a worse adhesion performance with bitumen. Furthermore, filler mineralogy plays a non-negligible role in the bitumen-filler interaction capability. The main rock-forming minerals of four waste fillers (Wuestite, C3S, magnetite, and gehlenite) show a higher W_{ad} value than that of mineral fillers, indicating a better adhesion performance with bitumen. It can be foreseen that waste fillers will exhibit a greater interaction ability with bitumen than mineral fillers for the selected materials in this study, and the role of filler mineralogy for the bitumen-mineral interaction cannot be ignored.

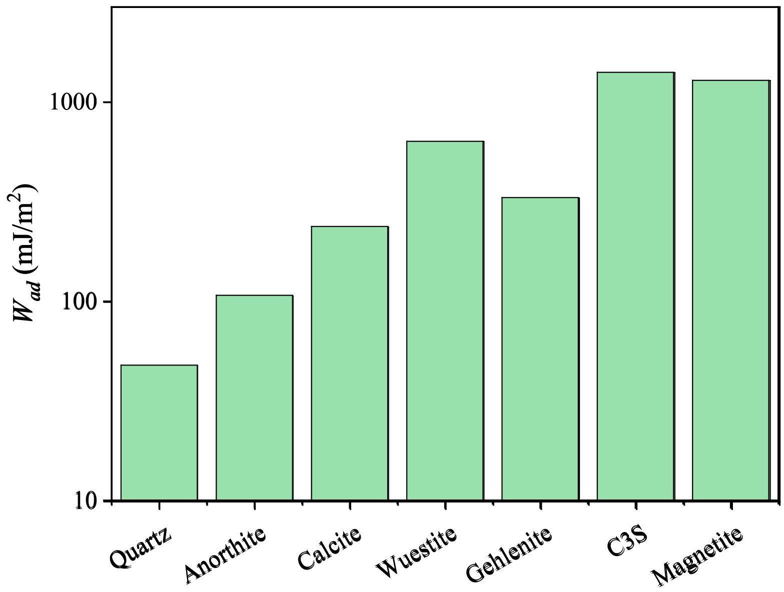

Figure 3.10 W_{ad} results between bitumen and different rock-forming minerals

3.2.1.2 Structural and thermodynamic characteristics of the adsorbed bitumen layer

RDF *g(r)* describes how density varies as a function of distance from a reference particle. The RDFs between the surface atoms of the rock-forming mineral and the geometry centroid of the bitumen layer were calculated and presented in Figure 8. It can be found that the RDF between the quartz mineral and the bitumen layer is apparently lower than that of other rock-forming minerals, indicating that the enrichment level of bitumen molecules on the surface of quartz minerals is significantly lower than that of the other six rock-forming minerals. The strong interaction between the rock-forming mineral and the bitumen layer is responsible for the aggregation of the bitumen molecules in the near-surface region [130]. It can be concluded that the interaction ability between the quartz mineral and the bitumen layer is weaker than that of other minerals selected in this study, which is consistent with the conclusion of Figure 3.11.

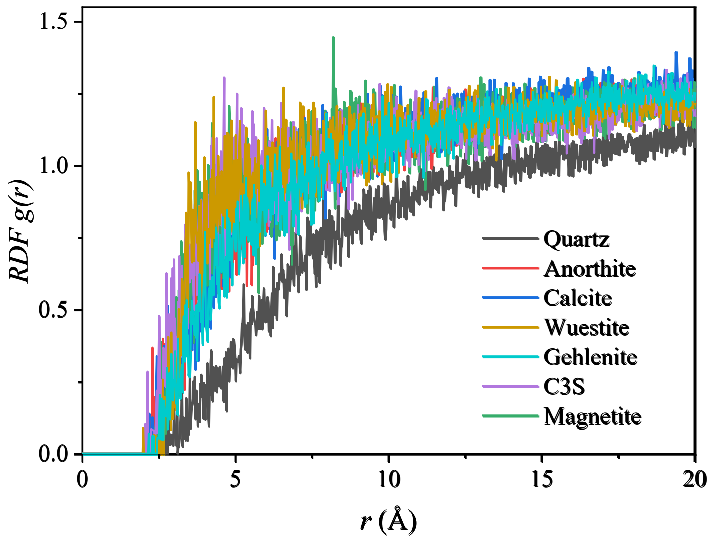

Figure 3.11 *g(r)* results between mineral surface and centroid-of-geometry of bitumen layer

Mean squared displacement (MSD) refers to the deviation of the position of a particle with respect to a reference position over time. In this study, the MSDs of bitumen layers for the bitumen-mineral interface modes with different rock-forming minerals are calculated and shown in Figure 3.12. As a comparison, the MSD of the independent bitumen molecular model rather than interfacial models is calculated and presented in Figure 3.12 (a). To more accurately determine the movement pattern of absorbed bitumen molecules, the MSDs of the model in the components of three directions of *xx*, *yy*, and *zz*, were calculated in detail and shown in the figures. Apparently, the total MSD is the sum of MSDs in three directions. From the figures, firstly, compared to the independent bitumen molecular model, the total MSDs of the interface model significantly increase after the rock-forming mineral model is loaded. This is because the total MSD of independent bitumen molecular models mainly comes from the free motion of molecules. After installing the rock-forming mineral model, the forces between the absorbed bitumen layer and the rock-forming mineral model, such as van der Waals forces, undoubtedly promote the movement of bitumen molecules, thereby increasing the total MSDs. This can also be verified from MSDs in the components of three directions of *xx*, *yy*, and *zz*. For the independent bitumen molecular model, its MSDs in the three directions are basically identical, as this is the free diffusion of bitumen molecules and should not show any differences in the three directions. As for the bitumen-mineral interface model, the MSDs in the components of three directions are no longer equal. It is worth noting that the MSD in the *zz* direction is the lowest value among the three directions. This indicates that the interaction between the bitumen layer and rock-forming mineral models reduces the degree of freedom of adsorbed bitumen molecules in the vertical direction (*zz*).

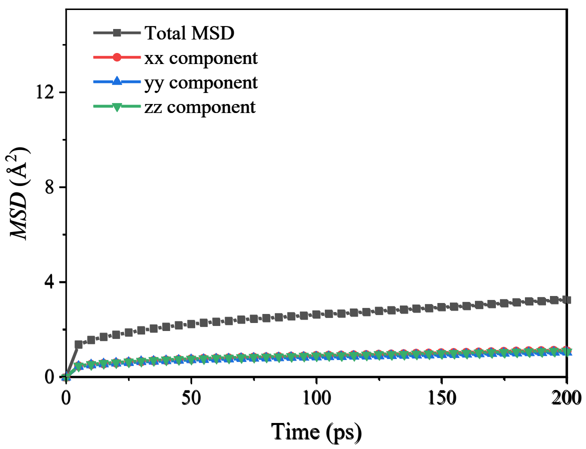

(a)

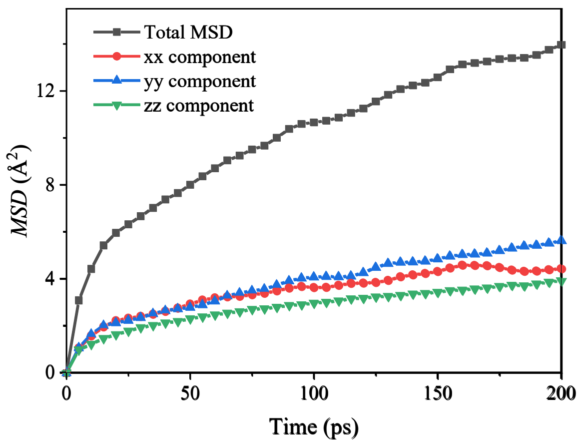

(b)

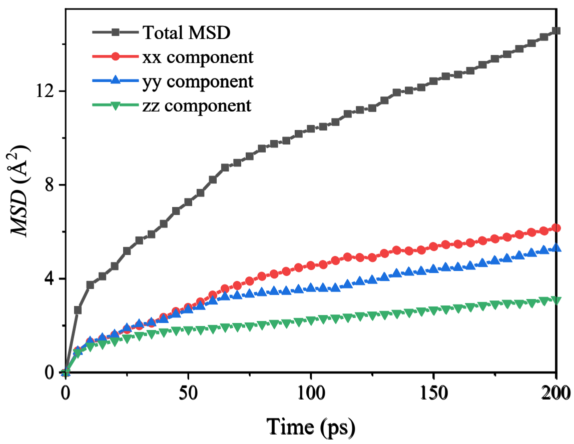

(c)

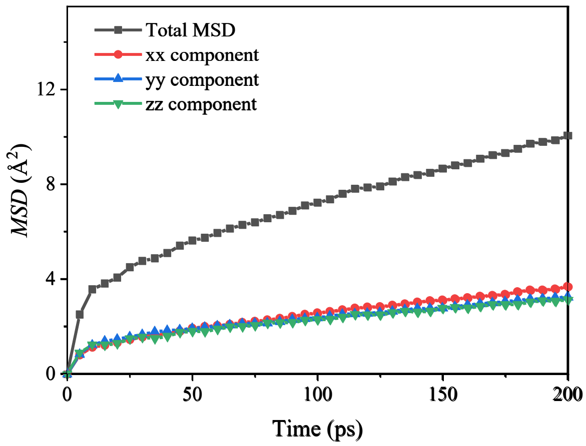

(d)

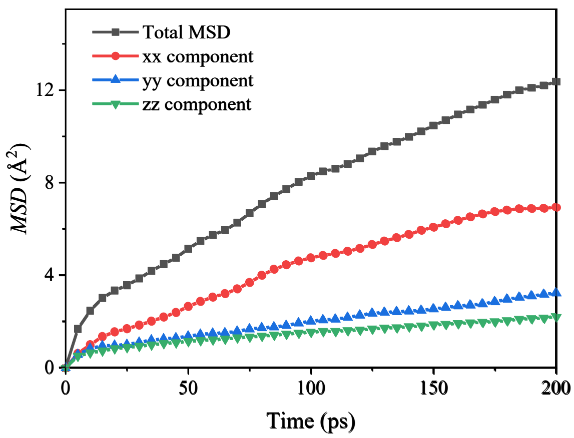

(e)

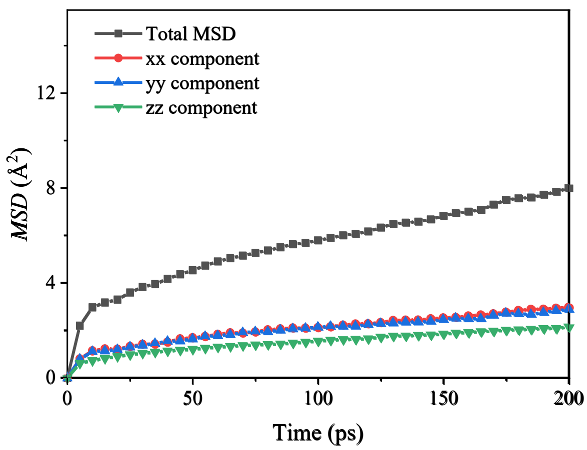

(f)

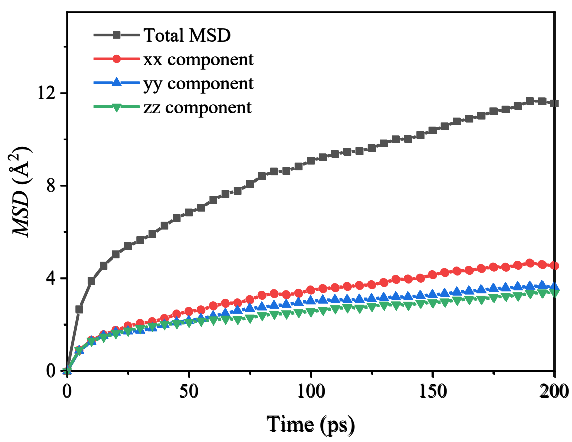

(g)

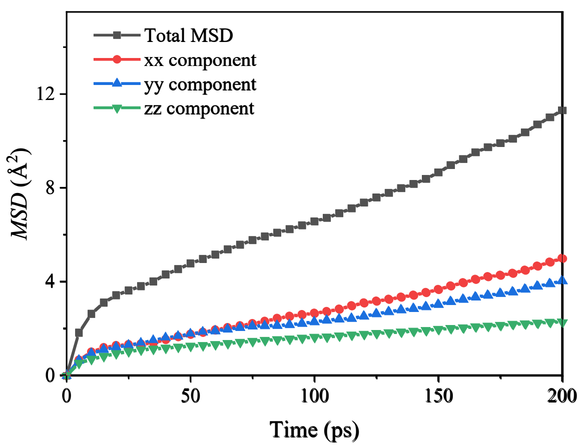

(h)

Figure 3.12 *MSDs* of bitumen layers for different mineral models of (a) Bulk bitumen; (b) Quartz; (c) Anorthite; (d) Calcite; (e) Wuestite; (f) Gehlenite; (g) C3S and (h) Magnetite

In addition, to more accurately characterize the diffusion ability of adsorbed bitumen molecules in the vertical direction, the diffusion coefficient D_{zz} in the *zz* direction of the adsorbed bitumen layer was further calculated for each bitumen-mineral interface model. The calculation equation for the diffusion coefficient (*D*) is shown in the following Equation (3-15):

$$D = \frac{1}{6} \lim_{\Delta t \to \infty} \frac{dMSD}{d\Delta t} \tag{3-15}$$

where *t* is the time. Figure 3.13 shows the D_{zz} results of bitumen layers for different bitumen-mineral interface models. It can be found that the main rock-forming minerals of three mineral fillers (quartz, anorthite, and calcite) exhibit higher D_{zz} than that of four waste fillers, indicating less mobility of bitumen molecules in the perpendicular direction of the mineral surface of waste fillers. This is most likely due to the stronger adsorption of bitumen onto the mineral surface of waste fillers, which verifies the conclusion of the work of adhesion (W_{ad}) above.

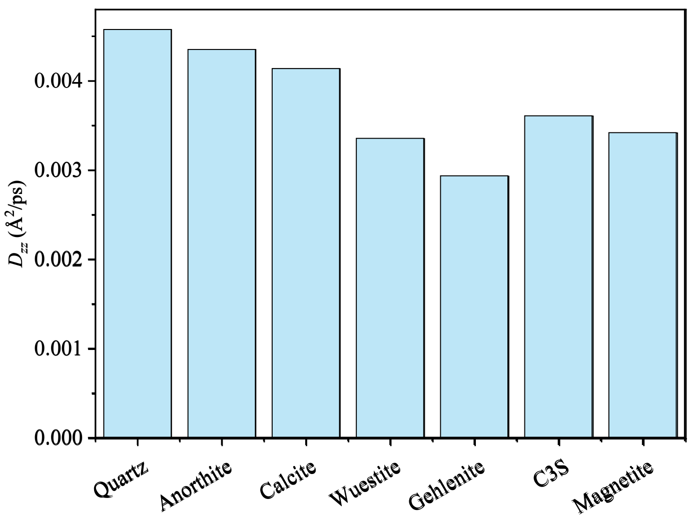

Figure 3.13 Diffusion coefficients at *zz* direction of bitumen layers for different bitumen-mineral interface models

3.2.1.3 Adsorption configuration of the bitumen fractions on the rock-forming mineral models

To investigate the adsorption configuration of the bitumen fractions on the rock-forming mineral models, the relative concentration distributions of the bitumen layers of different bitumen-mineral interface models in the perpendicular direction (*zz* direction) are collected and presented in Figures 3.14 and 3.15. Especially, Figures 3.14 and 3.15 show the relative concentrations of the overall bitumen layers and the four fractions of SARA of the bitumen layers, respectively. From Figure 3.14, the shape of the relative concentration curve of the adsorbed bitumen layer for different bitumen-mineral interface models is similar. The surface of rock-forming minerals is defined as the zero point in the *zz* direction. Firstly, the vertical axis of the curve is 0 at the beginning stage, which is due to the existence of a vacuum region between the mineral model and the bitumen layer that does not contain any molecules, as can be intuitively observed in Figure 3.4. Subsequently, when the distance in the *zz* direction is approximately 5 Å, the concentration curve sharply rises, reaching the first peak, and then enters the oscillation phase (the second stage). Finally, when the distance in the *zz* direction is around 40 Å, the concentration curve enters the descending stage and gradually decreases to 0 (the third stage). The higher the relative concentration, the higher the degree of aggregation of bitumen molecules. It can also be observed from Figure 3.14 that the first peak of the second stage of the relative concentration curve of the quartz mineral is significantly lower than that of the surfaces of other rock-forming minerals. This indicates that the degree of aggregation of bitumen molecules on the surface of the quartz mineral is lower than that of other rock-forming minerals. This is mainly due to the weaker adsorption of the quartz mineral on the bitumen layer compared to other rock-forming minerals, which is consistent with the conclusions derived from the results of W_{ad}, RDF, and D_{zz} above.

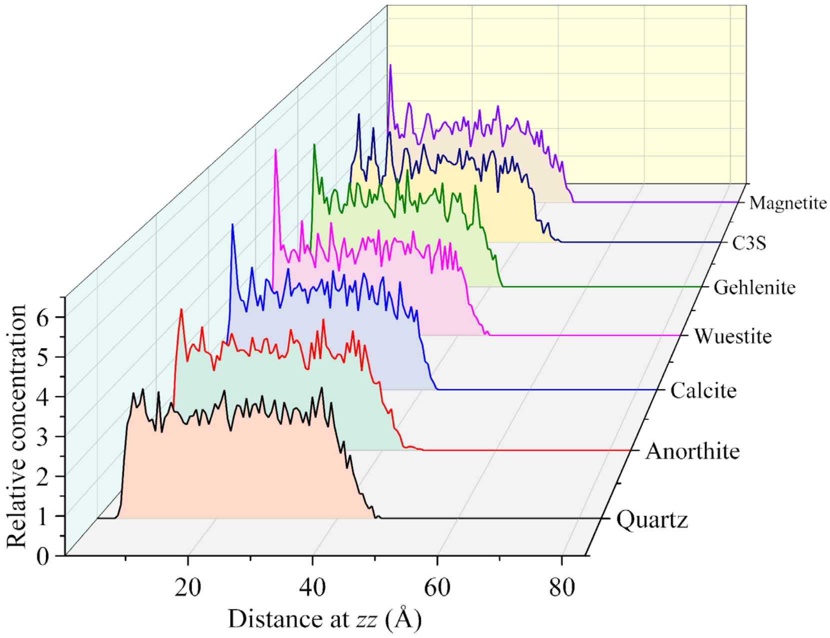

Figure 3.14 Relative concentrations of the absorbed bitumen layers on the *zz* direction

The relative concentration distributions of the four fractions of SARA of the bitumen layers in Figure 3.15 verify the finding of the distributions of the overall bitumen layer above. The relative concentration curves of the SARA exhibit similar shapes to those of the overall bitumen layer, and quartz mineral presents the lowest initial peak at the oscillation phase than that of other rock-forming minerals. In addition, it was found through observation that the relative concentration distribution rules of SARA in the adsorbed bitumen layer of all mineral models are consistent. As the distance along the *zz* direction increases, the relative concentration of resin is highest in the first stage. Continuing into the second stage, the relative concentration curve of resin decreases while the asphaltene curve occupies the highest position. Continuing into the third stage, the relative concentration of saturate is the highest. In the final fourth stage, the aromatic curve occupies the highest position. To summarize, the distribution characteristics of adsorbed bitumen molecules on the surface of rock-forming minerals can be divided into four regions along the perpendicular direction. Here, the quartz mineral is taken as an example for regional division, as shown in Figure 3.15 (h).

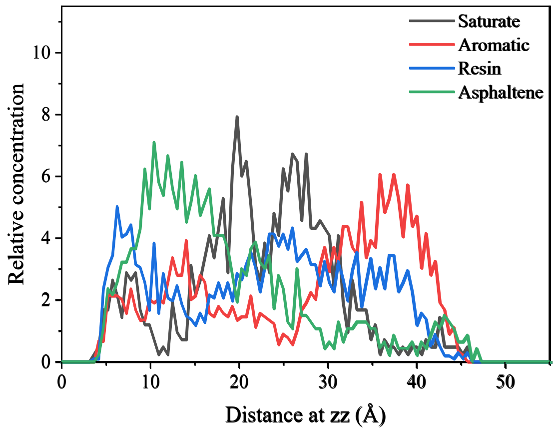
Saturate
Aromatic
Resin
Asphaltene
Relative concentration
Distance at zz (Å)
0
2
4
6
8
10
0
10
20
30
40
50

(a)

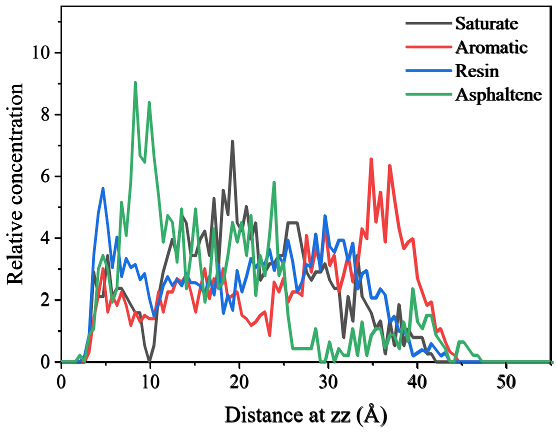
Saturate
Aromatic
Resin
Asphaltene
Relative concentration
Distance at zz (Å)
0
2
4
6
8
10
0
10
20
30
40
50

(b)

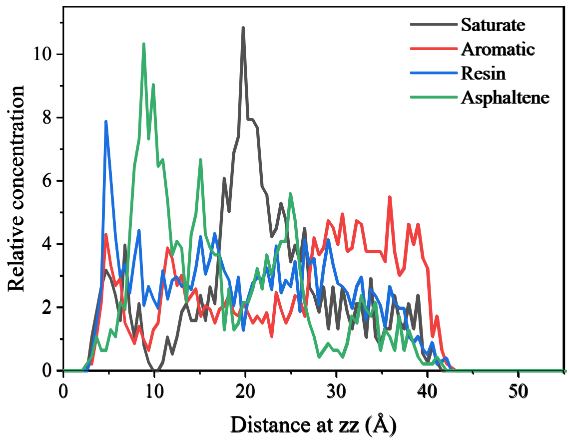
Saturate
Aromatic
Resin
Asphaltene
Relative concentration
Distance at zz (Å)
0
2
4
6
8
10
0
10
20
30
40
50

(c)

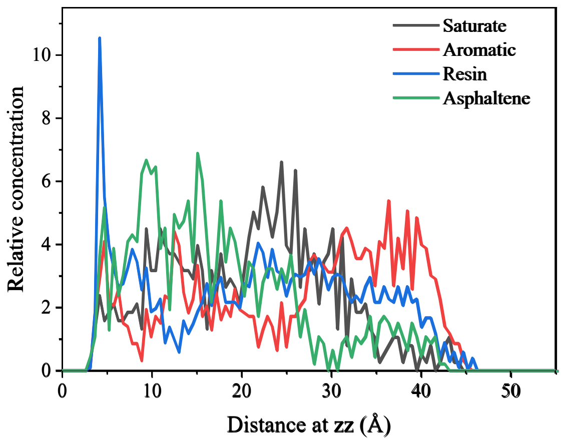
Saturate
Aromatic
Resin
Asphaltene
Relative concentration
Distance at zz (Å)
0
2
4
6
8
10
0
10
20
30
40
50

(d)

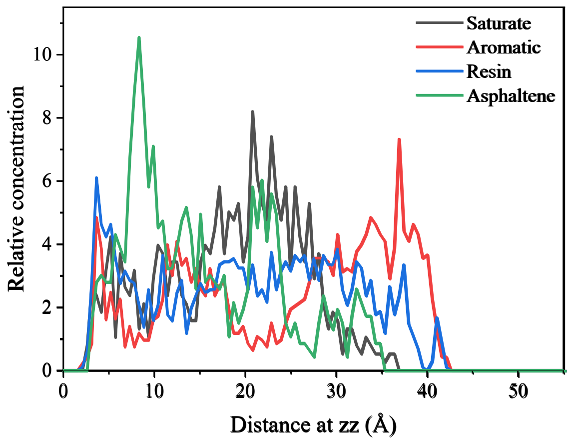
Saturate
Aromatic
Resin
Asphaltene
Relative concentration
Distance at zz (Å)
0
2
4
6
8
10
0
10
20
30
40
50

(e)

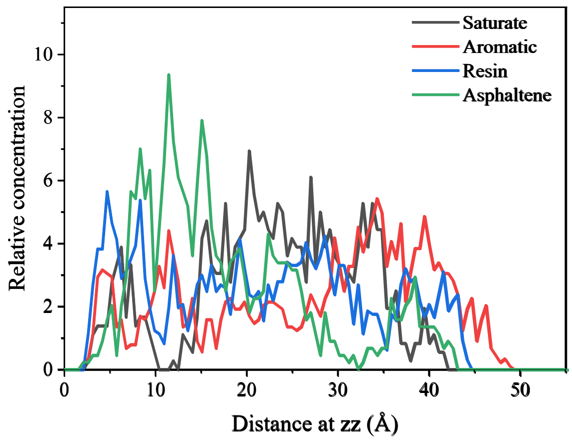
Saturate
Aromatic
Resin
Asphaltene
Relative concentration
Distance at zz (Å)
0
2
4
6
8
10
0
10
20
30
40
50

(f)

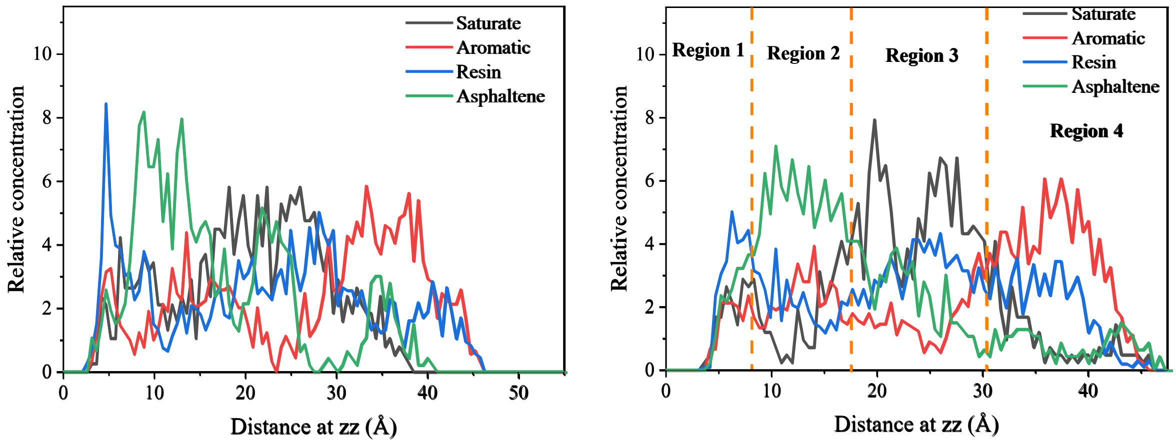

(g) (h)

Figure 3.15 Relative concentrations of the four bitumen components on various mineral surfaces of (a) Quartz; (b) Anorthite; (c) Calcite; (d) Wuestite; (e) Gehlenite; (f) C3S; (g) Magnetite; (h) Region division

Based on the above analysis, the schematic diagram of the adsorption configuration of the bitumen fractions on the rock-forming mineral models can be summarized and presented in Figure 3.16. The relative concentrations of the four bitumen components of SARA on mineral surfaces can be divided into four regions. It is worth noting that the four components of SARA are distributed in all four regions, with concentrations not 0, and occupy the main component positions in different regions. In the area closest to the mineral surface (region one), the Resin component occupies the main component. As the distance from the mineral surface increases, entering region two, the concentration of the Asphaltene component is highest. In region three, the saturate component holds a leading position, and the aromatic component in region four.

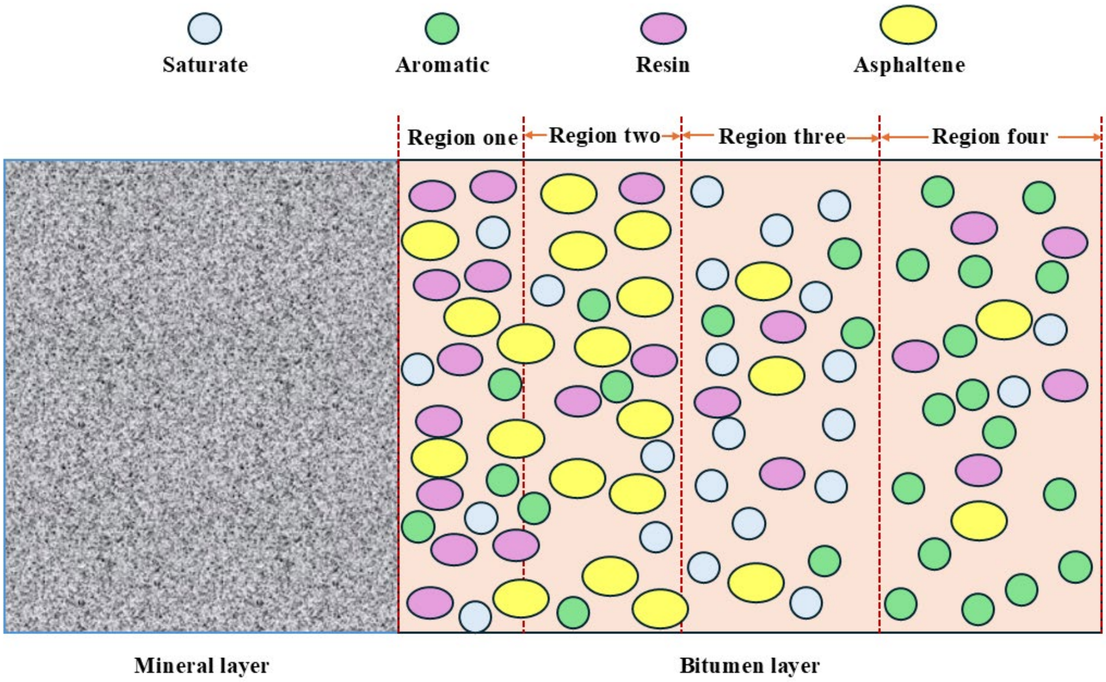

Figure 3.16 Schematic diagram of the adsorption configuration of the bitumen fractions on the rock-forming mineral models

3.2.2 MD simulation results of bitumen-mineral interfacial failure

3.2.2.1 Repeatability of the pull-off simulation

The quartz interface model was first selected as an example to validate the repeatability of the pull-off simulations before further analysis was performed. During the establishment process of the bitumen layer, the individual component molecules were randomly packed into the cell after which energy minimization and dynamic equilibrium were implemented. To identify the potential influence of the heterogeneity of bitumen microstructure arising from random generation, four replicates of bitumen models were constructed. These bitumen models were further used to establish the interface models with the quartz surface. The validation was then conducted by performing the pull-off simulation for the four replicates of the interface model at two different loading rates, 0.005Å/fs, and 0.0005Å/fs. The adopted simulation temperature was 25°C. The simulation results are presented in Figure 3.17. It is found that the traction-deformation curves obtained at the loading rate of 0.005 Å/fs are relatively smooth, but significant discreteness was observed for the traction-deformation curves obtained at the loading rate of 0.0005 Å/fs. The underlying mechanism of loading rate influence is to be discussed in the following section. However, the results presented in Figure 3.17 clearly demonstrate that the random generation process of the bitumen model hardly influences the pull-off simulation results.

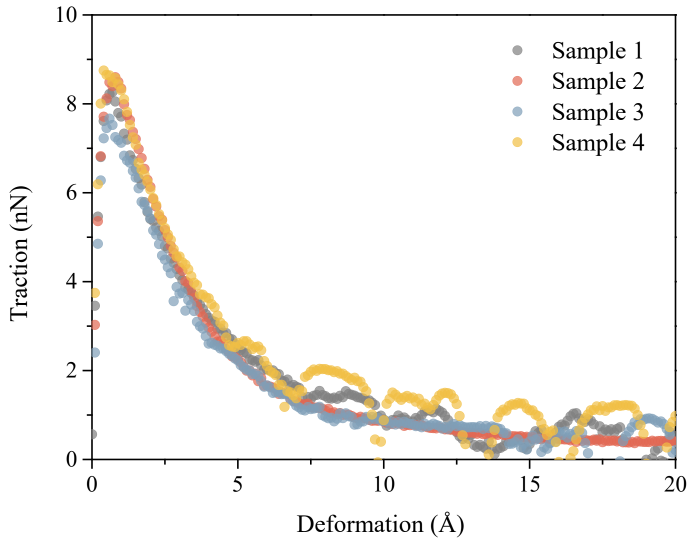

(a) 0.005 Å/fs

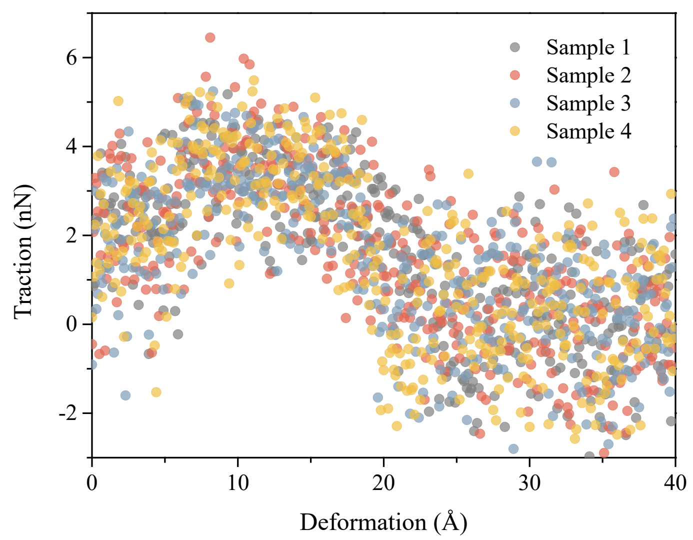

(b) 0.0005 Å/fs

Figure 3.17 Repeatability validation of the pull-off simulation for different samples

The stability of the pull-off simulation was also validated by repeating the simulation of the same interface model for four times, and the results are given in Figure 3.18. It shows that the traction-deformation curves produced in different replicates are very close to each other regardless of the loading rate. This verifies the good stability of the pull-off simulation method used in the current study. Based on the results from Figure 3.17 and Figure 3.18, one can easily conclude that the reliability of the interface model as well as the repeatability of the pull-off method used in this study are good enough so that no repeated simulation was conducted in the following analysis.

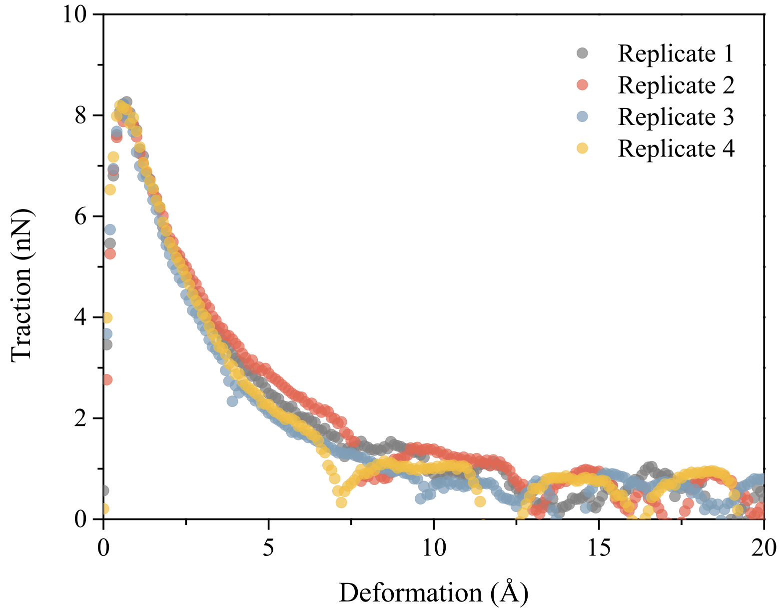

(a) 0.005 Å/fs

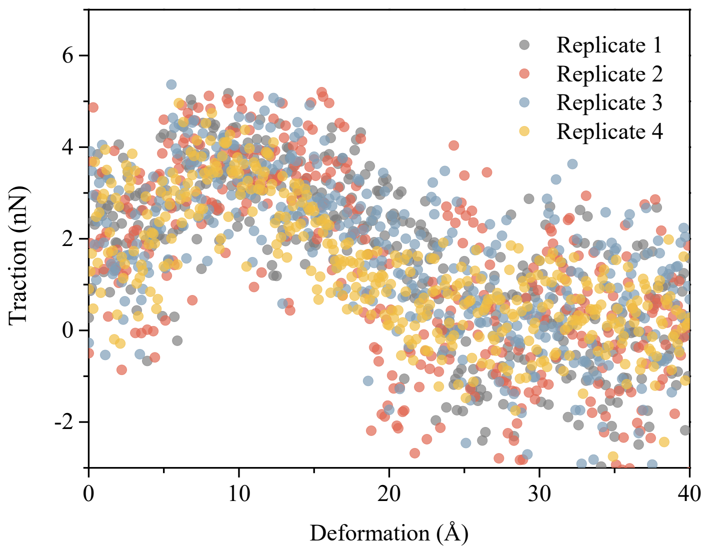

(b) 0.0005 Å/fs

Figure 3.18 Repeatability validation of the pull-off simulation for different replicates

3.2.2.2 Effect of loading rate

Based on MD simulations, the results of the traction-deformation curves of the bitumen-filler model are shown in Figures 3.19 to 3.23 at five loading rates of 0.01Å/fs, 0.005Å/fs, 0.001Å/fs, 0.0005Å/fs, 0.0001Å/fs. Since this section mainly discusses the effect of loading rate on bitumen-filler interface cracking, the bitumen-quartz interface model is selected as a representative, and the rules of other bitumen-filler interface models are consistent.

From Figure 3.19 (b), when the loading rate is 0.01 Å/fs, the cracking of the model all occurs at the interface of the bitumen-filler model, which indicates that the cohesive force inside the bitumen model at this point is much greater than the adhesion force of the bitumen-filler interface model. In addition, according to Figure 3.19 (a), the traction of the model goes through such a process. As the tensile deformation increases, the traction first increases rapidly to the highest point, then decreases rapidly, and finally the downward trend gradually slows down.

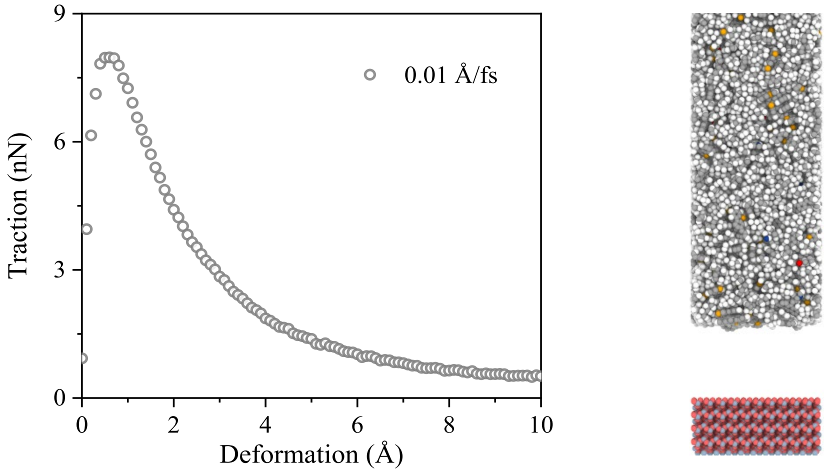

(a) (b)

Figure 3.19 The tensile simulation results of the bitumen-quartz interface at the loading rate of 0.01 Å/fs: (a) traction-deformation curve and (b) failure configuration

From Figure 3.20 (b), when the loading rate is 0.005 Å/fs, the cracking of the model mainly occurs at the interface of the bitumen-filler model. However, it can be observed that a small amount of bitumen molecular structure remains on the filler interface, which indicates that slight cracking has also occurred inside the bitumen model. It can be inferred that the cohesive force inside the bitumen model at this point is bigger than the adhesion force of the bitumen-filler interface model. What's more, according to Figure 3.20 (a), the variation pattern of the traction-deformation curve under this loading rate is consistent with that at the rate of 0.01 Å/fs. The difference is that there is a certain degree of dispersion in the curve during the later stage of loading, which may be due to a small amount of bitumen molecules remaining at the filler interface during interface failure.

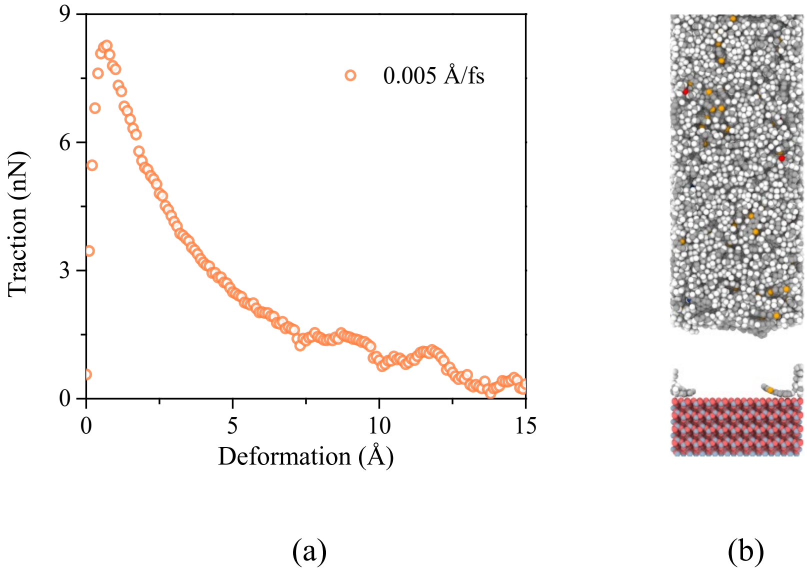

Figure 3.20 The tensile simulation results of the bitumen-quartz interface at the loading rate of 0.005 Å/fs: (a) traction-deformation curve and (b) failure configuration

From Figure 3.21 (b), when the loading rate is 0.001 Å/fs, the cracking of the bitumen-filler interface model all occurs inside the bitumen molecular model, which indicates that the cohesive force inside the bitumen model at this point is smaller than the adhesion force of the bitumen-filler interface model. According to Figure 3.21 (a), the variation pattern of the traction-deformation curve under this loading rate exhibits significant discreteness. Besides, compared with the traction-deformation curves at the loading rates of 0.01 Å/fs and 0.005 Å/fs, the maximum value of the traction decreases, and after reaching the maximum value, the traction goes through a plateau period (remaining unchanged) before starting to decline. As for the simulation results at the loading rate of 0.0005 Å/fs in Figure 3.22, the cracking mode of the interface model is basically consistent with that at the 0.001 Å/fs, and the difference is that the discreteness of the traction-deformation curve in Figure 3.22 (a) becomes more significant.

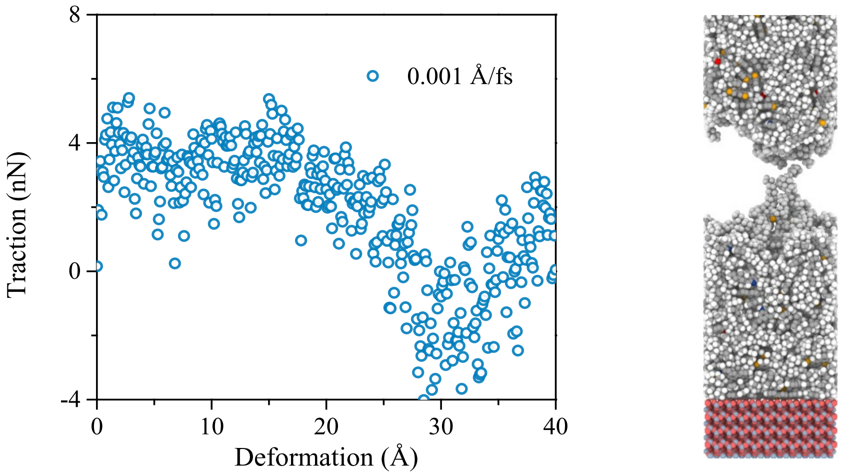

(a) (b)

Figure 3.21 The tensile simulation results of the bitumen-quartz interface at the loading rate of 0.001 Å/fs: (a) traction-deformation curve and (b) failure configuration

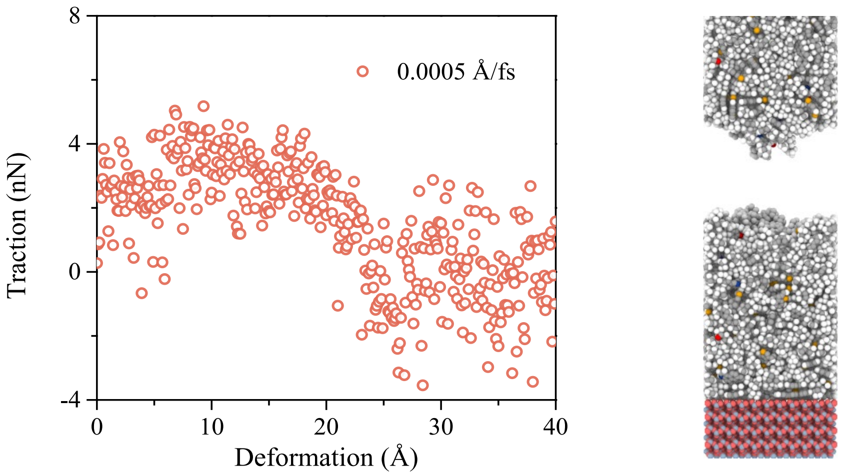

(a) (b)

Figure 3.22 The tensile simulation results of the bitumen-quartz interface at the loading rate of 0.0005 Å/fs: (a) traction-deformation curve and (b) failure configuration

From Figure 3.23, when the loading rate is 0.0001 Å/fs, the cracking of the bitumen-filler interface model all occurs inside the bitumen molecular model, which is consistent with the results in above Figures 3.21 and 3.22. However, it is worth noting that compared to the simulation results at 0.001 Å/fs and 0.0005 Å/fs, the fracture surface inside the bitumen model in Figure 3.23 (b) is smoother, indicating that the adhesive force between the bitumen-filler interface is much greater than the cohesive force inside the bitumen molecules. Moreover, when the loading rate further decreases to 0.0001 Å/fs from 0.0005 Å/fs, the plateau region in the traction-deformation curve no longer exists. In other words, when the traction reaches its highest point, it quickly begins to decline. In addition, compared to Figures 3.21 and 3.22, the discreteness in the traction-deformation curve in Figure 3.23 is even more remarkable.

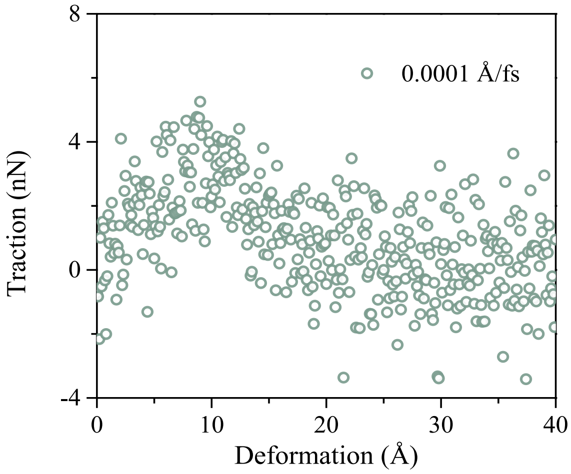

(a)

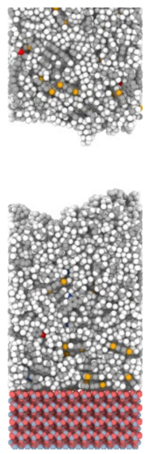

(b)

Figure 3.23 The tensile simulation results of the bitumen-quartz interface at the loading rate of 0.0001 Å/fs: (a) traction-deformation curve and (b) failure configuration

According to the above analysis results, the cracking modes of the bitumen-filler interface model under different loading rates can be summarized into the following three types, as shown in Figure 3.24. When the loading rate is low as presented in Figure 3.24 (a), the cracking mode of the bitumen-filler interface model can be divided into three stages of elastic stage, the softening stage, and the debonding stage. At the initial elastic stage, the traction grows rapidly to the highest value. Subsequently, the model enters the softening stage, and the traction begins to go down. When traction drops to 0, the model enters the debonding stage. The simulation results at 0.0001 Å/fs in Figure 3.23 are typical cracking modes of the bitumen-filler interface model at low loading rates.

When the loading rate is intermediate, the cracking mode of the bitumen-filler interface model can be summarized in Figure 3.24 (b), which has an additional plastic stage compared to the cracking mode under low loading rates. This plastic stage is the plateau period mentioned earlier, that is, the traction remains at the highest point for a period. The simulation results at 0.001 Å/fs and 0.0005 Å/fs in Figures 3.21 and 3.22 above are typical cracking modes of the bitumen-filler interface model at intermedia loading rates.

When the loading rate increases further, the cracking mode of the bitumen-filler interface model returns to the three-stage mode. In addition, it is worth mentioning that the elastic stage at this point is much shorter than that under the low loading rate. In other words, the traction reaches its maximum value very quickly. The simulation results at 0.01 Å/fs in Figure 3.19 above are the typical cracking mode of the bitumen-filler interface model at high loading rates.

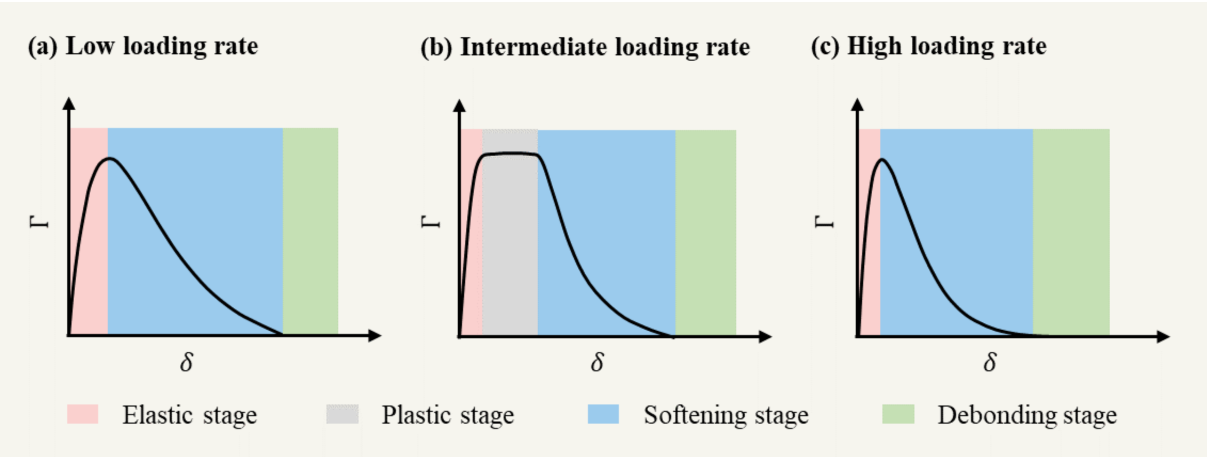

Figure 3.24 Stage division of cracking modes of bitumen-filler interface model at different loading rates

Furthermore, in this study, the cracking mechanism of the bitumen-filler interface model under different loading rates is summarized as presented in Figure 3.25. When the bitumen-filler interface model is at the equilibrium state, the adhesive force between the mineral surface and the interface bitumen is basically equal to the cohesive force between the interface bitumen and bulk bitumen, and there is no cracking occurs.

When a low loading rate is applied to the bitumen-filler interface model, the adhesive force between the mineral surface and the interface bitumen is much larger than the cohesive force between the interface bitumen and bulk bitumen, and the cracking of the interface model occurs between the interface bitumen and bulk bitumen.

When an intermediate loading rate is applied to the bitumen-filler interface model, the adhesive force between the mineral surface and the interface bitumen is larger than the cohesive force between the interface bitumen and bulk bitumen, and the cracking of the interface model mainly occurs between the interface bitumen and bulk bitumen.

When the loading rate further increases to a high rate, the adhesive force between the mineral surface and the interface bitumen is much lower than the cohesive force between the interface bitumen and bulk bitumen, and the cracking of the interface model occurs between the mineral surface and the interface bitumen.

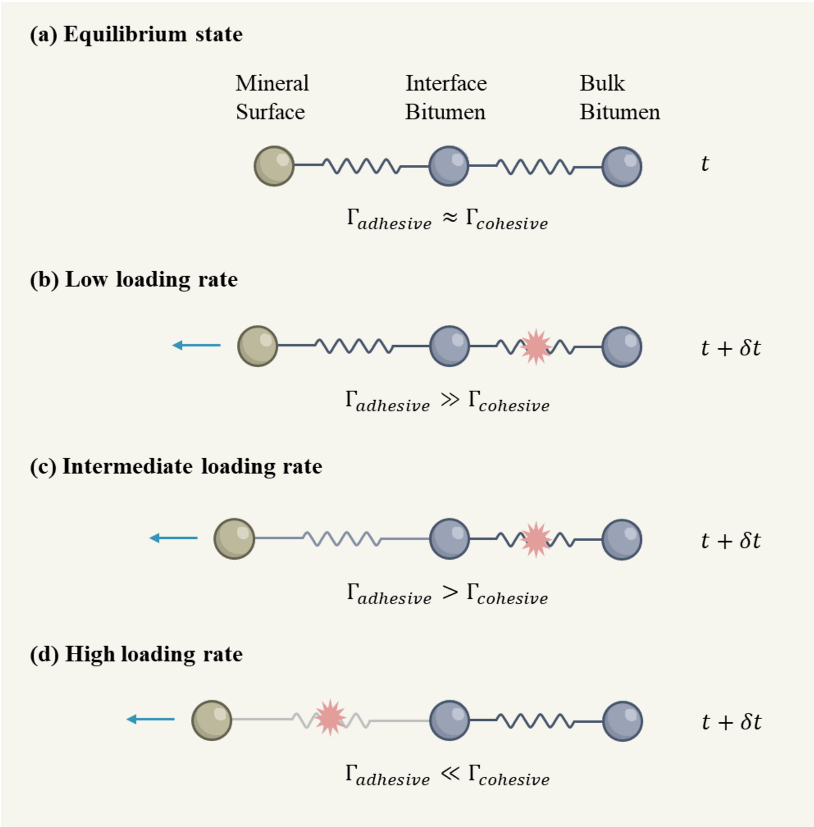

Figure 3.25 Schematic illustration of cracking modes of bitumen-filler interface model at different loading rates.

Figures 3.26 - 3.28 presents the cracking process of the bitumen-filler interface model under different loading rate, and a snapshot is taken every 5 Å to record the progress of cracking. It can be seen from the figure that the cracking mode of the interface model under different loading rates is exactly as illustrated in Figure 3.25. It can be seen from the results at the high loading rate in Figure 3.26 that when the pull-off is at the beginning stage and the deformation is 5 Å, the adhesive force between the mineral surface and the interface bitumen (close to 0) is much lower than the cohesive force between the interface bitumen and bulk bitumen, and the cracking of the interface model occurs between the mineral surface and the interface bitumen. In addition, as the debonding process proceeds, the traction of the fracture surface between the mineral surface and the interface bitumen continues to increase.

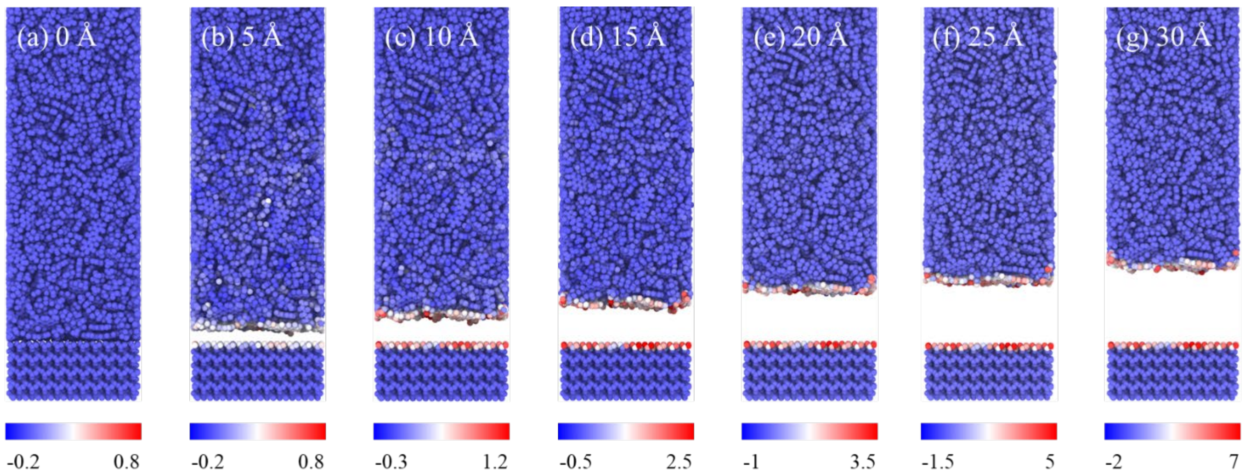

Figure 3.26 Cracking process of bitumen-filler interface model under the high loading rate

From the simulation results at the intermediate loading rate in Figure 3.27, when the pull-off simulation is at the beginning stage and the deformation is 5 Å, the cohesive force between the interface bitumen and bulk bitumen is lower than the adhesive force between the mineral surface and the interface bitumen. In addition, it is worth noting that there are also some weak points at the interface between filler and bitumen at this point, that is, points with lighter colours indicating smaller traction. However, as the pull-off simulation proceeds, the traction between the interface bitumen and bulk bitumen continues to increase and the weak points at the interface between filler and bitumen gradually disappear. Finally, the cracking of the interface model happens between the interface bitumen and bulk bitumen.

From the simulation results at the low loading rate in Figure 3.28, when the pull-off simulation is at the beginning stage and the deformation is 5 Å, the cohesive force between the interface bitumen and bulk bitumen is significantly lower than the adhesive force between the mineral surface and the interface bitumen. As the pull-off simulation continues, the traction between the interface bitumen and bulk bitumen keeps increasing, and the cracking happens between the interface bitumen and bulk bitumen finally. Moreover, compared with the pull-off results at the same deformation in Figure 3.27, the debonding process of the bitumen-filler interface model at the low loading rate in Figure 3.28 proceeds faster. This is because the difference between the adhesion between the mineral surface and the interface bitumen and the internal cohesion of bitumen molecules at a low loading rate is much greater than that at an intermediate loading rate, which verifies the analysis results above.

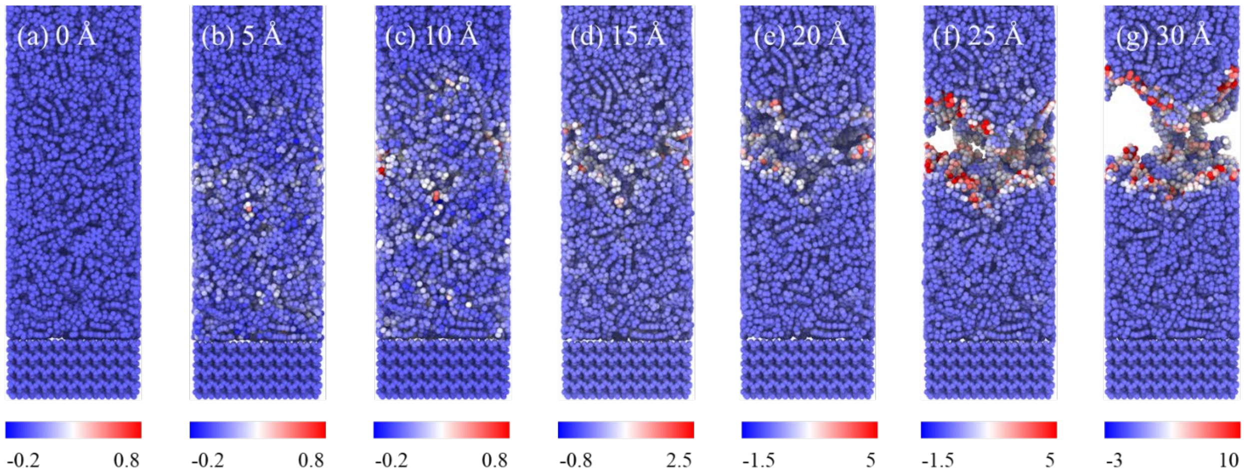

Figure 3.27 Cracking process of bitumen-filler interface model under the intermediate loading rate

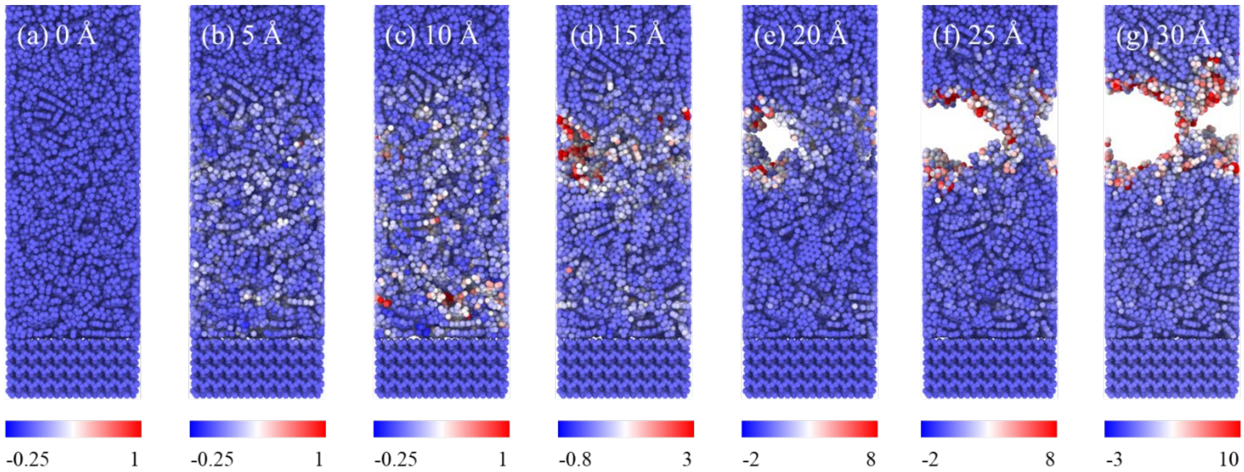

Figure 3.28 Cracking process of bitumen-filler interface model under the low loading rate.

3.2.2.3 Effect of filler mineralogy

Figure 3.29 presents the traction-deformation curves and failure configurations of the different bitumen-mineral interface models. The failure mode of all interface models under constant tensile rate is the same, which can be divided into two stages. In the first stage, as the deformation increases, the traction continues to increase until it reaches a peak value. The second stage is the debonding stage. As the traction increases, the traction gradually decreases, and the interface model fails due to adhesion/cohesion. Until the traction drops to 0, the interface model is completely cracked. It can be found from the figures that the adhesion between two minerals of wuestite and magnetite and bitumen molecules is dramatically higher than in other rock-forming mineral models. This can also be verified from the cracking patterns of different bitumen-mineral interface models. The cracking modes of the bitumen-wuestite and bitumen-magnetite interface models are cohesion and adhesion failure simultaneously. As a comparison, the cracking mode of other minerals is a purely adhesive failure. It is because the interface strength of the bitumen-wuestite and bitumen-magnetite is much greater than other interface models.

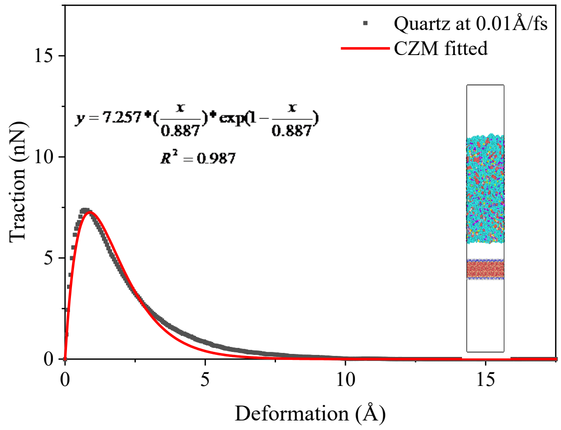
Quartz at 0.01Å/fs
CZM fitted
$y = 7.257*(\frac{x}{0.887})*\exp(1-\frac{x}{0.887})$
$R^2 = 0.987$
Traction (nN)
Deformation (Å)

(a)

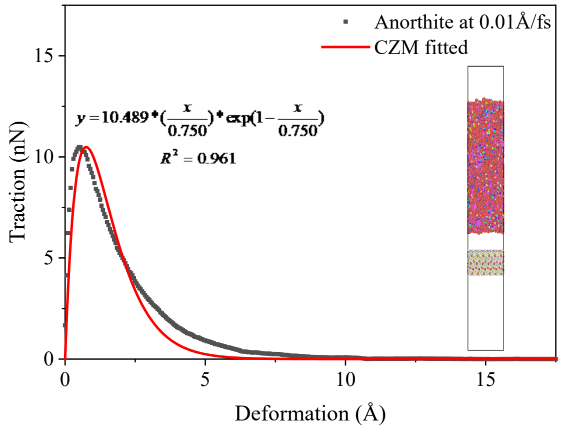
Anorthite at 0.01Å/fs
CZM fitted
$y = 10.489*(\frac{x}{0.750})*\exp(1-\frac{x}{0.750})$
$R^2 = 0.961$
Traction (nN)
Deformation (Å)

(b)

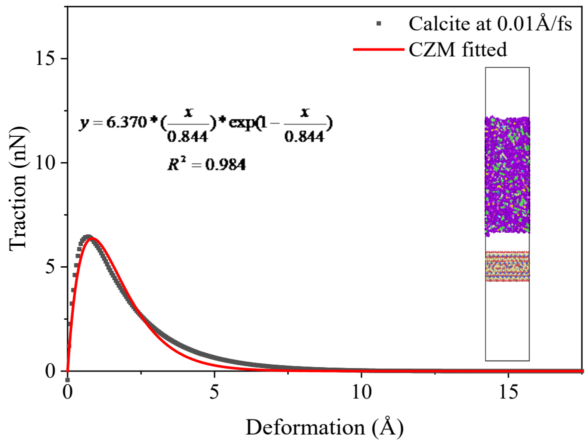
Calcite at 0.01Å/fs
CZM fitted
$y = 6.370*(\frac{x}{0.844})*\exp(1-\frac{x}{0.844})$
$R^2 = 0.984$
Traction (nN)
Deformation (Å)

(c)

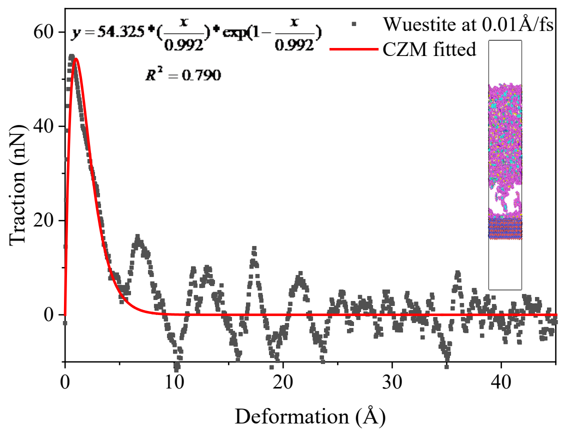
Wuestite at 0.01Å/fs
CZM fitted
$y = 54.325*(\frac{x}{0.992})*\exp(1-\frac{x}{0.992})$
$R^2 = 0.790$
Traction (nN)
Deformation (Å)

(d)

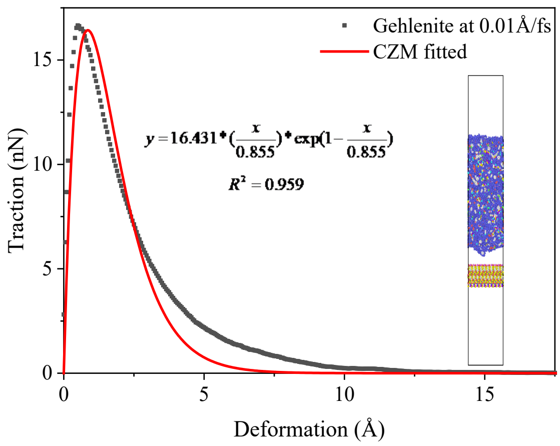
Gehlenite at 0.01Å/fs
CZM fitted
$y = 16.431*(\frac{x}{0.855})*\exp(1-\frac{x}{0.855})$
$R^2 = 0.959$
Traction (nN)
Deformation (Å)

(e)

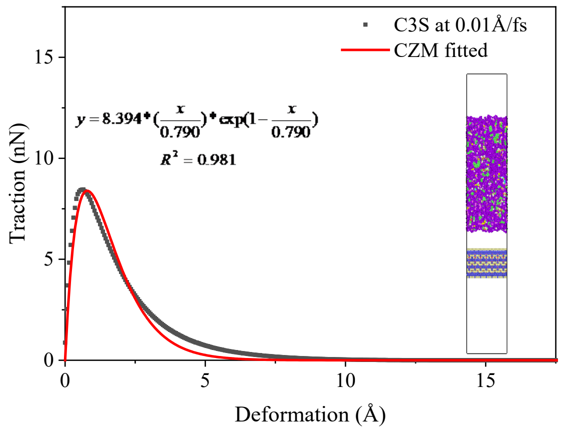
C3S at 0.01Å/fs
CZM fitted
$y = 8.394*(\frac{x}{0.790})*\exp(1-\frac{x}{0.790})$
$R^2 = 0.981$
Traction (nN)
Deformation (Å)

(f)

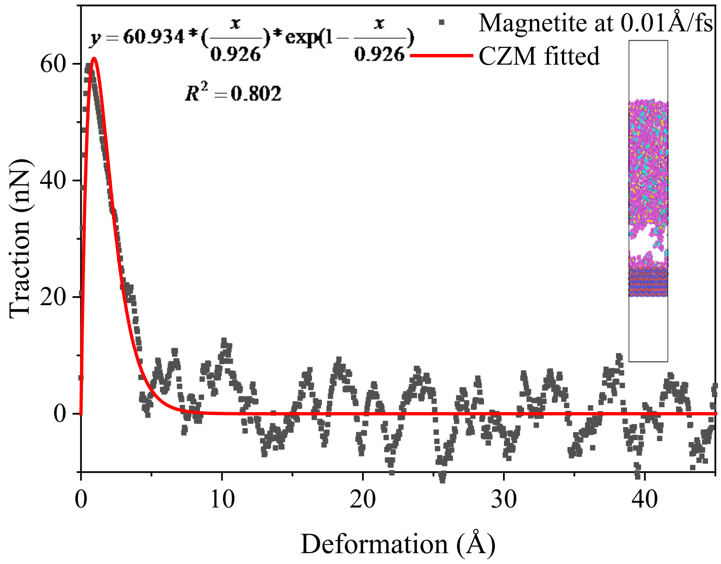

(g)

Figure 3.29 Traction-deformation curves and failure configurations of different bitumen-mineral interface models at 0.01 Å/fs: (a) Quartz; (b) Anorthite; (c) Calcite; (d) Wuestite; (e) Gehlenite; (f) C3S and (g) Magnetite

The exponential cohesive zone model (CZM) was adopted to fit the traction-deformation curves of the bitumen-filler model as follows [136, 137]:

$$F = F_c\left(\frac{\delta}{\delta_c}\right)\exp\left(1-\frac{\delta}{\delta_c}\right) \tag{3-16}$$

$$\sigma_c = \frac{F_c}{A} \tag{3-17}$$

$$\Gamma_{fe} = e*\sigma_c*\delta_c \tag{3-18}$$

where F and F_c are the traction and peak traction, respectively; δ and δ_c are the deformation and critical deformation, respectively; σ_c is the peak stress of the bitumen-mineral interface model; A is the cross-sectional area of the mineral model; e is the Euler number; and Γ_{fe} is the fracture energy. Table 3-6 lists the fitting result of the traction-deformation curves of interface models at 0.01 Å/fs based on the CZM. It can be found that the exponential CZM achieves superior fitting results for traction-deformation curves in this study, with the goodness of fit R^2 of five interface models (quartz, anorthite, calcite, gehlenite, and C3S) being higher than 0.95. As for the remaining two interface models, their R^2 is slightly reduced because the interface cracking modes of the bitumen-wuestite and bitumen-magnetite have both cohesion and adhesion failure. Cohesion failure will cause fluctuations in the traction-deformation curves, negatively affecting the fitting accuracy. Besides, the results of σ_c and Γ_{fe} precisely verify the conclusions of Figure 3.29. The σ_c and Γ_{fe} values of wuestite and magnetite are much higher than those of other rock-forming mineral models, indicating that the interaction and adhesion between these two minerals and the bitumen layer are significantly higher than that of other minerals, followed by gehlenite, anorthite, and C3S, and the last are quartz and calcite.

Table 3-6 Fitting result of the traction-deformation curves of bitumen-mineral interface models based on the CZM

Bitumen-minerals	F_c (nN)	σ_c (GPa)	δ_c (Å)	Γ_{fe} (J/m^2)	R^2
Quartz	7.257	0.290	0.887	0.0699	0.987
Anorthite	10.489	0.420	0.750	0.0855	0.961
Calcite	6.370	0.255	0.844	0.0585	0.984
Wuestite	54.325	2.173	0.992	0.586	0.790
Gehlenite	16.431	0.657	0.855	0.153	0.959
C3S	8.394	0.336	0.790	0.0721	0.981
Magnetite	60.934	2.437	0.926	0.613	0.802

Figure 3.30 presents the traction-deformation curves of bitumen-quartz and bitumen-wuestite interface models at the loading rates of 0.001 and 0.0001 Å/fs. As mentioned above, cohesive failure will greatly increase the discreteness of the traction-deformation curve. The data at this time is too discrete to be accurately analyzed. Therefore, only the failure configuration of the bitumen-mineral interface is discussed in detail. Figures 3.31 and 3.32 show the failure configuration of the interface model at two tensile rates of 0.001 and 0.0001 Å/fs. Based on Figures 3.29, 3.31, and 3.32, it can be concluded that the bitumen-mineral interface model

exhibits different failure modes at various loading rates. As the tensile rate continues to decrease, the interface model gradually transitions from adhesive failure to a combination of adhesive failure and cohesive failure, ultimately transitioning to cohesive failure. Mineral models with high interface strength with the bitumen model, such as wuestite and magnetite, are less prone to adhesive failure. Based on the failure configurations of the interface models under three loading rates, the rock-forming minerals in this study can be divided into three categories. The first category is wuestite and magnetite, whose failure modes of the interface model remain adhesive failure and cohesive failure coexisting at a high tensile rate of 0.01 Å/fs. The second category includes anorthite, gehlenite, and C3S, which maintain a cohesive failure mode at an intermediate tensile rate of 0.001 Å/fs. The third category is quartz and calcite, where the failure mode only transitions to cohesive failure at a low rate of 0.0001 Å/fs.

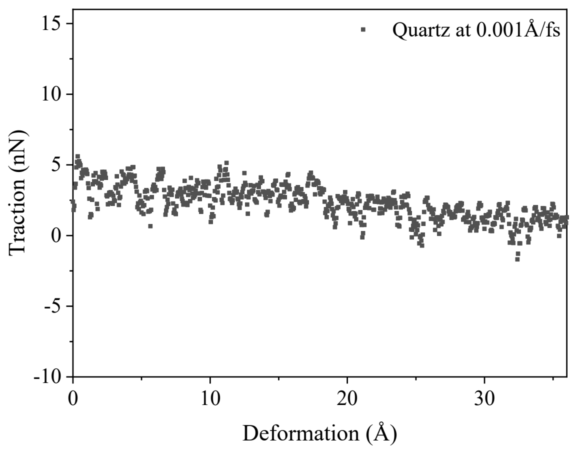

(a)

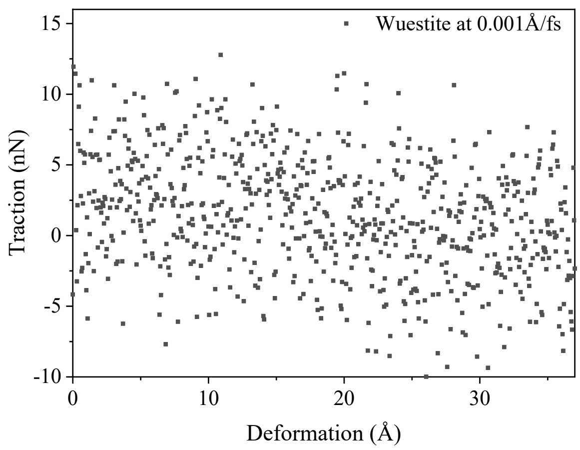

(b)

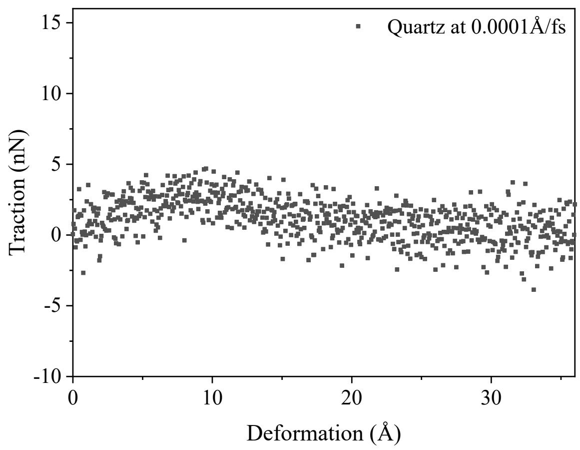

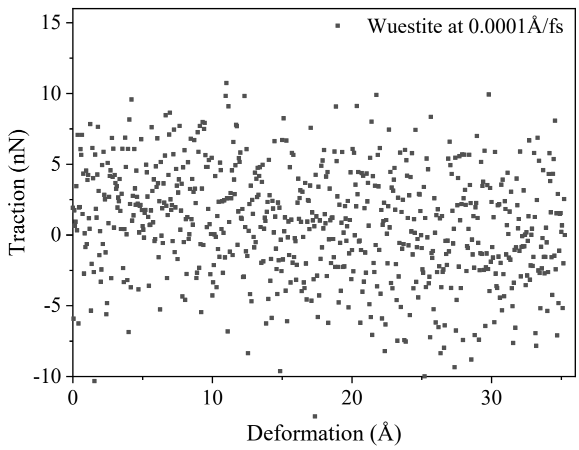

(c) (d)

Figure 3.30 Traction-deformation curves of different interface models: (a) quartz at 0.001 Å/fs; (b) wuestite at 0.001 Å/fs; (c) quartz at 0.0001 Å/fs; (d) wuestite at 0.0001 Å/fs

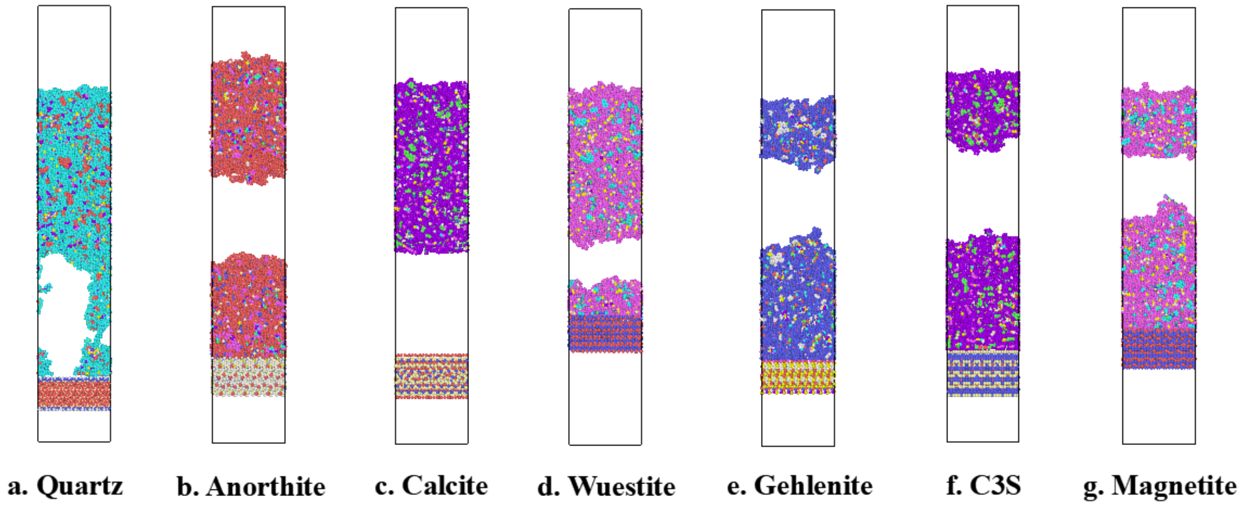

Figure 3.31 Failure configurations of bitumen-mineral interface models at 0.001 Å/fs

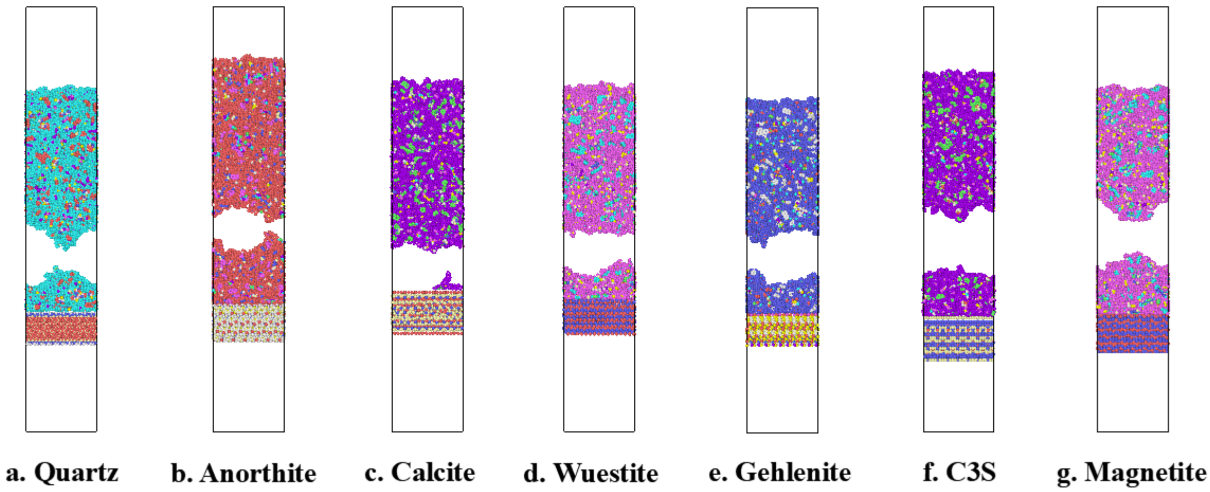

Figure 3.32 Failure configurations of bitumen-mineral interface models at 0.0001 Å/fs

3.2.3 Experimental results of interaction behaviour of bitumen-filler

3.2.3.1 DENT test results

Figure 3.33 presents the load-displacement curves in the DENT test results of asphalt mastics. From the figure, after the addition of fillers, the peak load of mastics rises significantly, where there is no obvious change in the ultimate displacement of materials. This indicates that using fillers effectively improves the toughness of bitumen. Waste fillers exhibit a greater improvement effect than mineral fillers, especially for SS, followed by IT, CE, and BF. Based on the load-displacement data, the CTOD of different asphalt mastics was computed and shown in Figure 3.34. It can be found from the figure that the asphalt mastic with SS has the best cohesive failure resistance among five types of solid waste fillers, followed by IT, CE, BF, and DG. In contrast, the use of mineral fillers has a significant effect on the ability of bitumen to resist cohesion failure, but there is still a certain gap from the effect of waste fillers. This verifies the conclusion of the MD simulation above to a certain extent. At the molecular scale, as the main rock-forming minerals of SS and IT, Wuestite and magnetite show the strongest interaction and adhesion with bitumen molecules. In the macroscopic DENT test, SS and IT also exhibit the best cohesive failure resistance after being added to bitumen.

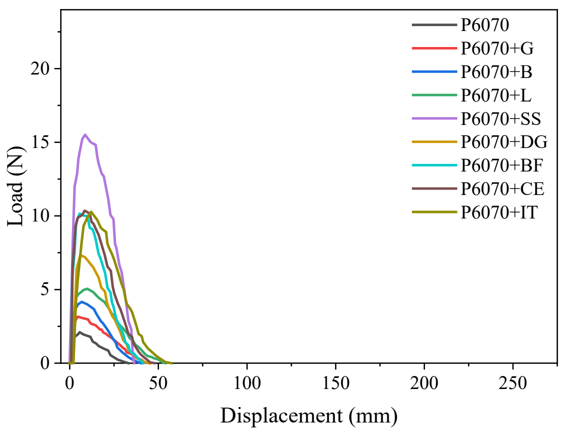

(a)

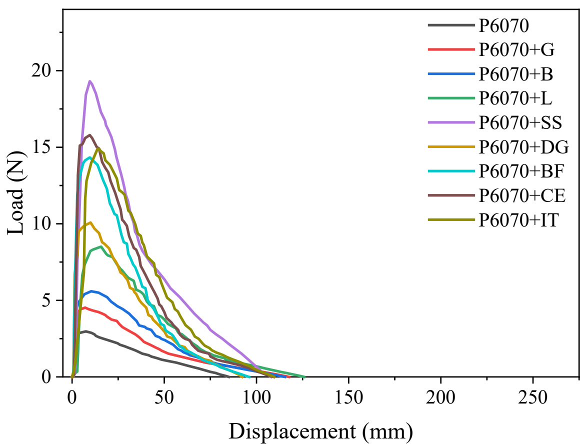

(b)

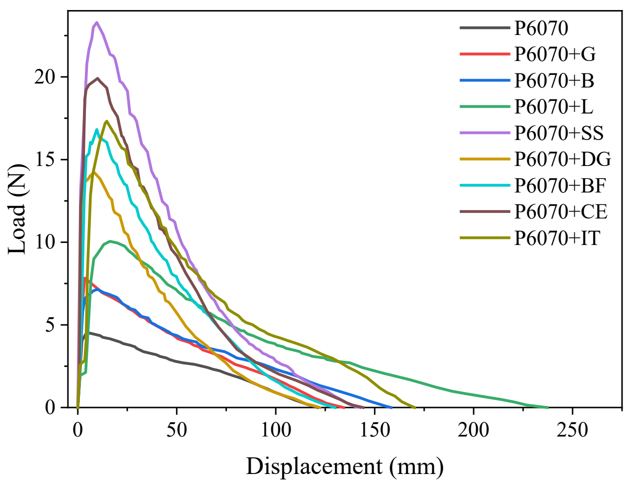

(c)

Figure 3.33 Displacement-load curves of DENT test results of asphalt mastics at different ligament lengths: (a) 5mm; (b) 10mm and (c) 15mm

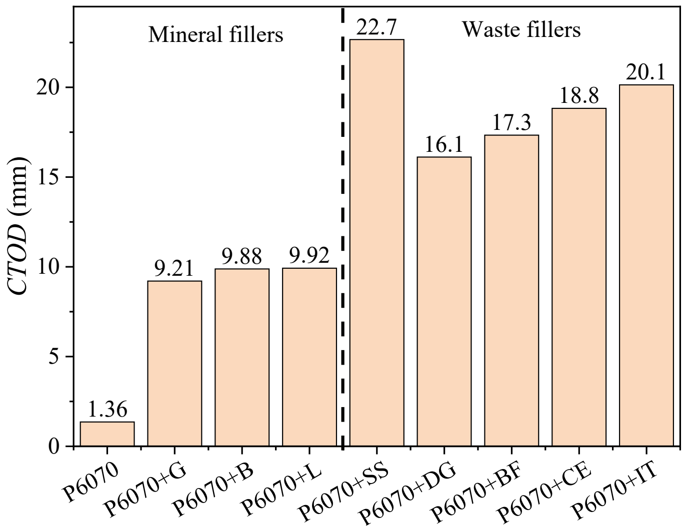

Figure 3.34 CTOD results in the DENT test results of asphalt mastics

3.2.3.2 Contact angle test results

Figure 3.35 presents the surface energy indicators results between asphalt mastics and aggregates based on the contact angle test. Generally, the use of all fillers improves the adhesion performance between asphalt mastics and aggregates, indicating as the rise of four surface energy indicators of W_{MA}, W_{MAW}, ER_1, and ER_2. It is worth noting that the rules reflected by the three indicators of W_{MAW}, ER_1, and ER_2 are consistent. Asphalt mastics mixed with SS and IT present the greatest adhesion properties with aggregates, followed by CE, and other fillers show similar levels which are prominently lower than the above three. The difference between the W_{MA} results of various asphalt mastics is not noticeable, it may be because the indicator is not sensitive to the mineralogy of different fillers [18]. In addition, the contact angle test basically verified the findings of the MD simulation above. Two solid waste fillers of SS and IT show the strongest interaction and adhesion performance with bitumen, which is also consistent with the results of the above DENT tests.

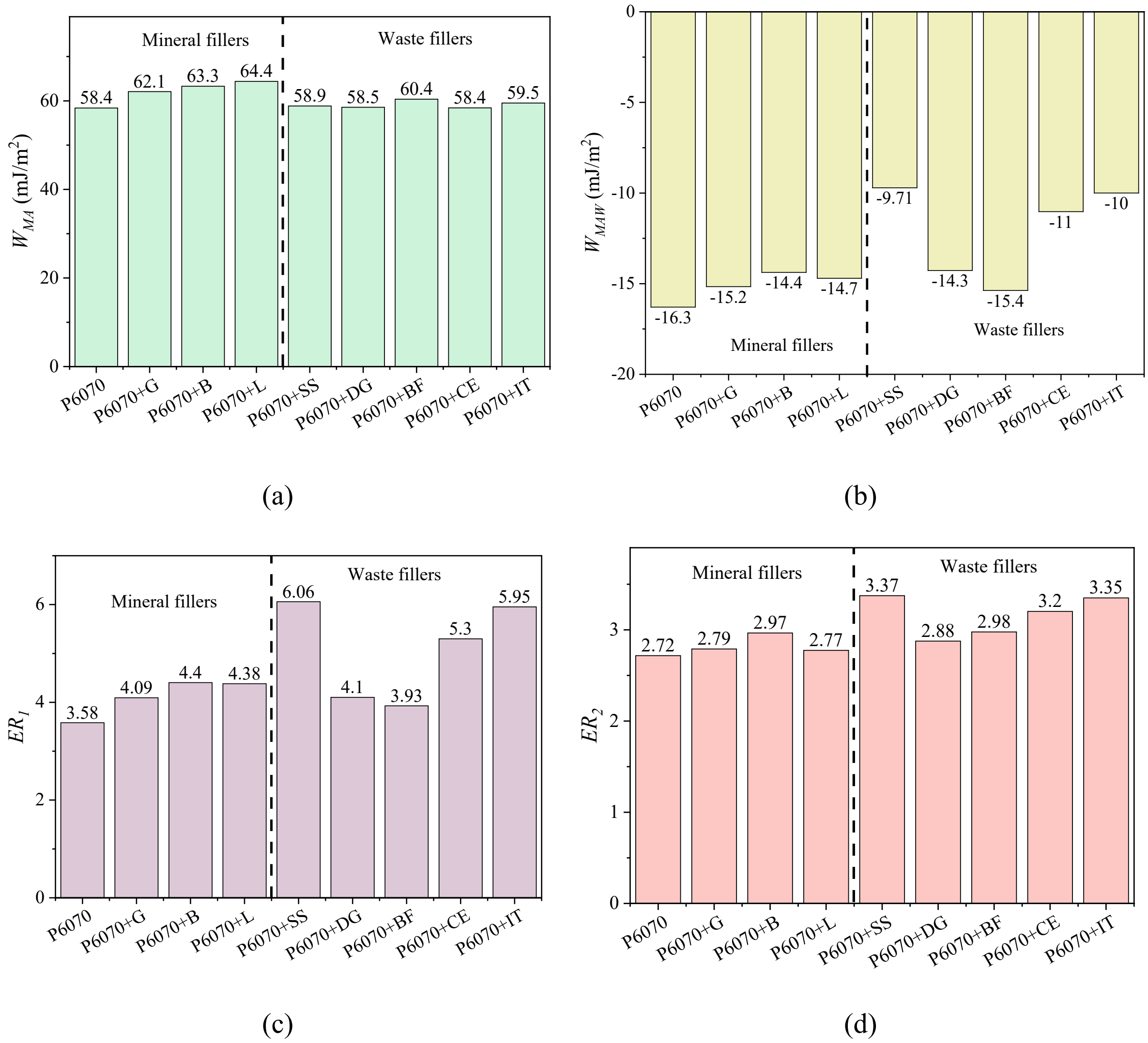

Figure 3.35 Contact angle test results of asphalt mastics: (a) W_{MA}; (b) W_{MAW}; (c) ER_1 and (d) ER_2

3.2.3.3 BBS test results

Figure 3.36 presents the BBS test results between asphalt mastics and aggregates of dry and immersion groups. In the figure, BS_{dry} and BS_{wet} represent the bonding strength at the dry and wet conditions, respectively. It can be found that asphalt mastics mixed with SS and IT show the strongest bonding strength with aggregates, followed by CE, DG, BF, L, B, and G. It can be concluded that asphalt mastics with solid waste fillers exhibit a remarkable adhesion performance than that of mineral fillers, especially for SS and IT. This completely verifies the findings of the MD simulation, DENT test, and contact angle test above.

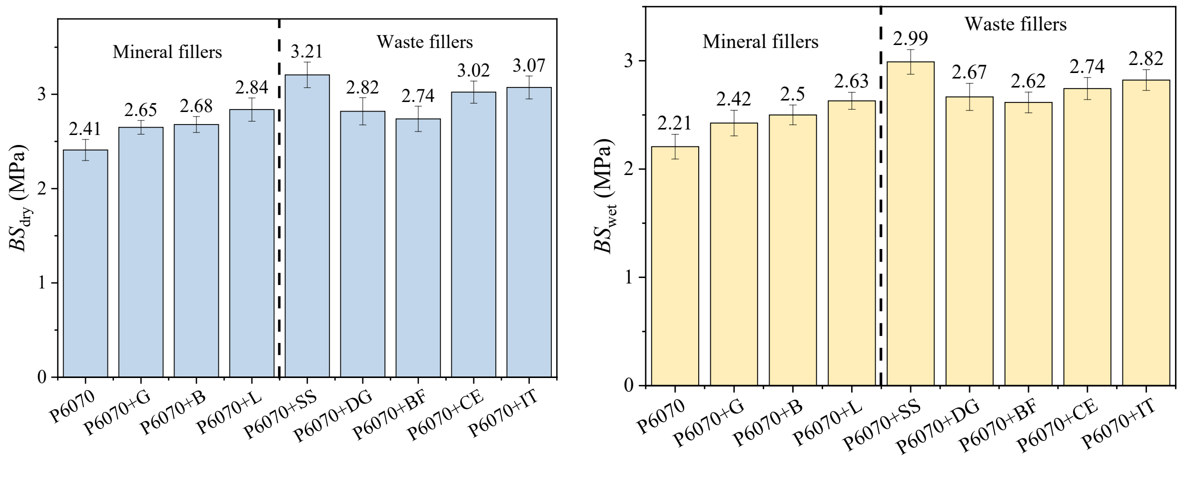

(a) (b)

Figure 3.36 BBS test results of asphalt mastics: (a) BS_{dry} and (b) BS_{wet}

3.2.3.4 Characterization results based on rheological indexes

Figures 3.37~3.39 present the three rheological index results of B_{G^*}, A_δ, and B_δ at three test temperatures of 48 °C, 60 °C and 72 °C. The higher the B_{G^*} and B_δ, the lower the A_δ, the stronger the interaction between the filler and bitumen. By comparing the calculation results of these indicators, it is not difficult to find that the rules reflected by the three indicators are not the same. Besides, it is worth noting that, unlike the other seven fillers, the rheological index results of the IT filler are very sensitive to changes in shear frequency, and its interaction ranking may undergo significant changes in the high-frequency and low-frequency domains. This phenomenon can be observed in all three rheological indexes.

First, according to the B_{G^*} results at 48 °C in Figure 3.37 (a), the SS filler exhibits the highest interaction with the bitumen, followed by CE, B, IT, BF, DG, L, and G. From the B_{G^*} results at 60 °C in Figure 3.37 (b), the SS filler shows the biggest interaction with the bitumen, followed by IT (or CE), B, DG, BF, L, and G. From the B_{G^*} results at 72 °C in Figure 3.37 (c), for the first half of the curve, the IT filler shows the highest interaction with the bitumen, followed by SS, CE, B, DG (BF), L, and G. For the latter half of the curve in Figure 3.37 (c), the SS filler exhibits the greatest interaction with the bitumen, followed by IT, CE, B, DG (BF), L, and G.

This is generally consistent with the conclusions obtained from the MD simulation, as well as the results of the DENT, contact angle, and BBS experiments above. Three kinds of solid waste fillers, SS, CE, and IT, exhibit stronger interaction with bitumen than that of other fillers. Another interesting finding is that the interaction between the B filler and bitumen is significantly greater than the other two mineral fillers, which supports the conclusion of MD simulation.

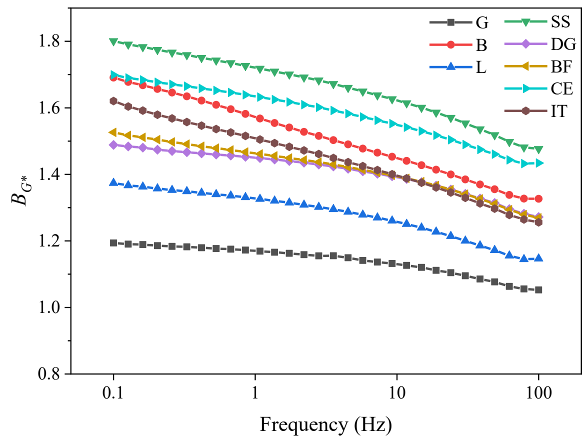

(a)

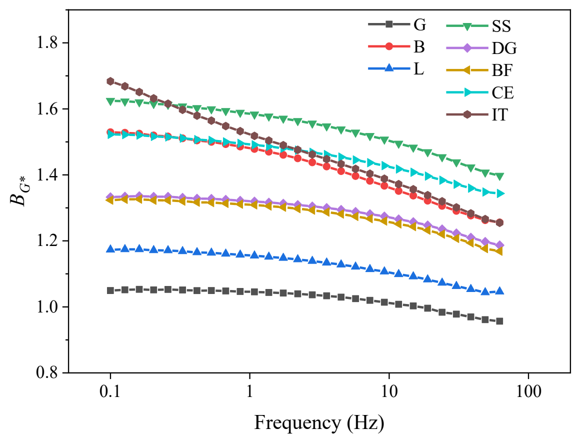

(b)

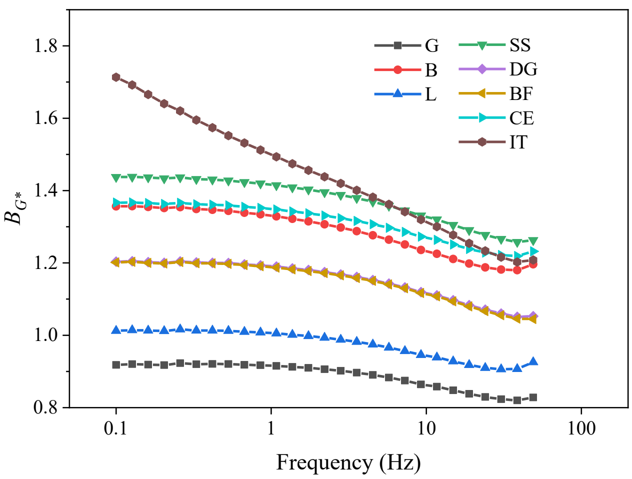

(c)

Figure 3.37 B_{G^*} results of asphalt mastics at (a) 48 °C; (b) 60 °C and (c) 72 °C

Second, from the A_δ results at 48 °C in Figure 3.38 (a), for the first half of the curve, the interaction between the B filler and bitumen is the strongest, followed by IT, SS, CE, L, BF, DG, and G. For the latter half of the curve, the interaction between B and bitumen is the strongest, followed by SS, CE, L, IT, BF, DG, and G. According to the A_δ results at 60 and 72 °C in Figures 3.38 (b) and (c), for the first half of the curve, the interaction between the IT filler and bitumen is the greatest, followed by B, SS, CE, L, BF, DG, and G. For the latter half of the curve, the interaction between B and bitumen is the greatest, followed by SS (or IT), CE, L, BF, DG, and G. It can be found that the difference between the B_{G^*} and A_δ indexes lies mainly in the inconsistent ranking of the filler B. The results of the A_δ index show that the interaction between filler B and bitumen is the strongest, while according to the results of the B_{G^*} index, the interaction of filler B is weaker than that of the three solid waste fillers (SS, IT, and CE).

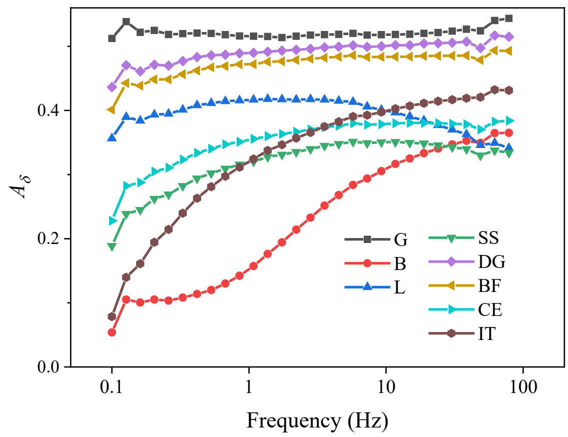

(a)

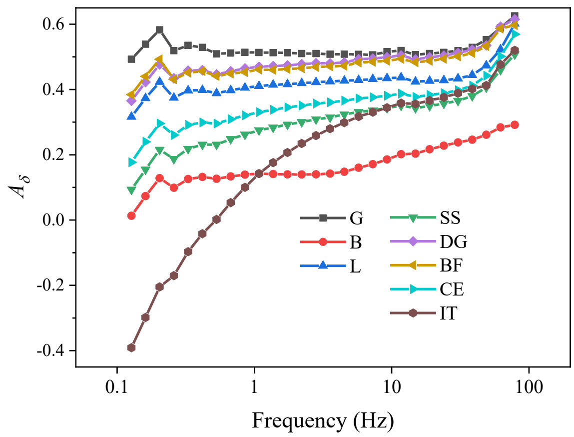

(b)

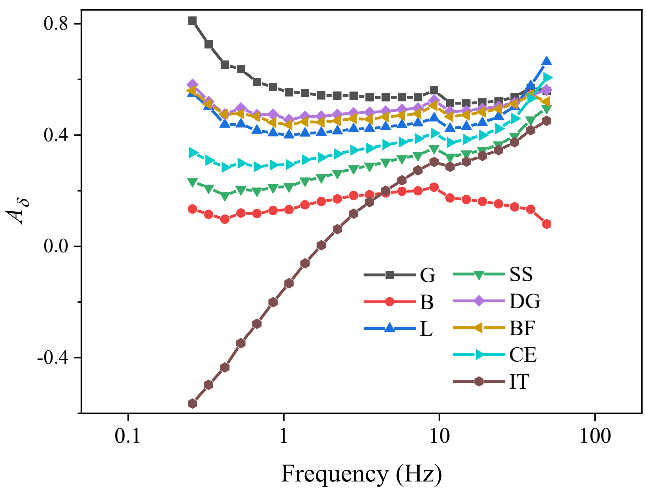

(c)

Figure 3.38 A_δ results of asphalt mastics at (a) 48 °C; (b) 60 °C and (c) 72 °C

Third, the B filler exhibits the highest interaction with bitumen according to the B_δ results at 48 °C in Figure 3.39 (a), followed by IT, SS, CE, L, BF, DG, and G at the first half of the curve, and followed by SS, CE, L, IT, BF, DG, and G at the latter half of the curve. From the B_δ results at 60 and 72 °C in Figures 3.39 (b) and (c), for the first half of the curve, the IT filler shows the greatest interaction with bitumen, followed by B, SS, CE, L, BF (and DG), and G. For the latter half of the curve, the interaction between the B filler and bitumen is the strongest, followed by SS (or IT), CE, L, BF, DG, and G. It can be found that the conclusions of B_δ and A_δ are completely consistent.

Overall, it can be concluded that the three rheological indicators of B_{G^*}, A_δ, and B_δ have shown good applicability in characterizing the interaction between bitumen and fillers. Among them, B_{G^*} showed the strongest sensitivity to different mineralogy of fillers, which accurately verified the conclusions of the MD simulation, DENT test, contact angle test, and BBS test above and is recommended as the best rheological index of interaction characterization. The other two indexes of A_δ and B_δ are accurate for most fillers but overestimate the interaction between basalt and bitumen.

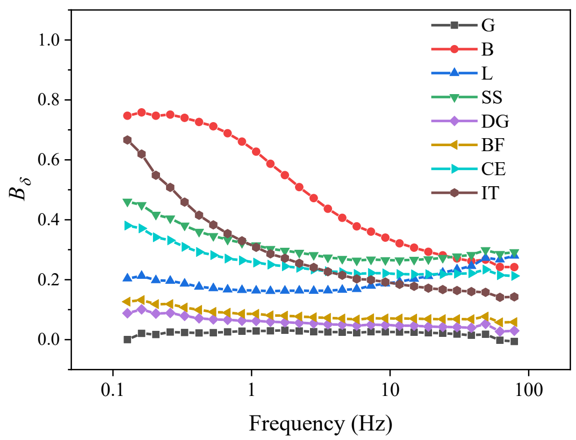

(a)

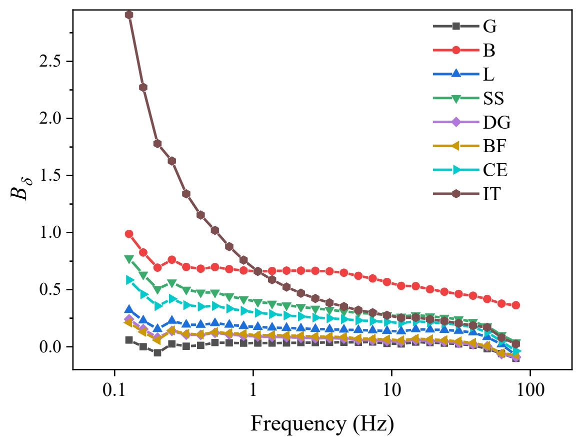

(b)

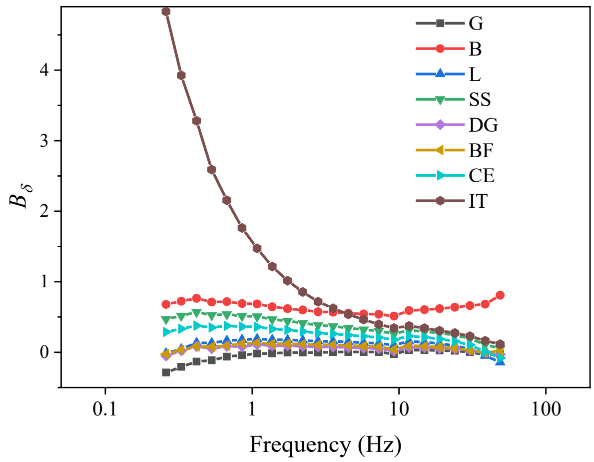

(c)

Figure 3.39 B_δ results of asphalt mastics at 48 °C; (b) 60 °C and (c) 72 °C

3.3 Summary

This chapter selected five kinds of solid wastes from three categories and investigated their interaction behaviours with bitumen based on the surface energy theory, binder bonding strength test, DENT test, and rheological indicators, and three mineral fillers were adopted for comparison. The representative mineral molecular models and bitumen-mineral interface models were constructed, and the adsorption configuration and interfacial failure mechanism of the bitumen-filler interface were revealed at the atom level. The main conclusions of this chapter can be summarized as follows:

1) The solid wastes utilized in this study exhibit stronger adhesion properties and interaction with bitumen, especially iron tailings (IT), waste cement (CE), and steel slag (SS). The filler mineralogy provides a molecular-scale explanation for this considerable difference between solid wastes and conventional mineral fillers, manifested as higher adhesion work and lower diffusion coefficient of the adsorbed bitumen molecules on the rock-forming mineral surface of solid wastes.

2) The adsorption configuration of bitumen components on the minerals can be divided into four regions. The concentration of the four components of bitumen varies in different

regions. According to the distance from the mineral surfaces, resin, asphaltene, saturate, and aromatic occupy the leading components alternately in the four regions.

3) The cracking mechanisms of the asphalt-filler interface model under different loading rates can be summarized into three patterns. At low tensile rates, the cracking process includes three stages: elastic, softening, and debonding. Initially, the traction force rapidly peaks in the elastic stage, then declines during the softening stage, and finally reaches zero in the debonding stage. At medium loading rates, an additional plastic stage is introduced, where the traction force remains at its peak for a period. At high loading rates, the model reverts to the three-stage mechanism.

4) When the asphalt-filler interface model is in equilibrium, the interfacial adhesion between the filler and asphalt equals the internal cohesion of the asphalt. Under high tensile rates, failure occurs purely through interfacial adhesive cracking, with adhesion significantly lower than cohesion. At medium rates, failure involves both adhesive and cohesive damage, with adhesion exceeding cohesion. At low rates, failure shifts entirely to cohesive cracking, where adhesion far surpasses cohesion.

5) The K.D. Ziegel-B-G^* method is recommended as the best rheological index in characterizing the interaction of bitumen-filler in this study. The other two indexes of the Luis Ibrarra-A-δ and K.D. Ziegel-B-δ may overestimate the interaction between the bitumen and some fillers.

To further promote the application of solid waste fillers in pavement engineering, more studies, such as the pavement performances and the LCA of asphalt mixtures with solid waste fillers, are necessary in the future.

CHAPTER 4 MACROSCOPICAL AND MICROSCOPICAL EXPERIMENTAL CHARACTERIZATION OF ASPHALT MASTIC PERFORMANCE AND ITS RELATIONSHIP WITH RAW MATERIAL PROPERTIES

In the three-level dispersion system of asphalt mixtures, the asphalt mastic composed of bitumen and filler serves as the actual bonding agent and simultaneously represents the weakest link in the structural strength of the mixture. Consequently, asphalt mastic stands as a pivotal component that governs both the durability and pavement performance of asphalt mixtures[78, 93]. Chapter 3 has previously delved into the interfacial interaction mechanisms between bitumen and filler, alongside the macroscopic characteristics of these interactions, thereby shedding light on the potential mechanisms underlying adhesion failure between asphalt mastic and aggregate. As an applied science, pavement engineering is inherently directed towards practical production, with its ultimate focus resting on the pavement performance of asphalt pavement materials. Hence, the ensuing chapter will embark on a study of the mechanical properties of asphalt mastic, endeavouring to establish the composition-performance relationship between the mastic's performance and its compositional structure (bitumen and filler). Furthermore, this chapter also seeks to validate the research findings presented in Chapter 3, thereby exploring the extent to which bitumen-filler interactions influence the mechanical properties of asphalt mastic.

In view of this, five distinct sources of bitumen and five types of fillers were meticulously selected to fabricate twenty-five variants of asphalt mastic. Through a combination of macroscopic and microscopic testing methodologies, the mechanical properties of asphalt mastic were scrutinized across multiple scales. Grey relational analysis (GRA) was employed to probe the qualitative composition-performance relationship between the mastic's performance and its compositional components. This chapter furnishes a foundational understanding of how superior performance in asphalt mastic can be attained by judiciously controlling the source of bitumen and the characteristics of fillers. It thereby offers valuable guidance for optimizing the performance design of asphalt mastic and enhancing the service durability of road infrastructure.

4.1 Experimental Program

4.1.1 Materials and specimen preparation

4.1.1.1 Bitumen

To investigate the effects of the origins, penetration grades, and component differences of the base bitumen on the performance of asphalt mastics, five base bitumen (A, B, C, D, and E) with five sources and three penetration grades (60/70, 70/80, and 90/100) were selected in this study. Table 4-1 lists the basic properties of five base bitumen. The performance grade (PG) was tested according to American Association of State Highway and Transportation Officials (AASHTO) M 320-21, and the SARA (Saturates, Aromatics, Resins, and Asphaltenes) fractions were tested, referring to American Society for Testing and Materials (ASTM) D4124-09.

Table 4-1 Basic properties of the base bitumen

Properties		A	B	C	D	E
PG (°C)	High PG	66.68	65.35	66.42	69.48	66.86
	Low PG	-22.98	-22	-21.85	-29.41	-30.72
Penetration at 25 °C (0.1 mm)		62.2	68.4	66.5	76.2	93.9
SARA fractions (%)	Saturates	12.78	11.12	31.11	8.00	10.99
	Aromatics	40.78	47.96	30.53	37.73	31.45
	Resins	30.06	25.63	24.13	47.17	50.43
	Asphaltenes	16.38	15.29	14.23	7.10	7.13

4.1.1.2 Fillers

Five kinds of fillers were selected in this study. As a considerable amount of solid waste, the application of steel slag as filler in asphalt pavement has gained some attention [138, 139]. In addition, cement is increasingly widely used as a filler in asphalt pavement due to the excellent moisture resistance and aging resistance of cement as a substitute for limestone powder [140, 141]. Besides, the recycling of huge reserves of expired and deteriorated cement has always been a difficult problem that has troubled people. Therefore, steel slag powder and cement were also selected in addition to three mineral fillers (granite, basalt, and limestone). Table 4-2 lists the basic properties of the fillers used in this study. In the table, SSA refers to the specific surface area of fillers. D10, D50, and D90 refer to the corresponding particle diameter when the pass rate of the filler is 10%, 50% 90%. P20, P10, and P5 refer to the content of fillers with a diameter of less than 0.02 mm, 0.01mm, and 0.005mm, respectively. More parameters of the filler, such as P45 and P75, were not included, which is because the values of these parameters for fillers were all 100%. It should be noted that in this study, a laser diffraction particle size analyser was employed to determine particle size parameters such as D10, D50, and D90, as well as P20, P10, and P5. In addition, the contents of the two main components (SiO_2 and CaO) in the mineral composition of the fillers are also listed in Table 4.2. Besides, Table 4.2 also presents the volume fractions of each filler. In this study, the bitumen-filler mass ratio for all asphalt mastics was fixed to 1:1.

Table 4-2 Basic properties of the fillers

Characteristics	Granite	Basalt	Limestone	Steel slag	Cement
Density (g/cm^3)	2.673	2.874	2.696	3.19	3.045
SSA (m^2/kg)	252.0	238.2	308.5	477.6	335.8
D10 (μm)	3.48	3.77	3.00	2.66	2.90
D50 (μm)	16.20	17.18	10.63	5.79	9.38
D90 (μm)	25.62	25.80	23.62	8.68	22.42
P20 (%)	65.64	63.13	77.58	100	84.05
P10 (%)	34.03	30.33	47.34	98.08	53.27
P5 (%)	15.49	13.39	21.88	41.17	24.86
SiO_2 (%)	67.39	40.57	2.68	22.00	15.98
CaO (%)	3.08	8.99	74.61	29.54	50.00
Volume fraction (%)	28.20	26.76	28.03	24.76	25.64

4.1.1.3 Preparation of asphalt mastics

First, the filler sieved through the 0.075mm standard sieve was put into an oven at the temperature of 145°C for two hours to evaporate the potential moisture, and base bitumen was put into an oven at the temperature of 145°C for one hour. Second, the filler was slowly added into the bitumen in several small portions for mixing. The mixing temperature was 150°C, the shear rate was 1000 rate per minute, and the shear time was 0.5h. Until there was no obvious bubble in the mastic, it indicated that a uniformly dispersed asphalt mastic had been prepared. Finally, the asphalt mastic was quickly poured into a sealed aluminium tank and stored for use. It is worth mentioning that, to prevent the precipitation of the filler caused by the long storing time of the asphalt mastic, the asphalt mastic must be stirred evenly before each sampling.

4.1.2 Microscopic test methods of fillers and asphalt mastics

4.1.2.1 Scanning electron microscopy (SEM)

The microstructure of the surface fracture morphology of the fillers was assessed using SEM

[142]. The experimental equipment was the dual beam scanning electron microscopy Helios Nanolab600i, and the electron beams were focused on a grid scanning mode. The test was conducted at a temperature of 20°C, and a thin layer of gold was sprayed on the sample's surface before the test.

4.1.2.2 Fourier transform infrared spectroscopy (FTIR)

To detect the potential chemical reactions between the bitumen and fillers, the Nicolet iS50 Fourier Transform Infrared Spectrometer manufactured by Thermo Scientific Company of USA was adopted to conduct the FTIR test on the fillers, base bitumen, and asphalt mastics used in this study. For each sample, the tests were repeated three times. FTIR tests of bitumen and asphalt mastics adopted attenuated total reflection (ATR) mode, and tests of fillers adopted transmission mode of FTIR. The ATR mode does not require additional treatment for test sample, while the transmission mode needs to adopt the potassium bromide disc method for sample preparation, and the detailed steps can refer to the research of Usman et al [143].

4.1.2.3 Atomic force microscopy (AFM)

The microscopic surface morphology of base bitumen and asphalt mastics was captured by Bruker Dimension Fast Scan AFM. For the AFM samples, about 0.5g of the sample was dropped on the glass slide and heated in an oven at 160°C for 5min to spread the sample completely. After cooling to room temperature (25°C) in a desiccator, the microscopic surface topography of asphalt mastics was collected by peak force QNM Mode of AFM [144]. The scanning range was selected as 30 μm × 30 μm, and the test temperature was 25°C. Figure 4.1 presents the testing equipment adopted for three kinds of microscopic tests.

(a) SEM (b) FTIR (c) AFM

Figure 4.1 Testing equipment for three kinds of microscopic tests

4.1.3 Macroscopic test methods of asphalt mastics

4.1.3.1 Temperature sweep tests

To evaluate the rutting performance and medium-temperature fatigue performances of asphalt mastics, the temperature sweep tests were performed on the sample using the dynamic shear rheometer (DSR, DHR-3, TA Company, USA). For the high-temperature sweep tests, four test temperatures of 82°C, 76°C, 70°C, and 58°C were adopted, and the 25 mm parallel plate of DSR was employed, referring to AASHTO T 315. The findings of the temperature sweep test were used to compute the rutting factor and high-temperature continuous grading temperature. Before the temperature sweep test, the mastic samples were performed the rolling thin-film oven (RTFO) test. For the medium-temperature sweep tests, three test temperatures of 19°C, 22°C, and 25°C were selected, and the 8 mm parallel plate of DSR was employed, referring to AASHTO T 315. The findings of the temperature sweep test were used to compute the fatigue factor and medium-temperature continuous grading temperature. Before the temperature sweep test, the RTFO and pressurized aging vessel (PAV) procedures were performed on the mastic samples.

4.1.3.2 Multiple stress creep recovery (MSCR) test

The rutting factor parameter (*G/sinδ*) composed of complex modulus (*G*) and phase angle (*δ*) was not adopted in this study to evaluate the high-temperature performance of asphalt mastics. It is because *G/sinδ* is a parameter of materials in the linear viscoelastic range, it reflects the mechanical properties of materials in a non-damaged state [145]. The MSCR test was carried out according to AASHTO TP 70 to characterize the high-temperature damage performance of asphalt mastics by DSR (DHR-2, TA Company, USA). The RTFO procedure was performed on the samples before the test, and the test temperature was 60°C.

4.1.3.3 Linear amplitude sweep (LAS) test

Like the rutting factor, the fatigue factor (*G*sinδ*) is also a parameter that characterizes the mechanical properties of materials in a non-damaged state, and has no strong correlation with the fatigue cracking of asphalt pavement [146]. Thus, the LAS test was conducted according to AASHTO TP 101-12 to indicate the medium-temperature damage performance of asphalt mastics by DSR (DHR-2, TA Company, USA). The RTFO and PAV procedures were performed on the samples before the test, and the test temperature was 25°C.

4.1.3.4 Bending beam rheometer (BBR) test

To characterize the low-temperature cracking performance of asphalt mastics, the BBR test was carried out according to ASTM D6648-08 by the TE-BBR manufactured by Cannon Instrument Company of the USA. Before the BBR test, the RTFO and PAV procedures were performed on the samples, and three thin beams (127 ± 2 mm × 12.7 ± 0.05 mm × 6.35 ± 0.05 mm) were manufactured, and two test temperatures were set for each kind of asphalt mastic.

4.1.4 Grey relational analysis (GRA)

To further elucidate the composition-performance relationship between the service performance of asphalt mastic and its compositional structure (bitumen and filler), this study employed grey relational analysis (GRA) to systematically investigate the correlations among the chemical composition of bitumen, filler characteristics, and the key performance attributes of asphalt mastic. These attributes include high-temperature rutting resistance, intermediate-temperature fatigue resistance, and low-temperature crack resistance. This approach provides a comprehensive framework for understanding how the intrinsic properties of bitumen and filler influence the overall performance of asphalt mastic under varying service conditions. GRA is a multi-factor statistical method that obtains the grey correlation degree by processing the sample data of different factors [147]. It can describe the strength of the correlation degree between other factors, and the detailed procedures of GRA are as follows [147, 148]:

(1) Determine the reference sequence X_0 and the comparison sequence X_p:

$$X_0^* = \left\{X_0^*(1), X_0^*(2), ..., X_0^*(N)\right\} \tag{4-1}$$

$$X_p^* = \left\{X_p^*(1), X_p^*(2), ..., X_p^*(N)\right\} \tag{4-2}$$

(2) Calculate the dimensionless sequences of X_0 and X_p.

(3) Calculate the difference between the dimensionless series:

$$\Delta_i(k) = \left|x_0(k) - x_i(k)\right|, (k = 1, 2, 3, ..., n) \tag{4-3}$$

(4) Determine the maximum and minimum of the sequence differences:

$$\Delta_{\max} = \max_i \max_k \Delta_i(k), \Delta_{\min} = \min_i \min_k \Delta_i(k) \tag{4-4}$$

(5) Calculate the correlation coefficient $\gamma_{0i}(k)$:

$$\gamma_{0i}(k) = \frac{\Delta\min + \rho\Delta\max}{\Delta_i(k) + \rho\Delta\max} \tag{4-5}$$

Where ρ is the resolution factor, which is usually equal to 0.5.

(6) Calculate the grey relational degree γ_{0i}:

$$\gamma_{0i} = \frac{1}{n}\sum_{k=1}^{n}\gamma_{0i}(k) \tag{4-6}$$

Where *n* is the length of the comparison sequences. A higher γ_{0i} indicates that the sequences $X_i(k)$ and $X_0(k)$ are more strongly related.

4.2 Results and Discussion

4.2.1 Microscopic test results of fillers and asphalts

4.2.1.1 SEM test results of fillers

Figure 4.2 presents the SEM surface morphology of the fillers. From the figure, the granite particles have a smooth surface, a small specific surface area, and no apparent microporous structure, so it can be concluded that the surface morphology of granite has very limited benefits in terms of its adhesion ability to bitumen. As a comparison, the particle surface of the steel powder is rough and uneven, with rich folds and protrusions, which can effectively increase the bonding area between the bitumen and filler. Furthermore, many microporous structures are observed on the surface of steel powder particles, which means that components in bitumen easily penetrate the microporous structure of filler particles through the adsorption and capillarity, thus significantly improving the adhesion between the bitumen and steel powder filler. The surface morphology of the other three fillers (basalt, limestone, and cement) is between granite and steel powder.

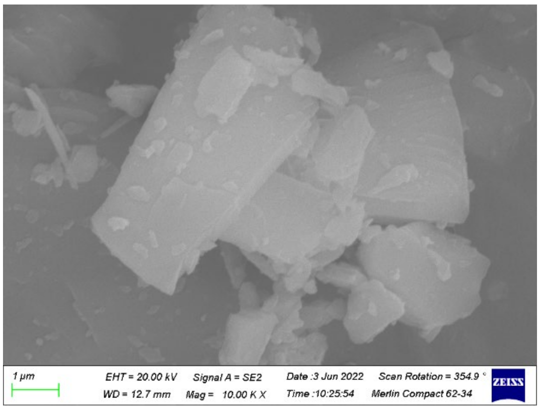

(a)

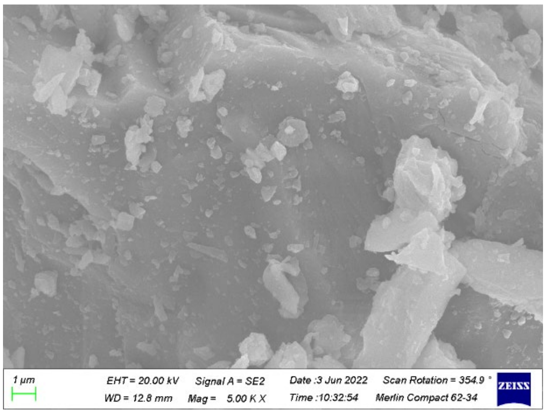

(b)

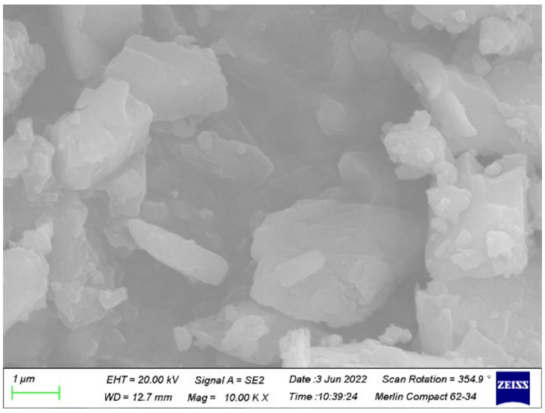

(c)

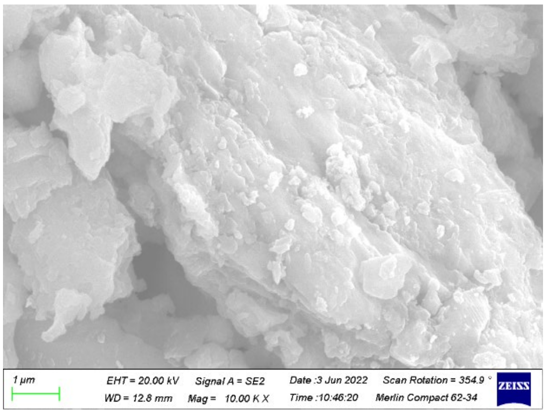

(d)

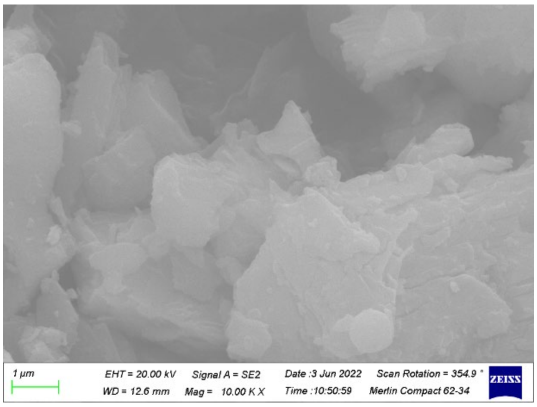

(e)

Figure 4.2 SEM surface morphology of fillers: (a) Granite; (b) Basalt; (c) Limestone; (d) Steel slag; (e) Cement

4.2.1.2 FTIR test results of asphalt mastics

Figure 4.3 (a) shows the FTIR test results of five fillers used in the study. First, the characteristic peaks at 1425 cm^{-1}, 876 cm^{-1}, and 712 cm^{-1} are the absorption peaks of CaO. Limestone has significant absorption peaks at these three places, and steel powder and cement have significant absorption peaks at 1425 cm^{-1} and 876 cm^{-1}, which indicates that one of the constituents of these fillers is calcium carbonate ($CaCO_3$). Secondly, the characteristic peaks at 1097 cm^{-1} and 1008 cm^{-1} are the anti-symmetric stretching vibration peaks of Si-O-Si. Granite has significant absorption peaks at 1097 cm^{-1} and 1008 cm^{-1}, basalt and steel powder have peaks at 1008 cm^{-1}, and cement at 1097 cm^{-1}. In addition, the characteristic peak at 514 cm^{-1} is the symmetric stretching vibration peak of the Si-O bond, which can be found in granite, basalt, steel powder, and cement.

Figures 4.3 (b) ~ (d) show the FTIR test results of asphalt mastics based on bitumen A. Because the laws observed from the FTIR test results of the five types of base bitumen are consistent, this part only takes bitumen A as an example. From the figures, the FTIR test results between the fillers and bitumen can be divided into two categories. The first category is mineral fillers, including granite, basalt, and limestone. For these three fillers, it can be seen from the figure that some new functional groups do appear on the FTIR curves of the asphalt mastic compared to that of the bitumen. For example, two new characteristic peaks can be found in the FTIR curves of A+Limestone at 876 cm^{-1} and 712 cm^{-1}, and two new characteristic peaks can be found in A+Granite at 1097 cm^{-1} and 1008 cm^{-1}. However, combined with the FTIR results of the fillers above, it is not difficult to see that these functional groups are native to the filler. It can be concluded that no prominent new characteristic peaks independent of bitumen and filler are observed in the asphalt mastics, indicating that the interaction between the bitumen and these three fillers is mainly physical adsorption, and there is no significant chemical reaction. The second category includes steel slag and cement. From the figures, three are also functional groups from the fillers found in the FTIR curves of the asphalt mastics, such as the characteristic peaks in the FTIR curves of A+Steel slag and A+Cement at 514 cm^{-1}. More importantly, it is found that the sulfoxide group (S=0 at 1030 cm^{-1}) in the base bitumen cannot be found in the FTIR curves of these two asphalt mastics (A+Steel slag and A+Cement). Thus, it is easy to infer that these strong alkaline fillers (steel slag and cement) produce chemical reactions with the acid group (sulfoxide group) in the base bitumen. According to previous literature, the products formed by the chemical reaction above have extremely firm adhesion [149, 150]. It is foreseeable that adding steel slag and cement will significantly improve the adhesion properties between the bitumen and aggregates. Combined with the above SEM test results above, it can be foreseen that the steel slag and cement will show better adhesion performance.

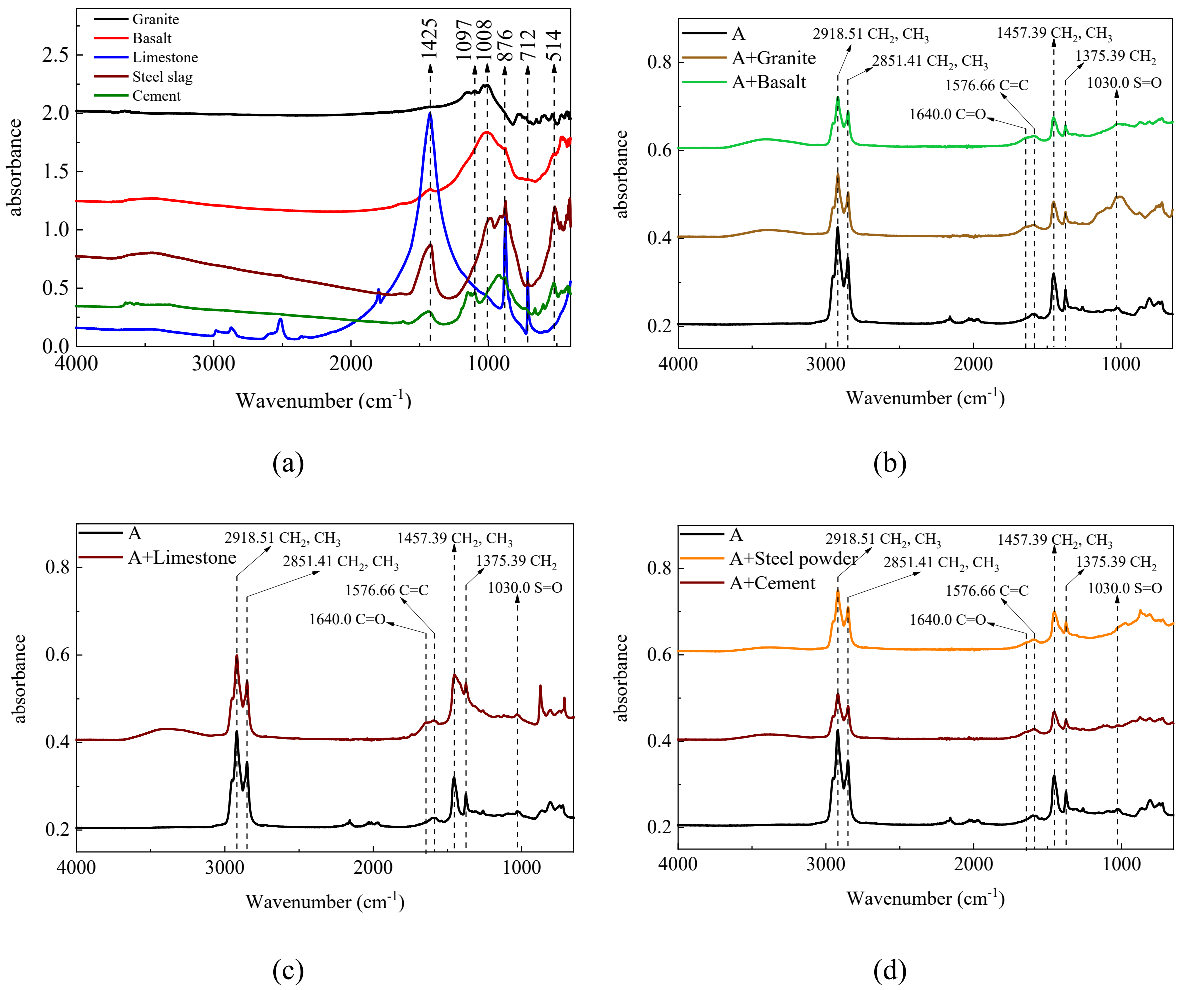

Figure 4.3 FTIR test results of (a) five fillers; (b) A+Granite and A+Basalt; (c) A+Limestone; (d) A+Steel slag and A+Cement

4.2.1.3 AFM test results of asphalt mastics

Figures 4.4 and 4.5 show the AFM 3D morphology results of asphalt mastics prepared based on base bitumen A and B, respectively. From the figure, after the addition of all fillers, the surface morphology fluctuation of asphalt mastics becomes smaller. Among the five fillers, the effect of Steel powder is the most significant, and its corresponding asphalt mastics have the smallest surface fluctuation. Taking asphalt mastics based matrix bitumen A as an example, the elevation change of base bitumen A is 64.4nm ~ -61.2nm, while the elevation changes of A+Steel powder is only 28.5nm~-24.2nm. The elevation change range of other asphalt mastics has also decreased to a certain extent compared to the base bitumen. In addition, it is worth noting that with the addition of fillers, the larger peaks and valleys on the 3D morphology of base bitumen transform into finer and sharper "needle peaks" and "needle valleys" in the 3D morphology of asphalt mastics. This indicates a significant decrease in the height of peaks and valleys, a marked increase in the number of peaks and valleys, and a denser distribution in bitumen. The peaks and valleys in these 3D images are reflected in the 2D image, which represents the typical "bee-like structures" of bituminous materials. To summary, the addition of fillers leads to a finer shape, lower height, more quantity, and denser distribution of peaks and valleys in bitumen, with Steel powder being the most significant among the five fillers.

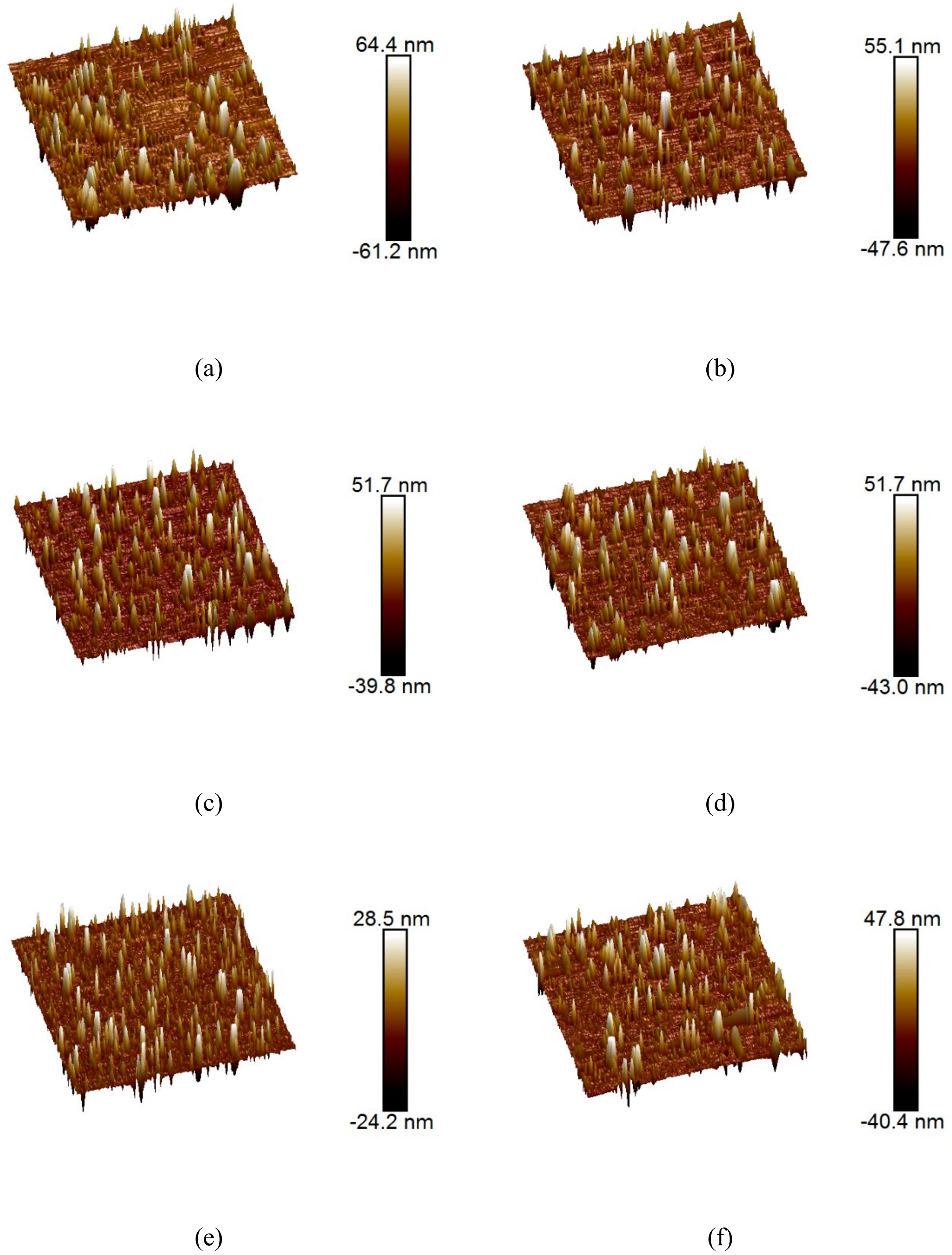

Figure 4.4 AFM 3D morphology results of asphalt mastics: (a) base bitumen A; (b) A+Granite; (c) A+Basalt; (d) A+Limestone; (d) A+Steel slag; (e) A+Cement

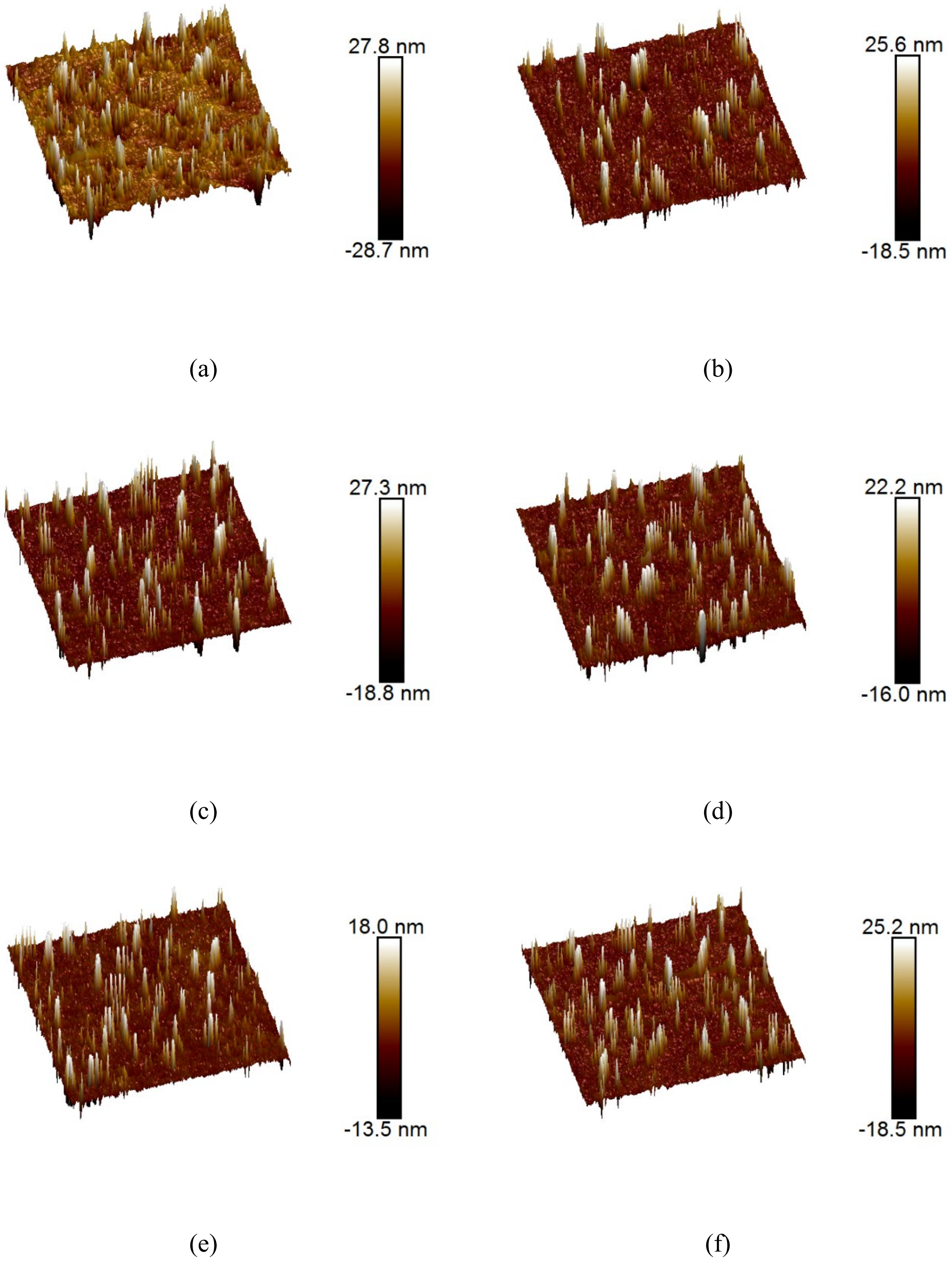

Figure 4.5 AFM 3D morphology results of asphalt mastics: (a) base bitumen B; (b) B+Granite; (c) B+Basalt; (d) B+Limestone; (d) B+Steel slag; (e) B+Cement

Furthermore, to further quantify the analysis results of AFM, the NanoScope analysis software's roughness analysis module was adopted to characterize the microscopic surface fluctuation of the bitumen, and the ratio between the entire area of the height sensor results and the area of the bee-like structures was calculated using MATLAB software. For the calculating of roughness and bee-like structures, five AFM samples were adopted for each bitumen material. The calculating results for roughness and bee-like structure area are shown in Table 3.3. In the table, the arithmetic mean roughness (R_a) and root-mean-square roughness (R_q) were defined to characterize the roughness of bitumen as follows:

$$R_q = \sqrt{\frac{\sum_{j=1}^{N}(Z_j)^2}{N}} \tag{4-7}$$

$$R_a = \frac{1}{N}\sum_{j=1}^{N} Z_j \tag{4-8}$$

where Z_j is the height in the height sensor results of AFM. Table 4-3 presents the calculation results of the R_q and R_a for twenty-five types of asphalt mastics prepared based on five origins of base bitumen. From the table, the use of all fillers significantly reduces the roughness of bitumen, and the variation patterns of the two roughness parameters R_q and R_a are consistent. Among the five types of fillers, Steel powder has the most significant effect on reducing the roughness of bitumen, which is consistent with the conclusion obtained from the previous 3D morphology images above.

Table 4-3 Computation results of two roughness R_q and R_a of asphalt mastics

Base bitumen	Asphalt mastics	R_q (nm)	R_a (nm)
A	A	12.2	6.61
	A+Granite	12.8	5.22
	A+Basalt	8.77	4.44
	A+Limestone	8.92	4.53
	A+Steel slag	5.08	2.56
	A+Cement	8.61	4.43
B	B	5.98	3.82
	B+Granite	4.10	1.76
	B+Basalt	4.33	1.95
	B+Limestone	3.72	1.70
	B+Steel slag	3.26	1.56
	B+Cement	4.11	1.79
C	C	4.66	2.26
	C+Granite	4.45	2.13
	C+Basalt	4.17	2.15
	C+Limestone	4.25	2.16
	C+Steel slag	2.13	1.25
	C+Cement	3.94	2.19
D	D	1.50	1.16
	D+Granite	1.43	0.97
	D+Basalt	1.10	0.80
	D+Limestone	1.25	0.94
	D+Steel slag	0.80	0.60
	D+Cement	1.05	0.79
E	E	1.54	0.70
	E+Granite	0.82	0.61
	E+Basalt	0.63	0.48
	E+Limestone	0.71	0.55
	E+Steel slag	0.59	0.46
	E+Cement	0.95	0.75

Figures 4.6, 4.7, and 4.8 present the AFM two-dimensional height sensor results of asphalt mastics prepared based on base bitumen A, B, and C, respectively. The typical bee-like structures of bituminous materials can be captured from the figures. As shown in Figure 4.9, the catana phase is the bee-like structure, the peri phase is the peripheral area of the bee-like structure, and the para phase is the adjacent area of the peri phase. In some literature, they are also called “bee phase”, “bee casing phase” and “interstitial phase”. So far, there is no uniform conclusion about the origin of bee-like structures found in the AFM results of bituminous materials. Still, more and more researchers attribute it to the mutual aggregation and crystallization of wax components and polar components (asphaltenes) in bitumen at low

temperatures [151]. It is worth noting that in the other two types of base bitumen (D and E) selected in this study, which is presented in Figure 4.10, no obvious bee-like structures were observed. Therefore, this section only discusses asphalt mastics based on base bitumen A, B, and C.

From the figures, it can be intuitively seen that after the addition of fillers, the size of the bee-like structures of all asphalt mastics gradually decreases while the quantity increases, and a smaller and denser state of the bee-like structures is captured in the AFM 2D morphology results. This is because fillers can absorb the polar components in bitumen. Therefore, the polar components are uniformly distributed in bitumen due to the absorption of fillers. In other words, the addition of fillers promotes the uniform dispersion of the polar components and prevents the aggregation and crystallization of the polar components in bitumen. Since the origin of the bee-like structure is the aggregation and crystallization of the polar components (wax components and asphaltenes) in bitumen, the bee-like structure of bitumen in the AFM results decrease after fillers are added. In addition, it is not difficult to find that the bee-like structure in bitumen is the most fluctuating part of the height sensor results. Therefore, the reduction of bee-like structure is naturally accompanied by the decline of the roughness of bitumen. To conclude, the addition of fillers can absorb the polar components in bitumen and prevent its aggregation and crystallization, which is manifested as a decline in roughness and bee-like structure in the height sensor results of bitumen. Furthermore, it is worth noting that among all asphalt mastics, the bee-like structures distribution of Steel powder asphalt mastics is the smallest and densest.

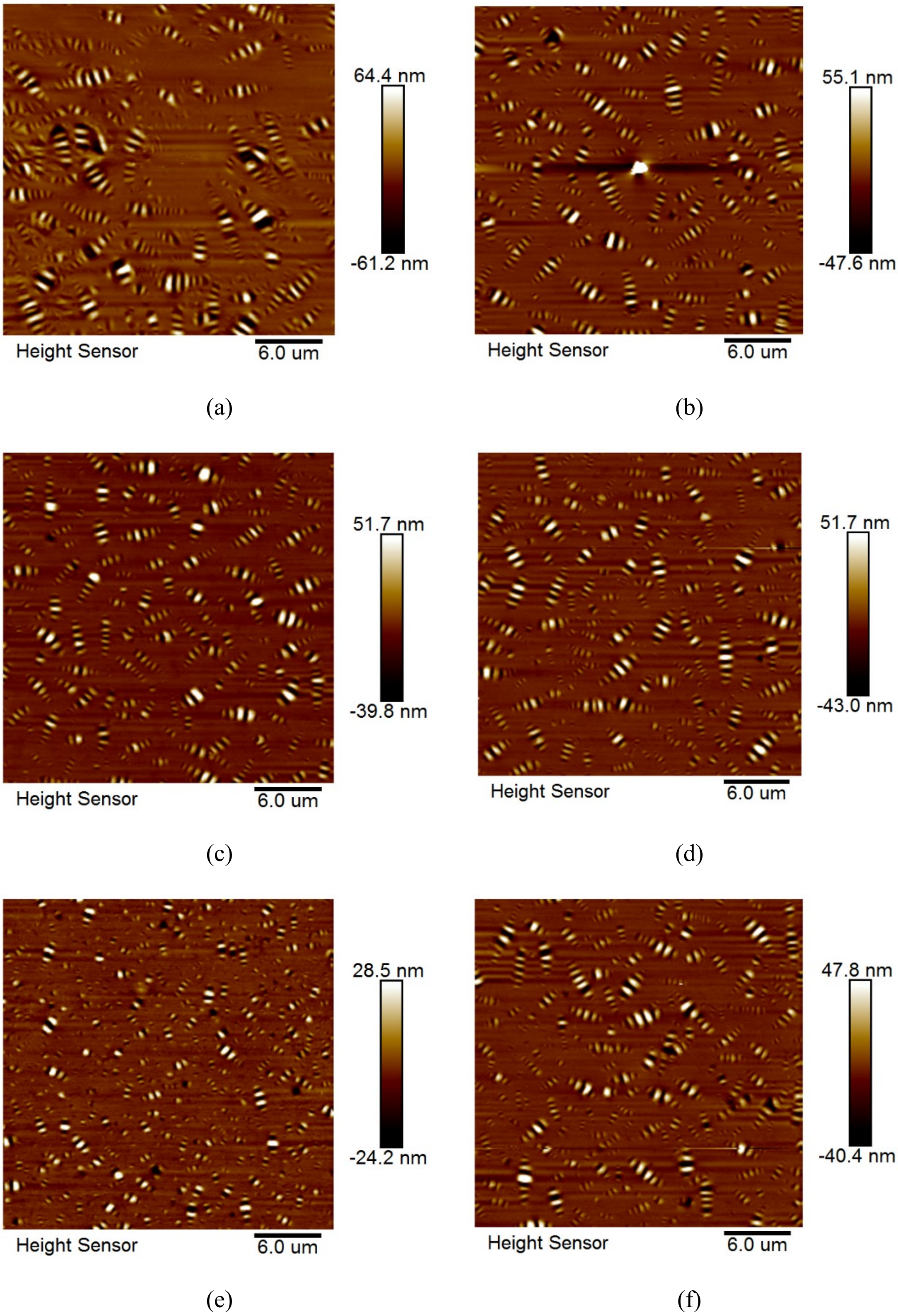

Figure 4.6 AFM 2D morphology results of asphalt mastics: (a) base bitumen A; (b) A+Granite; (c) A+Basalt; (d) A+Limestone; (d) A+Steel slag; (e) A+Cement

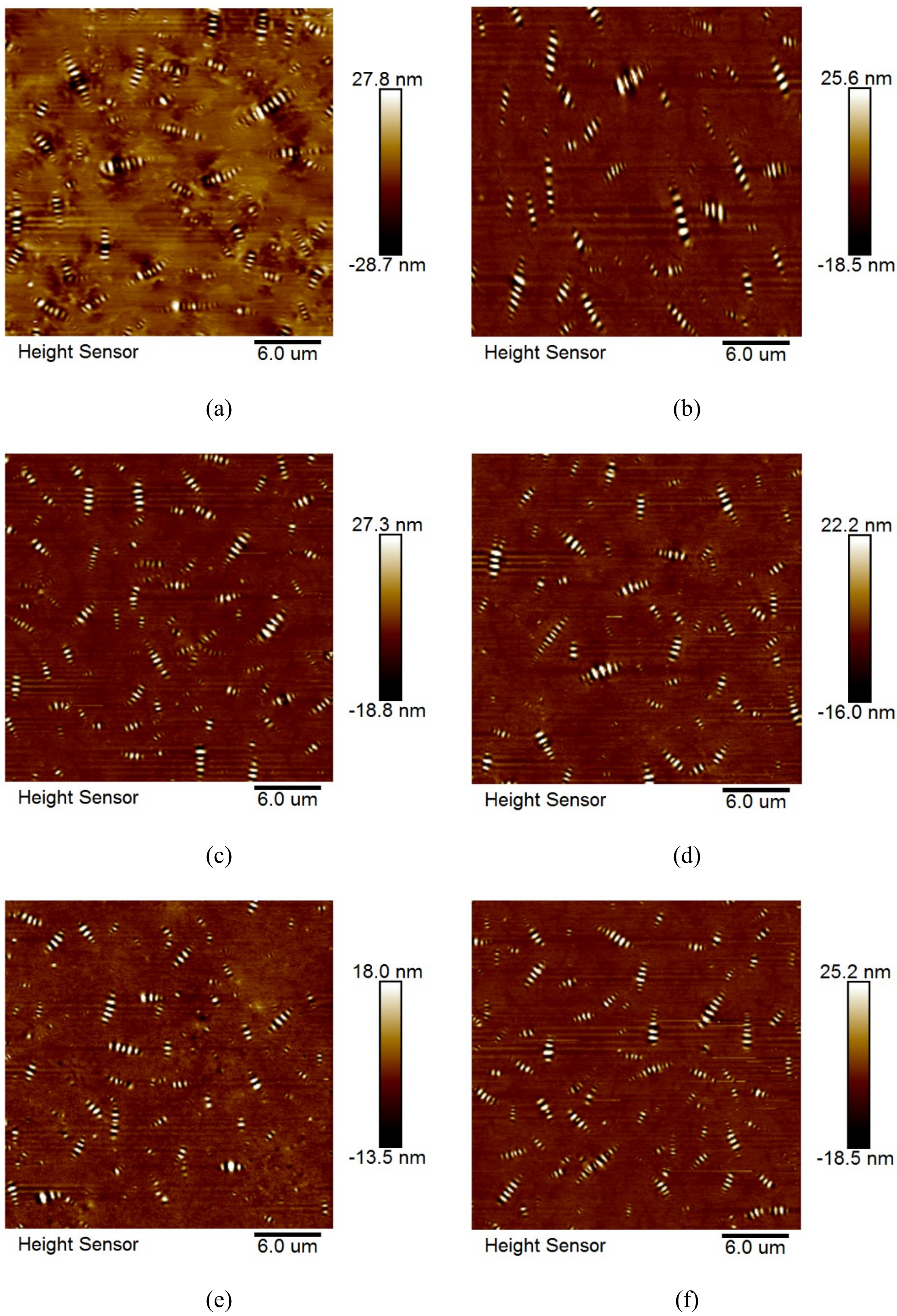

Figure 4.7 AFM 2D morphology results of asphalt mastics: (a) base bitumen B; (b) B+Granite; (c) B+Basalt; (d) B+Limestone; (d) B+Steel slag; (e) B+Cement

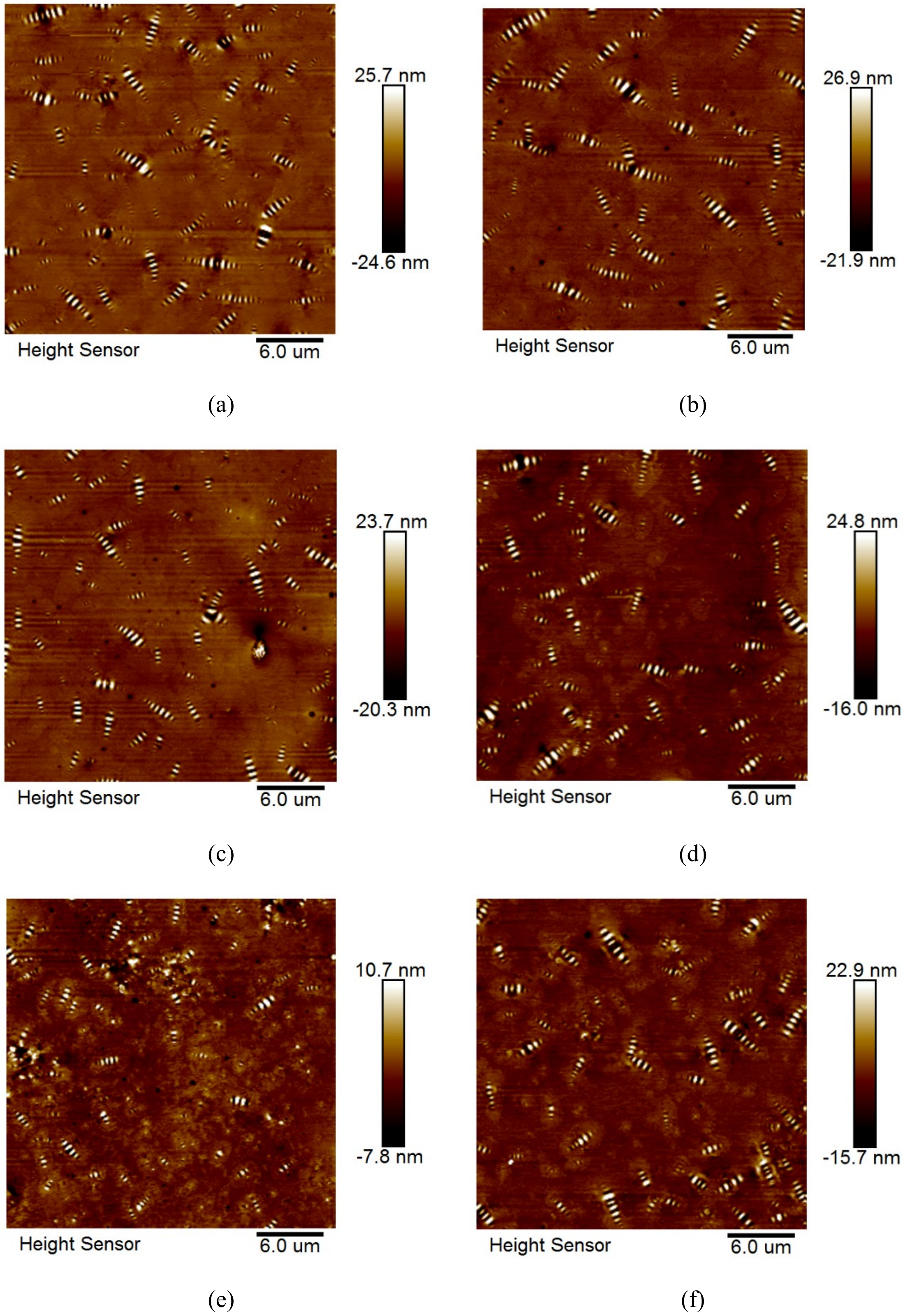

Figure 4.8 AFM 2D morphology results of asphalt mastics: (a) base bitumen C; (b) C+Granite; (c) C+Basalt; (d) C+Limestone; (d) C+Steel slag; (e) C+Cement

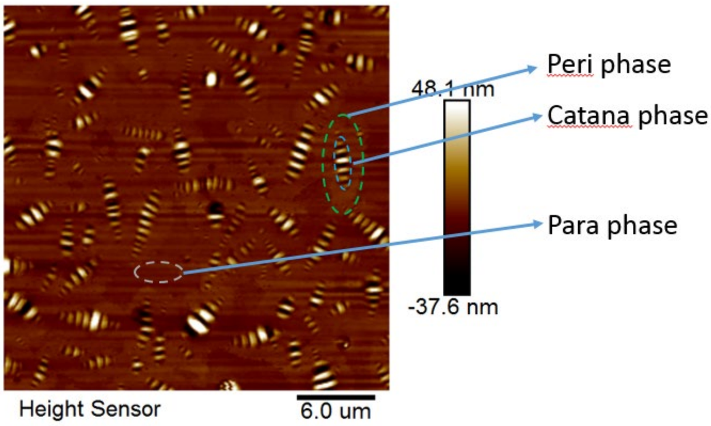

Figure 4.9 Schematic diagram for three phases of bituminous materials

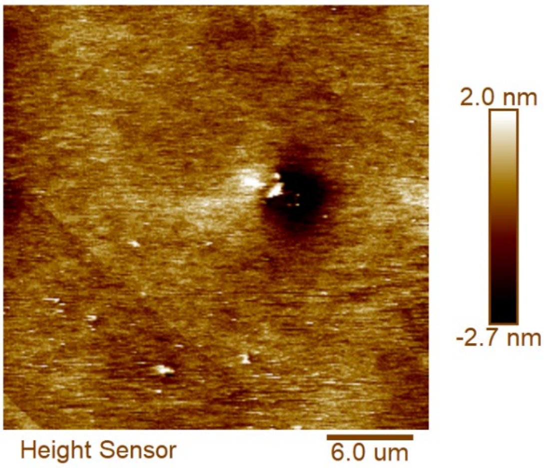

(a)

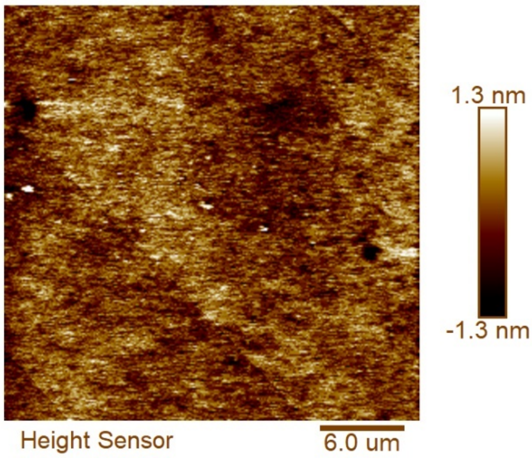

(b)

Figure 4.10 AFM 2D morphology results of: (a) base bitumen D; (b) base bitumen E

Furthermore, to further quantify the change in the bee-like structures of AFM 2D morphology of bitumen, the commercial software MATLAB was used to digitally process the AFM 2D image to calculate the area and proportion of the bee-like structures of bitumen and asphalt mastics. The digital image processing procedure is as follows. First, the AFM colour image is converted into a grayscale image, and then the grayscale image is converted into a binary image. Figure 4.11 is a schematic diagram of digital image processing (taking base bitumen A as an example). Finally, the areas and corresponding proportions of the black and white parts in the binarized image are calculated respectively, and the white part is the area of the bee-like structures.

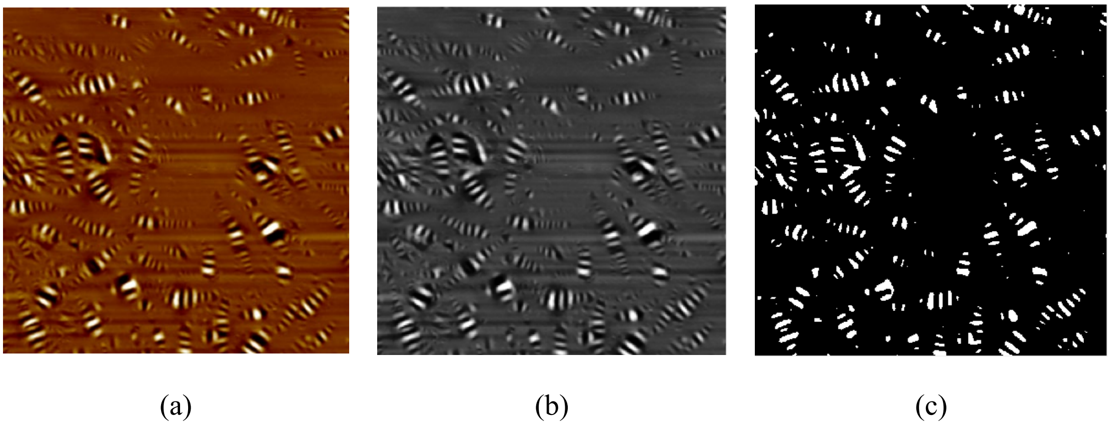

Figure 4.11 Digital image processing program of AFM 2D images: (a) colour image; (b) grayscale image; (c) binarized image

Table 4-4 lists the calculation results of the bee-like structure areas of asphalt mastics based on bitumen A, B, and C. From the table, the addition of all fillers reduced the total area, average area, and proportion of the bee like structures in bitumen, while increasing the number of bee-like structures. That is, the bee-like structures of asphalt mastics present a smaller and denser distribution, which verifies the observation results of AFM 2D morphology results. In addition, among five fillers, Steel powder has the highest number, the smallest area, and the lowest proportion of bee-like structures. This pattern is basically present in the three types of asphalt mastics. Existing research has shown that the density of the bee-like structures of bitumen to some extent reflects the superiority of its performance. The denser the bee-like structures, the more uniform the distribution of asphaltene in bitumen, and the more stable the cementitious system of bituminous materials. This to some extent indicates that Steel powder asphalt mastics will exhibit the best mechanical properties compared to other asphalt mastics.

Table 4-4 Computation results of bee-like structure areas of asphalt mastics

Bitumen	Asphalt mastics	Total area(μm^2)	Proportion (%)	Number	Average area(μm^2)
A	A	57.16	6.35	270	0.212
	A+Granite	53.28	5.92	281	0.190
	A+Basalt	50.18	5.58	296	0.170
	A+Limestone	48.23	5.36	311	0.155
	A+Steel slag	40.59	4.51	400	0.101
	A+Cement	49.44	5.49	326	0.152
B	B	44.10	4.90	200	0.220
	B+Granite	24.02	2.67	209	0.115
	B+Basalt	28.85	3.21	286	0.101
	B+Limestone	24.21	2.69	246	0.098
	B+Steel slag	22.55	2.51	232	0.097
	B+Cement	28.65	3.18	228	0.126
C	C	32.22	3.58	237	0.136
	C+Granite	28.91	3.21	294	0.098
	C+Basalt	27.47	3.05	229	0.120
	C+Limestone	30.59	3.40	241	0.127
	C+Steel slag	21.85	2.43	352	0.062
	C+Cement	26.29	2.92	264	0.100

4.2.3 Macroscopic test results of asphalt mastics

4.2.3.1 Temperature sweep test results of asphalt mastics

Table 4-5 lists the rutting factor ($G^*/\sin\delta$) and high-temperature PG test results of asphalt mastics. From the table, adding all fillers significantly enhanced the high-temperature performance of the five kinds of base bitumen. In general, the fillers have the most substantial rutting enhancement effect on A and E with the increasement of high-temperature PG by 10.64°C and 10.30°C on average, respectively. Nevertheless, the rutting factor and high-temperature PG seem unable to distinguish the high-temperature performance between different types of asphalt mastics based on the same bitumen matrix because these values are very close.

Table 4-5 Rutting factor and high-temperature PG of the asphalt mastics

Bitumen	Asphalt mastic	$G^*/\sin\delta$ (kPa)				High-temperature PG (°C)
		82°C	76°C	70°C	64°C	
A	A	0.195	0.363	0.702	1.373	66.68
	A+Granite	0.644	1.261	2.539	5.324	78.07
	A+Basalt	0.660	1.299	2.613	5.478	78.32
	A+Limestone	0.594	1.160	2.331	4.893	77.33
	A+Steel slag	0.506	0.979	1.944	4.020	75.81
	A+Cement	0.580	1.128	2.262	4.728	77.08
B	B	0.161	0.298	0.575	1.174	65.35
	B+Granite	0.393	0.740	1.432	2.901	73.26
	B+Basalt	0.374	0.707	1.373	2.789	72.86
	B+Limestone	0.407	0.763	1.485	3.024	73.57
	B+Steel slag	0.448	0.852	1.679	3.469	74.58
	B+Cement	0.436	0.812	1.574	3.222	74.11
C	C	-	0.342	0.655	1.332	66.42
	C+Granite	0.552	1.056	2.082	4.299	76.50
	C+Basalt	0.539	1.029	2.124	4.400	76.27
	C+Limestone	0.558	1.063	2.100	4.361	76.57
	C+Steel slag	0.499	0.948	1.863	3.856	75.50
	C+Cement	0.516	0.980	1.926	3.981	75.81
D	D	-	0.495	0.945	1.898	69.48
	D+Granite	0.741	1.407	2.746	5.558	79.19
	D+Basalt	0.704	1.347	2.638	5.353	78.75
	D+Limestone	0.747	1.415	2.765	5.615	79.26
	D+Steel slag	0.772	1.462	2.851	5.768	79.57
	D+Cement	0.772	1.466	2.863	5.806	79.58
E	E	-	0.372	0.699	1.387	66.86
	E+Granite	0.588	1.110	2.152	4.333	76.99
	E+Basalt	0.600	1.146	2.226	4.487	77.26
	E+Limestone	0.598	1.130	2.191	4.396	77.16
	E+Steel slag	0.604	1.138	2.201	4.436	77.23
	E+Cement	0.601	1.131	2.189	4.402	77.17

Table 4-6 lists the fatigue factor ($G^{*}*\sin\delta$) and medium-temperature PG test results of asphalt mastics. Considering that the rules of different base bitumen are similar, only the test results of two base bitumen (A and B) are listed here. From the table, the use of fillers significantly weakened the fatigue performance of asphalt, manifested as a significant increase in the fatigue factor and medium-temperature PG of asphalt mastics. In addition, like the rutting factor, the fatigue factor cannot distinguish the fatigue performance of different types of asphalt mastics based on the same bitumen matrix. In conclusion, the linear viscoelastic parameters, such as the rutting factor and fatigue factor, are no longer appropriate for the performance evaluation of asphalt mastics.

Table 4-6 Fatigue factor and medium-temperature PG of the asphalt mastics

Bitumen	Asphalt mastic	$G^{*}*\sin\delta$ (kPa)			Medium-temperature PG (°C)
		19°C	22°C	25°C	
A	A	7619.36	5438.81	3785.76	22.70
	A+Granite	20493.85	14935.95	10560.95	31.47
	A+Basalt	17297.30	12634.45	8966.39	30.11
	A+Limestone	18895.58	15121.45	10824.75	31.93
	A+Steel slag	17425.15	12605.10	8861.47	29.87
	A+Cement	18601.90	13620.40	9671.92	30.78
B	B	5372.60	3812.12	2614.76	19.63
	B+Granite	16255.85	11837.95	8311.52	29.31
	B+Basalt	15314.30	11051.40	7703.73	28.59
	B+Limestone	16213.40	11592.40	8003.69	28.81
	B+Steel slag	16885.25	12298.75	8608.63	29.57
	B+Cement	15302.60	11081.70	7744.81	28.66

4.2.3.2 MSCR test results of asphalt mastics

Figures 4.12 ~ 4.16 shows the results of the average percent recovery (*R*) and non-recoverable creep compliance (J_{nr}) of the MSCR test of asphalt mastics under the two stress levels of 0.1kPa and 3.2kPa, respectively.

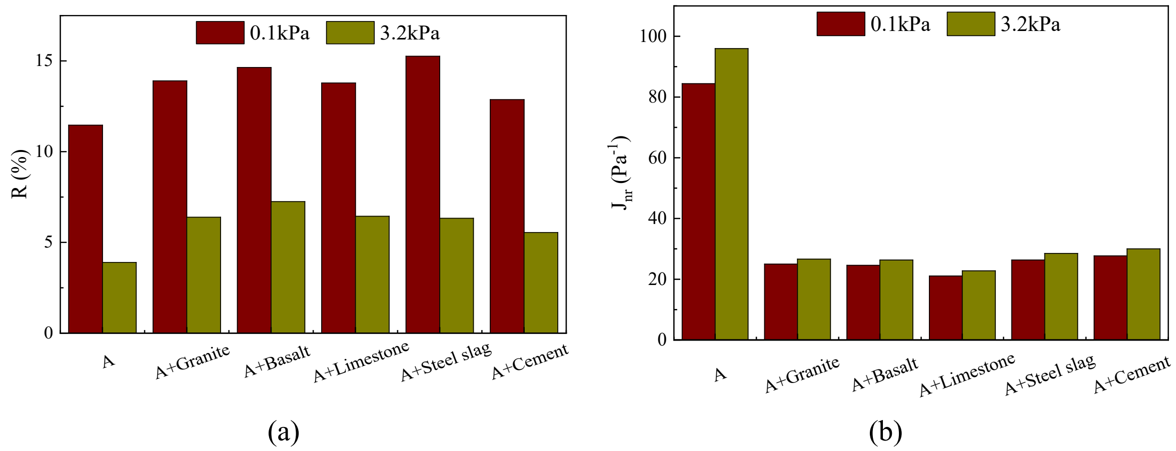

Figure 4.12 MSCR test results of asphalt mastics: (a) *R* of bitumen A; (b) J_{nr} of bitumen A

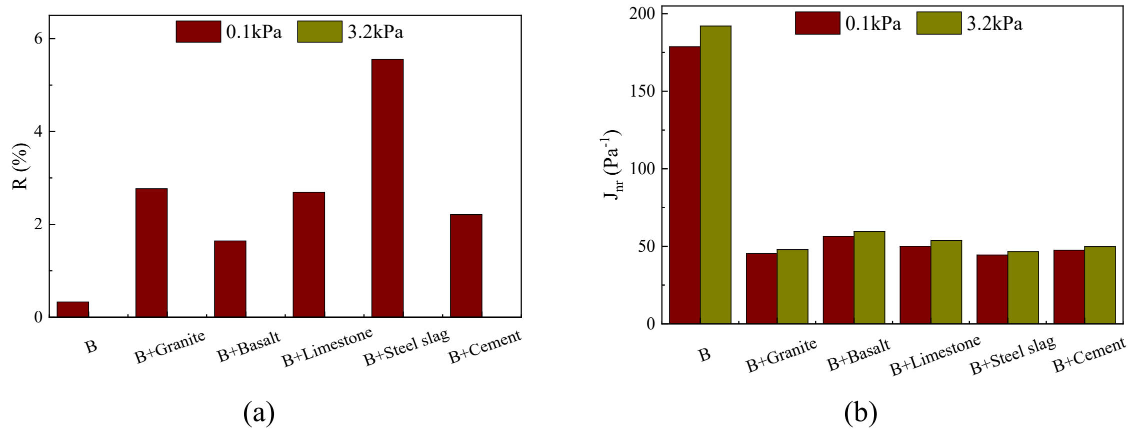

Figure 4.13 MSCR test results of asphalt mastics: (a) *R* of bitumen B; (b) J_{nr} of bitumen B

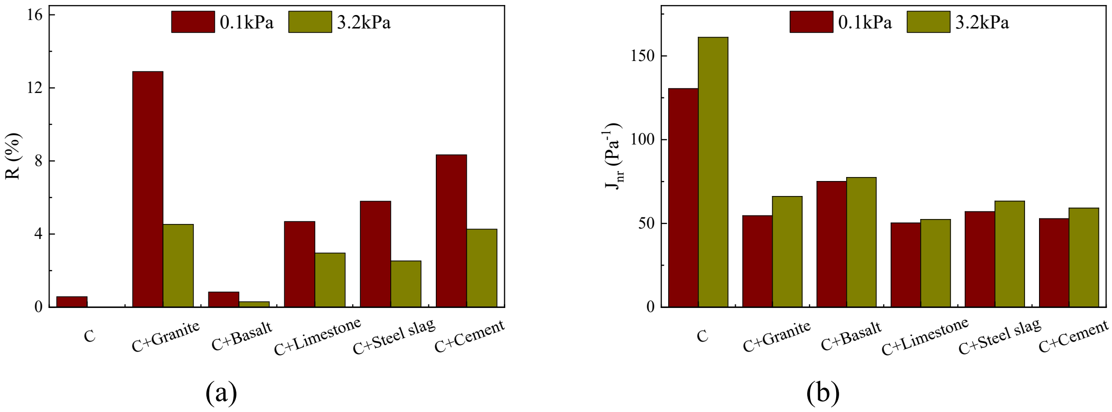

Figure 4.14 MSCR test results of asphalt mastics: (a) *R* of bitumen C; (b) J_{nr} of bitumen C

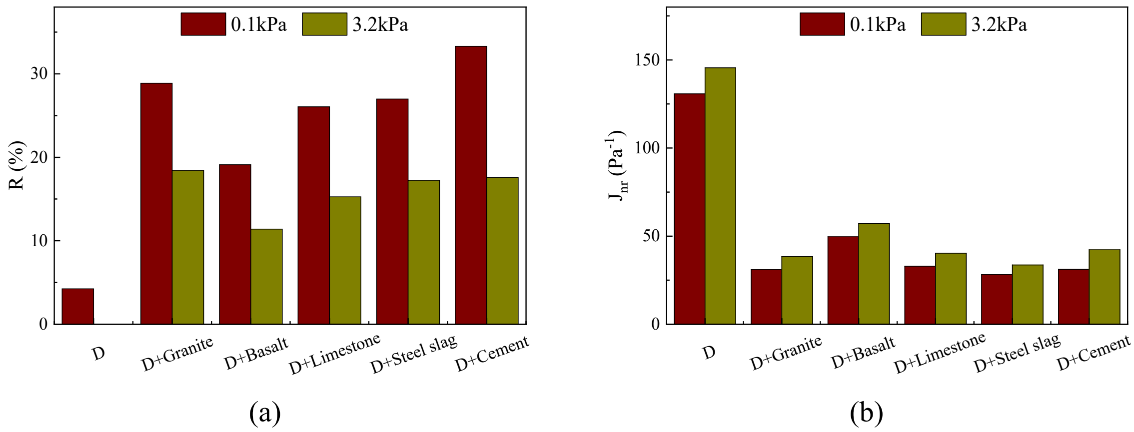

Figure 4.15 MSCR test results of asphalt mastics: (a) *R* of bitumen D; (b) J_{nr} of bitumen D

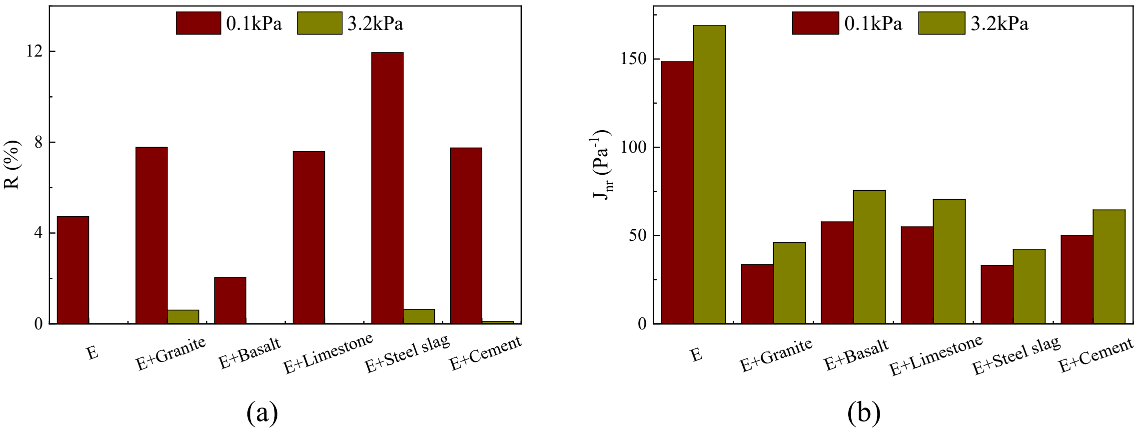

Figure 4.16 MSCR test results of asphalt mastics: (a) *R* of bitumen E; (b) J_{nr} of bitumen E

The higher the *R*, the lower the J_{nr}, and the better the high-temperature damage resistance of asphalt mastics. Firstly, the MSCR test can clearly distinguish the high-temperature performance between different types of asphalt mastics based on the same bitumen matrix. As far as the five kinds of base bitumen in this study are concerned, among the five fillers, basalt has a minor enhancement on the high-temperature performance of the base bitumen in most cases. In addition, the enhancement effect of fillers on the base bitumen mainly manifests in the significant decrease of J_{nr}, while the increase in *R* is not substantial. This rule is shown in the other four base bitumen except for bitumen D.

4.2.3.3 LAS test results of asphalt mastics

Figure 4.17 presents the stress-strain curves of asphalt mastics. It can be seen from the figure that the peak stress of the stress-strain curves of asphalt mastics is significantly increased due to the addition of fillers. Among the five kinds of base bitumen, bitumen A, and bitumen C have the most significant increase, both of which can be increased from 4.0E5Pa to 1.2E6Pa. And the shapes of the stress-strain curves of different asphalt mastics based on the same bitumen matrix are similar. In addition, in the stress-strain curve, the strain corresponding to the peak stress represents the toughness of bituminous materials. The larger the strain value, the better the toughness of asphalt mastics. It can be seen intuitively that steel slag modified asphalt mastics has the strongest toughness among all asphalt mastics.

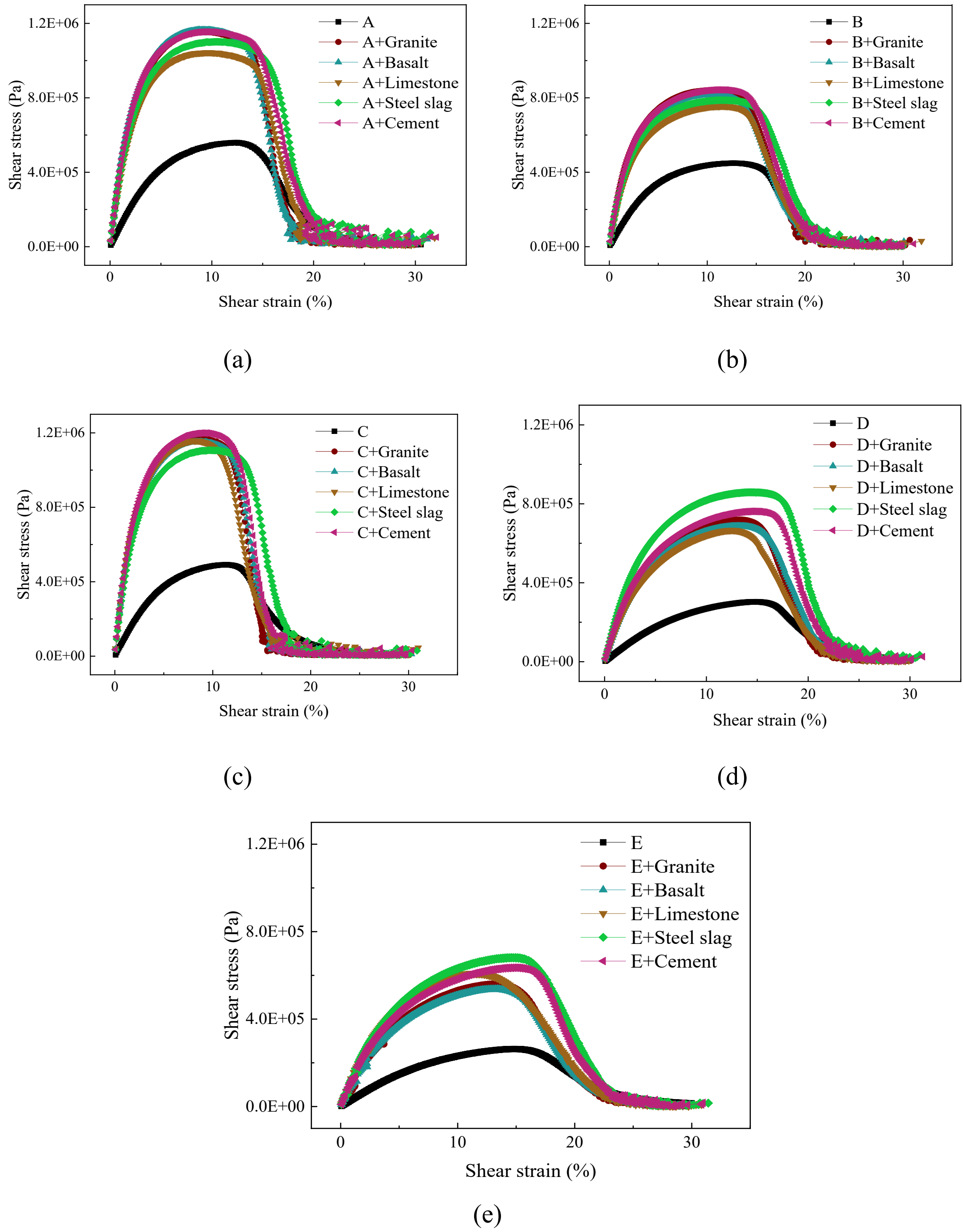

Figure 4.17 Stress-strain curves of asphalt mastics: (a) bitumen A; (b) bitumen B; (c) bitumen C; (d) bitumen D; (e) bitumen E

Figure 4.18 presents the integrity parameter curves of asphalt mastics, which describes the change of the integrity parameter with the damage integrity. The lower the integrity parameter, the more seriously the material is damaged. From the figures, the integrity parameter of bitumen is much higher than that of the asphalt mastic under the same damage integrity, which indicates that the use of fillers significantly weakens the fatigue damage properties of bitumen judging from the integrity parameters. In addition, there is no significant difference in the integrity parameter curves between the asphalt mastics based on the same bitumen matrix.

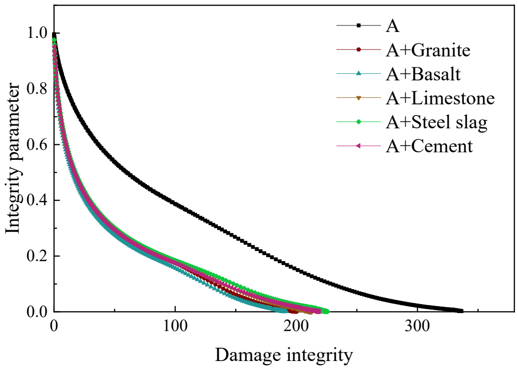

(a)

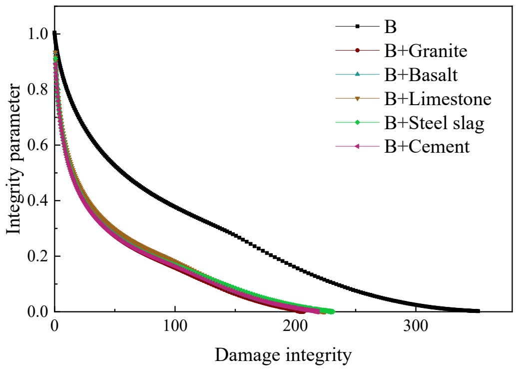

(b)

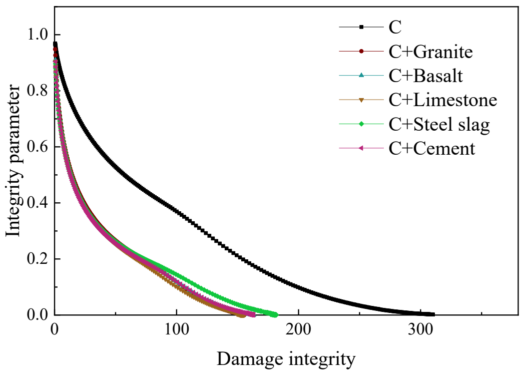

(c)

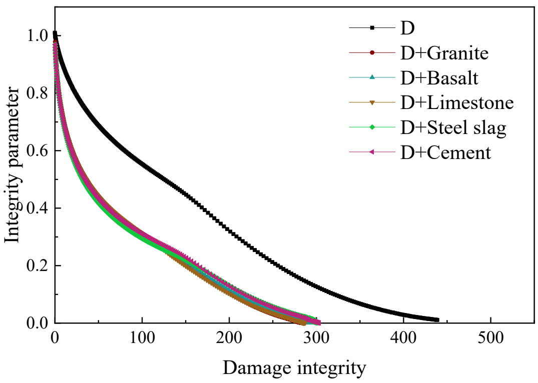

(d)

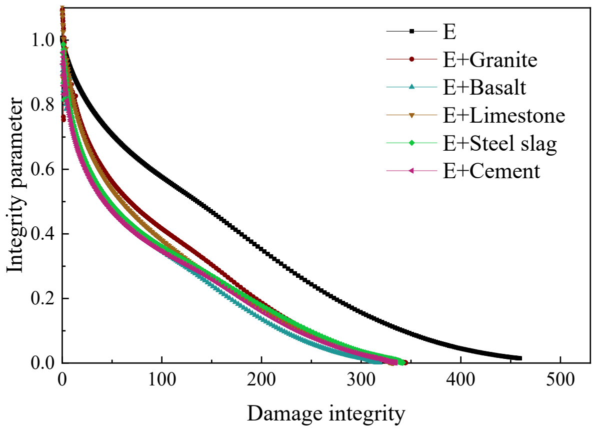

(e)

Figure 4.18 Damage integrity curves of asphalt mastics: (a) bitumen A; (b) bitumen B; (c) bitumen C; (d) bitumen D; (e) bitumen E

The integrity parameter (C_f) and damage accumulation parameter (D_f) of asphalt mastic at fatigue failure are illustrated in Figure 4.19. Firstly, from Figure 4.19 (a), it can be observed that the use of fillers reduces the C_f of the bitumen, indicating that the addition of fillers increases the critical reduction range of modulus that the bitumen can achieve at fatigue failure. This means the bitumen can withstand a greater range of modulus reduction, suggesting improved toughness. From Figure 4.19 (b), it is evident that the addition of fillers also reduces the D_f of the bitumen, indicating that the inclusion of fillers decreases the critical fatigue damage accumulation that the bitumen can achieve, making the bitumen more brittle. It is not difficult to notice that the conclusions drawn from the two indicators, C_f and D_f, are contradictory. According to the definitions of C_f and D_f, a lower C_f and a higher D_f correspond to better fatigue performance of the asphalt mastic. This is because the addition of fillers has a dual impact on the fatigue performance of asphalt mastic, with both positive enhancing effects and negative weakening effects. On one hand, the addition of fillers increases the modulus of the bitumen, making it more brittle and thereby weakening its fatigue performance. On the other hand, the addition of fillers has a particle filling enhancement effect on the bitumen, as it creates numerous bitumen-filler interfaces within the bitumen, providing a reinforcing effect. Moreover, the mastic samples need to break more bitumen-filler interfaces during fatigue failure. Waste fillers (steel slag and cement) demonstrate greater advantages in particle filling enhancement compared to mineral fillers, as waste fillers have finer particle sizes and larger specific surface areas, forming more bitumen-filler interfaces at the same volume concentration. Consequently, asphalt mastic samples need to break more filler-asphalt interfaces during fatigue failure, meaning the crack propagation path becomes longer, thereby improving the fatigue life to some extent. In this study, the first negative weakening effect is referred to as physical hardening, and the second positive effect is termed particle filling enhancement. The impact of filler addition on the fatigue performance of asphalt is explained as a competitive mechanism between physical hardening and particle filling enhancement.

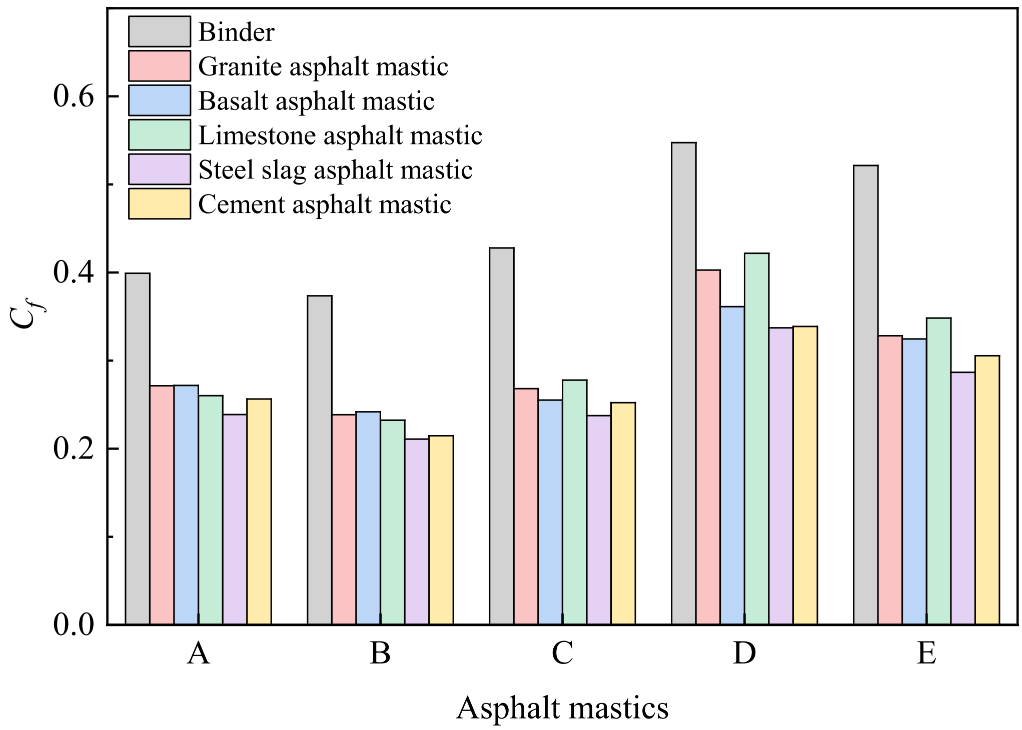

(a)

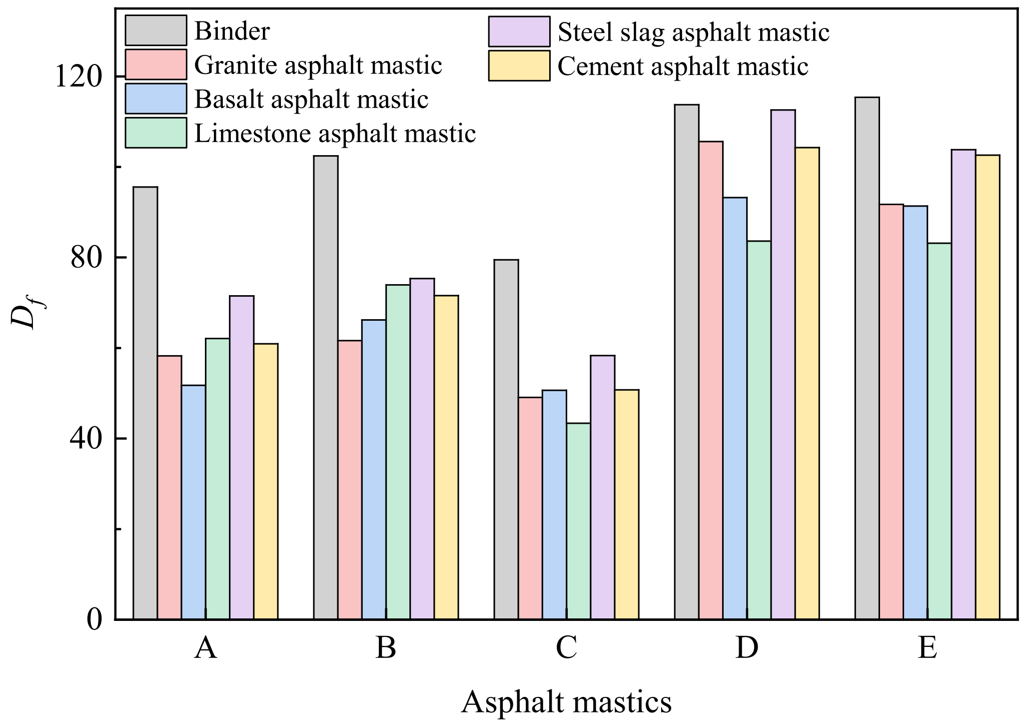

(b)

Figure 4.19 Critical parameters of asphalt mastics at fatigue failure: (a) C_f; (b) D_f

According to the competitive mechanism theory above, it can be anticipated that the asphalt mastic incorporating waste fillers will exhibit a longer fatigue life compared to that with mineral fillers. The results of C_f and D_f validate this prediction, as waste fillers demonstrate a lower C_f and a higher D_f at the same filler-bitumen ratio. This is because, among the five types of fillers, steel slag filler has the smallest particle size and the largest specific surface area, resulting in the highest number of asphalt-filler interfaces when added to asphalt, followed by cement filler.

Figure 4.20 shows the fatigue life (N_f) of asphalt mastics at different strain levels. In addition to the two most used strain levels of 2.5% and 5% for the LAS test, two strain levels of 10% and 15% were added in this study. Firstly, the effect of fillers on the fatigue life of bitumen may be related to the strain level selected. Some fillers like steel slag and cement may extend the fatigue life of bitumen at low strain levels (2.5% and 5%), but the extension effect no longer exists when the strain level becomes larger (10% and 15%). In other words, the strain levels of 2.5% and 5% are problematic for computing the fatigue life of asphalt mastics whose modulus is much bigger than bitumen binder, which was also mentioned in a recent study by the research team that proposed the LAS test [152]. In addition, as far as the base bitumen used in this study is concerned, steel slag exhibits the strongest fatigue performance among the five asphalt mastics prepared from each base bitumen, followed by cement. At the same time, the other three types of fillers do not draw uniform rules in different base bitumen. This also validates the earlier speculation regarding C_f and D_f, as well as the competitive mechanism proposed in this study concerning the impact of fillers on the fatigue performance of asphalt mastics.

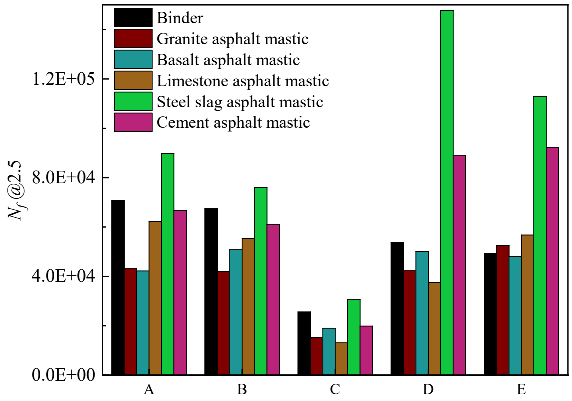

(a)

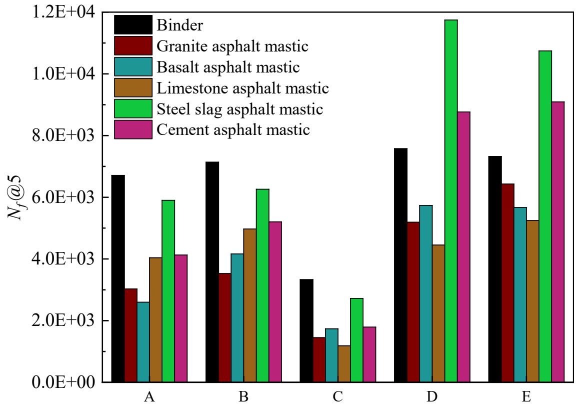

(b)

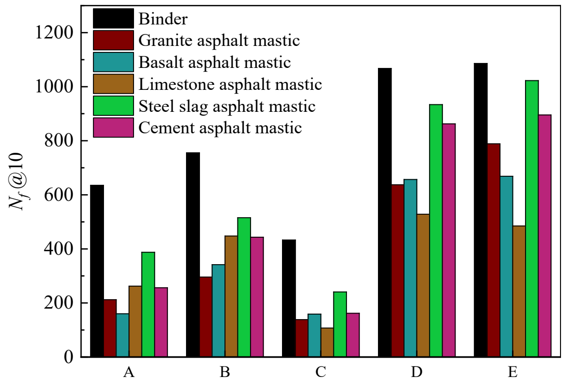

(c)

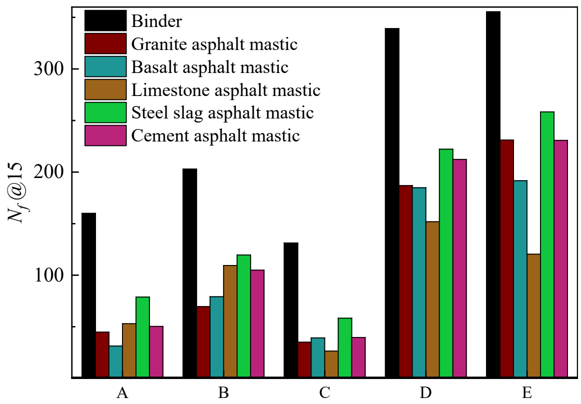

(d)

Figure 4.20 The fatigue life of asphalt mastics at different strain levels of (a) 2.5%; (b) 5%; (c) 10%; (d) 15%

4.2.3.4 BBR test results of asphalt mastics

Figures 4.21 ~ 4.25 show the BBR test results of asphalt mastics, and the low-temperature PG of asphalt mastics was calculated based on the BBR test data and listed in Table 4-7. It is evident that the addition of all fillers significantly weakens the low-temperature cracking resistance of base bitumen. Among the five fillers, limestone and cement have the least negative effect on the low-temperature performance of base bitumen, which is the same among the five base bitumen used in this study. This may be due to the lower hardness of sedimentary rock (limestone) and cement compared with igneous rocks (granite and basalt) and steel slag, which leads to better low-temperature performance. In addition, it is worth noting that the BBR test only reflects the hardness and relaxation properties of bituminous materials. As mentioned above, the addition of fillers will improve the toughness of bitumen. To comprehensively evaluate the crack resistance of asphalt mastics, some tests characterizing the fracture toughness of materials, such as single-edge notch bending [153] and DENT tests [154], can be taken into consideration as the supplement of BBR test.

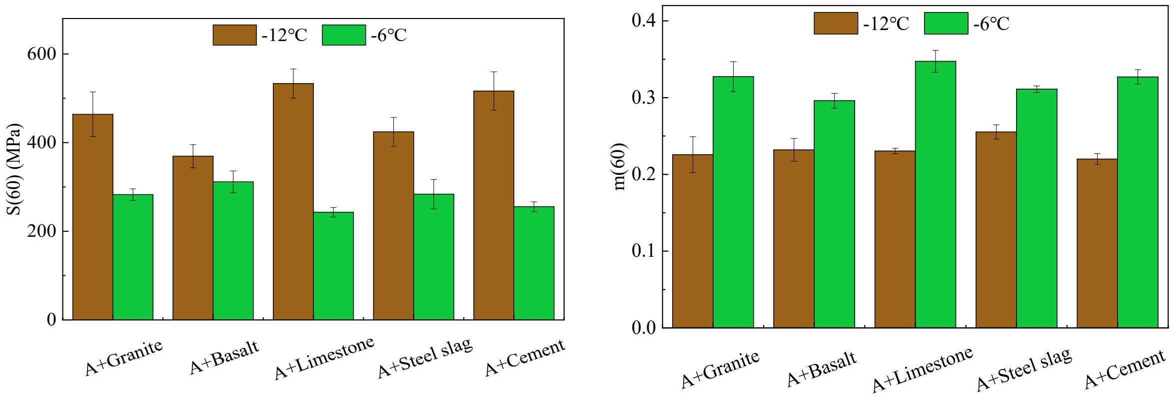

(a) (b)

Figure 4.21 BBR test results of asphalt mastics: (a) *S* of bitumen A; (b) m-value of bitumen A

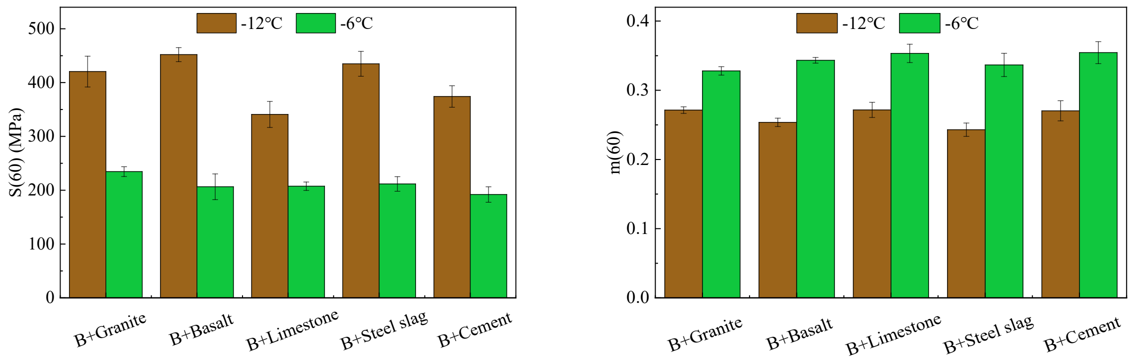

(a) (b)

Figure 4.22 BBR test results of asphalt mastics: (a) *S* of bitumen B; (b) m-value of bitumen B

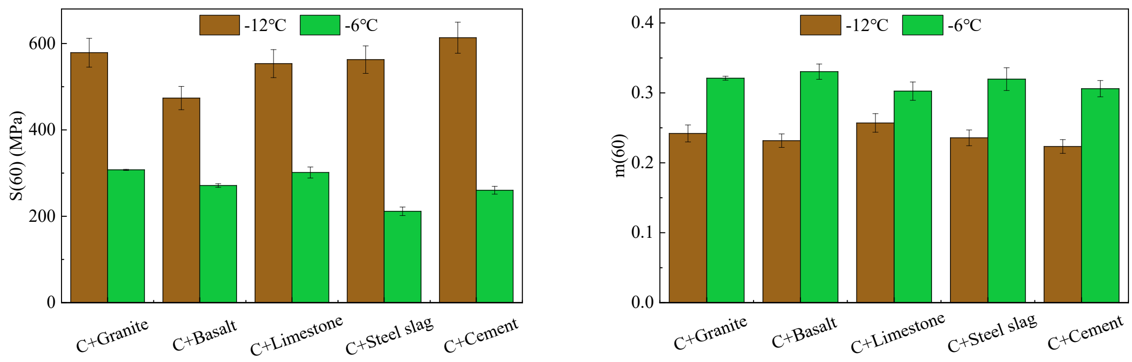

(a) (b)

Figure 4.23 BBR test results of asphalt mastics: (a) *S* of bitumen C; (b) m-value of bitumen C

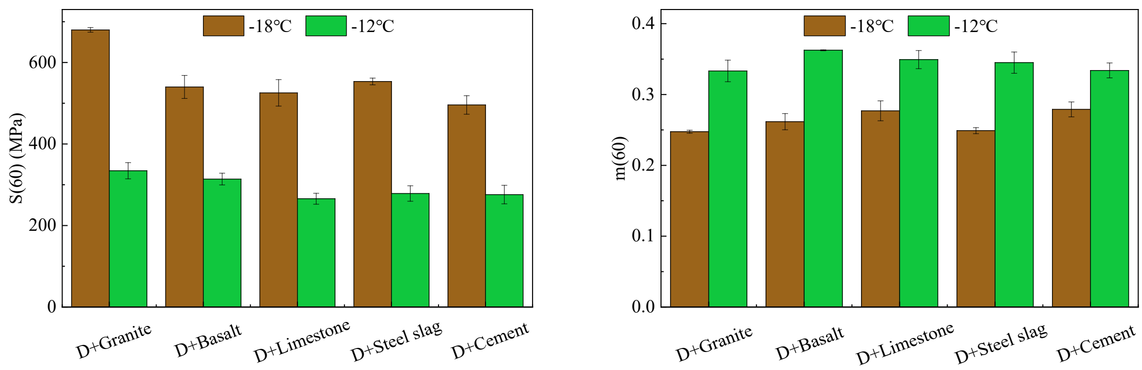

(a) (b)

Figure 4.24 BBR test results of asphalt mastics: (a) *S* of bitumen D; (b) m-value of bitumen D

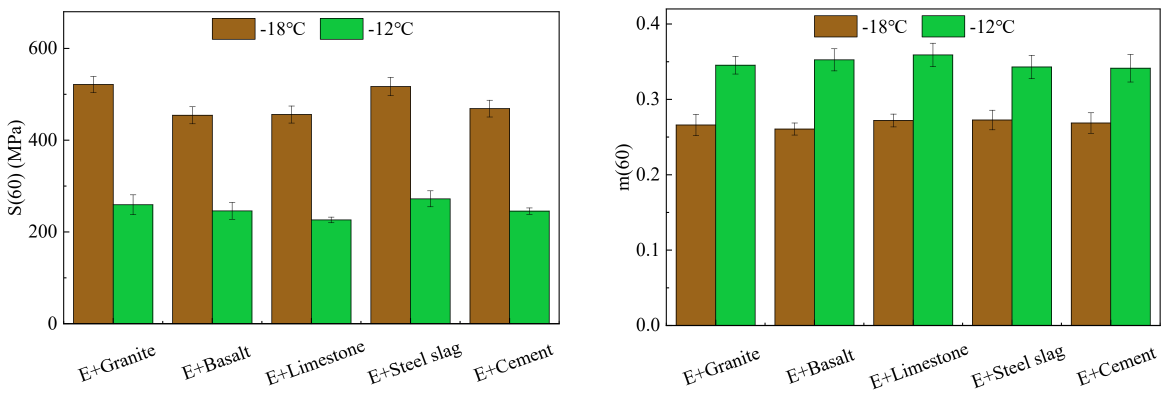

(a) (b)

Figure 4.25 BBR test results of asphalt mastics: (a) *S* of bitumen E; (b) m-value of bitumen E

Table 4-7 Low-temperature PG of the asphalt mastics

Bitumen	Asphalt mastics	T_S (°C)	T_m (°C)	Low-temperature PG (°C)
A	A	-27.55	-26.98	-26.98
	A+Granite	-16.72	-17.61	-16.72
	A+Basalt	-14.68	-15.63	-14.68
	A+Limestone	-17.64	-18.91	-17.64
	A+Steel slag	-16.83	-15.86	-15.86
	A+Cement	-17.37	-17.74	-17.37
B	B	-27.38	-22.00	-22.00
	B+Granite	-18.53	-18.96	-18.53
	B+Basalt	-18.86	-18.90	-18.86
	B+Limestone	-19.65	-19.92	-19.65
	B+Steel slag	-18.90	-18.35	-18.35
	B+Cement	-20.01	-19.88	-19.88
C	C	-26.63	-21.85	-21.85
	C+Granite	-15.76	-17.59	-15.76
	C+Basalt	-20.92	-20.16	-20.16
	C+Limestone	-22.05	-21.67	-21.67
	C+Steel slag	-19.86	-20.60	-19.86
	C+Cement	-21.01	-21.56	-21.01
D	D	-30.25	-29.41	-29.41
	D+Granite	-21.08	-24.33	-21.08
	D+Basalt	-21.49	-25.72	-21.49
	D+Limestone	-23.07	-26.09	-23.07
	D+Steel slag	-22.65	-24.81	-22.65
	D+Cement	-22.86	-25.71	-22.86
E	E	-30.72	-30.72	-30.72
	E+Granite	-23.25	-25.43	-23.25
	E+Basalt	-23.94	-25.43	-23.94
	E+Limestone	-24.42	-26.07	-24.42
	E+Steel slag	-22.91	-25.67	-22.91
	E+Cement	-23.92	-25.87	-23.92

4.2.4 Results of GRA

4.2.4.1 GRA results of high-temperature performances

Since the use of fillers does not significantly affect the R of asphalt mastics, the J_{nr} at the two stress levels of 0.1kPa and 3.2kPa was selected as the parameters reflecting the high-temperature performance of asphalt mastics in this study. Figure 4.26 presents the grey relational grades between the high-temperature indexes and the raw material characteristics (including components and penetrations of bitumen and filler characteristics). It can be seen from the figures that the penetrations of bitumen properties, and fineness parameters (D10 and

D90) and P20 of filler characteristics are the most significant factors affecting the high-temperature performance of asphalt mastics. This study adopted the same criteria as the literature [147], stating that when the grey correlation degree is greater than 0.75, it indicates a substantial correlation between the raw material characteristics and the performances of asphalt mastics. In the GRA results of $J_{nr-0.1}$ and $J_{nr-3.2}$, the correlation degrees of D10, penetrations, D90 and P20 are the highest, all of which are greater than 0.75 and followed by some bitumen components (asphaltene and aromatics), as well as the SSA and D50 of the fillers. In addition, the mineral powder composition of the fillers (SiO_2 and CaO) is the least influential factor among all raw material characteristics. Moreover, it is worth mentioning that, compared with P5 and P10, the correlation between P20 and J_{nr} is significantly higher than that of the former two. To conclude, the high-temperature performance of the mastics mainly depends on the fineness parameters (D10 and D90) of the fillers and the penetrations of bitumen. Besides, the content of fillers with a diameter of less than 0.02 mm (P20) is also a critical parameter affecting the high-temperature performance.

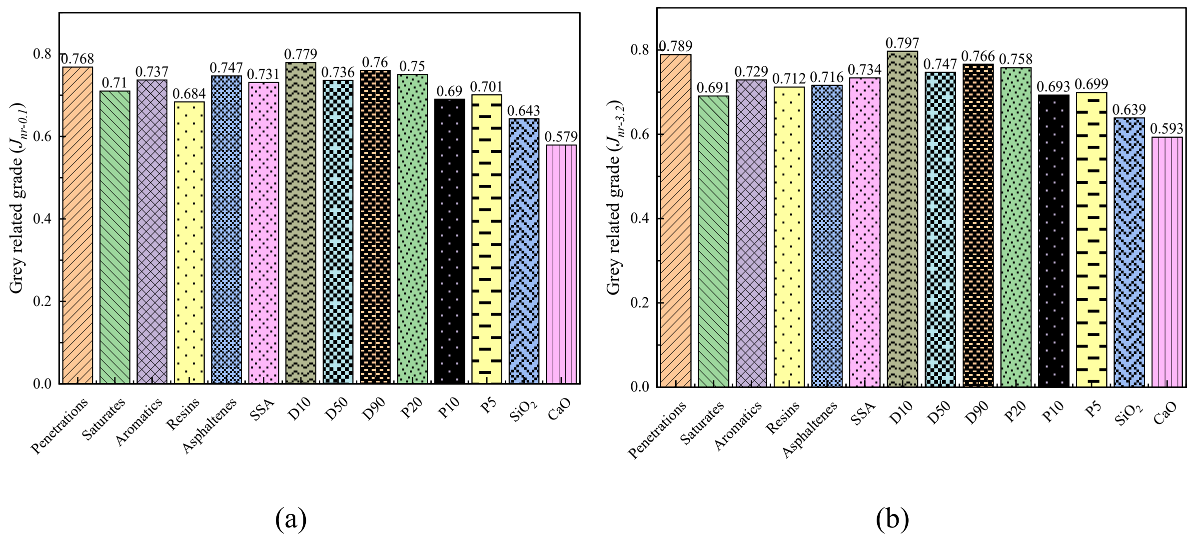

Figure 4.26 Grey relational grades between the high-temperature indexes and the raw material characteristics: (a) $J_{nr-0.1}$; (b) $J_{nr-3.2}$

4.2.4.2 GRA results of medium-temperature performances

Figure 4.27 presents the grey relational grades between the medium-temperature indexes (N_f at four strain levels of 2.5%, 5%, 10%, and 15%) and the raw material characteristics. From the figures, when N_f is at a low strain level (2.5%), the SSA and P20 of fillers have the most significant impact on the fatigue performance of the mastics, followed by P5 and P10, and the next are the aromatics and resins contents, and penetrations of bitumen. In other words, at low strain levels, the fatigue performance of the mastics mainly depends on the SSA and small particle proportion parameters (P20, P5, and P10) of fillers. When the strain level was increased (5%, 10%, and 15%), the resins content of bitumen was the most remarkable factor affecting the fatigue performance of the mastics, followed by SSA of the filler, the small particle proportion parameters (P20, P10, and P5) and the fineness parameters (D10, D50, and D90). To sum up, to achieve a better fatigue performance of asphalt mastics, the key is controlling the resin content of bitumen and the SSA and fineness of fillers.

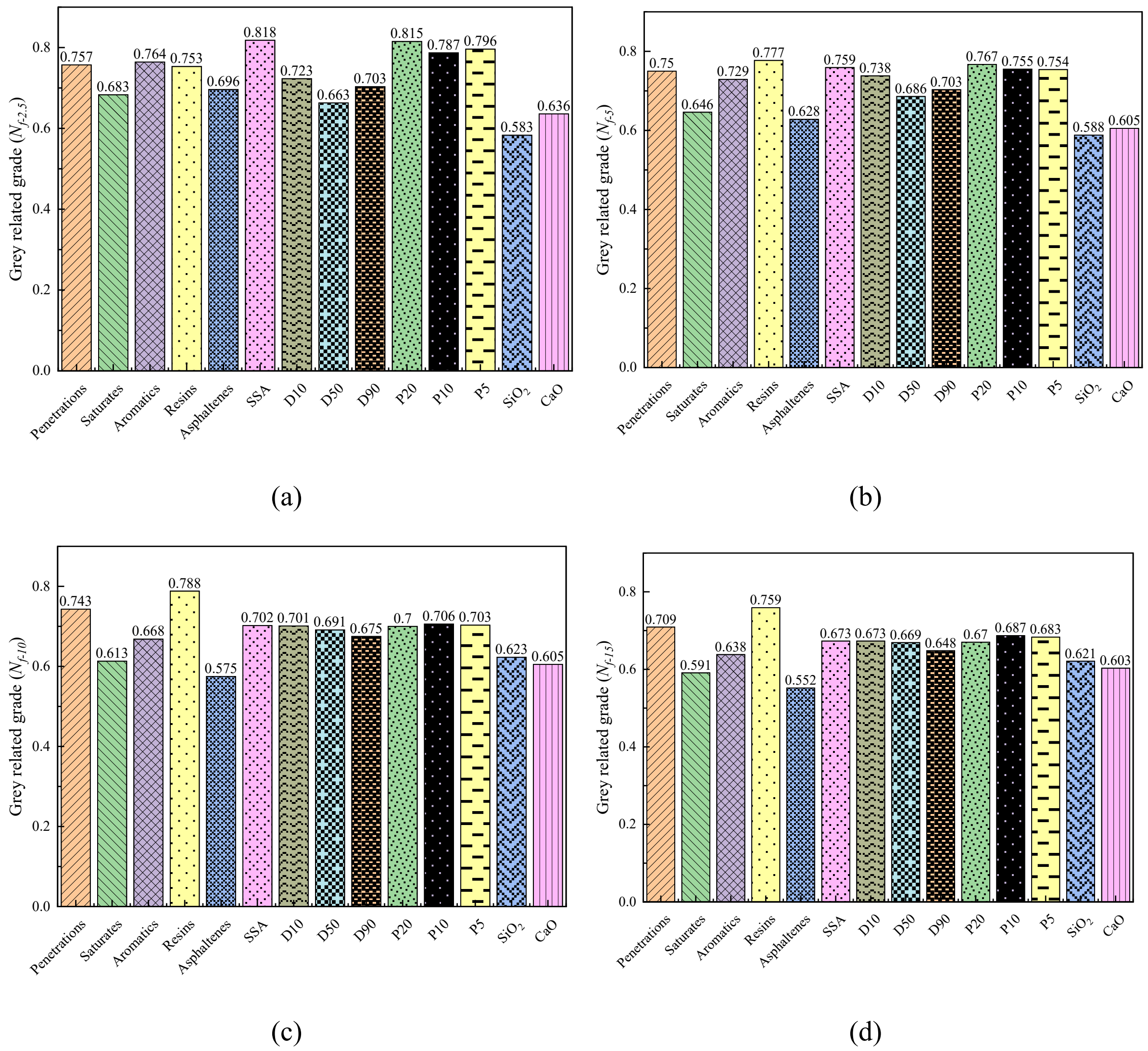

Figure 4.27 Grey relational grades between the medium-temperature indexes and the raw material characteristics: (a) $N_{f-2.5}$; (b) N_{f-5}; (c) N_{f-10}; (d) N_{f-15}

4.2.4.3 GRA results of low-temperature performances

Figure 4.28 presents the grey relational grades between the low-temperature indexes (T_S and T_m) and the raw material characteristics. It can be found from the figure the penetrations of bitumen were the most significant factor affecting the low-temperature performance of the mastics. D10 and P20 are the two factors most closely related to the low-temperature properties among the filler characteristics. These are followed by the SSA of fillers and resin content of bitumen, followed by D90 and the aromatics content of bitumen. Among all the raw material characteristics, the mineral composition of fillers (CaO and SiO_2) was the least relevant factor, which is also consistent with the previous results. To summarize, the low-temperature performance of asphalt mastics mainly depends on penetrations of bitumen, and some characteristics of fillers such as D10, P20, and SSA. Moreover, the resin content of bitumen also has a high contribution to the low-temperature performance.

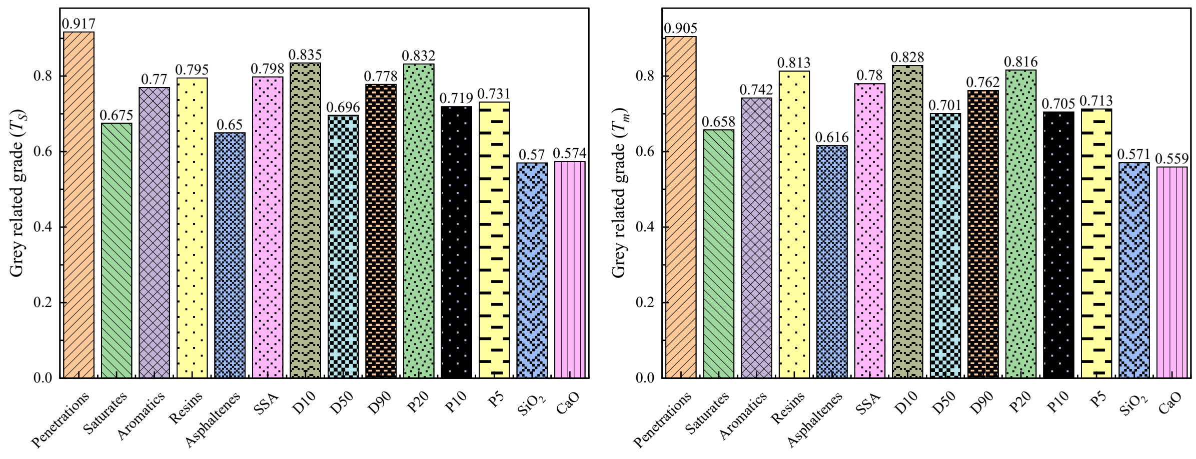

(a) (b)

Figure 4.28 Grey relational grades between the low-temperature indexes and the raw material characteristics: (a) T_S; (b) T_m

4.3 Summary

This chapter comprehensively characterizes the performance of asphalt mastic through an integrated approach combining microscopic and macroscopic testing techniques. Building on this foundation, the study employs GRA to systematically explore the qualitative composition-performance relationship between the service performance of asphalt mastic and its compositional structure, providing valuable insights into the interplay between material composition and functional behaviour. The major conclusion from this chapter includes:

1) Overall, the performance characteristics of asphalt mastic—including high-temperature rutting resistance, intermediate-temperature fatigue resistance, and low-temperature crack resistance—demonstrate a strong correlation with the material properties of its compositional structure. The qualitative analysis of the composition-performance

relationship governing the performance of asphalt mastic is anticipated to offer valuable guidance for the optimization and design of mastic performance tailored to specific service conditions.

2) The resin content of bitumen is suggested to be one of the most influential properties on the fatigue performance of asphalt mastics. With the increase in strain levels, the difference between the grey correlation degree of resins and that of other factors is more significant. In addition, the contents of resins and aromatics also exhibit a specific contribution to the low-temperature performance of asphalt mastics.

3) D10 of filler has the highest correlation with the high-temperature and low-temperature performances of asphalt mastics. P20 of the filler also shows a relatively high correlation with these properties of mastics. Furthermore, these two parameters exhibit a higher correlation than similar parameters (D50, D90, P10, and P5). Therefore, D10 and P20 are recommended as two critical indicators for selecting fillers.

4) The filler characteristics such as fineness and SSA will significantly affect the fatigue performance of asphalt mastics because the effect of fillers on the fatigue performance of mastics is the competitive mechanism between physical hardening and particle-filling enhancement. The filler with small particle size and large SSA can prolong and increase the propagation path of fatigue cracks, thus effectively improving the fatigue performance of asphalt mastics.

5) The addition of all fillers absorb the polar components in bitumen, thus promoting the dispersion of polar components and effectively preventing the mutual aggregation and crystallization of wax components and asphaltenes in bitumen, which is manifested as a decline in roughness and bee-like structure in the AFM results. Among the five fillers, Steel powder has the highest number, the smallest area, and the lowest proportion of bee-

like structures. This to some extent indicates that steel slag exhibits the best interaction ability with base bitumen.

This chapter systematically characterizes the performance of asphalt mastic through a combination of macroscopic and microscopic testing methods. Furthermore, it explores the qualitative composition-performance relationship between the mastic's performance and its compositional structure (bitumen and filler) using multifactor statistical analysis. This chapter focuses on qualitative analysis derived from statistical data, the subsequent phase of research will employ micromechanical modelling approaches to establish a quantitative relationship between the modulus of asphalt mastic and its compositional structure, thereby advancing the understanding of material behaviour at a more fundamental level.

CHAPTER 5 MICROMECHANICAL PREDICTION OF MODULUS OF ASPHALT MASTICS AND MIXTURES CONSIDERING INTERPARTICLE INTERACTIONS

Asphalt mastic, as a critical component in asphalt mixture composites, plays an indispensable role in determining the overall service performance of the mixture. Chapter 3 investigated the interaction between bitumen and filler from a multi-scale perspective, encompassing molecular and macroscopic levels, and elucidated the underlying mechanisms and macroscopic characteristics of this interaction, which provides a foundation for understanding the cohesive failure mechanisms at the bitumen-filler interface and the adhesive failure mechanisms at the mastic-aggregate interface. Chapter 4 further explored the service performance of asphalt mastic through a combination of macroscopic and microscopic experiments, employing multifactor statistical analysis to qualitatively analyse the relationship between the mastic's performance and its compositional structure. Building on these findings, this chapter continues to focus on establishing the quantitative composition-performance relationship of asphalt mastic by leveraging micromechanics theory to develop a cross-scale relationship between the macroscopic performance (modulus) of the mastic and its compositional structure.

Micromechanics theory, as a research tool that bridges the microstructure, compositional characteristics, and interfacial constitutive behaviour of composite materials, provides a robust framework for constructing cross-scale composition-performance relationships in asphalt mastic composites. As a typical multiphase particulate composite material, the particles within asphalt mastic and asphalt mixtures exhibit varying interactions under different loading and environmental conditions. Establishing a quantitative relationship between microstructural parameters and macroscopic mechanical performance to enable accurate performance prediction has long been a focal point in pavement engineering research. This chapter, grounded in micromechanics theory, employs five classical micromechanical models and the recently proposed Ju-Chen model to construct the relationship between the macroscopic properties and structural parameters of asphalt mastic, with the aim of estimating its complex shear modulus. Furthermore, the Ju-Chen model is enhanced by incorporating the Percus-Yevick function to solve the radial distribution function between particles, thereby effectively accounting for particle interactions. By revealing the quantitative relationship between the modulus property and compositional structure of asphalt mastic, this chapter aims to provide guidance for the design of high-performance mastic and to enhance the service durability of road infrastructure.

5.1 Materials and Methodology

5.1.1 Materials and sample preparation

To investigate the effects of bitumen origins on the micromechanical prediction of asphalt mastics, five sources of base bitumen and five kinds of fillers were adopted in this study. The material scheme used in this chapter is the same as that in Chapter 4. Five base bitumen including A (JB70#), B (ZH70#), C (YN70#), D (XJ70#), and E (XJ90#), and five kinds of fillers including granite, basalt, limestone, steel slag, and cement were adopted. For more detailed information on material properties and preparation methods of asphalt mastics, please refer to Chapter 4.1.1 Materials and specimen preparation above.

5.1.2 Classical micromechanical models

5.1.2.1 Homogenization theory

When predicting the macroscopic mechanical behaviours of heterogeneous composites such as bituminous materials using the continuum mechanics-based micromechanical models, its essence is to establish the correlation model between the properties of sub-phases, microstructural parameters, and the macroscopic behaviours of composites through the homogenization theory. The basic idea is to treat the composites as a homogeneous representative volume element that is filled with several sub-phases. As for the asphalt mastic composite, it is usually regarded as a two-phase composite, with the filler acting as the isotropic spherical inclusion and the asphalt serving as the matrix phase. Based on the distribution of asphalt and filler and the pertinent mechanical parameters, the effective modulus of the asphalt mastic composite is anticipated. The composite's effective stiffness tensor can be stated as follows in accordance with the homogenization theory [155]:

$$L_c = L^0 + \sum_{r=1}^{n} \phi_r \left(L^r - L^0 \right) A^r \tag{5-1}$$

Where L_c is the effective stiffness tensor of the *r*-phase composite; L^0 is the effective stiffness tensor of the matrix phase; L^r is the effective stiffness tensor of the *r*-th phase inclusions; ϕ_r is the volume fraction of the *r*-th phase composite; A^r is the strain localization tensor of the *r*-th phase composite. As mentioned before, asphalt mastic can be thought of as a two-phase composite. Thus equation (5-1) can be rewritten as follow:

$$L_c = L_b + \phi \left(L_f - L_b \right) A_r \tag{5-2}$$

Where L_c is the shear modulus of asphalt mastic composite; L_b is the shear modulus of bitumen as the matrix phase in asphalt mastic composite; L_f is the shear modulus of filler as the inclusion phase in asphalt mastic composite; ϕ is the volume fraction of filler in asphalt mastic; Subscripts *c*, *b*, and *f* denote asphalt mastic composite, binder, and filler, respectively. It can be seen from the above that the key to the prediction of the effective modulus of composite lies in the solution of the strain localization tensor A_r. Diverse micromechanical models were created to calculate the A_r, each according to Eshelby's ground-breaking solution for an elliptical or spherical inclusion embedded in an infinite matrix. In the section that follows, four popular micromechanical models for the two-phase composite will be introduced.

5.1.2.2 Dilute model (DM)

The DM assumes that the particles are sparsely distributed throughout the matrix. Since the spacing between the particles is much larger than their diameter, the interactions between the particles can be ignored. Following is the expression for the strain localization tensor A_r^{DM} in the DM [156]:

$$A_r^{DM} = \left[I + S_b \left(L_b \right)^{-1} (L_f - L_b) \right]^{-1} \tag{5-3}$$

Where S_b is Eshelby's tensor derived from the bitumen matrix's characteristics; *I* is the fourth-order unit tensor. The schematic illustration of DM is presented in Figure 5.1 (b).

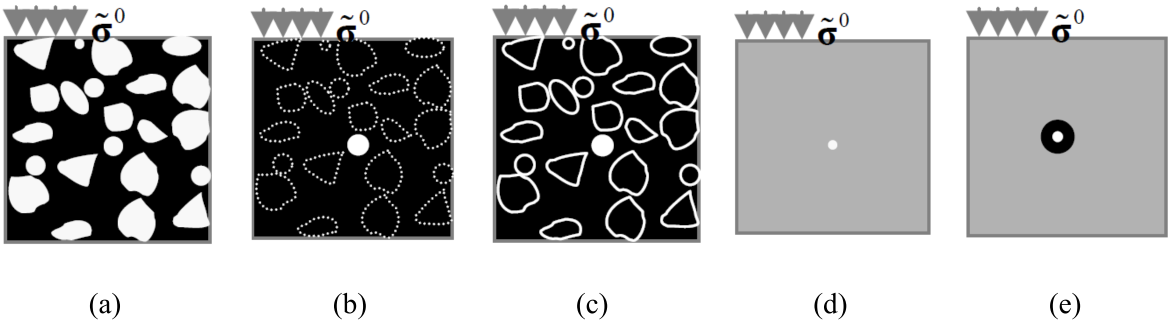

Figure 5.1 Schematic illustration for estimating averaged strain of the particle phase by four micromechanical models: (a) Actual mastic under external loading; (b) DM; (c) MTM; (d) SCM; (e) GSCM [78]

5.1.2.3 Mori-Tanaka model (MTM)

To consider the interaction between particles, the MTM assumes that each particle has an identical strain to the average strain of the matrix in which it is embedded. Thus, the strain localization tensor A_r^{MT} in the MTM can be calculated based on the A_r^{DM} [156]:

$$A_r^{MT} = A_r^{DM}\left[(1-\phi)I + \phi A_r^{DM}\right]^{-1} \tag{5-4}$$

The schematic illustration of MTM is presented in Figure 5.1 (c).

5.1.2.4 Self-consistent model (SCM)

According to the SCM, each particle inclusion is thought to be contained within an infinite homogeneous matrix whose modulus is the same as the effective modulus of the composite. The strain localization tensor A_r^{SC} in the SCM can be expressed as below [78]:

$$A_r^{SC} = \left[I + S_c\left(L_c\right)^{-1}\left(L_f - L_c\right)\right]^{-1} \tag{5-5}$$

Where S_c is Eshelby's tensor derived from the asphalt mastic composite's characteristics. It is worth noting that the solution formula of A_r^{SC} contains the effective modulus L_c of the composite, so it can only be solved by a recursive method, and the initial value is assumed to be that of the matrix. The schematic illustration of SCM is presented in Figure 5.1 (d).

5.1.2.5 General self-consistent model (GSCM)

According to the GSCM, a spherical particle is assumed to be embedded in a spherical ring of the matrix material, which is itself embedded in an infinite medium with effective mechanical properties of the composite. The strain localization tensor in the GSCM can be expressed as follows [78]:

$$A\left(\frac{G_c}{G_b}\right)^2 + 2B\left(\frac{G_c}{G_b}\right) + C = 0 \tag{5-6}$$

Where G_c is the shear modulus of asphalt mastic composite; G_b is the shear modulus of bitumen matrix; *A*, *B*, and *C* are the functions of the modulus and volume fraction of each sub-phases, and the specific expressions can be found in the literature [157, 158]. The schematic illustration of GSCM is presented in Figure 5.1 (e).

5.1.2.6 Differential model (DFM)

To avoid considering the interparticle interactions of inclusion, the DFM [159] develops a differential procedure for gradually incorporating inclusions into the bitumen matrix, that is, a cyclic iterative process is formed through a small amount of addition and homogenization. Moreover, Kim et al. [160] gave the corresponding formula for calculating the bulk modulus K_c and shear modulus L_c of asphalt mastic composite as follows:

$$K_c = K_f - (1-\phi)\left(K_f - K_b\right)\left(\frac{3K_c + 4L_c}{3K_0 + 4L_0}\right) \tag{5-7}$$

$$L_c = L_f - (1-\phi)\left(L_f - L_b\right)\left(\frac{L_c}{L_b}\right)^{0.4}\left(\frac{3K_c + 4L_c}{3K_0 + 4L_0}\right)^{0.2} \tag{5-8}$$

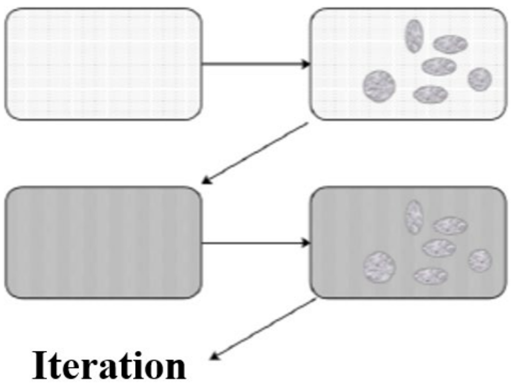

Figure 5.2 Schematic illustration of differential model (DFM) [161]

5.1.3 Micromechanical models considering interparticle interactions

5.1.3.1 Ju-Chen model (JCM)

The existing classical micromechanical models (DM, MTM, SCM, GSCM, and DFM) were all established based on the equivalent inclusion method proposed by Eshelby, which means that the inclusions are considered equivalent and have no mutual influence [162]. Hence, these models might also be referred to as single inclusion-based models. For composites with low particle volume fractions, these models can predict the properties of composites well. However, their applicability is significantly compromised for composites with medium and high particle volume fractions due to the inability of single-inclusion models to account for interparticle interactions. Therefore, this research adopted the micromechanical model proposed by Ju and Chen for two-phase composites that can consider interparticle interactions [163, 164]. The strategy of JCM is illustrated in Figure 5.3.

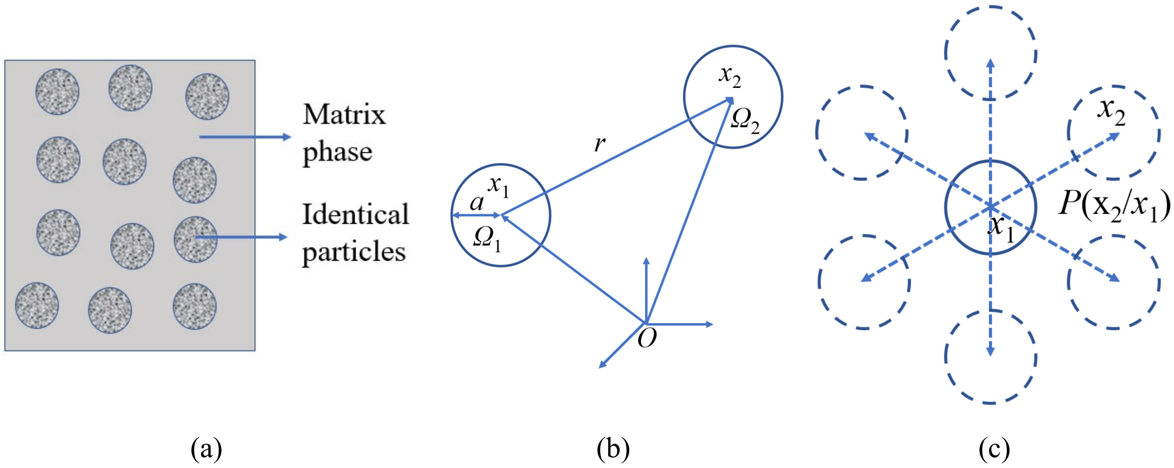

Figure 5.3 Schematic representation of JCM: (a) Two-phase particulate composite; (b) Pair-particle interaction; (c) Probabilistic pair-particle interaction

This scheme decomposes the n-particle interaction problem into two subproblems. At first, as depicted in Fig. 5.3 (b), an approximation of the pair interaction of two identical elastic spherical particles is proposed. Secondly, the conditional probability function $P(x_2/x_1)$ is introduced to solve the probabilistic pairwise particle interaction mechanism, as shown in Figure 1c. $P(x_2/x_1)$ refers to the probability of finding particle x_2 at any position when the position of particle x_1 is fixed, which is depended on the volume fraction and shape of inclusion particles. Assuming that all particles are statistically isotropic and uniform, the probability function can be written as follows:

$$P(x_2 / x_1) = \begin{cases} \frac{N}{V} g(r), r \geq 2a \\ 0, otherwise \end{cases} \tag{5-9}$$

Where $g(r)$ is the RDF; r is the distance between particle x_1 and particle x_2; a is the radius of the inclusion particle; N/V is the number density of particles in the composite, which has a connection with the particle volume fraction ϕ as follows:

$$\frac{N}{V} = \frac{4\pi a^3}{3\phi} \tag{5-10}$$

Finally, based on the coupling between the probabilistic pairwise particle interaction solution and the micromechanical field equation, equations in (5-11) and (5-12) can be used to represent the bulk modulus K_c and shear modulus G_c of the two-phase composites with identical spherical particles randomly dispersed in the matrix. The detailed derivation process can refer to the research of Ju and Chen [163, 164].

$$K_c = K_b + \frac{30(1-v_b)\phi(3\gamma_1 + 2\gamma_2)K_b}{3\alpha + 2\beta - 10(1+v_b)\phi(3\gamma_1 + 2\gamma_2)} \tag{5-11}$$

$$G_c = G_b + \frac{30(1-v_b)\phi\gamma_2 G_b}{\beta - 4(4-5v_b)\phi\gamma_2} \tag{5-12}$$

where v is the Poisson's ratio. The interim parameters α, β, γ_1, and γ_2 can be expressed as follows:

$$\alpha = 2(5v_b - 1) + 10(1-v_b)\left(\frac{K_b}{K_f - K_b} - \frac{G_b}{G_f - G_b}\right) \tag{5-13}$$

$$\beta = 2(4-5v_b) + 15(1-v_b) \times \frac{G_b}{G_f - G_b} \tag{5-14}$$

$$\gamma_1 = \frac{5\phi}{4\beta^2} Y(g)\xi_1 \tag{5-15}$$

$$\gamma_2 = \frac{1}{2} + \frac{5\phi}{4\beta^2} Y(g) \xi_2 \tag{5-16}$$

where:

$$\xi_1 = 12(13v_b - 14v_b{}^2) - \frac{96\alpha}{3\alpha + 2\beta}(1 - 2v_b)(1 + v_b) \tag{5-17}$$

$$\xi_2 = 6(25 - 34v_b + 22v_b{}^2) - \frac{36\alpha}{3\alpha + 2\beta}(1 - 2v_b)(1 + v_b) \tag{5-18}$$

$$Y(g) = \int_{2a}^{\infty} \frac{a^3}{r^4} g(r) dr = \int_{0}^{0.5} \rho^2 g(\rho) d\rho \tag{5-19}$$

where $\rho = a/r$. It is not difficult to find that, except for the RDF g(r), all parameters in the computational process of K_c and G_c have been given. Therefore, the following sections will discuss the g(r) of asphalt mastic composite in detail.

5.1.3.2 Modified Ju-Chen model (MJCM)

The radial distribution function (RDF) $g(r)$ is defined as the probability of finding other atoms distributed in space given a certain type of atom as the centre, describing how density varies with the distance from the reference particle. The RDF of hard-sphere systems holds a very important position in modern liquid theory, and researchers have conducted extensive studies on it. Wertheim [165] first proposed an analytical expression for the radial distribution function of hard spheres based on the Percus-Yevick equation, but this expression requires the potential function to have an inverse Laplace transform. Troop et al. [166] proposed a method for calculating the radial distribution function of hard spheres in spatial coordinates and provided numerical results in tabular form, although the table cannot encompass all volume fractions and distance parameters. In China, Sun and Yuan et al. [64] rederived the analytical expression for the radial distribution function of hard spheres in coordinate space. This study adopts the above research results and calculates the radial distribution function $g(r)$ within the asphalt mastic composite system based on the Percus-Yevick equation, as shown below:

$$\tilde{g}(r)=\begin{cases} 0,1\le r/2a \\ H(r-1)\times \tilde{g}_1(r)+H(r-2)\times \tilde{g}_2(r)+H(r-3)\times \tilde{g}_3(r),1<r/2a<4 \\ 1,r/2a\ge 4 \end{cases} \quad (5\text{-}20)$$

where *H(r-n)* is the Heaviside function; $\tilde{g}_1(r)$, $\tilde{g}_2(r)$ and $\tilde{g}_3(r)$ are the functions of the volume fraction and spacing between particles, and the specific expressions can be found in the literature [64]. Based on equation (5-20), the normalized RDF $\tilde{g}(r)$ at different volume fractions ϕ and *r/2a* can be computed. Figure 5.4 presents the $\tilde{g}(r)$ at five ϕ of 0.05, 0.15, 0.30, 0.45, and 0.60. From the figure, as the decrease of ϕ and the increase of *r/2a*, $\tilde{g}(r)$ gradually approaches 1.

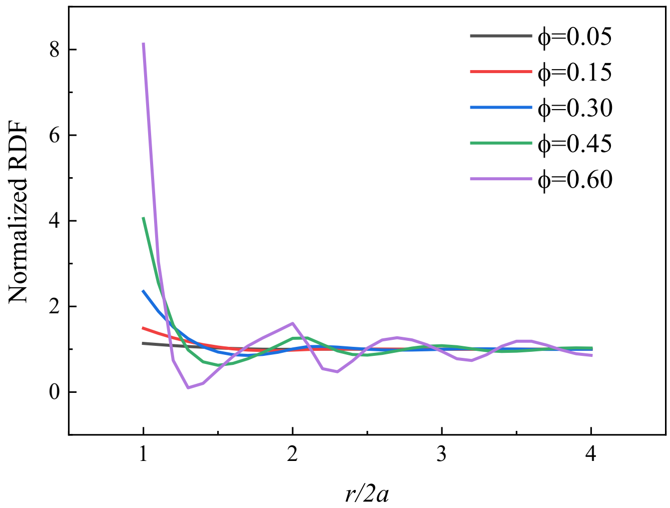

Figure 5.4 Normalized RDF at four volume fractions of 0.05, 0.15, 0.30, 0.45, and 0.60

By substituting equations (5-20) and (5-19) into equations (5-15) and (5-16), the updated expressions for parameters γ_1 and γ_2 can be obtained as below:

$$\gamma_1 = \frac{5\phi}{4\beta^2} * (\int_0^{0.125} \rho^2 g(\rho) d\rho + \int_{0.125}^{0.5} \rho^2 g(\rho) d\rho) * \xi_1 = \frac{5\phi}{4\beta^2} * (k + \int_{0.125}^{0.5} \rho^2 \tilde{g}(\frac{1}{2\rho}) d\rho) * \quad (5\text{-}21)$$

$$\gamma_2 = \frac{1}{2} + \frac{5\phi}{4\beta^2} * (k + \int_{0.125}^{0.5} \rho^2 \tilde{g}(\frac{1}{2\rho}) d\rho) * \xi_2 \quad (5\text{-}22)$$

Where $k = \int_0^{0.125} \rho^2 g(\rho) d\rho$, $g(\rho) = 1$ in this interval, so k is a constant. Finally, based on formulas (5-11) ~ (5-14) and formulas (5-17) ~ (5-22), the K_c and G_c of asphalt mastics can be further calculated. It is worth mentioning that the Ju-Chen model was selected as our foundation due to its feasible consideration of particle-particle interactions in composite systems, making it well-suited for predicting the modulus of complex, heterogeneous materials such as asphalt mixtures. However, its original formulation lacks a precise solution for the RDF, which is essential for accurately capturing local particle packing and microstructure. To address this limitation, we specifically modified the model to improve its RDF solving. The model's framework facilitated this enhancement, resulting in significantly improved prediction accuracy.

5.1.4 Experimental methods

5.1.4.1 Dynamic shear rheometer test

The frequency sweep test was conducted to measure the complex shear modulus of bitumen and asphalt mastics by DSR (ARES G2, TA Company, USA). The temperature ranged from 0 to 84°C with an interval of 12°C, and the frequency range was 0.1~30Hz. The reference temperature was determined to be 48°C, and the test results at other test temperatures were translated to the reference temperature to synthesize the complex modulus master curves of asphalt mastics. The Williams-Landel-Ferry (WLF) equation was used to compute the shift factors, as indicated below [167]:

$$\log \alpha_T(T) = \frac{-C_1(T - T_{ref})}{C_2 + (T - T_{ref})} \tag{5-23}$$

where $\alpha_T(T)$ is the shift factor; C_1 and C_2 are the regression coefficients; T and T_{ref} correspond to the test temperature and reference temperature, respectively. Moreover, the master curves of complex modulus were fitted using the Christensen-Anderson-Marasteanu (CAM) model [168], as illustrated below:

$$G^* = \frac{G_g}{\left[1 + \left(w_c / w_r\right)^v\right]^{w/v}} \tag{5-24}$$

Where G^* is the complex modulus, Pa; G_g is the glass complex shear modulus, Pa; w_c is the crossover frequency, rad/s; w_r is the reduced frequency, rad/s; w and v are the fitting coefficients.

5.1.4.2 Goodness-of-fit statistics of models

The models utilized in this work were subjected to goodness-of-fit statistics so as to quantitatively compare the prediction accuracy of several micromechanical models on the complex modulus of asphalt mastics. Two statistical indicators of S_e/S_y and R^2 were calculated as follows [156, 169]:

$$S_y = \sqrt{\frac{\sum_{i=1}^{n} (G_{mi}^* - \bar{G}_m^*)^2}{n}} \tag{5-25}$$

$$S_e = \sqrt{\frac{\sum_{i=1}^{n} (G_{pi}^* - G_{mi}^*)^2}{n-k}} \tag{5-26}$$

$$R^2 = 1 - \frac{n-k}{n-1}\left(\frac{S_e}{S_y}\right)^2 \tag{5-27}$$

Where n is the number of data points; G_{mi}^* and G_{pi}^* are the measured and predicted shear moduli of asphalt mastics, respectively; $\overline{G}_m^*$ is the average value of measured shear modulus; k is the number of independent variables in the models. S_y is the standard deviation of the measured shear modulus; S_e is the standard error; S_e/S_y is the relative prediction error; R^2 is the coefficient of determination. The lower the S_e/S_y and the higher the R^2, the higher the prediction accuracy of models [156].

5.2 Results and Discussion

5.2.1 Dynamic shear rheometer test results of asphalt mastics

Figure 5.5 illustrates the complex modulus master curves of the asphalt mastics. As depicted in the figures, the incorporation of fillers results in a notable upward shift in the complex modulus master curves of the bitumen. This indicates that the addition of fillers effectively hardens the bitumen, thereby improving its high-temperature performance while simultaneously compromising its low-temperature performance. Furthermore, it is important to highlight that, under the bitumen-filler mass ratio employed in this study (1:1), the complex modulus master curves of different asphalt mastics derived from the same base bitumen exhibit minimal variation.

Figure 5.6 presents the phase angle master curves of the asphalt mastics. It can be found from the figures that the phase angle master curves of bitumen and asphalt mastics basically coincide, which indicates that the use of fillers has little effect on the phase angle of bitumen. To conclude, under the bitumen-filler mass ratio selected in this study, the master curves of complex modulus and phase angle of asphalt mastics based on the same type of base bitumen basically coincide, which shows that the filler types have little influence on the master curves. Therefore, the following research can better consider the effects of filler types and bitumen origins on the accuracy of different micromechanical models.

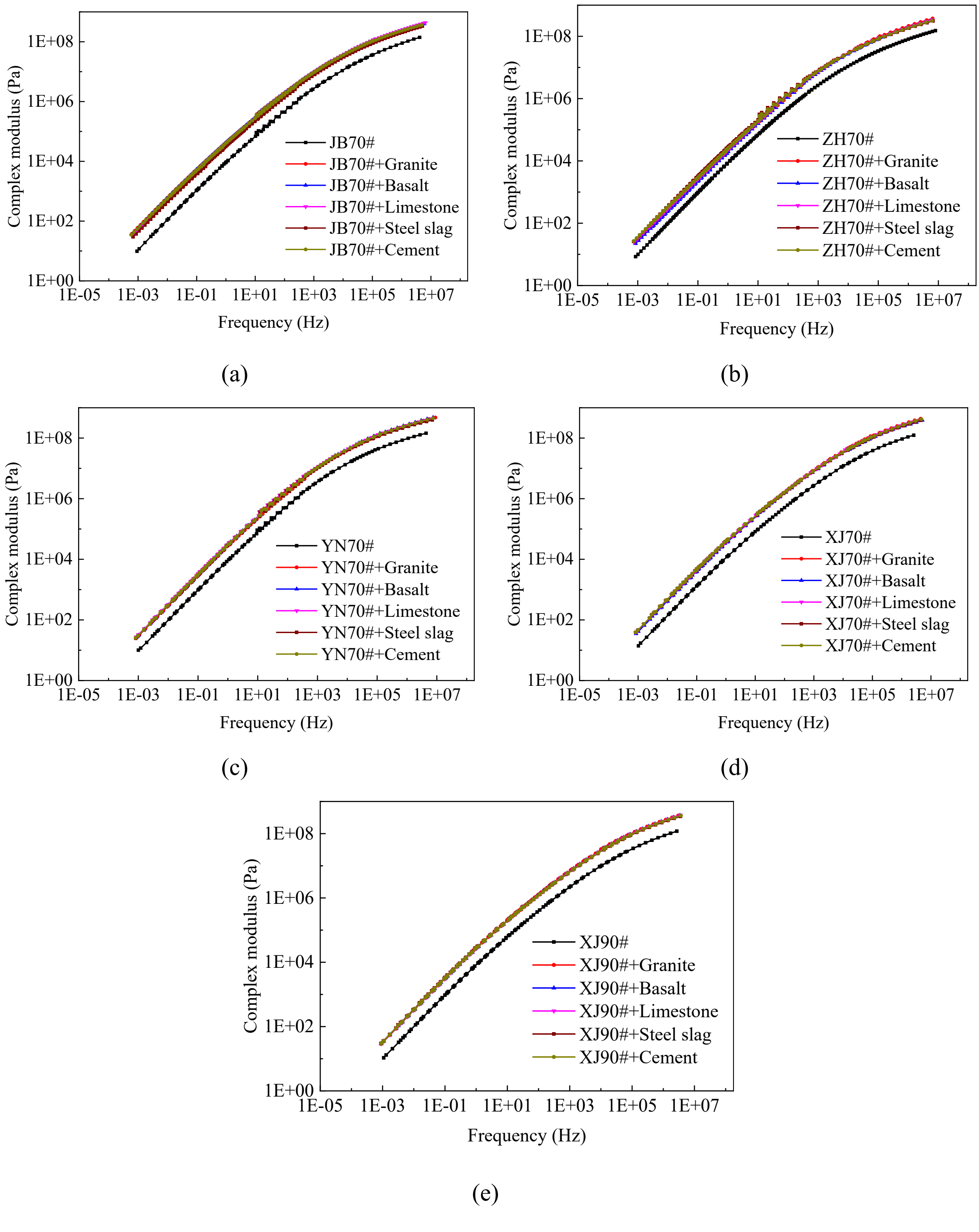

Figure 5.5 Complex modulus master curves of the asphalt mastics: (a) JB70#; (b) ZH70#; (c) YN70#; (d) XJ70#; (e) XJ90#

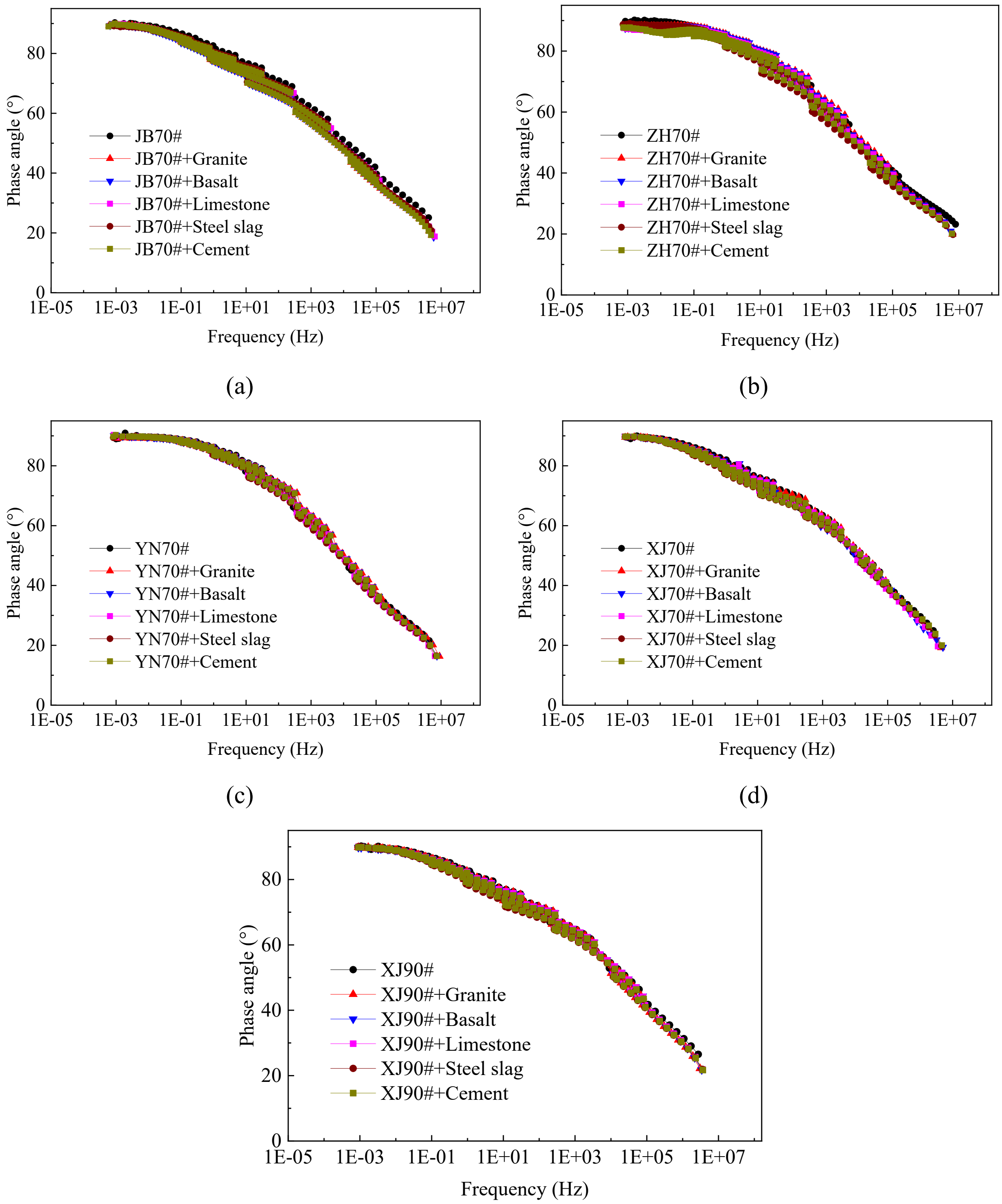

(e)

Figure 5.6 Phase angle master curves of the asphalt mastics: (a) JB70#; (b) ZH70#; (c) YN70#; (d) XJ70#; (e) XJ90#

5.2.2 Prediction results of asphalt mastics by classical micromechanical models

5.2.2.1 Comparison of classical models considering the effects of bitumen origins

Considering that many filler types were employed in this study, we only take granite as an example and discuss the prediction results of the micromechanical models of the asphalt mastics. Figure 5.7 presents the comparison between the complex modulus master curves of granite asphalt mastics predicted by different classical micromechanical models based on five bitumen origins. It is found from the figures that the existing micromechanical models exhibit inconsistent fitting effects based on various base bitumen. Firstly, in the high-frequency (low-temperature) region, the DM overestimates the complex modulus of each asphalt mastic. In the low-frequency (high-temperature) region, DM only underestimates the complex modulus of JB70# asphalt mastic, and the predicted modulus of DM is close to the experimental modulus for the other four asphalt mastics. The difference in the prediction accuracy of the DM is mainly reflected in the high-frequency (low-temperature) region, and the difference between the predicted modulus and the measured modulus in ZH70# and YN70# asphalt mastics is significantly greater than that in XJ70# and XJ90# asphalt mastics, which indicates that DM exhibits higher accuracy in XJ70# and XJ90#. For the three micromechanical models of the MTM, SCM, and DFM, they underestimate the complex modulus of all asphalt mastics in the whole frequency domain.

Furthermore, the gap between the predicted modulus and the experimental modulus for these three models in XJ70# and XJ90# asphalt mastics is significantly larger than that in JB70#, ZH70#, and YN70# asphalt mastics, which indicates that these three models exhibit higher accuracy in JB70#, ZH70#, and YN70#. In addition, it is not difficult to find that the accuracy of DFM is the lowest among the five models. For the GSCM, it underestimates the complex modulus of all asphalt mastics in the low-frequency (high-temperature) region. In the high-frequency (low-temperature) region, the predicted modulus of GSCM in the three asphalt mastics of JB70#, ZH70#, and YN70# is close to the experimental modulus, while the predicted modulus of GSCM is significantly lower than the experimental modulus in the other two kinds of asphalt mastics (XJ70# and XJ90#).

According to the effects of existing micromechanical models on base bitumen, two groups can be made from the five base bitumen employed in this study: the first group consists of JB70#, ZH70#, and YN70# with higher low-temperature moduli (PG 64-22), while the second group consists of XJ70# and XJ90# with lower low-temperature moduli (PG 64-28). The following research refers to the first group of bitumen as PG 64-22 and the second group as PG 64-28. To conclude, DM overestimates the complex modulus of each asphalt mastic in the high-frequency (low-temperature) region and exhibits higher accuracy in PG 64-28. GSCM underestimates the complex modulus of all asphalt mastics in the low-frequency (high-temperature) region and demonstrates higher accuracy in PG 64-22. MTM, SCM, and DFM underestimate the complex modulus of all asphalt mastics in the entire frequency domain and exhibit higher accuracy in PG 64-22. It is found that GSCM has the highest precision, and DFM has the lowest accuracy among the five micromechanical models.

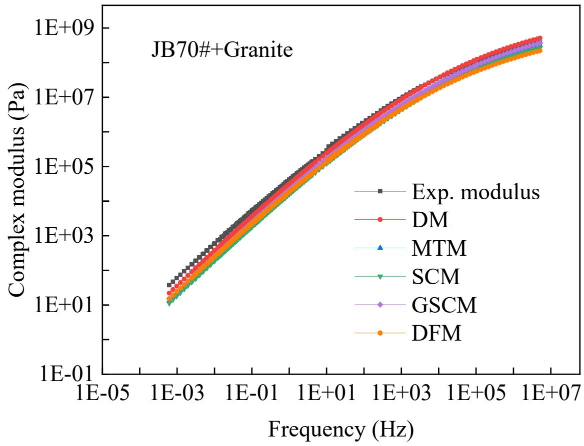

(a)

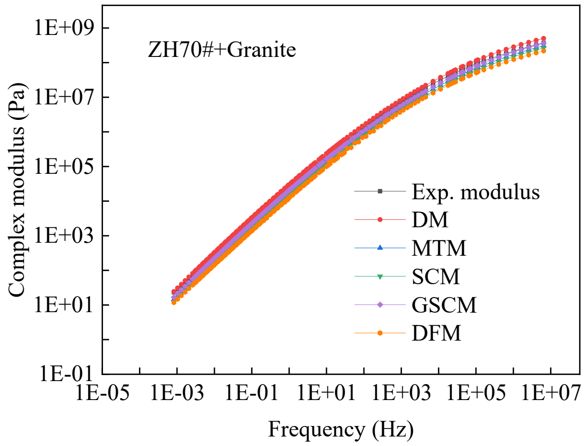

(b)

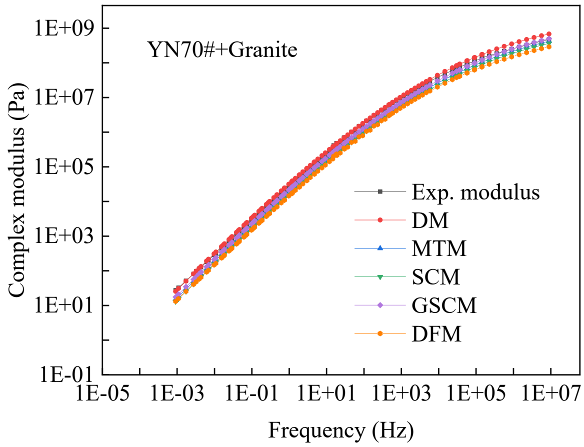

(c)

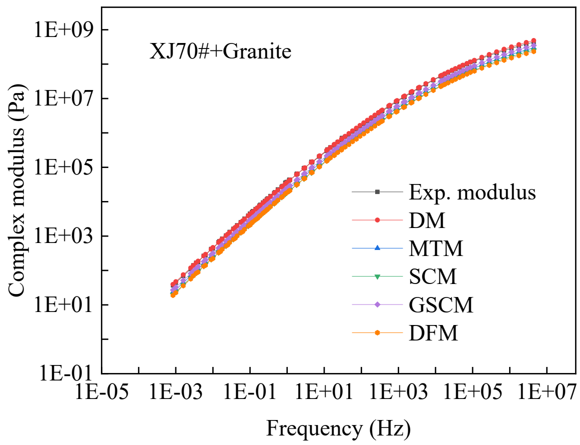

(d)

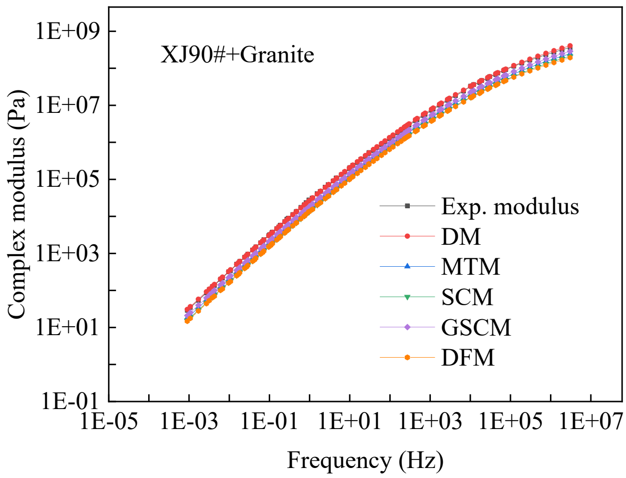

(e)

Figure 5.7 Comparison between complex modulus master curves of granite asphalt mastics predicted by different models based on base bitumen of (a) JB70#; (b) ZH70#;(c) YN70#; (d) XJ70#; (e)XJ90#

Table 5-1 lists the goodness-of-fit statistics results of granite asphalt mastics predicted by different micromechanical models. When the goodness of fit (R^2) is below 0.9, it is marked in bold in the table. It can be found that, as analysed above, GSCM exhibits the best accuracy, with the lowest R^2 of 0.938 and highest S_e/S_y of 0.248 in five kinds of asphalt mastics. Especially for the PG 64-22 (JB70#, ZH70#, and YN70#), the R^2 of GSCM is close to 0.990 and the S_e/S_y is lower than 0.11. Among the five micromechanical models, the accuracy of DFM is the lowest, with the highest R^2 of 0.810 and lowest S_e/S_y of 0.438 at YN70#+Granite. The R^2 of DFM fails to reach 0.75 and S_e/S_y is higher than 0.51 at PG 64-28 (XJ70# and XJ90#). For DM, it exhibits excellent accuracy in PG 64-28 (XJ70# and XJ90#), with R^2 higher than 0.99 and S_e/S_y lower than 0.11. However, for the other three bitumen of PG 64-22, the R^2 of DM fails to exceed 0.9 and S_e/S_y is higher than 0.33. In addition, the R^2 of SCM in PG 64-22 is also greater than that in PG 64-28, and the Se/Sy is lower than that of PG 64-28.

To conclude, it is not difficult to find that the accuracy of different micromechanical models depends to a certain extent on the origins of base bitumen. DM exhibits higher accuracy in XJ70# and XJ90#. In contrast, the other four models (MTM, SCM, GSCM, and DFM) indicate higher accuracy in the other three base bitumen of JB70#, ZH70#, and YN70#. Nevertheless, in general, among the five micromechanical models, GSCM has the highest accuracy, and DFM has the lowest accuracy, which is entirely consistent with the analysis conclusion above. The authors believe that the interparticle interactions between fillers are not very strong under the filler-bitumen ratio selected in this study (1:1). Thus, GSCM can predict the complex modulus of asphalt mastics relatively well. In addition, among these classical micromechanical models, the assumption of GSCM can most accurately characterize the microstructure of asphalt mastics at this filler-bitumen ratio.

Table 5-1 Goodness-of-fit statistics of granite asphalt mastics predicted by different models

Models	Asphalt mastics	Se/Sy	R^2
DM	JB70#+Granite	0.329	**0.892**
	ZH70#+Granite	0.348	**0.880**
	YN70#+Granite	0.445	**0.804**
	XJ70#+Granite	0.108	0.989
	XJ90#+Granite	0.100	0.990
MTM	JB70#+Granite	0.242	0.942
	ZH70#+Granite	0.210	0.956
	YN70#+Granite	0.164	0.973
	XJ70#+Granite	0.364	**0.869**
	XJ90#+Granite	0.369	**0.865**
SCM	JB70#+Granite	0.354	**0.875**
	ZH70#+Granite	0.324	**0.896**
	YN70#+Granite	0.285	0.920
	XJ70#+Granite	0.461	**0.790**
	XJ90#+Granite	0.465	**0.786**
GSCM	JB70#+Granite	0.113	0.987
	ZH70#+Granite	0.074	0.995
	YN70#+Granite	0.066	0.996
	XJ70#+Granite	0.240	0.942
	XJ90#+Granite	0.248	0.938
DFM	JB70#+Granite	0.467	**0.783**
	ZH70#+Granite	0.447	**0.802**
	YN70#+Granite	0.438	**0.810**
	XJ70#+Granite	0.512	**0.740**
	XJ90#+Granite	0.513	**0.739**

Furthermore, this study averaged the goodness-of-fit statistics of the micromechanical models of five asphalt mastics consisting of each type of filler to comprehensively consider the effect of bitumen origins on the accuracy of each model. Figure 5.8 compares the average values of goodness-of-fit statistics of micromechanical models based on different bitumen origins. From the figures, the conclusion drawn from the average values of goodness-of-fit statistics is entirely consistent with that of granite asphalt mastics above. DM exhibits higher accuracy in PG 64-28 (XJ70# and XJ90#), while the other four models (MTM, SCM, GSCM, and DFM) exhibit higher accuracy in PG 64-22 (JB70#, ZH70#, and YN70#). Among the five micromechanical models, the most accurate is GSCM, followed by DM and MTM, DFM is the least accurate, and SCM is the second least accurate.

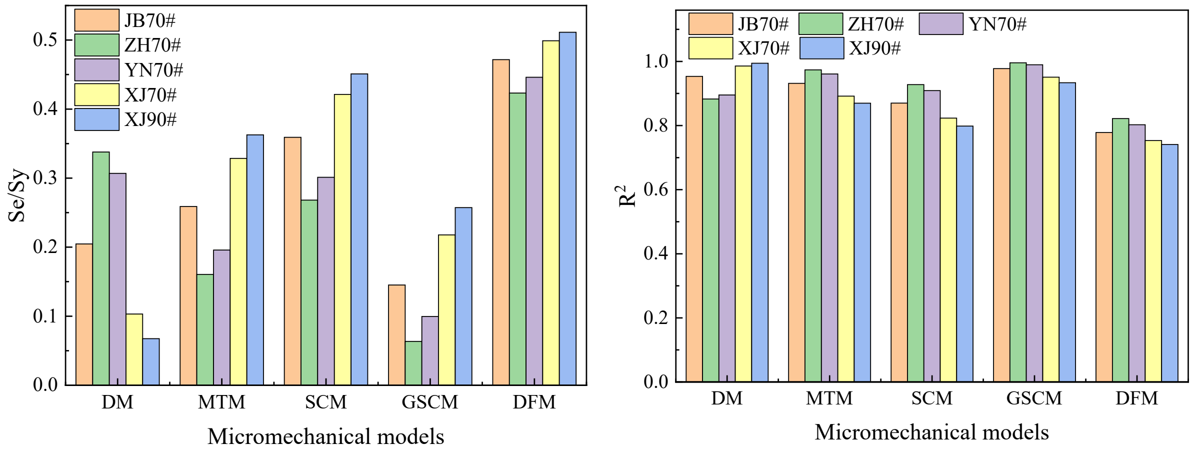

(a) (b)

Figure 5.8 Comparison between the average values of goodness-of-fit statistics of micromechanical models based on different bitumen origins: (a) Se/Sy; (b) R^2

5.2.2.2 Comparison of classical models considering the effects of filler types

Similarly, considering that many bitumen origins were adopted in this study, we only take ZH70# (one of PG 64-22) and XJ90# (one of PG 64-28) as examples and discuss the prediction results of the micromechanical models of the asphalt mastics consisting of these two bitumen origins and five kinds of fillers in this section. The above discussion results also confirm that the existing micromechanical models exhibit different accuracy in these two groups of bitumen. Therefore, this study selects one bitumen from each of these two groups of bitumen for discussion.

Figure 5.9 presents the comparison between complex modulus master curves of ZH70# asphalt mastics predicted by different models based on five fillers. Firstly, DM overestimates the complex modulus of all ZH70# asphalt mastics in the high-frequency (low-temperature) region. For MTM, SCM, and DFM, these three models underestimate the complex moduli of all asphalt mastics in the whole frequency domain. For GSCM, it underestimates the complex modulus of ZH70# asphalt mastics in the low-frequency (high-temperature) region, and its predicted modulus is close to the experimental modulus in the high-frequency (low-temperature) region.

This is because ZH70# belongs to PG 64-22, consistent with the previous conclusion.

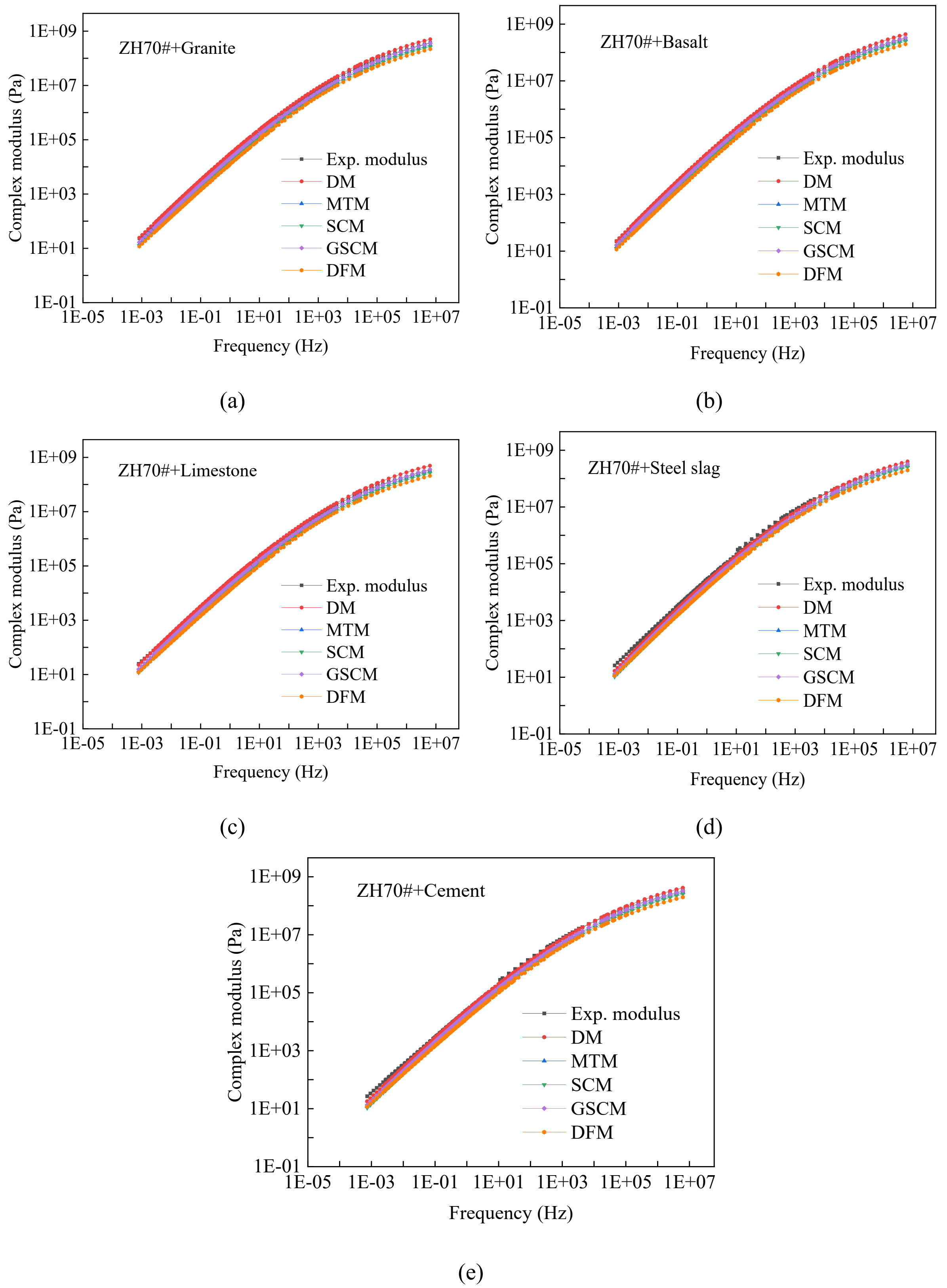

Figure 5.9 Comparison between complex modulus master curves of ZH70# asphalt mastics predicted by different models based on fillers of (a) Granite; (b) Basalt;(c) Limestone; (d) Steel slag; (e) Cement

Table 5-2 lists the goodness-of-fit statistics results of ZH70# asphalt mastics predicted by different micromechanical models. From the table, except for GSCM, which achieves excellent accuracy in all ZH70# asphalt mastics, the rest of the micromechanical models achieve the worst accuracy on ZH70#+Granite. This is due to the highest volume fraction of granite among the five fillers in the asphalt mastics, resulting in the greatest interaction between filler particles. In addition, in most cases, all micromechanical models achieve the highest accuracy on ZH70#+Steel slag, which is manifested by lower S_e/S_y and higher R^2. This is also due to the lowest volume fraction of steel slag among the five fillers in the asphalt mastics. In the final analysis, the effects of filler types on the accuracy of micromechanical models depend primarily on their volume fractions.

Table 5-2 Goodness-of-fit statistics of ZH70# asphalt mastics predicted by different models

Models	Asphalt mastics	Se/Sy	R^2
DM	ZH70#+Granite	0.348	**0.880**
	ZH70#+Basalt	0.368	**0.865**
	ZH70#+Limestone	0.434	**0.813**
	ZH70#+Steel slag	0.261	0.932
	ZH70#+Cement	0.278	0.923
MTM	ZH70#+Granite	0.210	0.956
	ZH70#+Basalt	0.136	0.982
	ZH70#+Limestone	0.154	0.977
	ZH70#+Steel slag	0.145	0.979
	ZH70#+Cement	0.157	0.975
SCM	ZH70#+Granite	0.324	**0.896**
	ZH70#+Basalt	0.248	0.939
	ZH70#+Limestone	0.273	0.926
	ZH70#+Steel slag	0.239	0.943
	ZH70#+Cement	0.258	0.934
GSCM	ZH70#+Granite	0.074	0.995
	ZH70#+Basalt	0.049	0.998
	ZH70#+Limestone	0.053	0.997
	ZH70#+Steel slag	0.075	0.994
	ZH70#+Cement	0.067	0.995
DFM	ZH70#+Granite	0.447	**0.802**
	ZH70#+Basalt	0.415	**0.829**
	ZH70#+Limestone	0.425	**0.821**
	ZH70#+Steel slag	0.410	**0.833**
	ZH70#+Cement	0.420	**0.825**

Figure 5.10 presents the comparison between complex modulus master curves of XJ90# asphalt mastics predicted by different models based on five fillers. Since XJ90# is PG 64-28, DM exhibits excellent accuracy in all XJ90# asphalt mastics. For MTM, SCM, GSCM, and DFM, these four micromechanical models underestimate the complex moduli of all asphalt mastics in the entire frequency domain. The four models' accuracy rankings are as follows: GSCM is the most accurate, DFM is the least accurate.

Table 5-3 lists the goodness-of-fit statistics results of XJ90# asphalt mastics predicted by different micromechanical models. As analysed above, DM shows the highest accuracy among five micromechanical models, with all R^2 above 0.99 and all S_e/S_y under 0.11. The accuracy of GSCM is only inferior to DM, with a minimum R^2 of 0.925 and a maximum S_e/S_y of 0.274. In addition, the effect of filler types on the prediction accuracy of micromechanics was not found in the two models. Among the other three models (MTM, SCM, and DFM), it is not difficult to find that these three models have the highest prediction accuracy in XJ90#+Steel slag and the lowest accuracy in XJ90#+Granite. As mentioned above, different filler types correspond to different volume concentrations in asphalt mastics, leading to differences in the interactions between filler particles.

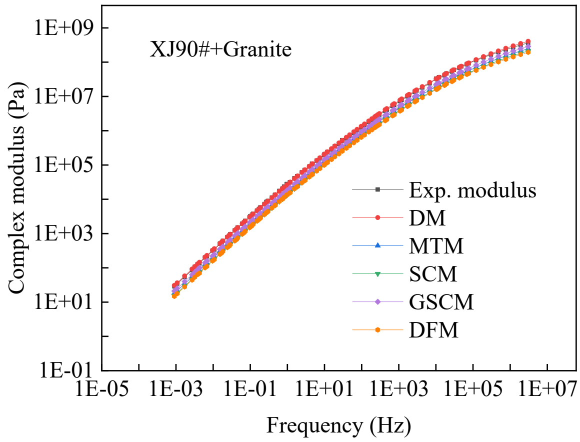

(a)

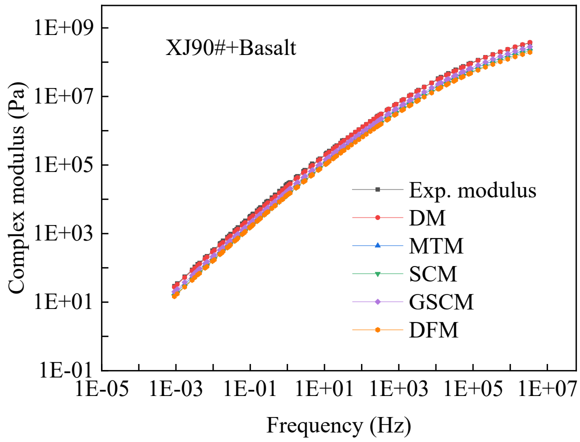

(b)

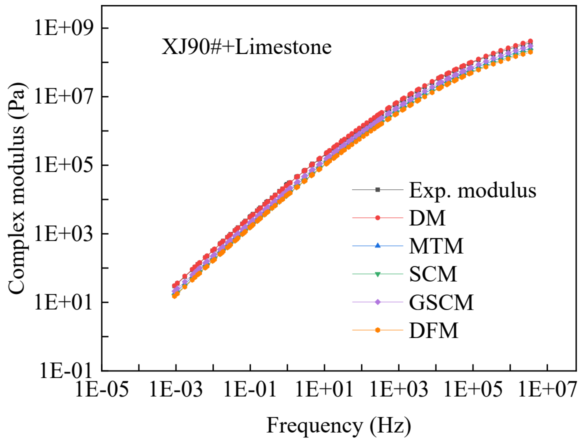

(c)

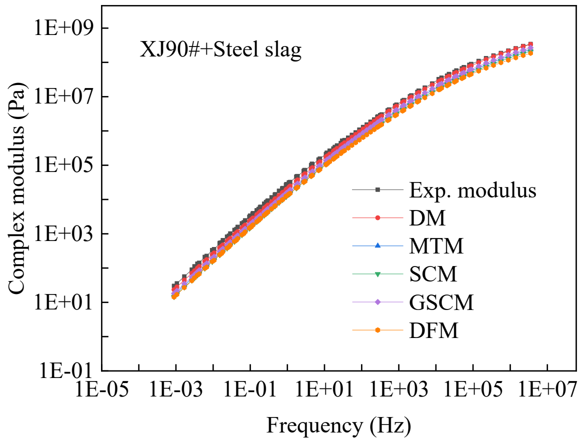

(d)

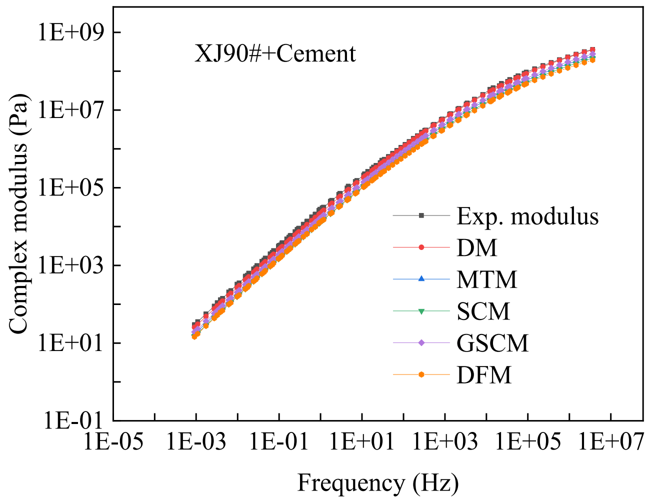

(e)

Figure 5.10 Comparison between complex modulus master curves of XJ90# asphalt mastics predicted by different models based on fillers of (a) Granite; (b) Basalt;(c) Limestone; (d) Steel slag; (e) Cement

Table 5-3 Goodness-of-fit statistics of XJ90# asphalt mastics predicted by different models

Models	Asphalt mastics	Se/Sy	R^2
DM	XJ90#+Granite	0.100	0.990
	XJ90#+Basalt	0.026	0.999
	XJ90#+Limestone	0.108	0.989
	XJ90#+Steel slag	0.058	0.997
	XJ90#+Cement	0.045	0.998
MTM	XJ90#+Granite	0.369	**0.865**
	XJ90#+Basalt	0.370	**0.864**
	XJ90#+Limestone	0.356	**0.874**
	XJ90#+Steel slag	0.351	**0.878**
	XJ90#+Cement	0.367	**0.866**
SCM	XJ90#+Granite	0.465	**0.786**
	XJ90#+Basalt	0.458	**0.792**
	XJ90#+Limestone	0.453	**0.797**
	XJ90#+Steel slag	0.430	**0.817**
	XJ90#+Cement	0.449	**0.800**
GSCM	XJ90#+Granite	0.248	0.938
	XJ90#+Basalt	0.265	0.930
	XJ90#+Limestone	0.235	0.945
	XJ90#+Steel slag	0.264	0.930
	XJ90#+Cement	0.274	0.925
DFM	XJ90#+Granite	0.513	**0.739**
	XJ90#+Basalt	0.514	**0.738**
	XJ90#+Limestone	0.508	**0.744**
	XJ90#+Steel slag	0.507	**0.745**
	XJ90#+Cement	0.514	**0.738**

Similarly, this study averaged the goodness-of-fit statistics of the micromechanical models of five asphalt mastics consisting of each base bitumen to comprehensively consider the effect of filler types on the accuracy of each model. Figure 5.11 compares the average values of goodness-of-fit statistics of micromechanical models based on different filler types. For DM, steel slag and cement asphalt mastics exhibit the best prediction accuracy, while granite and limestone asphalt mastics show the worst prediction accuracy, which is because steel slag and cement are the two with the lowest volume fractions in asphalt mastics among the five fillers, while granite and limestone are the two with the highest volume fractions. In addition, steel slag asphalt mastic exhibits the best prediction accuracy on MTM, SCM, and DFM, which may be because steel slag corresponds to the lowest volume fraction in asphalt mastics among the five fillers. For GSCM, the types of filler do not seem to significantly impact its prediction accuracy, which is consistent with the previous conclusions. It was also not found that the filler types significantly impacted the prediction accuracy of GSCM in the ZH70# and XJ90# asphalt mastics above.

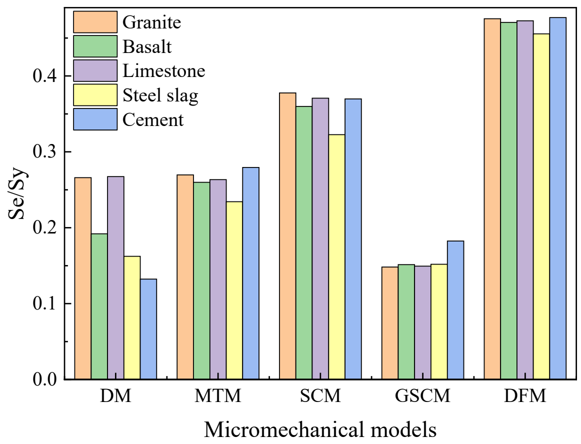

(a)

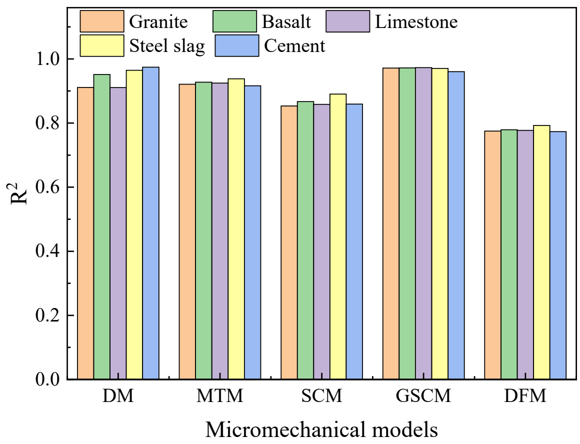

(b)

Figure 5.11 Comparison between the average values of goodness-of-fit statistics of micromechanical models based on different filler types: (a) Se/Sy; (b) R^2

5.2.3 Prediction results of asphalt mastics by micromechanical models considering interparticle interactions

5.3.3.1 Comparison of advanced models considering the effects of bitumen origins

Figure 5.12 presents the comparison between the complex modulus master curves of granite asphalt mastics predicted by the GSCM and JCM based on five bitumen origins. To compare the classical micromechanical models with JCM and MJCM more effectively, the classical micromechanical model with the highest accuracy, GSCM, was selected as the representative and plotted on the graphs. It is important to note that the JCM here assumes that filler particles are uniformly distributed within the asphalt mastic composite and that the filler volume fraction is very low. Under this condition, $g(r)$ is equal to 1, and $Y(g)$ is equal to 1/24. The MJCM represents the modified Ju-Chen model, which incorporates the radial distribution function derived from the Percus-Yevick (P-Y) function, as previously described.

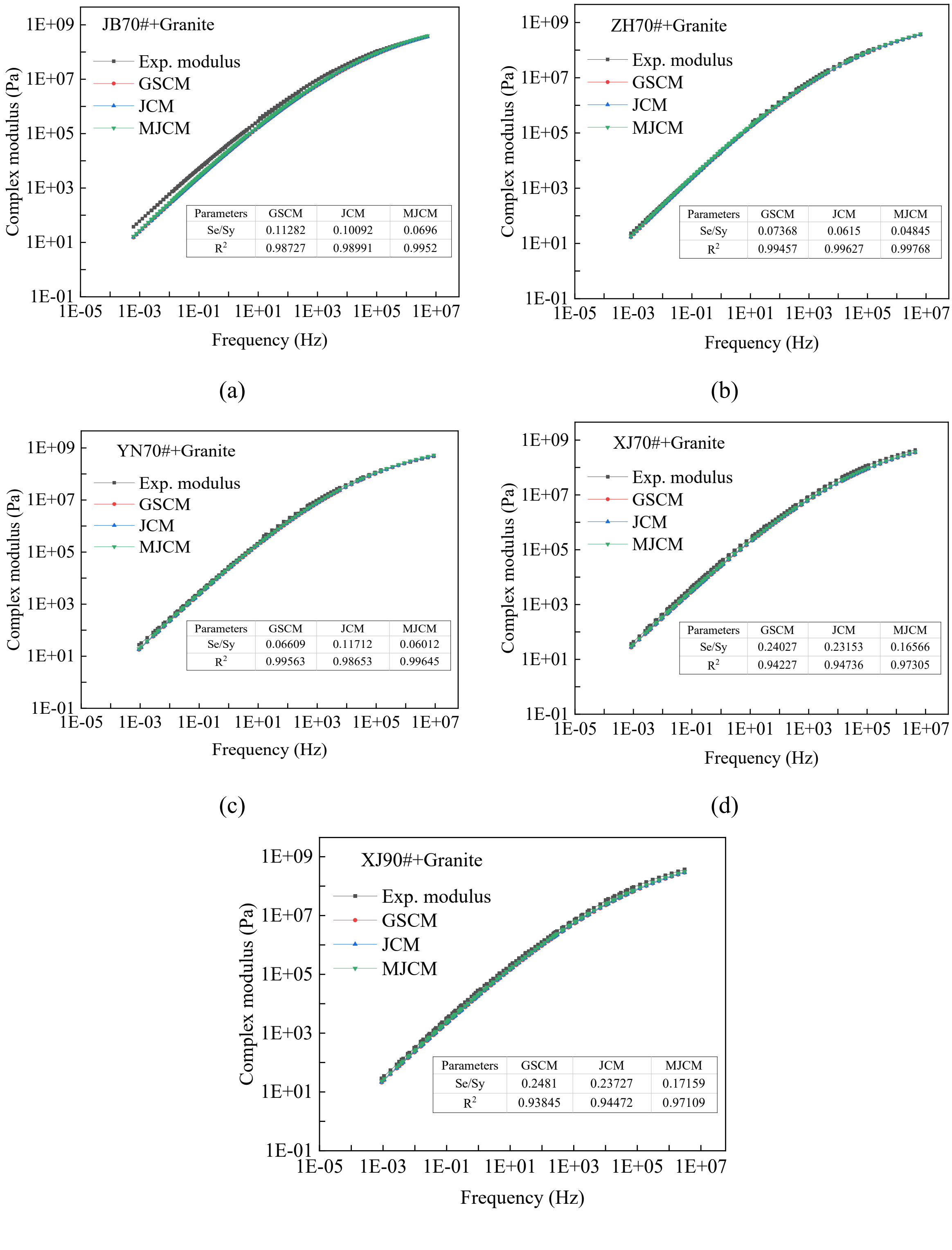

(e)

Figure 5.12 Comparison between complex modulus master curves of granite asphalt mastics predicted by GSCM and JCM based on base bitumen of (a) JB70#; (b) ZH70#;(c) YN70#; (d) XJ70#; (e)XJ90#

From Figure 5.12, the predicted moduli of JCM and MJCM are very close to that of GSCM, both exhibiting excellent accuracies. In comparison, the accuracies of JCM and GSCM are generally close, while MJCM demonstrates the best prediction accuracy among all granite asphalt mastics. In addition, the two JCMs also underestimate the complex modulus of asphalt mastics in the low-frequency (high-temperature) region, which is consistent with the GSCM model, and the underestimation degree of MJCM is smaller than that of JCM. Furthermore, it is worth noting that two JCMs exhibit dependence on bitumen origins. Specifically, JCM and MJCM exhibit higher prediction accuracy in PG 64-22 (JB70#, ZH70#, and YN70#) than in PG 64-28 (XJ70# and XJ90#), which is consistent with the MTM, SCM, GSCM, and DFM above.

Figure 5.13 compares the average values of goodness-of-fit statistics of GSCM and JCM based on different bitumen origins. It can be found from the figures that JCM and MJCM exhibit higher prediction accuracy in PG 64-22 (JB70#, ZH70#, and YN70#) than in PG 64-28 (XJ70# and XJ90#). Among the three models in the figures, MJCM exhibits the highest prediction accuracy, and JCM and GSCM demonstrate similar accuracy, which verifies the conclusion above. The reason is that the interparticle interactions are not particularly strong under the filler-bitumen ratio used in this study. Thus, JCM exhibits a similar predictive precision as GSCM without considering interparticle interactions. As a contrast, MJCM, which can accurately solve the radial distribution function, still exhibits the highest prediction accuracy, with an average goodness-of-fit of 0.984 for 25 kinds of asphalt mastics. This again proves the necessity of proposing MJCM, and it can be foreseen that MJCM will demonstrate more substantial superiority as the filler volume fraction increases.

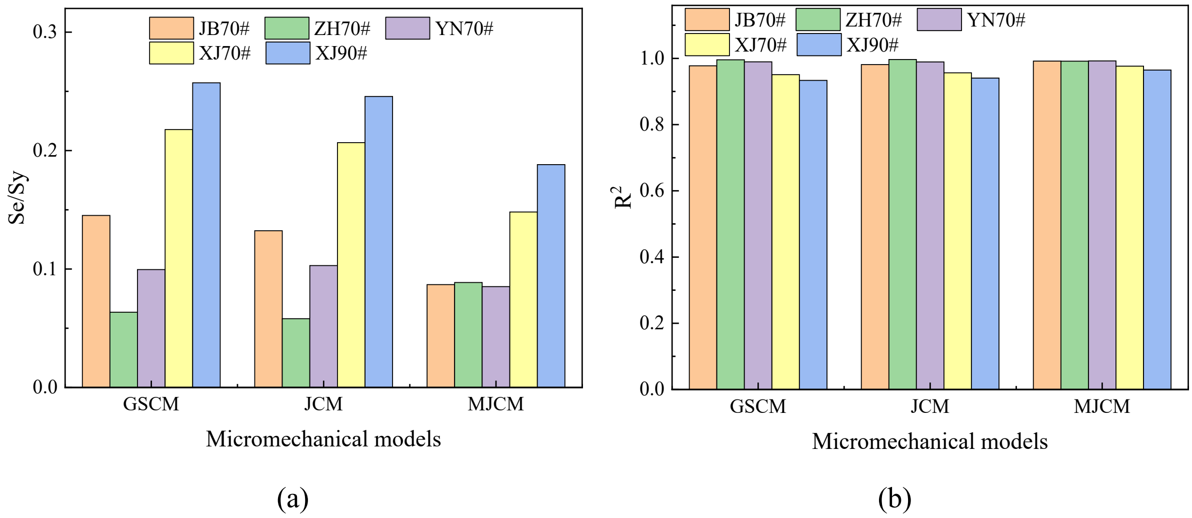

Figure 5.13 Comparison between the average values of goodness-of-fit statistics of GSCM and JCM based on different bitumen origins: (a) Se/Sy; (b) R^2

5.3.3.2 Comparison of advanced models considering the effects of filler types

Figures 5.14 and 5.15 compare the complex modulus master curves of JB70# and XJ70# asphalt mastics predicted by GSCM and JCM based on five filler types. As far as the effect of filler types on the prediction accuracy of the three micromechanical models is concerned, no regular conclusions can be drawn from the results of JB70# and XJ70# asphalt mastics. For example, the prediction accuracy of steel slag in JB70# asphalt mastic is the highest, but this is not the case in XJ70# asphalt mastic. To summarize, the results based on these two types of asphalt mastics cannot capture a uniform regularity.

Figure 5.16 compares the average goodness-of-fit statistics of GSCM and JCM based on different filler types. From the figures, the filler types have basically no effect on the prediction accuracy of the three micromechanical models of JCM, MJCM, and GSCM, which is consistent with the above analysis results. In addition, among these three models, the accuracy of MJCM is slightly higher than the other two, verifying the previous conclusion.

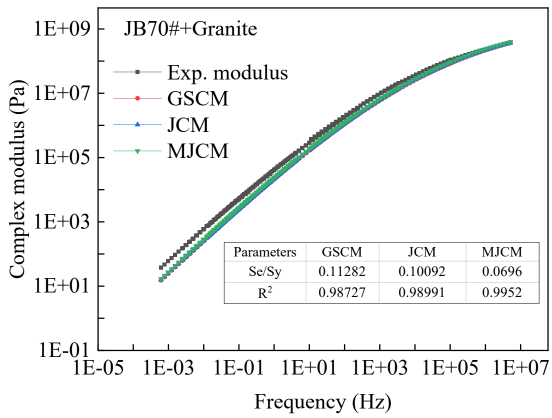

(a)

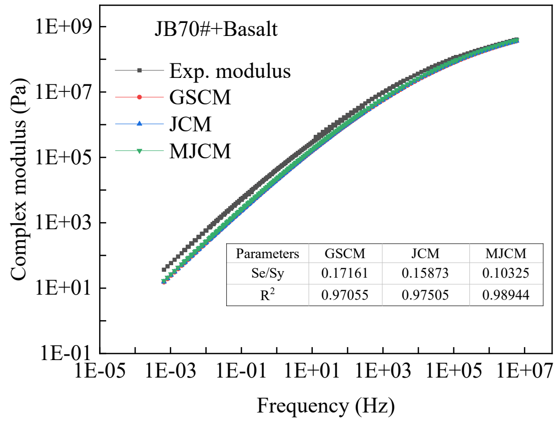

(b)

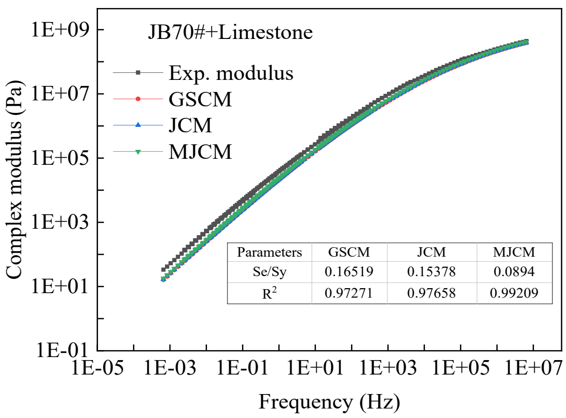

(c)

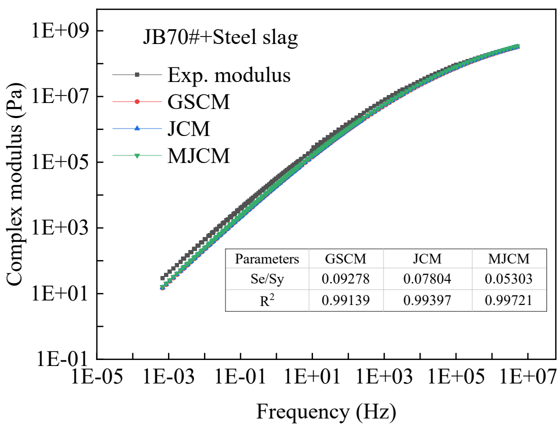

(d)

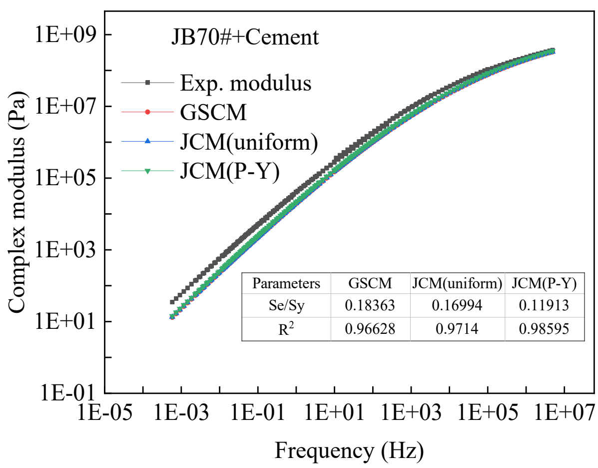

(e)

Figure 5.14 Comparison between complex modulus master curves of JB70# asphalt mastics predicted by GSCM and JCM based on fillers of (a) Granite; (b) Basalt;(c) Limestone; (d) Steel slag; (e) Cement

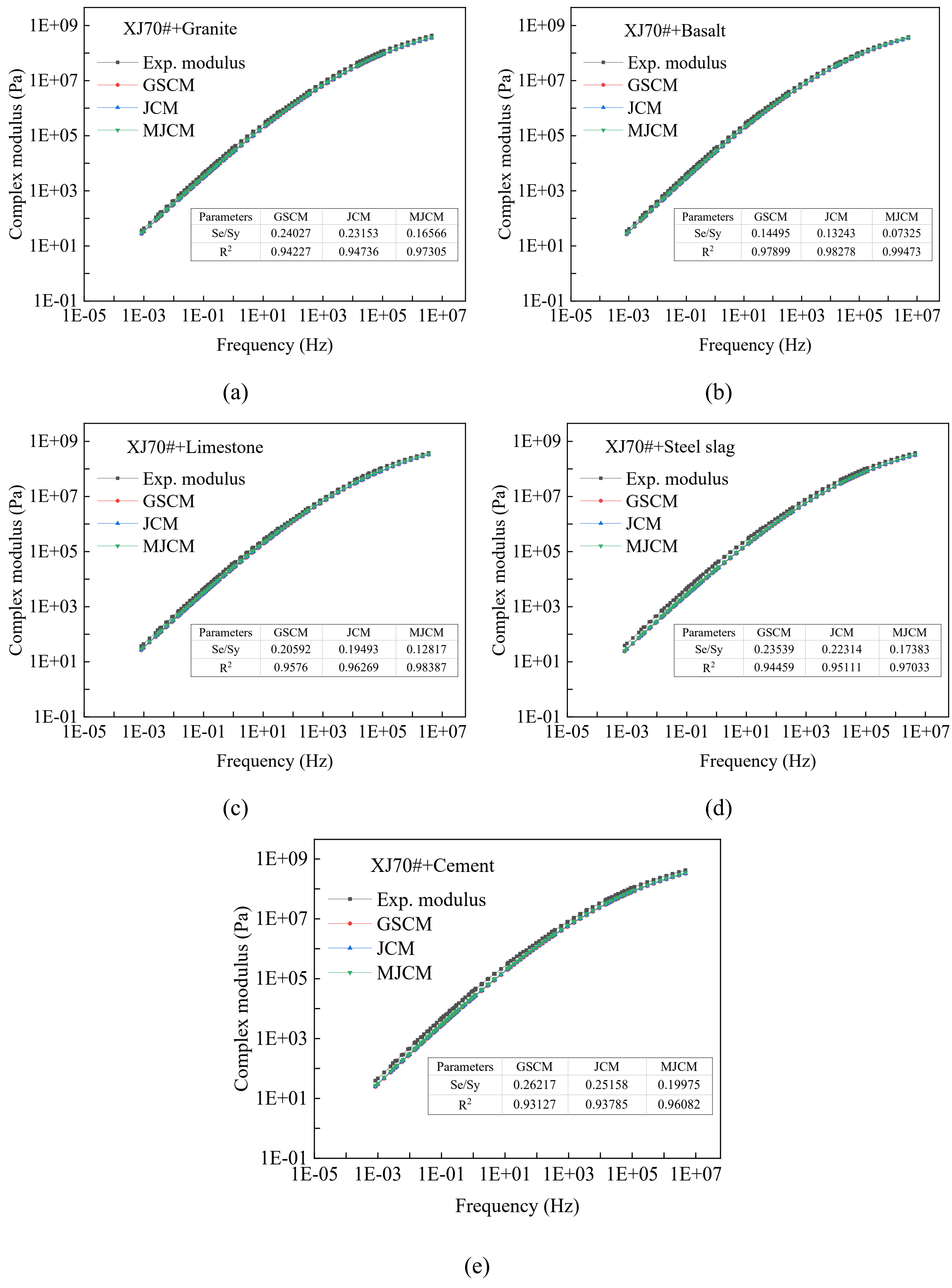

Figure 5.15 Comparison between complex modulus master curves of XJ70# asphalt mastics predicted by GSCM and JCM based on fillers of (a) Granite; (b) Basalt;(c) Limestone; (d) Steel slag; (e) Cement

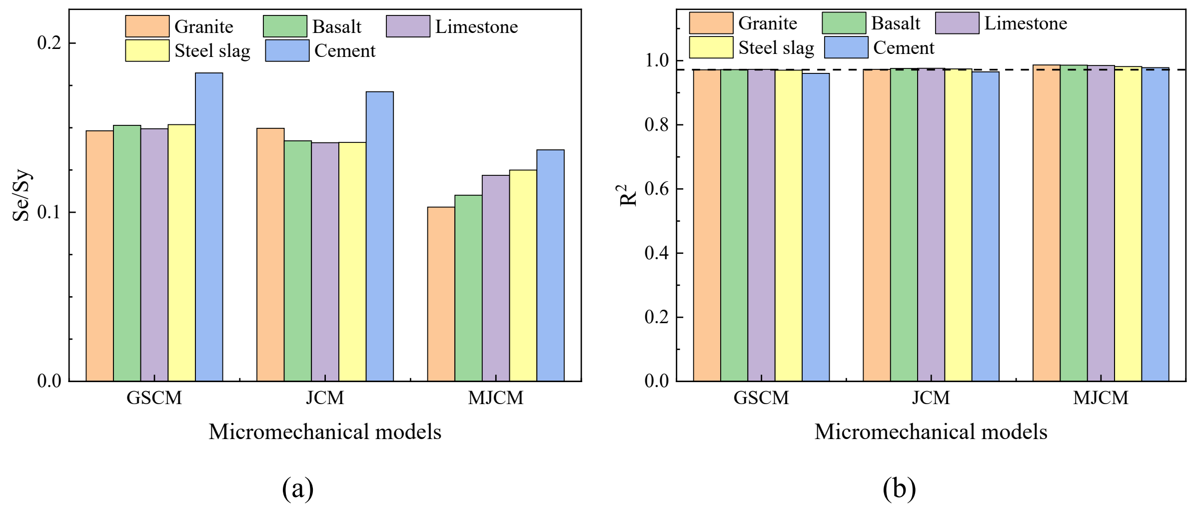

Figure 5.16 Comparison between the average values of goodness-of-fit statistics of GSCM and JCM based on different filler types: (a) Se/Sy; (b) R^2

5.2.4 Prediction results of asphalt mixtures

5.2.4.1 Two-step homogenization scheme

The asphalt mixture is a heterogeneous, anisotropic granular composite material consisting of aggregates of various sizes, irregular shapes, and random orientations embedded in an asphalt matrix. As a typical multi-component composite material, the prediction of the performance of asphalt mixtures has always been the focus of researchers. In this study, we proposed a prediction scheme of the dynamic modulus of asphalt mixtures based on the micromechanical models. This study regards asphalt mixture as a three-phase composite material consisting of asphalt mortar, coarse aggregate, and voids, and adopts a two-step prediction method to calculate the dynamic modulus of asphalt mixture. In the first step, the coarse aggregate is treated as an isotropic inclusion and put into the matrix phase of the asphalt mortar. The binary composite material formed by the asphalt mortar and the coarse aggregate is called the intermediate effective medium, and the dynamic modulus of this effective medium is predicted. In the second step, the void is equivalent to a special particle inclusion with a modulus of zero, which is put into the matrix phase of the intermediate effective media to form the final asphalt mixture composite material, and the dynamic modulus of the mixture is predicted. The schematic diagram is shown in Figure 5.17 below.

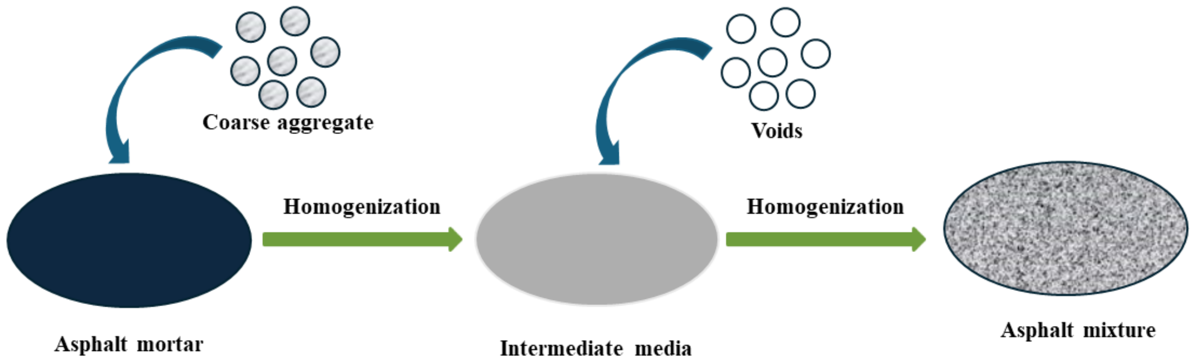

Figure 5.17 The schematic diagram of the two-step scheme of asphalt mixture dynamic modulus prediction

5.2.4.2 Modulus test results of asphalt mortars and asphalt mixtures

To verify the prediction accuracy of two-step scheme on the dynamic modulus of asphalt mixtures, the moduli of asphalt mortar and asphalt mixture were measured. A commonly used asphalt mixture gradation in China was selected in this study, as shown in Table 5-4.

Table 5-4 Gradation design of asphalt mixtures and asphalt mortars

Particle size (mm)	Passing ratio (%)	
	Asphalt mixture	Asphalt mortar
16	100	-
13.2	95	-
9.5	76.5	-
4.75	53	-
2.36	37	100
1.18	26.5	71.62
0.6	19	51.35
0.3	13.5	36.49
0.15	10	27.03
0.075	6	16.22

JB70# was selected as the representative base bitumen, with the fillers being the mineral fillers and solid waste fillers chosen for this study. The optimal asphalt content for the asphalt mixture was determined to be 4.8%. The gradation design of the asphalt mortar was derived by removing the coarse aggregates (particle size > 2.36 mm) from the gradation of the asphalt mixture. The only difference between the various mortars and asphalt mixtures lies in the type of filler used, while all other parameters remain consistent.

The shear modulus of mortars was determined using the MCR 702e DSR manufactured by Anton Paar GmbH, as shown in Figure 5.18. In the mortar modulus test, the test temperature range is 0 ~ 50 °C with an interval of 10 °C, and the test frequency range is 0.1 ~ 100 Hz. As an elastic stone-based material, the shear modulus and Poisson's ratio of coarse aggregate was taken as 19000MPa and 0.2 respectively in this study, and the Poisson's ratio of the mortar is assumed to be 0.3. The dynamic modulus of mixtures was determined referring to AASHTO T342. The test samples with a diameter and height of 100 mm were cored from SGC samples with a diameter of 150 mm and a height of 165 mm. Five test temperatures of -10.0, 4.4, 21.1, 37.8, and 54.0 °C and six test frequencies of 25, 10, 5, 1, 0.5, and 0.1 Hz were selected in the modulus tests of mixtures, as shown in Figure 5.19.

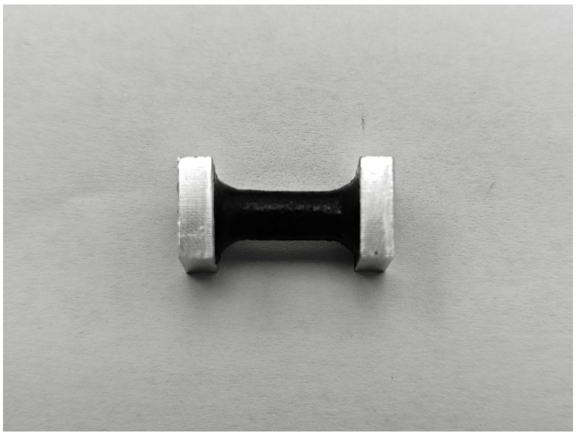

(a)

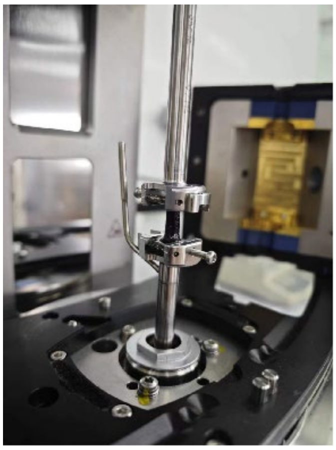

(b)

Figure 5.18 The apparatuses of the mortar modulus tests: (a) mortar sample; (b) test equipment

Figure 5.19 Dynamic modulus tests of asphalt mixtures

Figure 5.20 (a) presents the shear modulus test results of the asphalt mortar with Granite filler at six test temperatures. It can be found that the shear modulus of the mortar increases with the rise of the shear frequency and the decrease of the test temperature. In this study, 20 °C was selected as the reference temperature, and the test results at other test temperatures were shifted to the reference temperature to establish the shear modulus master curves of asphalt mortars, as shown in Figure 5.20 (b). According to the figure, the shear modulus master curves of asphalt mortars with different kinds of fillers overlap. It can be concluded that replacing only the filler type in the mortar will not have a significant impact on the modulus of the mortar under the premise that other conditions remain unchanged. This is consistent with the findings in the asphalt mastic stage above.

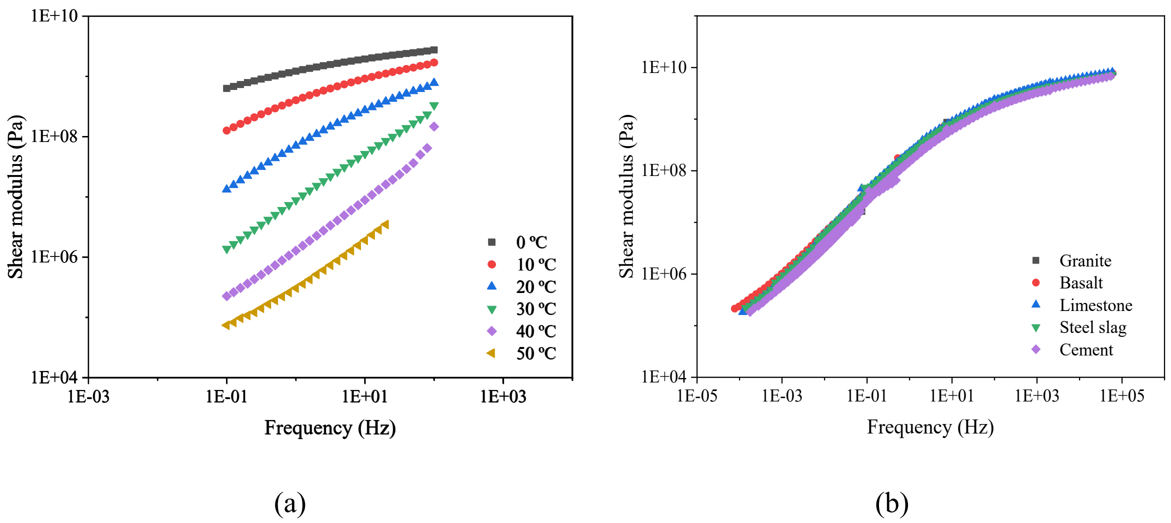

Figure 5.20 Shear modulus test results of asphalt mortars: (a) Results at different test temperatures; (b) Master curves.

Figure 21 (a) presents the dynamic modulus test results of the asphalt mixture with Granite filler at five test temperatures. It can be found that the dynamic modulus of the mixture increases with the rise of the test frequency and the decrease of the test temperature, which is consistent with the finding of the mortar above. Similarly, 20 °C was selected as the reference temperature, and the dynamic moduli at other test temperatures were shifted to the reference temperature to constitute the dynamic modulus master curves of mixtures, as shown in Figure 21 (b). It can be found that the dynamic modulus master curves of asphalt mixtures with different kinds of fillers overlap, which is consistent with the findings of the above mortar tests. Therefore, as shown in Figure 21 (b), in the following prediction results of dynamic modulus of asphalt mixtures, this study only selected four kinds of asphalt mixtures with two mineral fillers (Granite and Limestone) and one waste filler (Steel slag) for discussion.

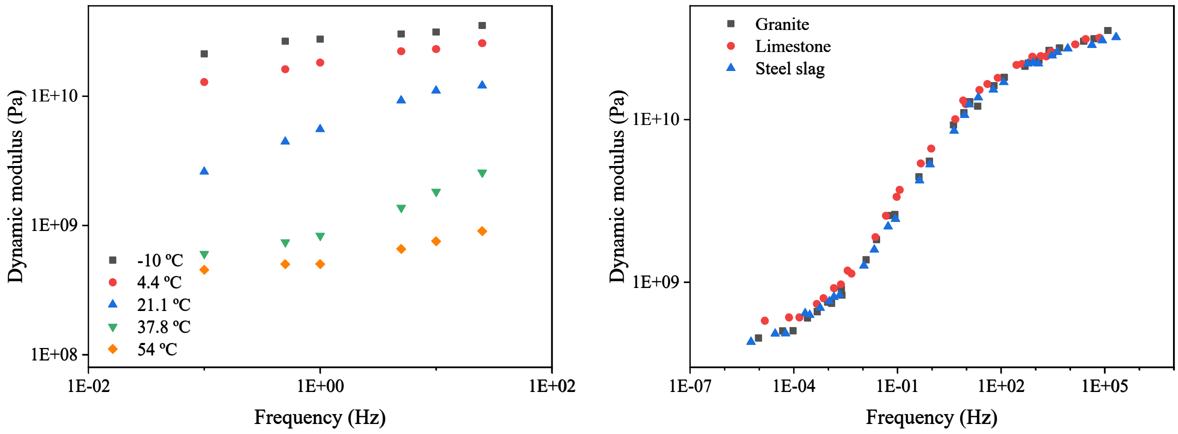

(a) (b)

Figure 5.21 Dynamic modulus test results of asphalt mixtures: (a) Results at different test temperatures; (b) Master curves

5.2.4.3 Prediction of dynamic modulus of asphalt mixtures

Figure 5.22 presents the prediction results of the dynamic modulus of asphalt mixtures based on MJCM and four micromechanical models of DM, MTM, SCM, and GSCM. The S_e/S_y and R^2 of different models are calculated and shown in Figure 5.23. It can be found that MJCM achieves excellent prediction accuracy. Whether in the high-frequency or the low-frequency region, the modulus predicted by MJCM is very close to the dynamic modulus test values of the mixtures. In contrast, the other four classical micromechanical models fail to achieve a good fitting effect in the full frequency range. Specifically, the DM, MTM, and SCM models exhibit high prediction accuracy in the high-frequency region but completely lose prediction accuracy in the low-frequency region. GSCM achieves higher prediction accuracy in the low-frequency region than the other three classical micromechanical models but performs the worst in the high-frequency region. This is mainly because the above classical micromechanics models fail to effectively consider the interaction between particles. For some cases with low inclusion concentrations, classical mechanics models can often achieve relatively good prediction accuracy, such as the prediction of the modulus of asphalt mastics and asphalt mortars. This can be found in previous studies, where several classic models achieved good prediction results for the modulus of different asphalt mastics and mortars. However, for asphalt mixtures where the inclusion concentration reaches more than 50%, the classic models tend to lose accuracy. Therefore, it can be concluded that MJCM and other classical micromechanical models do not show significant differences for cases where inclusion concentrations are low such as mastics. However, for asphalt mixtures where the concentration of particle inclusions is high and the interaction between particles is strong, MJCM is essentially different from the classic model and exhibits strong superiority.

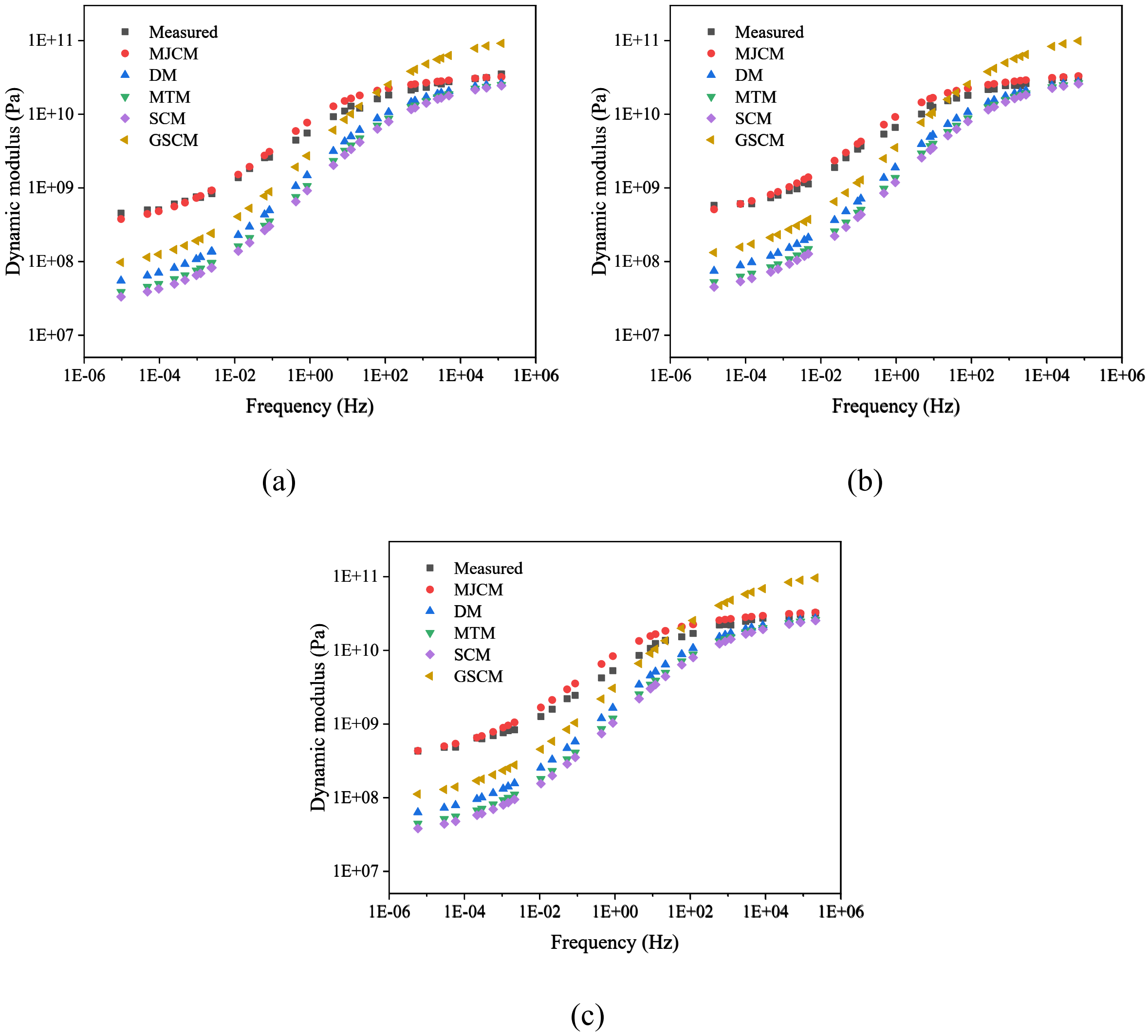

Figure 5.22 Comparison of prediction results of dynamic modulus of different kinds of asphalt mixtures: (a) G; (b) L; (c) SS

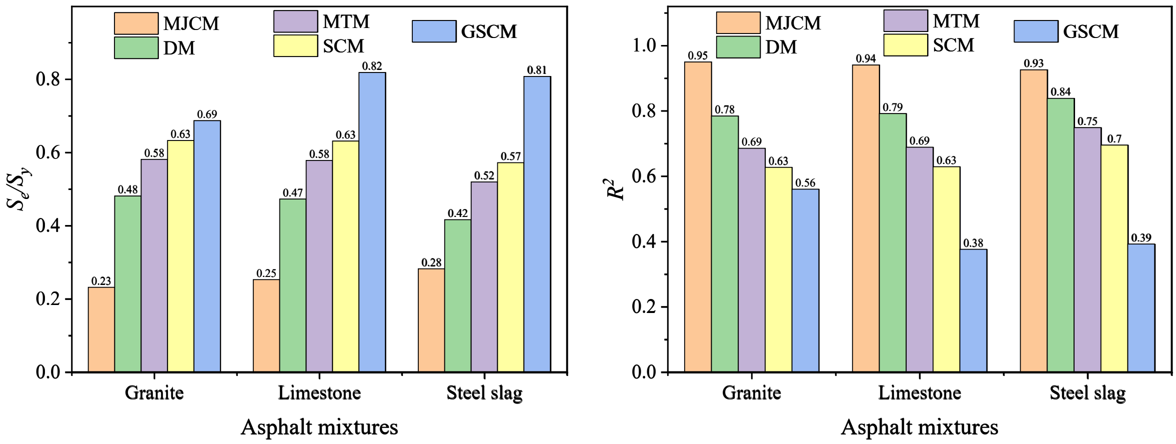

(a) (b)

Figure 5.23 Prediction accuracy of different micromechanical models: (a) S_e/S_y; (b) R^2

5.3 Summary

This chapter, based on micromechanics theory, employs five classical micromechanical models and the recently proposed Ju-Chen model to establish the quantitative composition-performance relationship between the macroscopic performance (modulus) and structural parameters of asphalt mastic, and estimates the complex shear modulus of the mastic. The Ju-Chen model was modified by solving the radial distribution function between particles, and the effects of bitumen source and filler type were considered. Finally, a cross-scale quantitative composition-performance relationship construction scheme for the modulus of asphalt mixtures was proposed based on the modified Ju-Chen model combined with the two-step homogenization scheme. The main conclusions of this chapter are as follows:

1) Based on micromechanics theory, the modulus of asphalt mastic can be accurately predicted using its compositional structural parameters (modulus of bitumen and filler, filler volume fraction). This effectively establishes a quantitative relationship between the macroscopic mechanical properties (modulus) of asphalt mastic and its compositional structure (bitumen and filler), i.e., a cross-scale composition-performance relationship at

the asphalt mastic scale and the bitumen scale. This provides a multi-scale control basis for the optimized design of asphalt mastic materials.

2) Among the five classical micromechanical models (DM, MTM, SCM, GSCM, and DFM), the Generalized Self-Consistent Model (GSCM) demonstrates the highest prediction accuracy for the shear modulus of asphalt mastics. Moreover, the accuracy of GSCM is comparable to that of the Ju-Chen Model (JCM), which assumes a uniform distribution for the radial distribution function (RDF). The modified Ju-Chen Model (MJCM), enhanced by solving the radial distribution function, achieves the highest accuracy among all models, with an average goodness-of-fit of 0.984 for all asphalt mastics.

3) DM exhibits higher accuracy in two soft bitumen (PG64-28), while the other five models, including MTM, SCM, GSCM, DFM, and JCM, exhibit higher accuracy in three hard bitumen (PG64-22).

4) Based on the two-step homogenization method combined with the MJCM, a quantitative relationship between the macroscopic mechanical properties (modulus) of asphalt mixtures and their compositional structure (asphalt mortar, coarse aggregates, and voids) has been effectively established. This approach enables the accurate prediction of the dynamic modulus of asphalt mixtures across the full frequency domain, representing a cross-scale composition-performance relationship for the modulus of asphalt mixtures. Unlike asphalt mastic, the inclusion concentration of particles in asphalt mixtures is significantly increased, which greatly amplifies the interactions between the included particles. As a result, classical micromechanical models lose significant accuracy when applied to asphalt mixtures.

Further research is anticipated to expand the models used in this study to estimate the modulus of various asphalt mixtures with variable mixing gradations, bitumen sources, aggregate types, etc.

CHAPTER 6 RECYCLING OF SOLID WASTES AS ASPHALT MIXTURE FILLERS TOWARDS SUSTAINABLE PAVEMENTS: PERFORMANCE EVALUATION AND LIFE CYCLE ASSESSMENT

The preceding chapters have elaborated on the interaction mechanisms between bitumen and fillers, the service performance and composition-performance relationship analysis of asphalt mastic, as well as the micromechanical prediction of asphalt mastic modulus and the construction of its cross-scale composition-performance relationship. The application of solid waste in asphalt pavement engineering ultimately aims to serve practical production. Therefore, this chapter will focus on actual engineering applications, analysing the pavement performance of asphalt mixtures incorporating solid waste as fillers. Additionally, three types of traditional mineral filler asphalt mixtures are selected for a detailed comparison of the mechanical performance differences between the two categories of mixtures. As a win-win solution for improper solid waste disposal and the shortage of mineral resources, replacing traditional mineral fillers with solid waste in asphalt pavements undoubtedly offers significant environmental advantages. This chapter will quantify these environmental benefits using Life Cycle Assessment (LCA). However, a critical issue that cannot be overlooked in the application of solid waste in asphalt pavements is the potential presence of excessive heavy metal content, which may pose risks to surrounding soil, water sources, and even human health through leaching behaviour. Based on above background, this chapter also investigates the environmental safety of solid waste fillers. Leaching tests are conducted to characterize the leaching behaviour of trace heavy metals during the service life of solid waste fillers, and their environmental safety for use in pavement engineering is determined by comparing the results with current national standards.

6.1 Materials and Methodology

6.1.1 Materials and sample preparation

Five kinds of solid wastes from three categories were adopted in this study, including three industrial wastes: SS, DG, and BF, one construction waste: CE, and one mining waste: IT. All waste fillers used in this study were sourced from recycling stations, where SS and IT were subjected to crushing and sieving procedures. As for CE, DG, and BF fillers, they are put into use only after passing the sieving procedure. As a comparison, three commonly used mineral fillers, including granite, basalt, and limestone, were adopted in this study. A base bitumen, with a penetration of 60/70 and a PG of 64-22, was used in this study. The bitumen and fillers used in this chapter are the same as these in Chapters 3. For more detailed information on material properties, please refer to Chapter 3.1.1 above. One commonly used mixture graduation in China with the nominal maximum aggregate size of 13 mm, AC-13, was adopted in this study. Table 6-1 presents the passing ratios of each sieve size of AC-13 graduation. The optimum bitumen content was 4.8% by the weight of the mixture and the target air void of asphalt mixtures was 3.80%.

Table 6-1 AC-13 gradation used in this study

Sieve size (mm)	16	13.2	9.5	4.75	2.36	1.18	0.6	0.3	0.15	0.075
Passing rate (%)	100	95	76.5	53	37	26.5	19	13.5	10	6

6.1.2 Experimental methods of asphalt mixtures

6.1.2.1 Hamburg Wheel-Track (HWT) Test

The immersion HWT test was conducted in this study to determine the high-temperature rutting resistance and moisture resistance of different asphalt mixtures with mineral and waste fillers in accordance with AASHTO T324, as shown in Figure 6.1. The test temperature was set as

50°C, and the termination condition of the test was set at the load cycles of 20,000 times or a rut depth of 20 mm. The rut depth and the stripping inflection point (SIP) were adopted to evaluate the rutting resistance and moisture resistance of asphalt mixtures, respectively [170].

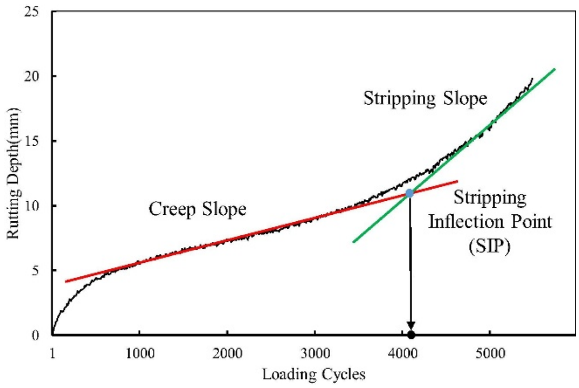

(a) (b)

Figure 6.1 Immersion Hamburg wheel-track test: (a) Test equipment and samples; (b) Definition of stripping inflection point [171]

6.1.2.2 Indirect tensile fatigue (ITF) test

The ITF test was performed to characterize the fatigue properties of asphalt mixtures with mineral and waste fillers. The test temperature was selected as 20 °C, and the cyclic haversine loading waveform with a frequency of 10 Hz was applied during the test. The ITF test was conducted using DTS-30 equipment. The diameter of the cylindrical specimen is 100 mm, while the thickness of the specimen is 60 mm. The specimen was formed using AC-13 mixtures by the gyratory compaction. For each asphalt mixture, six samples at different strain levels were tested. Referring to ASTM D7460, the fatigue life (N_f) of asphalt mixtures was calculated based on the dissipative energy theory, as shown in Equation (6-1):

$$NM = \frac{S_i \times N_i}{S_0 \times N_0} \tag{6-1}$$

where NM is the normalized modulus × cycles; S_i and S_0 are the stiffness modulus at the cycle

N_i at the initial (Pa), respectively; N_0 is the actual cycle number where initial stiffness modulus is estimated (the value of N_0 is 50 in this study). The number of load cycles corresponding to the maximum *NM* is defined as the fatigue life of the asphalt mixture, as shown in Figure 6.2.

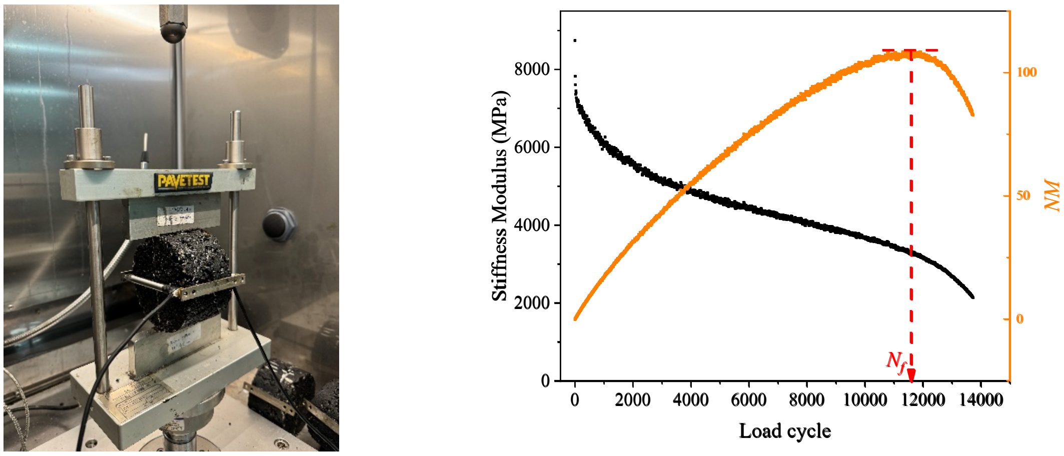

(a) (b)

Figure 6.2 Indirect tensile fatigue test: (a) Test equipment and samples; (b) Calculation of fatigue life N_f

6.1.2.3 Semi-circular bending (SCB) test

The SCB test was carried out on asphalt mixtures with mineral and waste fillers to evaluate their fracture potential in accordance with AASHTO T393. For each type of mixture, a Superpave gyratory compacted (SGC) specimen with a height of 150 mm and a diameter of 150 mm was prepared and then cut into 4 SCB specimens with a thickness of 50 mm. The SCB tests were conducted at 25 °C with a constant load-line displacement rate of 50 mm/min using a closed-loop, feedback-controlled servo-hydraulic loading device. In this test, the fracture energy and flexibility index (FI) are defined to estimate the cracking resistance of asphalt mixture as Equations (6-2) and (6-3), and Figure 6.3:

$$G_f = \frac{W_f}{Area_{lig}} = \frac{\int Pdu}{(r-a)t} \tag{6-2}$$

$$FI = \frac{G_f}{|m|} \times A \tag{6-3}$$

where G_f is the fracture energy (J/m^2); W_f is the work of fracture (J); P is the load (kN); u is the load line displacement (mm); $Area_{lig}$ is the ligament area = $(r\text{-}a) \times t$ (mm^2); r, a, t are the specimen radius, notch length, and specimen thickness, respectively (mm); $|m|$ is the absolute value of post-peak load slope (kN/mm).

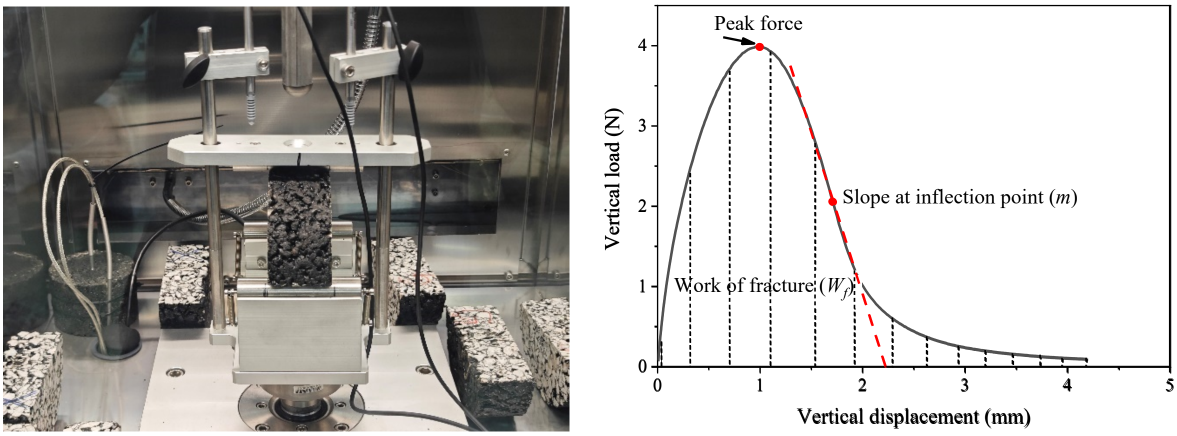

(a) (b)

Figure 6.3 Indirect tensile fatigue test: (a) Test equipment and samples; (b) Calculation of cracking indicators

6.1.3 Leaching test of solid waste fillers

In current research focusing on the application of solid waste materials in asphalt mixtures, most researchers concentrate on the improvements in mechanical performance and durability of asphalt pavements using solid waste fillers, while overlooking potential environmental pollution risks, as some solid waste fillers may contain heavy metal contaminants. This chapter conducts leaching tests on the five types of solid waste fillers selected for this study to assess their environmental safety.

Referring to the internationally recognized Toxicity Characteristic Leaching Procedure (TCLP) and existing research on leaching tests for fillers, aggregates, and their prepared asphalt mixtures [172, 173], leaching tests were performed on the five solid waste fillers used in this study. Leachate samples were prepared at a solid-to-liquid ratio of 4g:40ml, where 4g of solid waste filler sample was added to an extraction container containing 40ml of extraction fluid. The extraction container was stirred at a rate of 30 rpm for 24 hours to accelerate the leaching of contaminants from the fillers, as shown in Figure 6.4 (a). Following the TCLP guidelines, two different extraction fluids were prepared for the five solid waste fillers in this study. For Extraction Fluid 1, 5.7 mL of glacial acetic acid was dissolved in 500 mL of deionized water, followed by the addition of 64.3 mL of NaOH (1 mol/L concentration) to bring the total volume to 1 L. The pH of Extraction Fluid 1 was maintained within the range of 4.93 ± 0.05. For Extraction Fluid 2, 5.7 mL of glacial acetic acid was dissolved in deionized water and diluted to 1 L, with the pH maintained within the range of 2.88 ± 0.05. A 5.0 g sample was placed in a 500 mL beaker or conical flask, and 96.5 mL of deionized water was added. After magnetic stirring for 5 minutes, the pH was measured. If the pH was < 5.0, Extraction Fluid 1 was used; if the pH was > 5.0, Extraction Fluid 2 was employed.

After completing the leaching tests, leachate samples were collected using a 0.45 μm syringe filter. Finally, the concentrations of heavy metal leachates, including copper (Cu), zinc (Zn), cadmium (Cd), lead (Pb), chromium (Cr), barium (Ba), nickel (Ni), silver (Ag), arsenic (As), and selenium (Se), were analysed using Inductively Coupled Plasma Mass Spectrometry (ICP-MS), as illustrated in Figure 6.4 (b).

(a) (b)

Figure 6.4 Leaching test of solid waste fillers: (a) Preparation of leaching solution; (b) ICP-MS

6.1.4 LCA of asphalt mixtures mixed solid waste and mineral fillers

6.1.4.1 Goal and scope

LCA was conducted in this study to quantify and compare the emissions and energy consumption of the asphalt pavements using different mineral and waste fillers in accordance with ISO 14040 [174]. The surface layer of asphalt pavement with a length of 1 lane-kilometer in one direction was selected as the functional unit. The typical pavement structure of a highway in northern China was selected, which consists of three asphalt layers, including a 40mm-thick upper layer, 60mm-thick middle layer, and 100mm-thick lower layer. The width of the traffic lane is 3.75m. The mixtures used in the three asphalt layers are SMA-13, AC-20, and ATB-25 from top to bottom. Table 6-2 presents the detailed gradation parameters of the three-layer structure. The optimum bitumen contents for SMA-13, AC-20, and ATB-25 are 5.8%, 4.2%, and 3.8%, respectively. The binder used for the upper and middle layers is SBS-modified bitumen (with a SBS content of 4.5%), and the binder used for the lower layer is the base bitumen with a penetration of 60/70. Based on the above analysis, this study's research object and material formula can be summarized in Table 6-3, where the density of the asphalt mixture is set as 2500kg/m^3.

Table 6-2 Gradation of the three-layer structure used in LCA

Upper layer (SMA-13)		Middle layer (AC-20)		Lower layer (ATB-25)	
Sieve size (mm)	Passing rate (%)	Sieve size (mm)	Passing rate (%)	Sieve size (mm)	Passing rate (%)
16	100	26.5	100	31.5	100
13.2	92	19	97.5	26.5	98.7
9.5	64	16	85.3	19	71.4
4.75	26	13.2	73.4	16	64.7
2.36	22.5	9.5	57.7	13.2	58.5
1.18	19.7	4.75	37.8	9.5	46.2
0.6	16.4	2.36	26.3	4.75	30.3
0.3	13.7	1.18	20.8	2.36	21.5
0.15	11.9	0.6	15.5	1.18	15.5
0.075	9.9	0.3	11.1	0.6	10.5
-	-	0.15	8.1	0.3	7.7
-	-	0.075	5.3	0.15	6.3
-	-	-	-	0.075	4.9

Table 6-3 Research object and material formula used in LCA

Research object	Total mass of raw materials (kg)	Material composition	Proportion (%)	Single item mass (kg)
Upper layer (SMA-13)	2500 * 0.04 * 3.75 * 1000 = 375000	SBS modifier	0.25	936.6
		Base bitumen	5.55	20813.4
		Aggregate	84.87	318278.2
		Filler	9.33	34971.8
Middle layer (AC-20)	2500 * 0.06 * 3.75 * 1000 = 562500	SBS modifier	0.18	1017.3
		Base bitumen	4.02	22607.7
		Aggregate	90.72	510314.6
		Filler	5.08	28560.4
Lower layer (ATB-25)	2500 * 0.1 * 3.75 * 1000 = 937500	Base bitumen	3.80	35625.0
		Aggregate	91.49	857683.1
		Filler	4.71	44191.9
Sum	1875000	SBS modifier	-	1953.9
		Base bitumen	-	79046.1
		Aggregate	-	1686276.0
		Filler	-	107724.0

6.1.4.2 System boundary and life cycle inventory

The system boundary for LCA mainly includes material extraction, transportation, and pavement construction stages, as shown in Figure 6.5. The difference between SBS-modified asphalt mixture and base asphalt mixture is the production of SBS modifiers and SBS-modified bitumen. The life cycle inventory (LCI) data in this study are mainly collected from three sources, including public databases (such as ecoinvent, a widely used lifecycle data network worldwide), field investigations, and literature research.

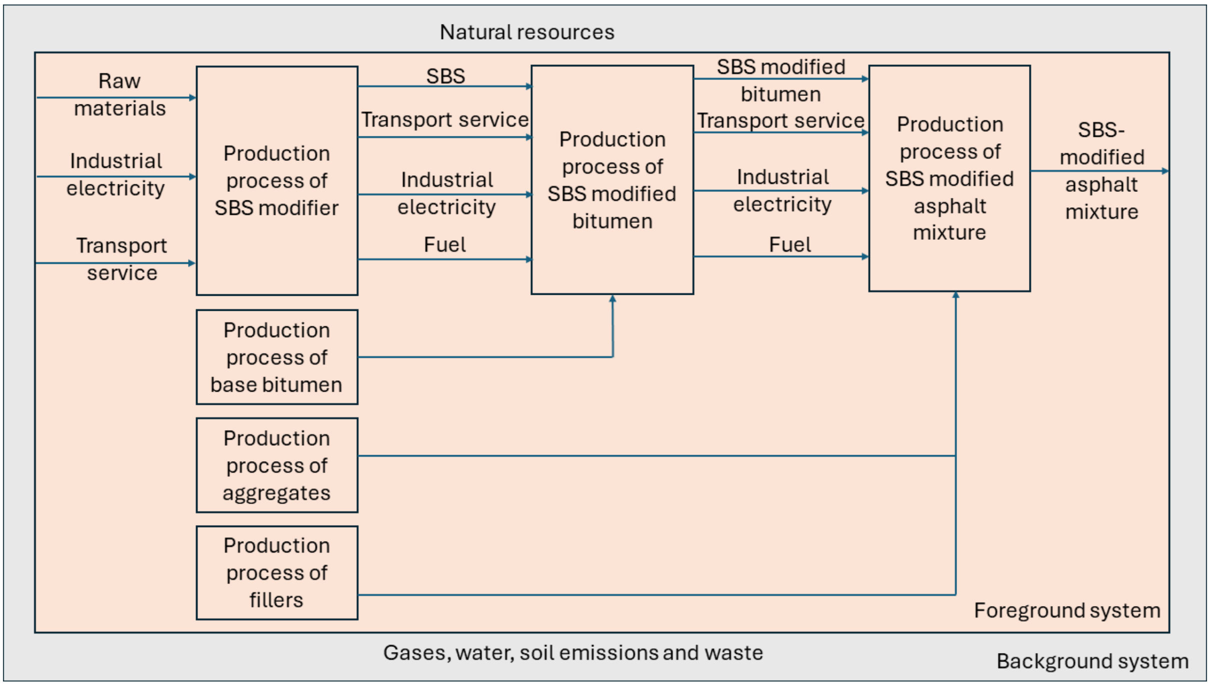

Figure 6.5 System boundaries of this study

The main difference between the LCIs of the conventional mineral fillers and waste fillers lies in the production stage of the fillers. The production stage of mineral fillers generally includes three steps: excavation, crushing, and sieving. The European Union’s Waste Framework Directive (2008/98/EC) defines "waste" as any substance or object that the holder discards, intends to dispose of, or is required to dispose of [175]. The waste fillers adopted in this study were collected from their respective industry landfills, so they can be considered as waste. Therefore, the production stage of these waste fillers does not include the excavation step. Specifically, the two types of waste fillers, SS and IT, only include the steps of crushing and sieving. The CE, DG, and BF collected in this study can be directly used to produce asphalt mixtures after simple sieving, so their production stage only includes the sieving step. Correspondingly, the waste fillers were further divided into two categories: W1 (SS and IT) and W2 (CE, DG, and BF).

6.1.4.3 Selection of LCA approaches

The LCA approaches can be broadly divided into two categories: midpoint and endpoint. The endpoint approach is commonly used to determine the ultimate outcome of environmental impacts, such as human health and ecosystem health, while the midpoint method focuses more on intermediate outcomes of environmental impacts, such as air pollution or water resource consumption. Based on the characteristics and requirements of LCA in this study, ReCiPe2016 [176], a widely used method, was selected to calculate and compare the LCA loads of asphalt pavements with different fillers. The ReCiPe2016 approach used in this study has 22 midpoint categories and 3 endpoint categories, which adopt a cause-effect chain approach to link the product's lifecycle stages with their corresponding environmental impacts. The logical chain of its internal modelling operations is shown in Figure 6.6.

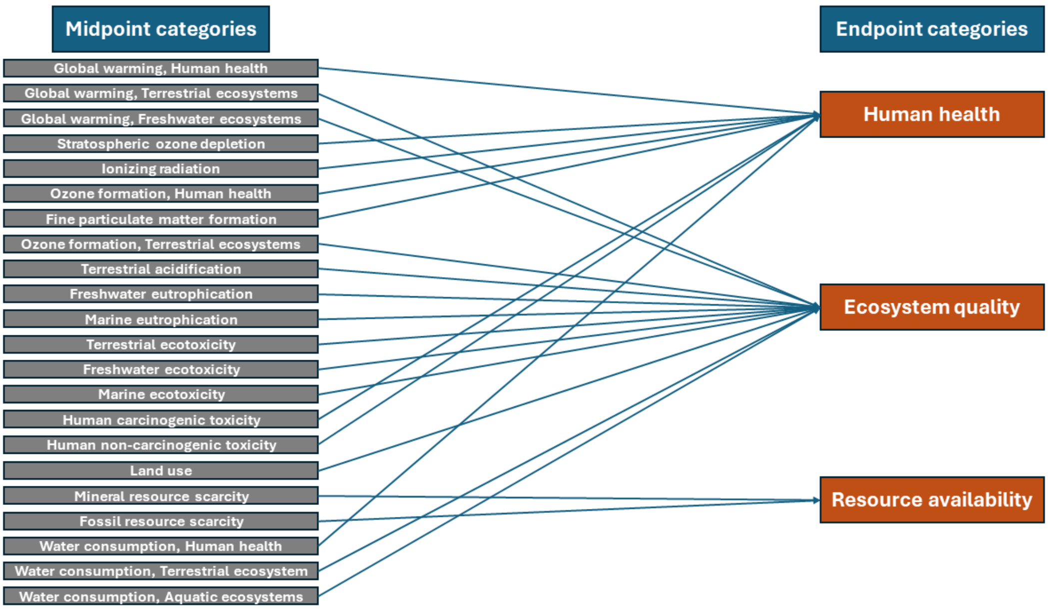

Figure 6.6 ReCiPe2016 LCA approach adopted in this study

6.2 Results and Discussion

6.2.1 Experimental results of asphalt mixtures

6.2.1.1 HWT test results

Figure 6.7 presents the HWT test results of asphalt mixtures with mineral and waste fillers. It can be found from the figures that the mixture with SS exhibits the best rutting and moisture resistance, followed by IT, CE, and the rest of the other five mixtures (L, B, BF, DG, and G) exhibit similar results. It can be concluded that recycling solid wastes SS and IT into asphalt mixtures instead of mineral fillers shows excellent moisture damage resistance. The reason behind this can be explained by the above MD simulation and experimental tests at the mastic scale. At the molecular scale, the interaction and interface strength between Wuestite and magnetite and bitumen molecules are higher than those of other rock-forming minerals. In the mastic-scale experiment, utilizing SS and IT into bitumen exhibits better cohesive failure resistance than other fillers, and mastics mixed with the two waste fillers show the strongest adhesion performances with aggregates. This is manifested in the greater moisture damage resistance of these two asphalt mixtures at the mixture scale.

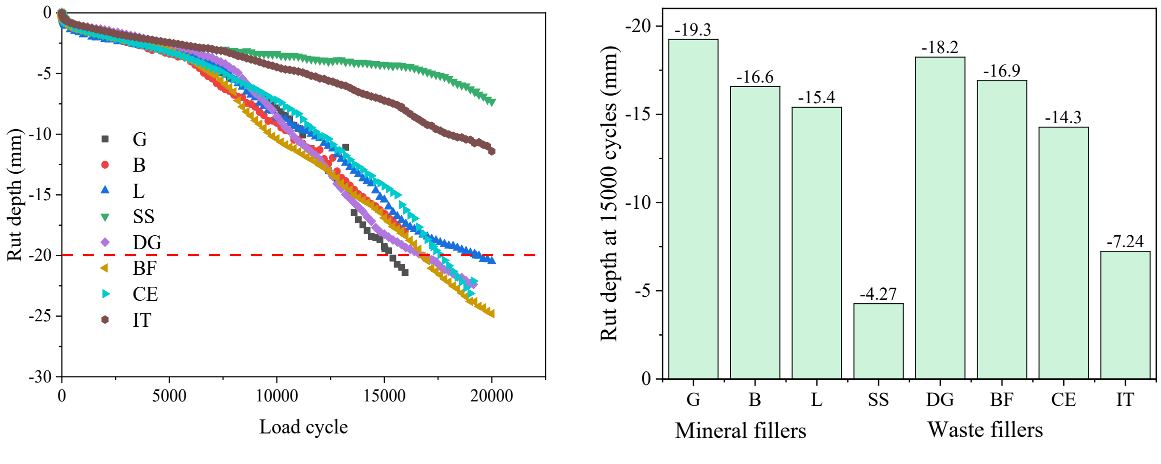

(a) (b)

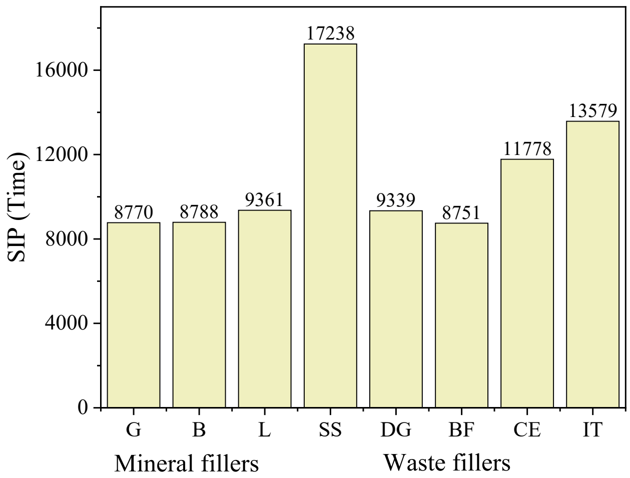

(c)

Figure 6.7 HWT test results of asphalt mixtures: (a) load cycle - rut depth curves; (b) rut depth at 15000 cycles and (c) SIP

6.2.1.2 ITF test results

Figure 6.8 presents the fatigue life of asphalt mixtures with mineral and waste fillers at different strain levels. The classical asphalt pavement fatigue model was adopted to describe the relationship between fatigue life and strain level, as shown in Equation (6-4) below:

$$N_f = k_1 \times (\frac{1}{\varepsilon})^{k_2} \tag{6-4}$$

ε is the strain level; k_1 and k_2 are the fitting parameters. It can be found from Figure 16 that the above classical fatigue model achieves a good fitting effect for the fatigue life fitting of mixtures in this study, with a goodness of fit (R^2) higher than 0.86. Among the eight types of mixtures, the mixture mixed with SS exhibits the longest fatigue life, followed by CE and IT, then BF, DG, L, B, and G. It is not difficult to find that mixtures with mineral fillers distinctly exhibit worse fatigue performance than that of solid waste fillers, especially for SS, IT and CE. The reasons behind this phenomenon have been explained above. In general, the interaction and adhesion between solid waste fillers and bitumen are stronger than those of mineral fillers, especially SS and IT. This study confirmed this in molecular-scale simulation, mastic-scale experiments and mixture-scale experiments. In addition, it is worth noting that the DENT test results have an excellent correlation with the fatigue test results of asphalt mixtures, showing a completely consistent performance ranking, which to some extent illustrates the potential of DENT test for predicting the fatigue performance of bituminous materials.

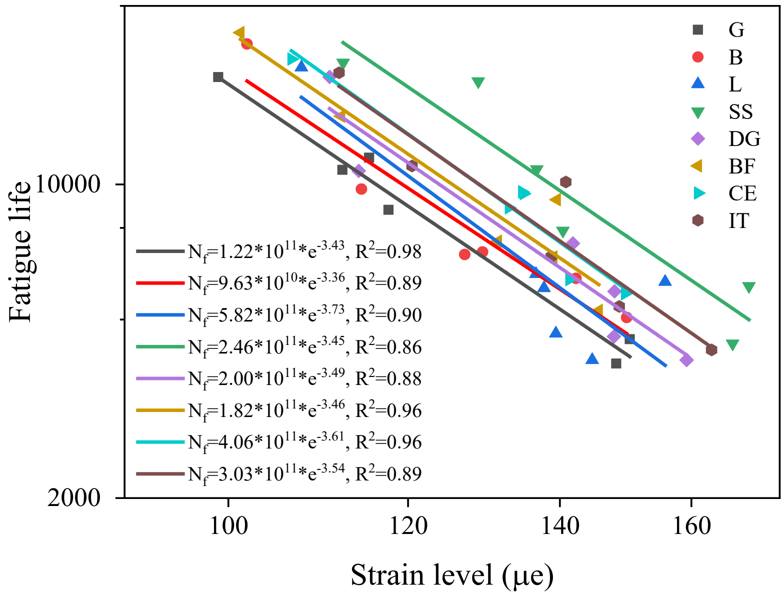

Figure 6.8 Fatigue life results of asphalt mixtures

6.2.1.3 SCB test results

The SCB test results of asphalt mixtures with mineral and waste fillers are presented in Figure 6.9. Asphalt mixtures with higher fracture energy and flexibility index usually exhibit better cracking resistance. It can be found that the shape of load-displacement curves of asphalt mixtures with different kinds of fillers are similar. Among eight kinds of asphalt mixtures in this study, the mixture with CE exhibits the best cracking resistance, followed by L and IT, and next are B, DG, and BF. Two kinds of asphalt mixtures, G and SS, show the highest fracture potential. This may be due to the higher hardness of these two fillers of G and SS [24]. It is worth noting that in the SCB test results of asphalt mixtures, solid waste fillers do not show an absolute advantage over mineral fillers, which is inconsistent with the previous findings. This indicates that the interaction and adhesion between bitumen and fillers mainly affect the moisture resistance and fatigue performance of asphalt mixtures but have little effect on cracking resistance.

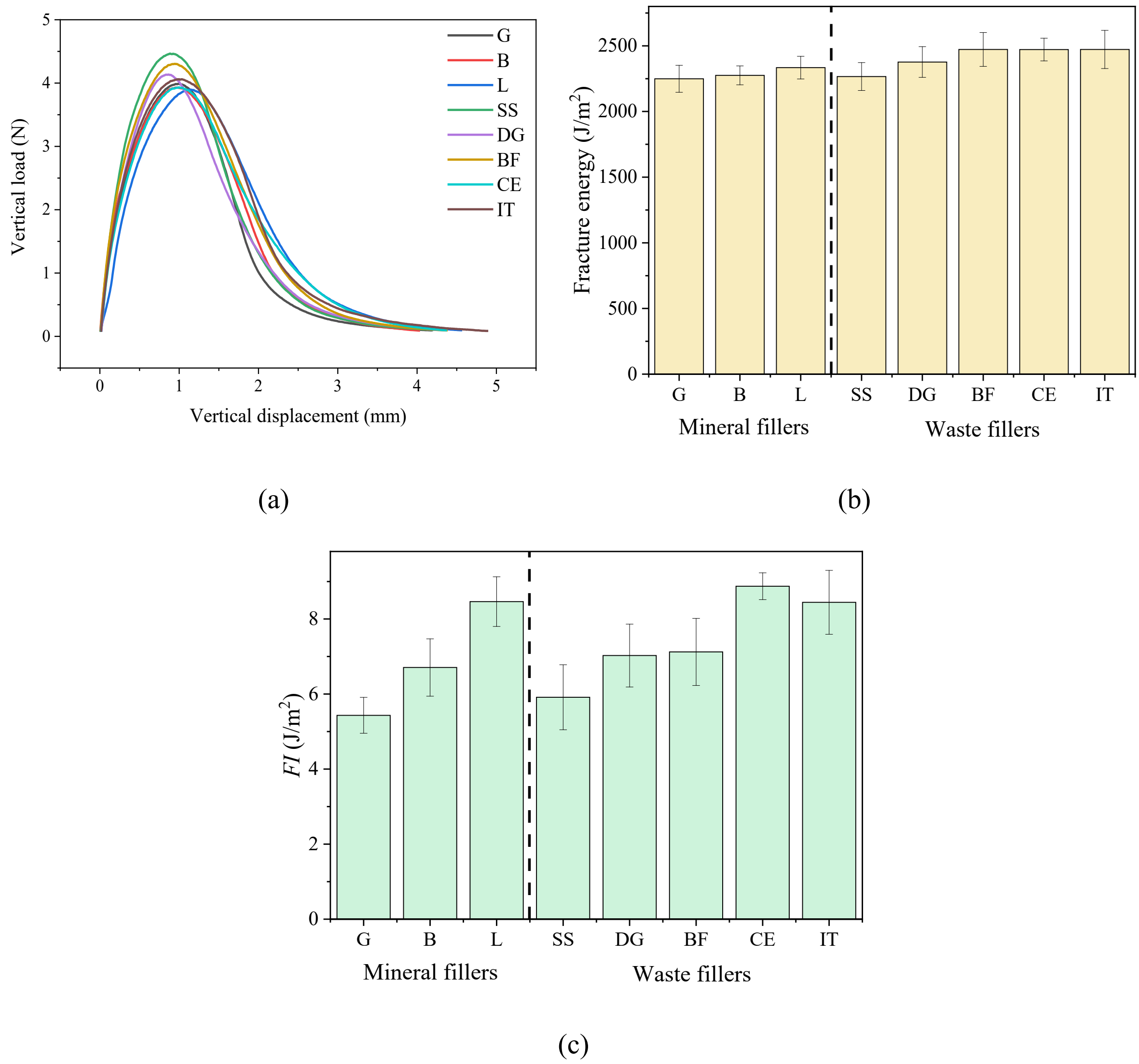

Figure 6.9 SCB test results of asphalt mixtures: (a) load-displacement curves; (b) Fracture energy; (c) Flexibility Index

6.2.2 Leaching behaviour of solid waste fillers

Table 6-4 presents the test results for heavy metal leachates from the five types of solid waste fillers. The results were evaluated based on the "General Rules for Identification of Hazardous Waste" (GB 5085.7-2019) issued by the Ministry of Ecology and Environment of the People's Republic of China to determine whether the five solid waste fillers selected for this study can be directly applied to asphalt pavements. It is noteworthy that a heavy metal content of 0 in the table indicates that the concentration of these elements in the fillers is below the detection limit (0.0001 mg/L) of the inductively coupled plasma mass spectrometry (ICP-MS) equipment. As shown in the table, the concentrations of all heavy metals in the five solid waste fillers used in this study are significantly lower than the thresholds specified by the national standard. This indicates that these solid waste fillers pose no leaching-related pollution risks or environmental safety concerns and can be directly applied to asphalt pavement engineering.

Table 6-4 Test results of heavy metal leaching characteristics in solid waste fillers

Heavy metal element	Concentrations of heavy metal leachates (mg/L)					Concentration limit (mg/L)
	SS	DG	BF	CE	IT	
Cu	0.0877	0.17745	0.18755	0.19575	0.867	100
Zn	0	0	0	0	0.3775	100
Cd	0	0	0	0	0	1
Pb	0	0	0	0	0	5
Cr	0	0	0	0	0	15
Ba	5.515	0	0	0	0	100
Ni	0	0	0	0	0	5
Ag	0.08235	0.1524	0.16165	0.15825	0.14115	5
As	0	0	0	0	0	5
Se	0.08755	0.0781	0.07635	0.09145	0.0747	1

6.2.2 LCA results of asphalt mixtures mixed solid waste and mineral fillers

Table 6-5 presents the results of the midpoint impact categories in LCA. As mentioned previously, the midpoint impact categories can be grouped into three endpoint impact categories: human health (HH), ecosystem quality (EQ), and resource availability (RA). For the first endpoint impact category of human health, its unit is the disability-adjusted life years (DALY), adopted to quantify the impact of premature death or disability that climate change has on the population [177]. Ecosystem quality has the units of species.yr (species lost in overtime) and USD2013 (U.S. dollar reference year in 2013), respectively [177]. In addition, Pavement-M represents the asphalt pavement constructed with mineral fillers, while Pavement-W1 and Pavement-W2 indicate the asphalt pavements constructed with waste fillers of category one (SS and IT) and category two (CE, DG, and BF), respectively. The difference of midpoint impact categories in LCA between Pavement-M and two Pavement-Ws was calculated as shown in Figure 6.10.

As expected, replacing conventional mineral fillers with waste fillers reduces the values of every midpoint impact category. Specifically, in terms of ecosystem quality, the replacement of mineral fillers with waste fillers resulted in the highest reduction in three ecotoxicity indicators, including freshwater ecotoxicity (FEC), territorial ecotoxicity (TE), and marine ecotoxicity (ME). This is easy to understand because the production stage of waste fillers does not require an excavation process compared to mineral fillers. After the cycle of the ecosystem, the excavation process clearly has a greater impact on ecotoxicity than other indicators such as terrestrial acidification (TA) and land use (LU). For the midpoint impact category belonging to human health, after replacing mineral fillers with waste fillers, the most significant changes are reflected in two human toxicity indicators of human carcinogenic toxicity (HCT) and human non-carcinogenic toxicity (HNCT). As explained in the ecosystem quality category, the impact of the excavation process of fillers on human health is mainly reflected in toxicity, rather than other indicators such as Global warming, Human health (GW, HH) or Stratospheric ozone depletion (SOD). Finally, although each midpoint impact category of Pavement-W2 is lower than that of Pavement-W1, the difference is insignificant. This is because W2 only omits the sieving process of fillers compared to W1. Within the entire LCA framework, the impact of the sieving process alone on the environment is negligible.

Table 6-5 Results of midpoint impact categories in LCA

Midpoint impact categories	Pavement-M	Pavement-W1	Pavement-W2
GW, HH (DALY)	4.73E-01	4.45E-01	4.38E-01
GW, TE (species.yr)	9.46E-04	8.91E-04	8.76E-04
GW, FE (species.yr)	2.58E-08	2.43E-08	2.39E-08
SOD (DALY)	3.22E-05	3.00E-05	2.97E-05
IR (DALY)	6.42E-06	6.02E-06	5.98E-06
OF, HH (DALY)	1.37E-04	1.28E-04	1.26E-04
FPMF (DALY)	3.13E-02	2.96E-02	2.91E-02
OF, TE (species.yr)	2.17E-05	2.04E-05	2.00E-05
TA (species.yr)	3.42E-05	3.23E-05	3.18E-05
FE (species.yr)	8.15E-07	7.46E-07	7.29E-07
ME (species.yr)	1.07E-09	1.01E-09	1.01E-09
TE (species.yr)	3.94E-07	3.57E-07	3.47E-07
FEC (species.yr)	3.43E-07	3.08E-07	2.97E-07
ME (species.yr)	1.95E-04	1.77E-04	1.72E-04
HCT (DALY)	1.68E-01	1.53E-01	1.49E-01
HNCT (DALY)	3.28E-01	2.98E-01	2.91E-01
LU (species.yr)	3.61E-06	3.39E-06	3.38E-06
MRS (USD2013)	1.79E+01	1.66E+01	1.63E+01
FRS (USD2013)	1.15E+04	1.04E+04	1.02E+04
WC, HH (DALY)	3.39E-05	3.10E-05	3.04E-05
WC, TE (species.yr)	3.83E-07	3.55E-07	3.51E-07
WC, AE (species.yr)	3.35E-11	3.08E-11	3.02E-11

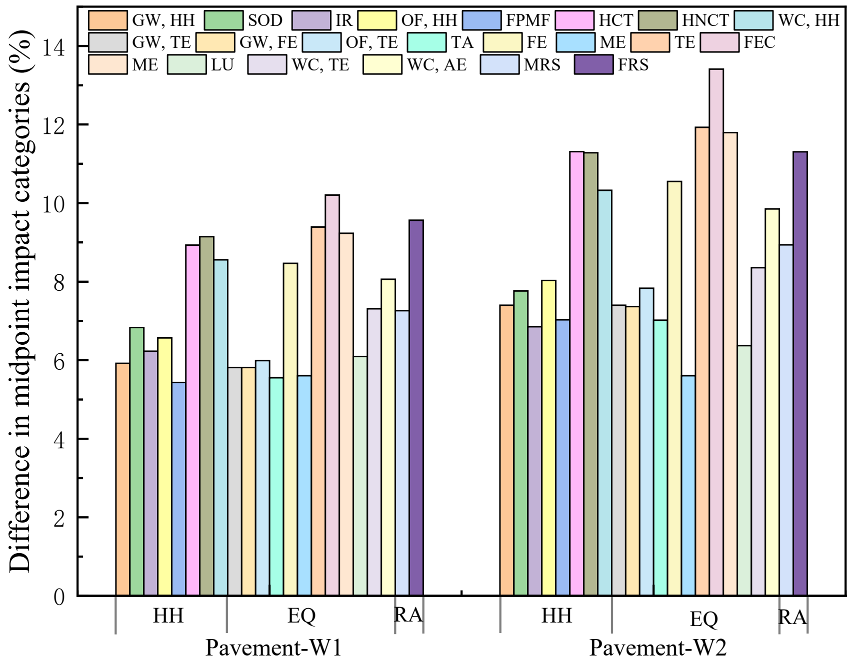

Figure 6.10 Difference of midpoint impact categories in LCA

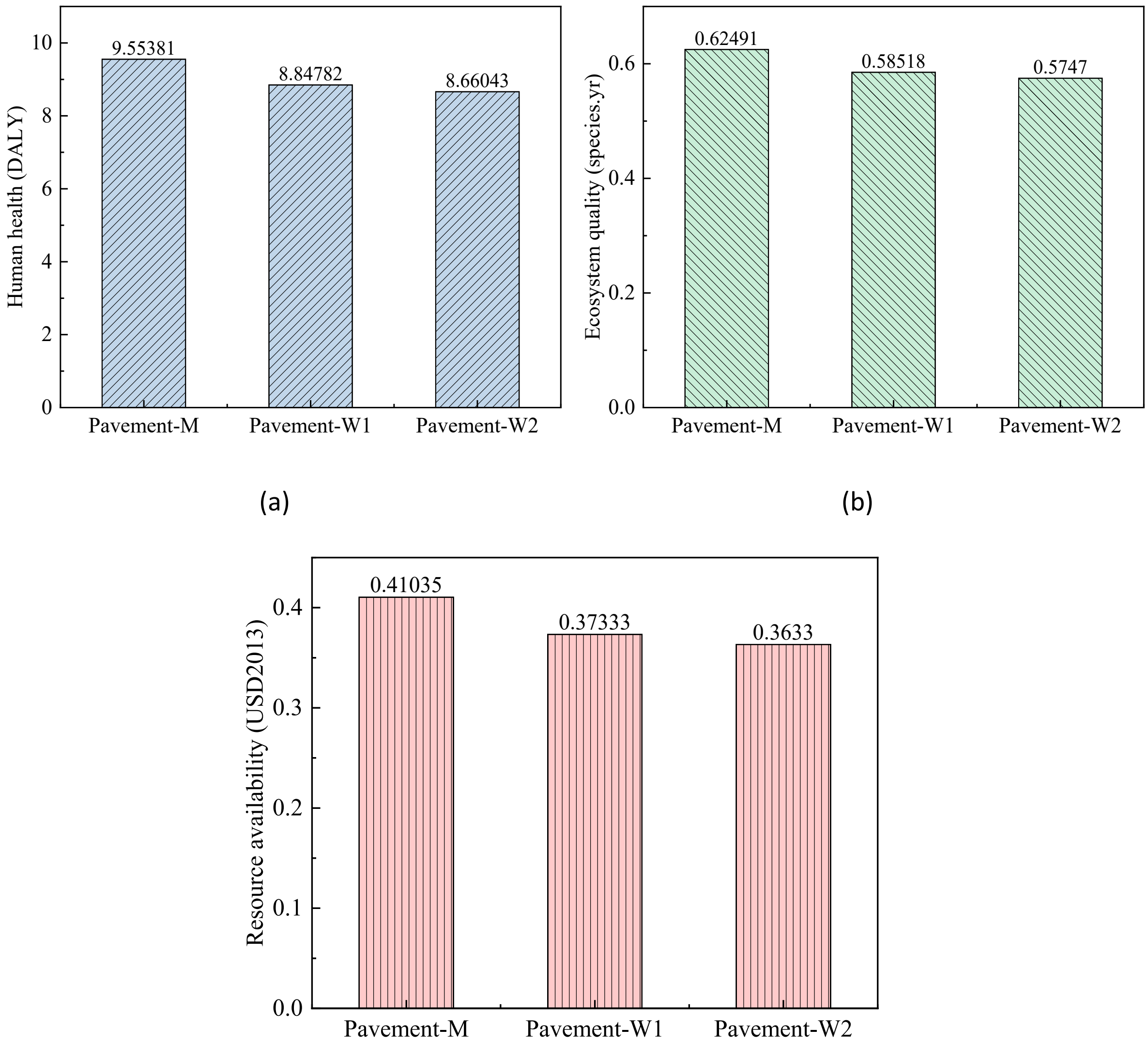

(a) (b)

(c)

Figure 6.11 Results of endpoint impact categories in LCA: (a) Human health; (b) Ecosystem quality; (c) Resource availability

The results of the endpoint impact categories in LCA were calculated as presented in Figure 6.11. After replacing conventional mineral fillers with waste fillers, the three endpoint impact categories show a significant decrease, which is consistent with the conclusion of the above midpoint impact categories. Specifically, compared to Pavement-M, Pavement-W1 and Pavement-W2 exhibit a descending range of 7.39% and 9.35% in human health, 6.36% and 8.04% in ecosystem quality, and 9.02% and 11.47% in resource availability, respectively. In summary, replacing mineral fillers with waste fillers has a significantly positive impact on the environment, with resource availability being the most prominent. This can be expected as recycling waste fillers into asphalt pavements reduces resource extraction. In addition, this recycling practice also has an undeniable improvement effect on human health and ecosystem quality.

6.3 Summary

This study investigated the recycling of solid wastes to replace mineral fillers in asphalt mixtures, and the high-temperature rutting, moisture, fatigue, and low-temperature cracking resistance of asphalt mixtures were characterized. The LCA was conducted to quantify the environmental benefits of replacing mineral fillers with waste fillers in asphalt pavements. The leaching behaviour of heavy metals during the service life of solid waste fillers was evaluated through leaching tests to determine the environmental safety of using these fillers in asphalt pavement engineering. The major findings of this chapter can be summarized as follows:

1) The utilization of solid waste fillers instead of mineral fillers in asphalt mixtures enhances the high-temperature rutting resistance, moisture resistance, and fatigue resistance of the mixtures while having little effect on the low-temperature cracking resistance. This is mainly due to the stronger interaction between solid waste fillers and bitumen, indicating that the interaction of bitumen-filler mainly affects the moisture damage and fatigue cracking damage of asphalt pavements.

2) The fatigue test results of the asphalt mixture have effectively verified the conclusion of the scale of asphalt mastics. The addition of solid waste fillers with a larger specific surface area and finer particle size to asphalt mixtures resulted in longer fatigue life. The asphalt mixture mixed with steel slag and granite exhibits poorer low-temperature cracking resistance, which may be due to the higher hardness of these two fillers and verifies the conclusion of the BBR test at the mastic scale.

3) The leaching test results for solid waste indicate that the concentrations of all heavy metals in the five types of solid waste fillers used in this study are significantly lower than the thresholds specified by national standards. This demonstrates that these solid waste fillers pose no pollution risks or environmental safety concerns during the leaching process and can be directly applied to asphalt pavement engineering.

4) Replacing conventional mineral fillers with waste fillers will significantly reduce all three endpoint impact categories of human health (HH), ecosystem quality (EQ), and resource availability (RA) in LCA, indicating that the recycling of waste fillers will bring significant environmental benefits. Among the three endpoint impact categories, the reduction in RA is the most prominent, mainly because recycling waste fill into asphalt pavements can reduce resource extraction. Regarding EQ, replacing mineral fillers with waste fillers resulted in the highest reduction of ecotoxicity indicators. As for HH, the most significant changes are reflected in human toxicity indicators.

Future research will expand the sources of bitumen and introduce commonly used bitumen modifiers such as SBS, investigating the application prospects of solid waste fillers in asphalt mixtures with different bitumen sources and the introduction of modifiers. Finally, the construction of road trials will be considered to validate the findings of this study.

CHAPTER 7 CONCLUSIONS AND RECOMMENDATIONS

The bitumen-filler-aggregate multiphase interfaces represent the critical transition zones, which are also typically weak locations, bridging the rigid and flexible components in asphalt mixtures. Understanding the physicochemical nature of bitumen-filler interactions and elucidating the mechanisms governing asphalt mastic's service performance and its cross-scale composition-performance relationships have remained challenges and research priorities in pavement engineering. Aligned with the strategic development of low-carbon, sustainable road infrastructure, recycling of solid wastes as fillers in asphalt mixture has emerged as a prominent research focus in recent years. This study addresses these critical issues through a comprehensive investigation. Initially, molecular dynamics simulations were conducted to reveal the interaction mechanisms and failure characteristics at the bitumen-filler interface. Subsequently, a combined approach of macro- and micro-scale testing coupled with multifactorial statistical analysis was adopted to develop the composition-performance relationship model between asphalt mastic's mechanical performance and its compositional architecture. Furthermore, micromechanical theory was applied to establish quantitative correlations between macroscopic modulus characteristics and meso-structural parameters of asphalt mastic. Finally, through systematic mixture testing, life cycle assessment, and leaching behaviour assessment, an optimum application strategy was developed for implementing solid wastes as sustainable fillers in asphalt pavement.

7.1 Findings

Based on the outcomes of this study, the following key findings have been obtained:

1. The bitumen-filler interface model developed in this study elucidates molecular-scale interaction differences between solid waste fillers and mineral fillers with bitumen, wherein filler mineral composition plays a pivotal role. The rock-forming mineral

molecules in solid waste fillers demonstrate substantially enhanced interfacial interactions and adhesion characteristics with asphalt molecules, as evidenced by increased interfacial adhesion work and reduced diffusion coefficients.

2. The adsorption configuration of bitumen molecules on mineral surfaces can be divided into four regions. The concentrations of the four bitumen fractions are nonzero in each region, with each fraction exhibiting a distinct distribution preference. According to their distance from the surface of the filler mineral molecules, the four fractions—resins, asphaltenes, saturates, and aromatics—alternately dominate as the main components in the four regions.

3. The interface cracking of the bitumen-filler interface model exhibits three failure modes at various loading rates. At high loading rates, the interface model exhibits adhesive failure. As the tensile rate decreases, the cracking mode of the interface model gradually transitions to the coexistence of adhesion and cohesion failure, ultimately leading to cohesive failure. The interaction between rock-forming minerals and bitumen molecules in solid waste is stronger than that of mineral fillers, and the corresponding interface model is less prone to adhesive cracking.

4. In the SARA components of bitumen, the content of resin has a good positive effect on the fatigue resistance of asphalt mastics, and this effect becomes more pronounced with the increase of strain level. The content of resins and aromatic contributes to the low-temperature performance of asphalt mastics. In addition, the correlation between the penetration of bitumen and the high- and low-temperature performances of mastics is significantly higher than other raw material parameters.

5. The D10 and P20 indicators of the filler show a good correlation with the high-temperature rutting, low-temperature cracking, and medium-temperature fatigue performances of the

asphalt mastics, and the corresponding grey correlation grades are the highest among similar indicators. Therefore, it is recommended to adopt D10 and P20 as key indicators for selecting fillers.

6. The fineness and SSA of fillers have a significant impact on the fatigue life of asphalt mastics, which can be attributed to the competitive mechanism between physical hardening and particle-filling enhancement in the effect of fillers on the fatigue performance of mastics. Fillers with smaller fitness and larger SSA can amplify the particle-filling enhancement effect, thus exhibiting longer fatigue life after adding into bitumen.

7. In comparison to conventional mineral fillers, solid waste fillers demonstrate significantly more complex and rougher surface microstructures. This enhanced surface morphology facilitates more effective adsorption of polar components in bitumen, resulting in the formation of superior interfacial structures. This phenomenon provides a potential explanation for the stronger interfacial interactions observed between solid waste fillers and bitumen.

8. In terms of the five classical micromechanical models selected in this study, GSCM presents significantly higher accuracy in predicting the modulus of asphalt mastics than the other four models, which is closed to the effect of Ju-Chen model under the uniform distribution assumption. The modified Ju-Chen Model (MJCM), enhanced by solving the radial distribution function, achieves the highest accuracy among all models, with an average goodness-of-fit of 0.984 for 25 kinds of asphalt mastics.

9. Micromechanics theory enables accurate prediction of asphalt mastic modulus using compositional parameters (bitumen/filler modulus, filler volume fraction), establishing a cross-scale composition-performance relationship between compositional structure and its

macroscopic mechanical properties, thus providing a solid theoretical basis for optimized mastic design.

10. In contrast to asphalt mastic, the higher particle concentration in asphalt mixtures intensifies the interactions between particles, thereby reducing the accuracy of classical micromechanical models. The two-step homogenization method with MJCM establishes a quantitative relationship between compositional structure (asphalt mortar, aggregates, voids) and asphalt mixture modulus, enabling full-frequency dynamic modulus prediction and cross-scale composition-performance analysis.
11. The recycling of solid waste as fillers in the production of asphalt mixtures has demonstrated superior pavement performances compared to traditional mineral fillers, especially in terms of high-temperature rutting, moisture, and fatigue resistance. This also indicates that the interaction between bitumen and fillers mainly affects the moisture damage resistance and fatigue cracking resistance of asphalt pavements.
12. The environmental benefits of recycling solid waste to replace traditional mineral fillers in the production of asphalt mixtures are reflected in the three endpoint indicators of LCA (human health (HH), ecosystem quality (EQ), and resource availability (RA)). Among them, RA is the most prominent, mainly because recycling waste fillers into asphalt pavements can reduce resource extraction.

7.2 Conclusions

Based on the major findings of this dissertation, the following conclusions can be drawn:

1. The mineral composition of fillers plays a pivotal role for the bitumen-filler interaction, with solid waste fillers exhibiting higher interfacial adhesion work and lower diffusion coefficients with bitumen molecules. Bitumen molecules display a four-region adsorption configuration on filler surfaces, where resin, asphaltene, saturates, and aromatics

components alternately dominate as the primary components in each region depending on the distance from the filler surface. The failure mechanism of bitumen-filler interface evolves with decreasing strain rate: from pure adhesive failure to mixed adhesive-cohesive failure, and ultimately to complete cohesive failure.

2. The interfacial interaction between solid waste fillers (notably wuestite in steel slag and magnetite in iron tailings) and bitumen molecules exhibits superior bonding strength compared to mineral fillers, resulting in enhanced adhesion damage resistance. This conclusion is consistently supported by a comprehensive experimental framework consisting of surface free energy analysis, bonding measurements, rheological characterization, and fracture mechanics, which provides an accurate evaluation for the interfacial interactions of bitumen-filler.

3. Adding fillers absorbs the polar components in bitumen, leading to a reduction in bee-like structures and surface roughness in the micro morphology of asphalt mastics. Unlike mineral fillers, solid waste fillers chemically react with weakly acidic bitumen, developing a more complex microstructure that significantly expands the bitumen-filler interface area.

4. The performance of asphalt mastic is highly dependent on its composition-structure: high-temperature property correlates with bitumen penetration and filler particle size distribution; fatigue resistance depends on filler specific surface area, fine particle content, and bitumen resin content; low-temperature performance shows significant relationships with bitumen penetration and filler D10/P20 characteristics. These established qualitative composition-performance relationships enable performance optimization of asphalt mastics for specific service conditions.

5. Micromechanics theory enables accurate prediction of asphalt mastic modulus through meso-structural parameters, establishing a quantitative composition-performance

relationship between mastic and bitumen scales. Extending this approach, the two-step homogenization method combined with the modified Ju-Chen model quantifies the relationship between mixture-scale modulus and meso-structural parameters of mixtures, creating a composition-performance framework bridging asphalt mixtures and mortar scales. These cross-scale relationships provide a scientific basis for optimizing asphalt pavement composite materials.

6. Solid waste fillers (notably steel slag, iron tailings, and expired cement) demonstrate superior performance in asphalt mixtures compared to mineral fillers, particularly in high-temperature property, moisture resistance, and fatigue performance. The five studied solid wastes exhibit heavy metal concentrations well below national leaching thresholds, confirming their environmental safety for pavement applications. Life cycle assessment reveals that replacing mineral fillers with solid waste alternatives generates significant environmental benefits, particularly in resource availability.

7.3 Recommendations for Future Work

Based on the major findings and conclusions of this dissertation research, future study is recommended in the following areas:

1. This study established a multi-scale evaluation framework for bitumen-filler interaction behaviour, demonstrating consistent inter-scale validation of research findings. However, critical challenges remain in establishing effective scale-transmission connections and elucidating cross-scale interaction mechanisms. Future research should focus on developing integrated models that incorporate molecular-scale parameters into micro- and macro-scale analyses.

2. The interface molecular model of bitumen-filler still needs further improvement, such as different bitumen sources and corresponding various SARA contents, filler surface

roughness, and the migration path of water molecules in the interface model, which still need to be investigated in future work.

3. While this study establishes a micromechanics-based composition-performance relationship for asphalt mastic and mixtures within the linear viscoelastic range, actual pavement service conditions predominantly operate in the nonlinear domain. Future work will focus on developing a micromechanical damage constitutive model under nonlinear loading conditions to accurately predict mixture viscoplastic and damage behaviour.

4. Previous studies have shown that the presence of fillers may have additional effects on the aging process of bitumen. Future research will focus on revealing the role of fillers in the aging process of bitumen and the impact of bitumen aging on the interaction between bitumen and fillers.

5. This study focused exclusively on various bitumen sources and filler types, excluding modified bitumen systems such as SBS or crumb rubber-modified bitumen. Future research will expand the scope to include modified bitumen, enabling comprehensive investigation of the interaction mechanisms within the bitumen-modifier-filler three-phase system and the composition-performance relationships of composite materials.

REFERENCES

[1] A. F. Al-Shawabkeh, M. T. Awwad, I. I. Ikhries, Z. S. Abu-Hamatteh, and N. A. Al-Najdawi, "Assessing recycled polyvinyl chloride reinforced modified asphalt mixtures for sustainable paving applications," *Journal of Cleaner Production,* vol. 486, p. 144583, 2025/01/01/ 2025, doi: https://doi.org/10.1016/j.jclepro.2024.144583.

[2] J. Gao, G. Guo, H. Wang, D. Jin, Y. Bi, and D. Jelagin, "Research progress of bio-asphalt towards green pavement development: Preparation, properties, and mechanism," *Fuel,* vol. 381, p. 133409, 2025/02/01/ 2025, doi: https://doi.org/10.1016/j.fuel.2024.133409.

[3] J. Xu *et al.*, "Carboxylated styrene-butadiene latex (XSB) in asphalt modification towards cleaner production and enhanced performance of pavement in cold regions," *Journal of Cleaner Production,* vol. 372, p. 133653, 2022/10/20/ 2022, doi: https://doi.org/10.1016/j.jclepro.2022.133653.

[4] D. Hu *et al.*, "From asphalt molecular evolution to performance degradation: Understanding aging mechanisms, inhibition strategies, and rejuvenation techniques," *Fuel,* vol. 404, p. 136293, 2026/01/15/ 2026, doi: https://doi.org/10.1016/j.fuel.2025.136293.

[5] J. Feng *et al.*, "Microwave response mechanism and parameter optimization of microwave-responsive capsule (MRC) for asphalt pavement self-repairing," *Construction and Building Materials,* vol. 487, p. 142058, 2025/08/15/ 2025, doi: https://doi.org/10.1016/j.conbuildmat.2025.142058.

[6] Q. Gu, A. Kang, B. Li, P. Xiao, and H. Ding, "Effect of fiber characteristic parameters on the high and low temperature rheological properties of basalt fiber modified asphalt mortar," *Case Studies in Construction Materials,* vol. 17, p. e01247, 2022/12/01/ 2022, doi: https://doi.org/10.1016/j.cscm.2022.e01247.

[7] J. Zhang, X. Li, G. Liu, and J. Pei, "Effects of material characteristics on asphalt and filler interaction ability," *International Journal of Pavement Engineering,* vol. 20, no. 8, pp. 928-937, 2019/08/03 2019, doi: 10.1080/10298436.2017.1366765.

[8] X. Zhu, Z. Du, H. Ling, L. Chen, and Y. Wang, "Effect of filler on thermodynamic and mechanical behaviour of asphalt mastic: a MD simulation study," *International Journal of Pavement Engineering,* vol. 21, no. 10, pp. 1248-1262, 2020/08/23 2020, doi: 10.1080/10298436.2018.1535120.

[9] S. M. Motevalizadeh and K. Mollenhauer, "Use of multivariate clustering analysis to investigate the physicochemical interactions in bitumen mastics using micromechanical modeling and FTIR spectroscopy," *Construction and Building Materials,* vol. 448, p. 138230, 2024/10/18/ 2024, doi: https://doi.org/10.1016/j.conbuildmat.2024.138230.

[10] F. Li, Y. Yan, H. Yang, and J. Li, "Experimental Study of the Influence of SBS Modifier on Interaction Ability of Asphalt Binder to Mineral Fillers," *International Journal of Pavement Research and Technology,* 2025/07/29 2025, doi: 10.1007/s42947-025-00572-x.

[11] T. Yan *et al.*, "Elucidating the effects of metakaolin-based geopolymer filler on the performance of styrene-butadiene-styrene modified asphalt: Microstructural insights and mechanistic analysis," *Construction and Building Materials,* vol. 487, p. 142075, 2025/08/15/ 2025, doi: https://doi.org/10.1016/j.conbuildmat.2025.142075.

[12] M. Nazary and S. Kofteci, "Effect of filler types and asphalt penetration grade on properties of asphalt mastic," *Petroleum Science and Technology,* vol. 36, no. 18, pp. 1503-1509, 2018/09/17 2018, doi: 10.1080/10916466.2018.1501385.

[13] L. Pereira, A. C. Freire, M. Sá da Costa, V. Antunes, L. Quaresma, and R. Micaelo, "Experimental study of the effect of filler on the ductility of filler-bitumen mastics," *Construction and Building Materials,* vol. 189, pp. 1045-1053, 2018/11/20/ 2018, doi: https://doi.org/10.1016/j.conbuildmat.2018.09.063.

[14] Y. Cheng, C. Zhu, G. Tan, Z. Lv, J. Yang, and J. Ma, "Laboratory Study on Properties of Diatomite and Basalt Fiber Compound Modified Asphalt Mastic," *Advances in Materials Science and Engineering,* vol. 2017, no. 1, p. 4175167, 2017/01/01 2017, doi: https://doi.org/10.1155/2017/4175167.

[15] N. Liu, L. Liu, M. Li, and L. Sun, "Effects of zeolite on rheological properties of asphalt materials and asphalt-filler interaction ability," *Construction and Building Materials,* vol. 382, p. 131300, 2023/06/13/ 2023, doi: https://doi.org/10.1016/j.conbuildmat.2023.131300.

[16] H. Sun *et al.*, "Influence of the physical morphological characteristics of mineral fillers on the bitumen-filler interfacial interaction," *Construction and Building Materials,* vol. 378, p. 131206, 2023/05/16/ 2023, doi: https://doi.org/10.1016/j.conbuildmat.2023.131206.

[17] Y. He *et al.*, "Experimental investigation of the interface interaction between asphalt binder and mineral filler from the aspects of materials properties," *Construction and Building Materials,* vol. 393, p. 132094, 2023/08/22/ 2023, doi: https://doi.org/10.1016/j.conbuildmat.2023.132094.

[18] H. Zhang, H. Li, A. Abdelhady, M. Jia, and N. Xie, "Investigation on surface free energy and moisture damage of asphalt mortar with fine solid waste," *Construction and Building Materials,* vol. 231, p. 117140, 2020/01/20/ 2020, doi: https://doi.org/10.1016/j.conbuildmat.2019.117140.

[19] S. B. A. Zaidi *et al.*, "Moisture susceptibility of hydrated lime modified mastics using adhesion test methods and surface free energy techniques," *International Journal of Pavement Engineering,* vol. 22, no. 7, pp. 829-841, 2021/06/07 2021, doi: 10.1080/10298436.2019.1648811.

[20] C. Li, Q. Liu, J. Lei, Z. Zhang, C. Fu, and F. Pan, "Influence of mineral fillers properties on the bonding properties of bitumen mastics," *Construction and Building Materials,* vol. 318, p. 126013, 2022/02/07/ 2022, doi: https://doi.org/10.1016/j.conbuildmat.2021.126013.

[21] O. Xu, S. Xiang, X. Yang, and Y. Liu, "Estimation of the surface free energy and moisture susceptibility of asphalt mastic and aggregate system containing salt storage additive," *Construction and Building Materials,* vol. 318, p. 125814, 2022/02/07/ 2022, doi: https://doi.org/10.1016/j.conbuildmat.2021.125814.

[22] P. Khanmoradi and A. Modarres, "Rheological and nano-mechanical characteristics of bituminous mastics containing waste and ordinary filler at different temperatures," *Construction and Building Materials,* vol. 411, p. 134228, 2024/01/12/ 2024, doi: https://doi.org/10.1016/j.conbuildmat.2023.134228.

[23] D. Wang, J. Wei, L. Hu, Q. Zhang, Y. Sun, and Y. Zheng, "Study of the Fatigue Damage Characteristics of Emulsified Asphalt Mastics," *Journal of Materials in Civil Engineering,* vol. 36, no. 11, p. 04024356, 2024/11/01 2024, doi: 10.1061/JMCEE7.MTENG-18009.

[24] J. Xu, Z. Fan, D. Wang, Z. Leng, G. Lu, and P. Liu, "Experimental characterization of the compatibility between bitumen and fillers from a perspective of bitumen components and filler characteristics," *Materials and Structures,* vol. 56, no. 7, p. 116, 2023/07/18 2023, doi: 10.1617/s11527-023-02207-8.

[25] F. Pan *et al.*, "Evaluation of Adhesive Properties of Different Mineral Compositions in Asphalt Mixtures with Experimental and Molecular Dynamics Analyses," *Buildings*, vol. 13, no. 5, doi: 10.3390/buildings13051207.

[26] Z. Du, X. Zhu, and Y. Zhang, "Diffusive Dynamics and Structural Organization of Moisture in Asphaltic Materials Based on Molecular Dynamics Simulation," *Journal of Materials in Civil Engineering,* vol. 33, no. 1, p. 04020403, 2021/01/01 2021, doi: 10.1061/(ASCE)MT.1943-5533.0003495.

[27] F. Li, L. Wang, X. Zhang, J. Li, Y. Gao, and N. Su, "Evaluating thermal activated coal gangue as alternative filler in asphalt binder using rheological experiments and molecular dynamic simulation," *Construction and Building Materials,* vol. 443, p. 137782, 2024/09/13/ 2024, doi: https://doi.org/10.1016/j.conbuildmat.2024.137782.

[28] X. Sun, H. Xu, X. Qin, Y. Zhu, and J. Jin, "Cross-scale study on the interaction behaviour of municipal solid waste incineration fly ash-asphalt mortar: a macro-micro approach," *International Journal of Pavement Engineering,* vol. 26, no. 1, p. 2469114, 2025/12/31 2025, doi: 10.1080/10298436.2025.2469114.

[29] R. W. Cahn, *The coming of materials science*. New York, 2001.

[30] H. Zhang *et al.*, "Unveiling micro-macro links in asphalt: An in-depth analysis of characterization and simulation approaches," *Fuel,* vol. 379, p. 132823, 2025/01/01/ 2025, doi: https://doi.org/10.1016/j.fuel.2024.132823.

[31] G. Li *et al.*, "Effect of genes on rheological properties of asphalt binders," *Fuel,* vol. 365, p. 131324, 2024/06/01/ 2024, doi: https://doi.org/10.1016/j.fuel.2024.131324.

[32] Q. T. Nguyen, B. V. Tran, M. L. Nguyen, T. T. N. Hoang, E. Chailleux, and V. P. Bui, "Relationships between 3D linear viscoelastic properties of bitumen, asphalt mastics and asphalt mixtures using micromechanical models," *Construction and Building Materials,* vol. 416, p. 135299, 2024/02/16/ 2024, doi: https://doi.org/10.1016/j.conbuildmat.2024.135299.

[33] B. Karami and M. H. Ghayesh, "Moving load excited dynamics of multi-layered imperfect microplates based on various micromechanical models," *International Journal of Engineering Science,* vol. 197, p. 104017, 2024/04/01/ 2024, doi: https://doi.org/10.1016/j.ijengsci.2024.104017.

[34] S. Ling, D. Jelagin, M. N. Partl, D. Sun, and H. Fadil, "Predicting the mechanical properties of semi-flexible pavement material with micromechanical modeling," *Materials & Design,* vol. 239, p. 112802, 2024/03/01/ 2024, doi: https://doi.org/10.1016/j.matdes.2024.112802.

[35] Z. Tao *et al.*, "Effects of specimen thickness and fiber length on tensile and cracking behavior of UHPFRC: Uniaxial tensile test and micromechanical modeling," *Cement and Concrete Composites,* vol. 155, p. 105828, 2025/01/01/ 2025, doi: https://doi.org/10.1016/j.cemconcomp.2024.105828.

[36] X. Yang *et al.*, "Investigation of graphite tailings as a substitute for filler in asphalt mastics," *International Journal of Pavement Engineering,* vol. 24, no. 1, p. 2172578, 2023/12/06 2023, doi: 10.1080/10298436.2023.2172578.

[37] J. Choudhary, B. Kumar, and A. Gupta, "Utilization of solid waste materials as alternative fillers in asphalt mixes: A review," *Construction and Building Materials,* vol. 234, p. 117271, 2020/02/20/ 2020, doi: https://doi.org/10.1016/j.conbuildmat.2019.117271.

[38] J. Choudhary, B. Kumar, and A. Gupta, "Application of waste materials as fillers in bituminous mixes," *Waste Management,* vol. 78, pp. 417-425, 2018/08/01/ 2018, doi: https://doi.org/10.1016/j.wasman.2018.06.009.

[39] W. Zhao and Q. Yang, "Life-cycle assessment of sustainable pavement based on the coordinated application of recycled asphalt pavement and solid waste: Environment and economy," *Journal of Cleaner Production,* vol. 434, p. 140203, 2024/01/01/ 2024, doi: https://doi.org/10.1016/j.jclepro.2023.140203.

[40] J. Wang *et al.*, "Performances of concrete with binder and/or aggregates replacement by all-solid waste materials," *Journal of Cleaner Production,* vol. 450, p. 141929, 2024/04/15/ 2024, doi: https://doi.org/10.1016/j.jclepro.2024.141929.

[41] R. Joumblat, A. Elkordi, J. Khatib, Z. Al Basiouni Al Masri, and J. Absi, "Characterisation of asphalt concrete mixes with municipal solid waste incineration fly ash used as fine aggregates substitution," *International Journal of Pavement Engineering,* vol. 24, no. 2, p. 2099855, 2023/01/28 2023, doi: 10.1080/10298436.2022.2099855.

[42] N. A. Mohd Shukry *et al.*, "Influence of diatomite filler on rheological properties of porous asphalt mastic," *International Journal of Pavement Engineering,* vol. 21, no. 4, pp. 428-436, 2020/03/20 2020, doi: 10.1080/10298436.2018.1483504.

[43] S. Li, F. Ni, Q. Dong, Z. Zhao, and X. Ma, "Effect of filler in asphalt mastic on rheological behaviour and susceptibility to rutting," *International Journal of Pavement Engineering,* vol. 22, no. 1, pp. 87-96, 2021/01/02 2021, doi: 10.1080/10298436.2019.1577423.

[44] J. Jiang, Y. Zhao, G. Lu, Y. Dai, F. Ni, and Q. Dong, "Effect of binder film distribution on the fatigue characteristics of asphalt Binder/Filler composite based on image analysis method," *Construction and Building Materials,* vol. 260, p. 119876, 2020/11/10/ 2020, doi: https://doi.org/10.1016/j.conbuildmat.2020.119876.

[45] K. Zhang, Z. Min, X. Hao, W. Huang, and K. Shao, "Experimental investigation of the properties of epoxy asphalt mastic," *Construction and Building Materials,* vol. 435, p. 136866, 2024/07/12/ 2024, doi: https://doi.org/10.1016/j.conbuildmat.2024.136866.

[46] D. Rys and C. Szydlowski, "Consideration of pseudo strain energy in determination of fatigue life and microdamage healing of asphalt mastics," *International Journal of Fatigue,* vol. 181, p. 108164, 2024/04/01/ 2024, doi: https://doi.org/10.1016/j.ijfatigue.2024.108164.

[47] C. Yan *et al.*, "Evaluation of high temperature performance of asphalt mastic sealing layer for hydraulic engineering," *Construction and Building Materials,* vol. 489, p. 142183, 2025/08/29/ 2025, doi: https://doi.org/10.1016/j.conbuildmat.2025.142183.

[48] Y. Tan and M. Guo, "Micro- and Nano-Characteration of Interaction Between Asphalt and Filler," *Journal of Testing and Evaluation,* vol. 42, no. 5, pp. 1089-1097, 2014, doi: 10.1520/JTE20130253.

[49] Q. Zhang and Z. Huang, "Investigation of the Microcharacteristics of Asphalt Mastics under Dry–Wet and Freeze–Thaw Cycles in a Coastal Salt Environment," *Materials*, vol. 12, no. 16, doi: 10.3390/ma12162627.

[50] W. Xu, X. Qiu, S. Xiao, H. Hong, F. Wang, and J. Yuan, "Characteristics and Mechanisms of Asphalt–Filler Interactions from a Multi-Scale Perspective," *Materials*, vol. 13, no. 12, doi: 10.3390/ma13122744.

[51] F. Li and Y. Yang, "Experimental investigation on the influence of interfacial effects of limestone and fly ash filler particles in asphalt binder on mastic aging behaviors," *Construction and Building Materials,* vol. 290, p. 123184, 2021/07/05/ 2021, doi: https://doi.org/10.1016/j.conbuildmat.2021.123184.

[52] S. M. Motevalizadeh, K. Mollenhauer, and J. Wetekam, "FTIR spectroscopy and multivariate discriminant analysis for classifying bituminous mastics: Exploring aging states and mastic composition," *Construction and Building Materials,* vol. 438, p. 137188, 2024/08/09/ 2024, doi: https://doi.org/10.1016/j.conbuildmat.2024.137188.

[53] M. Motevalizadeh and K. Mollenhauer, "Identification of chemical markers for blending phenomena in RAP mastics using FTIR spectroscopy and multivariate discriminant analysis," *Construction and Building Materials,* vol. 485, p. 141822, 2025/07/25/ 2025, doi: https://doi.org/10.1016/j.conbuildmat.2025.141822.

[54] S. M. Motevalizadeh and K. Mollenhauer, "Exploration of chemical changes in bituminous mastics induced by aging: insights from FTIR spectroscopy, DSR measurements, and machine learning," *International Journal of Pavement Engineering,* vol. 25, no. 1, p. 2418927, 2024/12/31 2024, doi: 10.1080/10298436.2024.2418927.

[55] Y. Cheng *et al.*, "Influence of the properties of filler on high and medium temperature performances of asphalt mastic," *Construction and Building Materials,* vol. 118, pp. 268-275, 2016/08/15/ 2016, doi: https://doi.org/10.1016/j.conbuildmat.2016.05.041.

[56] R. Moraes and H. U. Bahia, "Effect of mineral filler on changes in molecular size distribution of asphalts during oxidative ageing," *Road Materials and Pavement Design,* vol. 16, no. sup2, pp. 55-72, 2015/08/20 2015, doi: 10.1080/14680629.2015.1076998.

[57] B. Xing, C. Qian, H. Sun, J. Che, and Y. Lyu, "Reliability study on rheological and cracking behavior of mastics using different sized particles," *Advanced Powder Technology,* vol. 32, no. 6, pp. 2029-2042, 2021/06/01/ 2021, doi: https://doi.org/10.1016/j.apt.2021.04.015.

[58] B. Xing, W. Fan, L. Han, C. Zhuang, C. Qian, and X. Lv, "Effects of filler particle size and ageing on the fatigue behaviour of bituminous mastics," *Construction and Building Materials,* vol. 230, p. 117052, 2020/01/10/ 2020, doi: https://doi.org/10.1016/j.conbuildmat.2019.117052.

[59] M. Guo, Y. Tan, J. Yu, Y. Hou, and L. Wang, "A direct characterization of interfacial interaction between asphalt binder and mineral fillers by atomic force microscopy," *Materials and Structures,* vol. 50, no. 2, p. 141, 2017/02/24 2017, doi: 10.1617/s11527-017-1015-9.

[60] Y. Cheng *et al.*, "Characteristics and evolution mechanism of creep properties for asphalt binder/mastic under salt-erosion conditions," *Construction and Building Materials,* vol. 443, p. 137702, 2024/09/13/ 2024, doi: https://doi.org/10.1016/j.conbuildmat.2024.137702.

[61] C. Li *et al.*, "Microscopical properties of asphalt mastic under solution erosion and its deterioration mechanism," *Construction and Building Materials,* vol. 487, p. 142118, 2025/08/15/ 2025, doi: https://doi.org/10.1016/j.conbuildmat.2025.142118.

[62] N. Little Dallas and J. C. Petersen, "Unique Effects of Hydrated Lime Filler on the Performance-Related Properties of Asphalt Cements: Physical and Chemical Interactions Revisited," *Journal of Materials in Civil Engineering,* vol. 17, no. 2, pp. 207-218, 2005/04/01 2005, doi: 10.1061/(ASCE)0899-1561(2005)17:2(207).

[63] G. G. Al-Khateeb, M. F. Irfaeya, and T. S. Khedaywi, "A new simplified micromechanical model for asphalt mastic behavior," *Construction and Building Materials,* vol. 149, pp. 587-598, 2017/09/15/ 2017, doi: https://doi.org/10.1016/j.conbuildmat.2017.05.129.

[64] J. Zhang, Z. Fan, H. Wang, W. Sun, J. Pei, and D. Wang, "Prediction of dynamic modulus of asphalt mixture using micromechanical method with radial distribution functions," *Materials and Structures,* vol. 52, no. 2, p. 49, 2019/04/03 2019a, doi: 10.1617/s11527-019-1348-7.

[65] Y. Liu, Q. Dai, and Z. You, "Viscoelastic Model for Discrete Element Simulation of Asphalt Mixtures," *Journal of Engineering Mechanics,* vol. 135, no. 4, pp. 324-333, 2009/04/01 2009, doi: 10.1061/(ASCE)0733-9399(2009)135:4(324).

[66] T. Ma, H. Wang, D. Zhang, and Y. Zhang, "Heterogeneity effect of mechanical property on creep behavior of asphalt mixture based on micromechanical modeling and virtual creep test," *Mechanics of Materials,* vol. 104, pp. 49-59, 2017/01/01/ 2017, doi: https://doi.org/10.1016/j.mechmat.2016.10.003.

[67] J. Chen, H. Wang, and L. Li, "Virtual testing of asphalt mixture with two-dimensional and three-dimensional random aggregate structures," *International Journal of Pavement Engineering,* vol. 18, no. 9, pp. 824-836, 2017/09/02 2017, doi: 10.1080/10298436.2015.1066005.

[68] P. Karki, Y.-R. Kim, and D. N. Little, "Dynamic Modulus Prediction of Asphalt Concrete Mixtures through Computational Micromechanics," *Transportation Research Record,* vol. 2507, no. 1, pp. 1-9, 2015/01/01 2015, doi: 10.3141/2507-01.

[69] A. Shabani, D. Jelagin, and M. N. Partl, "Evaluating thermal contraction behaviour of basalt mastic using micromechanical finite element modelling," *Road Materials and Pavement Design,* vol. 26, no. sup1, pp. 194-213, 2025/05/20 2025, doi: 10.1080/14680629.2025.2483908.

[70] C. Pichler, R. Lackner, and E. Aigner, "Generalized self-consistent scheme for upscaling of viscoelastic properties of highly-filled matrix-inclusion composites – Application in the context of multiscale modeling of bituminous mixtures," *Composites Part B: Engineering,* vol. 43, no. 2, pp. 457-464, 2012/03/01/ 2012, doi: https://doi.org/10.1016/j.compositesb.2011.05.034.

[71] B. S. Underwood and Y. R. Kim, "A four phase micro-mechanical model for asphalt mastic modulus," *Mechanics of Materials,* vol. 75, pp. 13-33, 2014/08/01/ 2014, doi: https://doi.org/10.1016/j.mechmat.2014.04.001.

[72] C. Peng, J. Feng, S. Feiting, Z. Changjun, and F. Decheng, "Modified two-phase micromechanical model and generalized self-consistent model for predicting dynamic modulus

of asphalt concrete," *Construction and Building Materials,* vol. 201, pp. 33-41, 2019/03/20/ 2019, doi: https://doi.org/10.1016/j.conbuildmat.2018.12.165.

[73] X. Ma, H. Chen, P. Yang, M. Xing, D. Niu, and S. Wu, "Assessment of existing micro-mechanical models for asphalt mastic considering inter-particle and physico-chemical interaction," *Construction and Building Materials,* vol. 225, pp. 649-660, 2019/11/20/ 2019, doi: https://doi.org/10.1016/j.conbuildmat.2019.07.227.

[74] Y. Jia *et al.*, "Micromechanics prediction of dynamic modulus for asphalt mastic considering filler distribution characteristic: A new perspective," *Construction and Building Materials,* vol. 364, p. 129916, 2023/01/18/ 2023, doi: https://doi.org/10.1016/j.conbuildmat.2022.129916.

[75] P. Hajikarimi, A. Sadat Hosseini, and E. H. Fini, "A heterogeneous micromechanical model for bituminous composites containing rigid and flexible particulates," *Construction and Building Materials,* vol. 275, p. 122102, 2021/03/15/ 2021, doi: https://doi.org/10.1016/j.conbuildmat.2020.122102.

[76] Z. Wang, X. Jin, Y. Sun, and S. Wang, "Micromechanics approach to calculate the adsorbed asphalt film thickness on mineral fillers and evaluate physiochemical interactions," *International Journal of Pavement Engineering,* vol. 25, no. 1, p. 2303670, 2024/12/31 2024, doi: 10.1080/10298436.2024.2303670.

[77] J. Xu, Z. Fan, G. Lu, D. Wang, and P. Liu, "Effects of Bitumen Origins and Filler Types on the Micromechanics Prediction of Complex Modulus of Asphalt Mastics Considering Interparticle Interactions," *Journal of Materials in Civil Engineering,* vol. 36, no. 1, p. 04023521, 2024/01/01 2024, doi: 10.1061/JMCEE7.MTENG-16609.

[78] H. M. Yin, W. G. Buttlar, G. H. Paulino, and H. D. Benedetto, "Assessment of Existing Micro-mechanical Models for Asphalt Mastics Considering Viscoelastic Effects," *Road Materials and Pavement Design,* vol. 9, no. 1, pp. 31-57, 2008/01/01 2008, doi: 10.1080/14680629.2008.9690106.

[79] A. Rahim, A. Milad, N. I. Yusoff, G. Airey, and N. Thom, "Stiffening Effect of Fillers Based on Rheology and Micromechanics Models," *Applied Sciences*, vol. 11, no. 14, doi: 10.3390/app11146521.

[80] Z. Wang, N. Guo, X. Yang, and S. Wang, "Micromechanical Prediction Model of Viscoelastic Properties for Asphalt Mastic Based on Morphologically Representative Pattern Approach," *Advances in Materials Science and Engineering,* vol. 2020, no. 1, p. 7915140, 2020/01/01 2020, doi: https://doi.org/10.1155/2020/7915140.

[81] X. Jin *et al.*, "Research on Micro-Mechanics Modelling of TPU-Modified Asphalt Mastic," *Coatings*, vol. 12, no. 7*,* doi: 10.3390/coatings12071029.

[82] A. Tanakizadeh and G. Shafabakhsh, "Viscoelastic characterization of aged asphalt mastics using typical performance grading tests and rheological-micromechanical models," *Construction and Building Materials,* vol. 188, pp. 88-100, 2018/11/10/ 2018, doi: https://doi.org/10.1016/j.conbuildmat.2018.08.043.

[83] J. Pei, Z. Fan, P. Wang, J. Zhang, B. Xue, and R. Li, "Micromechanics prediction of effective modulus for asphalt mastic considering inter-particle interaction," *Construction and Building Materials,* vol. 101, pp. 209-216, 2015/12/30/ 2015, doi: https://doi.org/10.1016/j.conbuildmat.2015.10.053.

[84] A. Faheem and H. U. Bahia, "Conceptual phenomenological model for interaction of asphalt binders with mineral fillers," *Asphalt Paving Technology-Proceedings,* vol. 28, p. 679, 2009.

[85] A. F. Faheem and H. U. Bahia, "Modelling of Asphalt Mastic in Terms of Filler-Bitumen Interaction," *Road Materials and Pavement Design,* vol. 11, no. sup1, pp. 281-303, 2010/01/01 2010, doi: 10.1080/14680629.2010.9690335.

[86] X. Ma, H. Chen, X. Zhang, M. Xing, and P. Yang, "Effect of Asphalt Binder Characteristics on Filler–Asphalt Interactions and Asphalt Mastic Creep Properties," *Journal of Materials in Civil Engineering,* vol. 31, no. 8, p. 04019138, 2019/08/01 2019, doi: 10.1061/(ASCE)MT.1943-5533.0002773.

[87] J. Dong, K. Zhang, S. Liang, H. Ma, T. Huang, and R. Luo, "Evaluation of Moisture Sensitivity of Asphalt Mixtures Based on Surface Energy of Asphalt Mastic," *Journal of Materials in Civil Engineering,* vol. 36, no. 7, p. 04024191, 2024/07/01 2024, doi: 10.1061/JMCEE7.MTENG-17576.

[88] Y. Tan, X. Li, and J. Wu, "Evaluation indices of interaction ability of asphalt and aggregate based on rheological characteristics," *Journal of Wuhan University of Technology-Mater. Sci. Ed.,* vol. 27, no. 5, pp. 979-985, 2012/10/01 2012, doi: 10.1007/s11595-012-0585-1.

[89] G. Liu, Y. Jia, Y. Pan, T. Yang, Y. Zhao, and J. Zhang, "Quantitative comparison of evaluation indices for asphalt–filler interaction ability within filler critical volume fraction," *Road Materials and Pavement Design,* vol. 21, no. 4, pp. 906-926, 2020/05/18 2020, doi: 10.1080/14680629.2018.1531054.

[90] G. Liu, Y. Zhao, J. Zhou, J. Li, T. Yang, and J. Zhang, "Applicability of evaluation indices for asphalt and filler interaction ability," *Construction and Building Materials,* vol. 148, pp. 599-609, 2017/09/01/ 2017, doi: https://doi.org/10.1016/j.conbuildmat.2017.05.089.

[91] Y. Bi, R. Wei, R. Li, J. Zhang, and J. Pei, "Evaluation of rheological master curves of asphalt mastics and asphalt-filler interaction indices," *Construction and Building Materials,* vol. 265, p. 120046, 2020/12/30/ 2020, doi: https://doi.org/10.1016/j.conbuildmat.2020.120046.

[92] Y. Tan, J. Wu, X. Li, and L. Ji, "Evaluation indexes for interaction capability of asphalt and aggregate," *Journal of Harbin Institute of Technology,* vol. 41, no. 7, pp. 81-84, 2009.

[93] F. Li, Y. Yang, and L. Wang, "Evaluation of physicochemical interaction between asphalt binder and mineral filler through interfacial adsorbed film thickness," *Construction and Building Materials,* vol. 252, p. 119135, 2020/08/20/ 2020, doi: https://doi.org/10.1016/j.conbuildmat.2020.119135.

[94] Z. Hashin, "Complex moduli of viscoelastic composites—I. General theory and application to particulate composites," *International Journal of Solids and Structures,* vol. 6, no. 5, pp. 539-552, 1970/05/01/ 1970, doi: https://doi.org/10.1016/0020-7683(70)90029-6.

[95] Y. Tan and M. Guo, "Interfacial thickness and interaction between asphalt and mineral fillers," *Materials and Structures,* vol. 47, no. 4, pp. 605-614, 2014/04/01 2014, doi: 10.1617/s11527-013-0083-8.

[96] W. Wu *et al.*, "A review of asphalt-filler interaction: Mechanisms, evaluation methods, and influencing factors," *Construction and Building Materials,* vol. 299, p. 124279, 2021/09/13/ 2021, doi: https://doi.org/10.1016/j.conbuildmat.2021.124279.

[97] Y. Tan and M. Guo, "Using surface free energy method to study the cohesion and adhesion of asphalt mastic," *Construction and Building Materials,* vol. 47, pp. 254-260, 2013/10/01/ 2013, doi: https://doi.org/10.1016/j.conbuildmat.2013.05.067.

[98] Z. Liu and Y. Wang, "Laboratory research on asphalt mastic modified with activated carbon powder: rheology, micro-structure, and adhesion," *Road Materials and Pavement Design,* vol. 22, no. 6, pp. 1424-1441, 2021/06/03 2021, doi: 10.1080/14680629.2019.1691043.

[99] W. Xu, X. Qiu, S. Xiao, G. Hu, F. Wang, and J. Yuan, "Molecular Dynamic Investigations on the Adhesion Behaviors of Asphalt Mastic–Aggregate Interface," *Materials*, vol. 13, no. 22, doi: 10.3390/ma13225061.

[100] F. Li and Y. Yang, "Understanding the temperature and loading frequency effects on physicochemical interaction ability between mineral filler and asphalt binder using molecular dynamic simulation and rheological experiments," *Construction and Building Materials,* vol. 244, p. 118311, 2020/05/30/ 2020, doi: https://doi.org/10.1016/j.conbuildmat.2020.118311.

[101] H. Li, P. Chen, H. Wang, X. Luo, and Y. Zhang, "Pseudo energy-based crack initiation criterion for asphalt-filler composite system under a fatigue shear load," *Theoretical and Applied Fracture Mechanics,* vol. 119, p. 103333, 2022/06/01/ 2022, doi: https://doi.org/10.1016/j.tafmec.2022.103333.

[102] D. Luo, M. Guo, and Y. Tan, "Molecular Simulation of Minerals-Asphalt Interfacial Interaction," *Minerals*, vol. 8, no. 5, doi: 10.3390/min8050176.

[103] T. Radu *et al.*, "Industrial Wastes as Filler in Bituminous Materials for Construction Industry: Toward Circular Economy," *ACS Sustainable Chemistry & Engineering,* vol. 12, no. 1, pp. 433-441, 2024/01/08 2024, doi: 10.1021/acssuschemeng.3c05484.

[104] Y. Tian *et al.*, "Laboratory investigation on effects of solid waste filler on mechanical properties of porous asphalt mixture," *Construction and Building Materials,* vol. 279, p. 122436, 2021/04/12/ 2021, doi: https://doi.org/10.1016/j.conbuildmat.2021.122436.

[105] J. Choudhary, B. Kumar, and A. Gupta, "Evaluation of engineering, economic and environmental suitability of waste filler incorporated asphalt mixes and pavements," *Road*

Materials and Pavement Design, vol. 22, no. sup1, pp. S624-S640, 2021/06/01 2021, doi: 10.1080/14680629.2021.1905698.

[106] X. Xu, G. Xu, X. Huang, G. M. B. Alam, X. Chen, and A. Sreeram, "Material characterization and engineering performance evaluation of phosphogypsum as a high-performance filler for bituminous pavements," *Fuel,* vol. 393, p. 134977, 2025/08/01/ 2025, doi: https://doi.org/10.1016/j.fuel.2025.134977.

[107] B. Yang *et al.*, "Environmental impact of solid waste filler in porous asphalt mixture," *Construction and Building Materials,* vol. 303, p. 124447, 2021/10/11/ 2021, doi: https://doi.org/10.1016/j.conbuildmat.2021.124447.

[108] V. Antunes, A. C. Freire, L. Quaresma, and R. Micaelo, "Evaluation of waste materials as alternative sources of filler in asphalt mixtures," *Materials and Structures,* vol. 50, no. 6, p. 254, 2017/12/07 2017, doi: 10.1617/s11527-017-1126-3.

[109] J. Choudhary, B. Kumar, and A. Gupta, "Potential utilization of construction wastes in asphalt pavements as fillers using ranking framework," *Construction and Building Materials,* vol. 277, p. 122262, 2021/03/29/ 2021, doi: https://doi.org/10.1016/j.conbuildmat.2021.122262.

[110] F. Russo *et al.*, "Sustainable asphalt mastics made up recycling waste as filler," *Journal of Environmental Management,* vol. 301, p. 113826, 2022/01/01/ 2022, doi: https://doi.org/10.1016/j.jenvman.2021.113826.

[111] F. Russo, R. Veropalumbo, C. Oreto, D. Cassese, B. Papa, and S. Malvezzi, "Reusing bottom ash as a filler from a Waste-to-Energy plant for making asphalt mastics," *Case Studies in Construction Materials,* vol. 17, p. e01406, 2022/12/01/ 2022, doi: https://doi.org/10.1016/j.cscm.2022.e01406.

[112] J. Lin *et al.*, "Using recycled waste glass fiber reinforced polymer (GFRP) as filler to improve the performance of asphalt mastics," *Journal of Cleaner Production,* vol. 336, p. 130357, 2022/02/15/ 2022, doi: https://doi.org/10.1016/j.jclepro.2022.130357.

[113] L. Ou, R. Li, H. Zhu, H. Zhao, and R. Chen, "Upcycling waste phosphogypsum as an alternative filler for asphalt pavement," *Journal of Cleaner Production,* vol. 420, p. 138332, 2023/09/25/ 2023, doi: https://doi.org/10.1016/j.jclepro.2023.138332.

[114] P. Yin, B. Pan, and Y. Liu, "Effect of different filler substitution ratios on the service performance of asphalt mixtures: Using coal-based synthetic natural gas slag as substitute filler," *Construction and Building Materials,* vol. 456, p. 139245, 2024/12/20/ 2024, doi: https://doi.org/10.1016/j.conbuildmat.2024.139245.

[115] P. Yin, B. Pan, Y. Liu, F. Liu, and B. Wang, "Establishment and evaluation of dynamic viscoelasticity constitutive model for asphalt mixtures based on PCA model: Utilizing coal-based synthetic natural gas slag and phosphogypsum whisker as substitute fillers," *Construction and Building Materials,* vol. 446, p. 137974, 2024/10/04/ 2024, doi: https://doi.org/10.1016/j.conbuildmat.2024.137974.

[116] F. Li, X. Zhao, and X. Zhang, "Utilizing original and activated coal gangue wastes as alternative mineral fillers in asphalt binder: Perspectives of rheological properties and asphalt-filler interaction ability," *Construction and Building Materials,* vol. 365, p. 130069, 2023/02/15/ 2023, doi: https://doi.org/10.1016/j.conbuildmat.2022.130069.

[117] B. Lei *et al.*, "Recycling of copper tailing as filler material in asphalt paving mastic: A sustainable solution for mining waste recovery," *Case Studies in Construction Materials,* vol. 20, p. e03237, 2024/07/01/ 2024, doi: https://doi.org/10.1016/j.cscm.2024.e03237.

[118] H. Wang *et al.*, "Experimental study on the aging behavior of modified asphalt with different types of fine solid wastes under different aging conditions," *Construction and Building Materials,* vol. 291, p. 123308, 2021/07/12/ 2021, doi: https://doi.org/10.1016/j.conbuildmat.2021.123308.

[119] Y. Sun, X. Zhang, J. Chen, J. Liao, C. Shi, and C. Huang, "Mixing design and performance of porous asphalt mixtures containing solid waste," *Case Studies in Construction Materials,* vol. 21, p. e03644, 2024/12/01/ 2024, doi: https://doi.org/10.1016/j.cscm.2024.e03644.

[120] B. Ren, Y. Zhao, H. Bai, S. Kang, T. Zhang, and S. Song, "Eco-friendly geopolymer prepared from solid wastes: A critical review," *Chemosphere,* vol. 267, p. 128900, 2021/03/01/ 2021, doi: https://doi.org/10.1016/j.chemosphere.2020.128900.

[121] J. Guo, Y. Bao, and M. Wang, "Steel slag in China: Treatment, recycling, and management," *Waste Management,* vol. 78, pp. 318-330, 2018/08/01/ 2018, doi: https://doi.org/10.1016/j.wasman.2018.04.045.

[122] S. Liu, W. Liu, F. Jiao, W. Qin, and C. Yang, "Production and resource utilization of flue gas desulfurized gypsum in China - A review," *Environmental Pollution,* vol. 288, p. 117799, 2021/11/01/ 2021, doi: https://doi.org/10.1016/j.envpol.2021.117799.

[123] Y. Li *et al.*, "Environmental impact analysis of blast furnace slag applied to ordinary Portland cement production," *Journal of Cleaner Production,* vol. 120, pp. 221-230, 2016/05/01/ 2016, doi: https://doi.org/10.1016/j.jclepro.2015.12.071.

[124] Y. Yu, Y. Ge, and P. Liu, "Recycling of expired cement and aged supplementary cementitious materials based on close packing theory and space filling effect," *Journal of Cleaner Production,* vol. 239, p. 118064, 2019/12/01/ 2019, doi: https://doi.org/10.1016/j.jclepro.2019.118064.

[125] F. Han, L. Li, S. Song, and J. Liu, "Early-age hydration characteristics of composite binder containing iron tailing powder," *Powder Technology,* vol. 315, pp. 322-331, 2017/06/15/ 2017, doi: https://doi.org/10.1016/j.powtec.2017.04.022.

[126] N. Zhang, B. Tang, and X. Liu, "Cementitious activity of iron ore tailing and its utilization in cementitious materials, bricks and concrete," *Construction and Building Materials,* vol. 288, p. 123022, 2021/06/21/ 2021, doi: https://doi.org/10.1016/j.conbuildmat.2021.123022.

[127] D. D. Li and M. L. Greenfield, "Chemical compositions of improved model asphalt systems for molecular simulations," *Fuel,* vol. 115, pp. 347-356, 2014/01/01/ 2014, doi: https://doi.org/10.1016/j.fuel.2013.07.012.

[128] Z. Fan *et al.*, "Molecular Insights into the Adsorption Configuration of Bitumen Colloidal on Aggregate Surface," *Journal of Materials in Civil Engineering,* vol. 34, no. 4, p. 04022033, 2022/04/01 2022, doi: 10.1061/(ASCE)MT.1943-5533.0004180.

[129] Z. Fan, F. Pan, L. Sun, D. Wang, and P. Liu, "Multiscale investigation on bitumen-aggregate interfacial debonding using molecular dynamics and finite element method," *Construction and*

Building Materials, vol. 397, p. 132326, 2023/09/15/ 2023, doi: https://doi.org/10.1016/j.conbuildmat.2023.132326.

[130] Z. Fan, "Multiscale study of the bitumen-aggregate interfacial behavior based on molecular dynamics simulation and micromechanics," Dissertation, Rheinisch-Westfälische Technische Hochschule Aachen, 2021.

[131] J. Xu, Z. Fan, F. Accornero, D. Wang, A. Carpinteri, and J. Cai, "Atomic-Scale Mechanism of Bitumen–Aggregate Interfacial Cracking: Insights from Molecular Dynamics Simulation," *Journal of Materials in Civil Engineering,* vol. 37, no. 6, p. 04025130, 2025/06/01 2025, doi: 10.1061/JMCEE7.MTENG-19933.

[132] C. J. van Oss, M. K. Chaudhury, and R. J. Good, "Monopolar surfaces," *Advances in Colloid and Interface Science,* vol. 28, pp. 35-64, 1987/01/01/ 1987, doi: https://doi.org/10.1016/0001-8686(87)80008-8.

[133] Z. Al Basiouni Al Masri, A. Alarab, G. Chehab, and A. Tehrani-Bagha, "Assessing Moisture Damage of Asphalt-Aggregate Systems Using Principles of Thermodynamics: Effects of Recycled Materials and Binder Aging," *Journal of Materials in Civil Engineering,* vol. 31, no. 9, p. 04019190, 2019/09/01 2019, doi: 10.1061/(ASCE)MT.1943-5533.0002846.

[134] Q. Lv, W. Huang, N. Tang, and F. Xiao, "Comparison and relationship between indices for the characterization of the moisture resistance of asphalt–aggregate systems," *Construction and Building Materials,* vol. 168, pp. 580-589, 2018/04/20/ 2018, doi: https://doi.org/10.1016/j.conbuildmat.2018.02.177.

[135] J. Deng, P. Yang, Q. Dong, and D. Wang, "Research on CTOD for low-cycle fatigue analysis of central-through cracked plates considering accumulative plastic strain," *Engineering Fracture Mechanics,* vol. 154, pp. 128-139, 2016/03/01/ 2016, doi: https://doi.org/10.1016/j.engfracmech.2015.11.021.

[136] Z. Du, X. Zhu, F. Li, S. Zhou, and Z. Dai, "Failure of the Asphalt–Aggregate Interface under Tensile Stress: Insight from Molecular Dynamics," *Journal of Materials in Civil Engineering,* vol. 33, no. 3, p. 04021008, 2021/03/01 2021, doi: 10.1061/(ASCE)MT.1943-5533.0003601.

[137] G. Xu and H. Wang, "Molecular dynamics study of interfacial mechanical behavior between asphalt binder and mineral aggregate," *Construction and Building Materials,* vol. 121, pp. 246-254, 2016/09/15/ 2016, doi: https://doi.org/10.1016/j.conbuildmat.2016.05.167.

[138] C. Li, Z. Chen, S. Wu, B. Li, J. Xie, and Y. Xiao, "Effects of steel slag fillers on the rheological properties of asphalt mastic," *Construction and Building Materials,* vol. 145, pp. 383-391, 2017/08/01/ 2017, doi: https://doi.org/10.1016/j.conbuildmat.2017.04.034.

[139] Q. Li, Y. Qiu, A. Rahman, and H. Ding, "Application of steel slag powder to enhance the low-temperature fracture properties of asphalt mastic and its corresponding mechanism," *Journal of Cleaner Production,* vol. 184, pp. 21-31, 2018/05/20/ 2018, doi: https://doi.org/10.1016/j.jclepro.2018.02.245.

[140] K.-z. Yan, H.-b. Xu, and H.-l. Zhang, "Effect of mineral filler on properties of warm asphalt mastic containing Sasobit," *Construction and Building Materials,* vol. 48, pp. 622-627, 2013/11/01/ 2013, doi: https://doi.org/10.1016/j.conbuildmat.2013.07.085.

[141] D. Movilla-Quesada, A. C. Raposeiras, D. Castro-Fresno, and D. Peña-Mansilla, "Experimental study on stiffness development of asphalt mixture containing cement and Ca(OH)2 as contribution filler," *Materials & Design,* vol. 74, pp. 157-163, 2015/06/05/ 2015, doi: https://doi.org/10.1016/j.matdes.2015.02.026.

[142] Q. Yang *et al.*, "Performance evaluation of bitumen with a homogeneous dispersion of carbon nanotubes," *Carbon,* vol. 158, pp. 465-471, 2020/03/01/ 2020, doi: https://doi.org/10.1016/j.carbon.2019.11.013.

[143] K. R. Usman *et al.*, "A comparative assessment of the physical and microstructural properties of waste garnet generated from automated and manual blasting process," *Case Studies in Construction Materials,* vol. 14, p. e00474, 2021/06/01/ 2021, doi: https://doi.org/10.1016/j.cscm.2020.e00474.

[144] T. Li, H. Carreño Gómez Nicolás, G. Lu, D. Liang, D. Wang, and M. Oeser, "Use of Polyurethane Precursor–Based Modifier as an Eco-Friendly Approach to Improve Performance of Asphalt," *Journal of Transportation Engineering, Part B: Pavements,* vol. 147, no. 3, p. 04021031, 2021/09/01 2021, doi: 10.1061/JPEODX.0000279.

[145] J. Zhang, L. F. Walubita, A. N. M. Faruk, P. Karki, and G. S. Simate, "Use of the MSCR test to characterize the asphalt binder properties relative to HMA rutting performance – A laboratory study," *Construction and Building Materials,* vol. 94, pp. 218-227, 2015/09/30/ 2015, doi: https://doi.org/10.1016/j.conbuildmat.2015.06.044.

[146] M. Sabouri, D. Mirzaiyan, and A. Moniri, "Effectiveness of Linear Amplitude Sweep (LAS) asphalt binder test in predicting asphalt mixtures fatigue performance," *Construction and Building Materials,* vol. 171, pp. 281-290, 2018/05/20/ 2018, doi: https://doi.org/10.1016/j.conbuildmat.2018.03.146.

[147] B. Li, P. Liu, Y. Zhao, X. Li, and G. Cao, "Effect of graphene oxide in different phases on the high temperature rheological properties of asphalt based on grey relational and principal component analysis," *Construction and Building Materials,* vol. 362, p. 129714, 2023/01/02/ 2023, doi: https://doi.org/10.1016/j.conbuildmat.2022.129714.

[148] M. Gong, H. Zhang, B. Yang, and Q. Sun, "Analysis of the influencing factors on the anti-aging performance of a hybrid-modified asphalt mixture using the grey relational theory," *International Journal of Pavement Engineering,* vol. 22, no. 5, pp. 597-612, 2021/04/16 2021, doi: 10.1080/10298436.2019.1630738.

[149] Y.-R. Kim, I. Pinto, and S.-W. Park, "Experimental evaluation of anti-stripping additives in bituminous mixtures through multiple scale laboratory test results," *Construction and Building Materials,* vol. 29, pp. 386-393, 2012/04/01/ 2012, doi: https://doi.org/10.1016/j.conbuildmat.2011.10.012.

[150] D. Fee, R. Maldonado, G. Reinke, and H. Romagosa, "Polyphosphoric Acid Modification of Asphalt," *Transportation Research Record,* vol. 2179, no. 1, pp. 49-57, 2010/01/01 2010, doi: 10.3141/2179-06.

[151] A. Hung and E. H. Fini, "Surface Morphology and Chemical Mapping of UV-Aged Thin Films of Bitumen," *ACS Sustainable Chemistry & Engineering,* vol. 8, no. 31, pp. 11764-11771, 2020/08/10 2020, doi: 10.1021/acssuschemeng.0c03877.

[152] H. Chen and H. U. Bahia, "Modelling effects of aging on asphalt binder fatigue using complex modulus and the LAS test," *International Journal of Fatigue,* vol. 146, p. 106150, 2021/05/01/ 2021, doi: https://doi.org/10.1016/j.ijfatigue.2021.106150.

[153] R. Velasquez, H. Tabatabaee, and H. Bahia, "Low Temperature Cracking Characterization of Asphalt Binders by Means of the Single-Edge Notch Bending (SENB) Test," *Journal of the Association of Asphalt Paving Technologists,* vol. 80, 2011.

[154] J. Xu, Z. Guo, G. Lu, Z. Fan, D. Wang, and M. Oeser, "Reclamation of waste oils in asphalt modification towards enhanced low-temperature performance of pavement in cold region," *International Journal of Pavement Engineering,* pp. 1-16, 2022, doi: 10.1080/10298436.2022.2069244.

[155] H. Wang, X. Liu, H. Zhang, P. Apostolidis, S. Erkens, and A. Skarpas, "Micromechanical modelling of complex shear modulus of crumb rubber modified bitumen," *Materials & Design,* vol. 188, p. 108467, 2020/03/01/ 2020, doi: https://doi.org/10.1016/j.matdes.2019.108467.

[156] H. Wang, H. Zhang, X. Liu, A. Skarpas, S. Erkens, and Z. Leng, "Micromechanics-based complex modulus prediction of crumb rubber modified bitumen considering interparticle interactions," *Road Materials and Pavement Design,* vol. 22, no. sup1, pp. S251-S268, 2021/06/01 2021, doi: 10.1080/14680629.2021.1899965.

[157] R. M. Christensen and K. H. Lo, "Solutions for effective shear properties in three phase sphere and cylinder models," *Journal of the Mechanics and Physics of Solids,* vol. 27, no. 4, pp. 315-330, 1979/08/01/ 1979, doi: https://doi.org/10.1016/0022-5096(79)90032-2.

[158] D. Li, Z. Leng, H. Wang, R. Chen, and F. Wellner, "Structural and mechanical evolution of the multiphase asphalt rubber during aging based on micromechanical back-calculation and experimental methods," *Materials & Design,* vol. 215, p. 110421, 2022/03/01/ 2022, doi: https://doi.org/10.1016/j.matdes.2022.110421.

[159] R. McLaughlin, "A study of the differential scheme for composite materials," *International Journal of Engineering Science,* vol. 15, no. 4, pp. 237-244, 1977/01/01/ 1977, doi: https://doi.org/10.1016/0020-7225(77)90058-1.

[160] M. Kim and G. Buttlar William, "Differential Scheme Effective Medium Theory for Hot-Mix Asphalt E∗ Prediction," *Journal of Materials in Civil Engineering,* vol. 23, no. 1, pp. 69-78, 2011/01/01 2011, doi: 10.1061/(ASCE)MT.1943-5533.0000023.

[161] J. Zhang, Z. Fan, J. Pei, R. Li, and M. Chang, "Multiscale Validation of the Applicability of Micromechanical Models for Asphalt Mixture," *Advances in Materials Science and Engineering,* vol. 2015, no. 1, p. 937126, 2015/01/01 2015, doi: https://doi.org/10.1155/2015/937126.

[162] H. M. Yin, L. Z. Sun, and G. H. Paulino, "Micromechanics-based elastic model for functionally graded materials with particle interactions," *Acta Materialia,* vol. 52, no. 12, pp. 3535-3543, 2004/07/12/ 2004, doi: https://doi.org/10.1016/j.actamat.2004.04.007.

[163] J. W. Ju and T. M. Chen, "Micromechanics and effective moduli of elastic composites containing randomly dispersed ellipsoidal inhomogeneities," *Acta Mechanica,* vol. 103, no. 1, pp. 103-121, 1994/03/01 1994b, doi: 10.1007/BF01180221.

[164] J. W. Ju and T. M. Chen, "Effective elastic moduli of two-phase composites containing randomly dispersed spherical inhomogeneities," *Acta Mechanica,* vol. 103, no. 1, pp. 123-144, 1994/03/01 1994a, doi: 10.1007/BF01180222.

[165] M. S. Wertheim, "Exact Solution of the Percus-Yevick Integral Equation for Hard Spheres," *Physical Review Letters,* vol. 10, no. 8, pp. 321-323, 04/15/ 1963, doi: 10.1103/PhysRevLett.10.321.

[166] G. J. Throop and R. J. Bearman, "Numerical Solutions of the Percus—Yevick Equation for the Hard-Sphere Potential," *Journal of Chemical Physics,* vol. 42, pp. 2408-2411, April 01, 1965 1965, doi: 10.1063/1.1696308.

[167] X. Cheng, B. Zhong, and Z. Wu, "Material-specific coefficients C1 and C2 in Williams-Landel-Ferry equations and phase transition behaviors of asphalt binder reinforced by various basalt fibers," *Case Studies in Construction Materials,* vol. 21, p. e03619, 2024/12/01/ 2024, doi: https://doi.org/10.1016/j.cscm.2024.e03619.

[168] L. Xi, R. Luo, Q. Ma, C. Tu, and Y. Ibrahim Shah, "An improved method to establish continuous relaxation spectrum of asphalt materials," *Construction and Building Materials,* vol. 354, p. 129182, 2022/11/07/ 2022, doi: https://doi.org/10.1016/j.conbuildmat.2022.129182.

[169] H. Ceylan, W. Schwartz Charles, S. Kim, and K. Gopalakrishnan, "Accuracy of Predictive Models for Dynamic Modulus of Hot-Mix Asphalt," *Journal of Materials in Civil Engineering,* vol. 21, no. 6, pp. 286-293, 2009/06/01 2009, doi: 10.1061/(ASCE)0899-1561(2009)21:6(286).

[170] Q. Lv, W. Huang, H. Sadek, F. Xiao, and C. Yan, "Investigation of the rutting performance of various modified asphalt mixtures using the Hamburg Wheel-Tracking Device test and Multiple Stress Creep Recovery test," *Construction and Building Materials,* vol. 206, pp. 62-70, 2019/05/10/ 2019, doi: https://doi.org/10.1016/j.conbuildmat.2019.02.015.

[171] J. Zhang, W. Huang, Y. Zhang, Q. Lv, and C. Yan, "Evaluating four typical fibers used for OGFC mixture modification regarding drainage, raveling, rutting and fatigue resistance," *Construction and Building Materials,* vol. 253, p. 119131, 2020/08/30/ 2020, doi: https://doi.org/10.1016/j.conbuildmat.2020.119131.

[172] F. Zou *et al.*, "Kinetics and toxicological potential of heavy metal leaching from asphalt pavements," *Science of The Total Environment,* vol. 912, p. 169193, 2024/02/20/ 2024, doi: https://doi.org/10.1016/j.scitotenv.2023.169193.

[173] F. Zou, Z. Leng, D. Li, S. Zhang, Y. L. Yaphary, and G. Lu, "Leaching potential of metals and PAHs of asphalt rubber paving materials," *Transportation Research Part D: Transport and Environment,* vol. 125, p. 103984, 2023/12/01/ 2023, doi: https://doi.org/10.1016/j.trd.2023.103984.

[174] E. M. Technical Committee ISO/TC 207, *Environmental management-life cycle assessment-principles and framework*. International Organization for Standardization, 2006.

[175] D. Hall, "Waste management in Europe: framework, trends and issues," 2010.

[176] E. M. Alejandre, P. M. van Bodegom, and J. B. Guinée, "Towards an optimal coverage of ecosystem services in LCA," *Journal of Cleaner Production,* vol. 231, pp. 714-722, 2019/09/10/ 2019, doi: https://doi.org/10.1016/j.jclepro.2019.05.284.

[177] M. A. J. Huijbregts *et al.*, "ReCiPe2016: a harmonised life cycle impact assessment method at midpoint and endpoint level," *The International Journal of Life Cycle Assessment,* vol. 22, no. 2, pp. 138-147, 2017/02/01 2017, doi: 10.1007/s11367-016-1246-y.